Alma Mater Studiorum – Università di Bologna

DOTTORATO DI RICERCA IN

INGEGNERIA CIVILE ED AMBIENTALE

Ciclo XXVI

Settore Concorsuale di afferenza: **08/B2**

Settore Scientifico disciplinare: **ICAR 08**

Behaviour and applications of elastic waves in structures and metamaterials

Ing. MARCO MINIACI

Coordinatore Dottorato	Relatore
Prof. Ing. A. LAMBERTI	**Prof. Ing. E. VIOLA**
	Co-Relatore
	Ing. A. MARZANI

19 Maggio 2014

Behaviour and applications of elastic waves in structures and metamaterials

Marco Miniaci

Department of Civil, Chemical, Environmental and Materials Engineering - http://www.dicam.unibo.it

University of Bologna

A thesis submitted for the degree of

Doctor of Philosophy

19 May 2014

I would like to dedicate this thesis to my loving family.

Acknowledgements

I would like to express my deepest gratitude to my supervisor Professor Erasmo Viola for his continuous and excellent guidance throughout the whole thesis and to Researcher Alessandro Marzani for the invaluable time spent together to review the present work and for having introduced me to Acoustic Metamaterials.

A special thanks goes to Professor Wieslaw Ostachowicz and his team from Polish Academy of Sciences for their insightful discussions during my six-months stage abroad and for laser vibrometric measurements assistance.

I also want to thank Researchers Luca De Marchi and Nicola Testoni, who supported me with their experience in the ultrasonic experimental tests and Professor Massimo Garai and his team for the acoustic measurements.

The author would like to specifically thank Roberto Carli, Davide Betti, Gregorio Bartolotta for their infinite patience shown during the preparation of the experiments and all my current and former colleagues (especially Matteo Mazzotti), for their constant help and for creating such a friendly working environment.

A special thanks goes to Mattea Marino with whom I constantly shared my fears, desires and joys.

Finally, I am forever indebted to my family: my brother Gianluca, my father Lucio, my mother Maria Antonietta for their understanding, endless love and encouragement.

To them I dedicate this thesis.

Abstract

The present work focuses on elastic waves behaviour in ordinary structures as well as in acousto-elastic metamaterials via numerical and experimental applications.

After a brief introduction on (i) the behaviour of elastic guided waves in the framework of non-destructive evaluation (NDE) and structural health monitoring (SHM) and (ii) on the study of elastic waves propagation in acousto-elastic metamaterials, dispersion curves for thin walled beams and arbitrary cross-section waveguides are extracted via Semi-Analytical Finite Element (SAFE) methods. After complex multi-modal and dispersive behaviour for such geometries is predicted, a novel strategy tackling signal dispersion to locate defects in the case of irregular waveguides is proposed and numerically validated. Finally, a time-reversal and laser vibrometry based procedure for impact location is numerically and experimentally tested on a flat aluminium plate reinforced by two unidirectional eccentric stiffeners.

In the second part of the thesis, a general introduction and a brief review of the basic definitions necessary to describe elastic and acoustic metamaterials is provided. In addition, a numerical approach to extract dispersion properties in such structures is highlighted. Afterwards, solid-solid and solid-fluid phononic systems are discussed via numerical applications. In particular, band structures and transmission power spectra are predicted for 1P-2D, 2P-2D and 2P-3D phononic systems. In addition, attenuation bands in the ultrasonic as well as in the sonic frequency regimes are experimentally investigated. In the experimental validation, PZTs in a pitch-catch configuration and laser vibrometric measurements are performed on a PVC phononic plate in the ultrasonic frequency range and sound insulation index is computed for a 2P-3D phononic barrier in the sonic frequency range. In both cases the comparison between numerical and experimental results confirms the existence of the numerical predicted band gaps.

Finally, the feasibility of an innovative passive isolation strategy based on giant elastic metamaterials is numerically proved to be practical for civil structures. In particular, attenuation of seismic waves is demonstrated via finite elements analyses. Further, a parametric study shows that depending on the soil properties, such an earthquake-proof barrier could lead to significant reduction of the superstructure displacement.

Contents

Contents **v**

List of Figures **ix**

1 Introduction **1**

1.1 Introduction to GWs-based NDE 2
1.2 Introduction to metamaterials 3
1.3 Thesis outline 6

I Elastic guided waves **9**

2 Dispersion properties prediction **11**

2.1 Introduction 11
2.2 Dispersion curves extraction in thin walled beams structures . . . 12
  2.2.1 Mathematical formulation 13
    2.2.1.1 In-plane problem 13
    2.2.1.2 Out-of-plane problem 15
    2.2.1.3 Solution method 17
  2.2.2 Numerical applications and discussions 19
2.3 Dispersion curves extraction in waveguides with arbitrary cross-section 24
  2.3.1 Mathematical formulation 24
  2.3.2 Numerical applications and discussions 26
2.4 Conclusions 29

3 Dispersion compensation for defect detection and localization 31
3.1 Introduction 31
3.2 Group delay computation 33
3.2.1 Segments with uniform cross-section 34
3.2.2 Tapered segments 35
3.2.3 Group-delay of the reference (RP) and irregular (IP) portions 36
3.3 Signal dispersion compensation 37
3.3.1 The Warped Frequency Transform (WFT) 37
3.3.2 Step 1: compensation of dispersion due to the reference portion (RP) of the waveguide 38
3.3.3 Step 2: compensation of dispersion due to the irregular portion (IP) of the waveguide 40
3.4 Numerical validation 41
3.4.1 Straight waveguides with symmetric and antisymmetric tapering 44
3.4.2 Irregular waveguide with straight, curved and tapered segments 49
3.5 Conclusions 52

4 Time-reversal and laser-vibrometry based impact location 53
4.1 Introduction 53
4.2 A time-reversal based procedure for impact location 55
4.2.1 Time-reversal basic principles 55
4.2.2 Time-reversal for Lamb waves 57
4.2.3 Procedure description 61
4.3 Impact localization: numerical and experimental results 64
4.3.1 Description of the tested element 64
4.3.2 Numerical application 66
4.3.3 Experimental application 69
4.3.4 Further considerations on the acquired signals 71
4.4 Conclusions 71
4.5 Funding 74
4.6 Acknowledgements 75

II Acoustic metamaterials **77**

5 Elastic and acoustic metamaterials **79**
5.1 Introduction 79
5.2 Basic definitions 80
5.2.1 Crystal lattice 80
5.2.2 Basis vectors 81
5.2.3 The unit cell 82
5.2.4 Primitive versus non-primitive cells 83
5.2.5 Reciprocal lattice 83
5.2.6 Wigner-Seitz primitive cell 85
5.3 Phononic materials 86
5.4 Dispersion properties 89
5.4.1 Finite Element discretization 91

6 Numerical modelling of stress waves in metamaterials **95**
6.1 Introduction 95
6.2 1P-2D phononic materials 95
6.2.1 Dispersion properties of phononic materials 96
6.2.2 Effect of phononic region length 101
6.2.3 Effect of an applied prestrain/prestress field 107
6.2.3.1 Lamb waves in ordinary plates under prestrain . 109
6.2.3.2 Lamb waves in phononic plates under prestrain . 110
6.3 2P-2D phononic materials 111
6.3.1 Solid-solid PM 112
6.3.1.1 Transmission spectra 115
6.3.2 Solid-fluid PM 116
6.3.2.1 Band structures in sonic metamaterials 122
6.3.2.2 Sound barriers 123
6.3.2.3 FEM wave propagation analyses 125
6.3.2.4 Transmission power spectrum and pressure maps in the audible frequency range 128
6.3.2.5 Influence of the rows number on the PM attenuation 129

6.4 2P-3D Phononic materials 133
    6.4.1 Dispersion diagram in a phononic slab 135
    6.4.2 Effects of the slab thickness on dispersion diagram 135
    6.4.3 FE wave propagation in a 3D phononic system 137

7 Experimental applications **149**
7.1 Phononic materials in the ultrasonic range 149
    7.1.1 Introduction 149
    7.1.2 Sample description 150
    7.1.3 PZT in pitch-catch configuration 150
    7.1.4 Laser vibrometer experiments 153
    7.1.5 Results and discussion 160
7.2 Phononic materials in the audio range 161
    7.2.1 Introduction 161
    7.2.2 Sample description 163
    7.2.3 Measurements description 163
    7.2.4 Results and discussion 166

8 Seismic shields **169**
8.1 Introduction and state of the art 169
8.2 A potential passive seismic isolation strategy 172
    8.2.1 Strategy overview 175
8.3 Dispersion relations and attenuation zones 178
8.4 Parametric study 180
    8.4.1 Filling fraction 182
    8.4.2 Hosting material parameters investigation 182
    8.4.3 Hard material core parameters investigation 184
    8.4.4 Soft material parameters investigation 186
8.5 Numerical validation 187
    8.5.1 Responses to incident waves 189
8.6 Conclusions: some design considerations 195

References **199**

List of Figures

2.1 Schematic representation of the waveguide (a) and generic element (b). 14

2.2 (a) Multiply connected cross-section (8 elements, 16 nodes, 64 dofs); (b) simply connected cross-section (8 elements, 17 nodes, 68 dofs); (c) zoom for the line cut. 19

2.3 Phase, Attenuation and Group velocity curves for the multiply connected section (a, c, e) and for the simply connected section (b, d, f). 20

2.4 Differences emphasize between the Euler-Bernoulli EB beam theory and the $SAFE$ theory predictions in the $0-0.4$ kHz frequency range. 21

2.5 Wavestructures for the multiply connected cross-section calculated at 2 kHz frequency. 22

2.6 Wavestructures for the simply connected cross-section calculated at 0.5 kHz frequency. 23

2.7 example 25

2.8 Analysed cases: from a pristine cross-section (a) to damaged cross-sections (b,c,d). 27

2.9 Phase velocities curves and waveshapes for the pristine case. 28

2.10 (a) L(0,1) phase velocity dispersion curves for the four considered cases. (b) L(0,1) sensitivity curves for the elliptical notch. 29

3.1 Schematic representation of an irregular waveguide composed by uniform ($\bar{AB}$, $\bar{CD}$ and $\bar{FG}$), tapered ($\bar{BC}$ and $\bar{DE}$) and curved ($\bar{EF}$) segments. 34

3.2 Sketch of a waveguide segment with varying cross-section $\Omega_1 \rightarrow \Omega_N$. 36

3.3 Warping map $w(f)$ for A_0 wave dispersion compensation and its functional inverse $w^{-1}(f)$ designed according to Eq. (3.8). 38

3.4 Group velocity dispersion curves $cg(f, h)$ for the Lamb waves propagating in an aluminium $h = 1$ mm thick-plate (Young modulus $E = 69$ GPa, Poisson's coefficient $\nu = 0.33$, density $\rho = 2700\ kg/m^3$). 39

3.5 Schematic representation of the three straight irregular plate waveguides considered as cases (i), (ii) and (iii). Please note the different scale in the x and y-direction. 42

3.6 Schematic representation of the irregular waveguide considered as case (iv). 43

3.7 Time and frequency representation of the imposed displacement used to mainly excite the A_0 mode in the irregular waveguides. . . 44

3.8 Time-transient responses $v_A(t)$ acquired at x=250 mm for the three cases (i), (ii) and (iii) represented in Fig. 3.5. 45

3.9 (a) Spectrogram of the time-transient response $v_A(t)$ for case (i) represented in Fig. 3.8. The group delay curves for the A_0 wave computed with the proposed procedure considering different paths are overimposed: incipient wave (W1), notch and right edge reflections (W2a and W3a, respectively), left edge reflections (W2b and W3b). (b) Schematic representation of the different paths. 46

3.10 Warped version of the time-transient signals $v_A(t)$ represented in Fig. 3.8 for the three cases (i), (ii) and (iii). 47

3.11 Normalized H_{env} of the signals depicted in Fig. 3.10. The vertical lines mark the distance traveled by notch and edge reflected waves. 48

3.12 Time-transient response $v_A(t)$ for case (iv) along with its spectrogram. In the spectrogram the group delay curves for the incipient pulse (W1), notch and right edge reflections (W2a and W3a, respectively), W2a and W3a reflections from the left edge (W2b and W3b), have been overimposed. Group delays are estimated according to Eq. (3.5). 50

3.13 Warped version of $v_A(t)$ represented in Fig. 3.12 along with the spectrogram of the warped signal. In such plot the warped group delays of incipient pulse (W1), notch and right edge reflections (W2a and W3a, respectively), W2a and W3a reflections from the left edge (W2b and W3b), have been overimposed. 51

3.14 Normalized H_{env} of the signal depicted in Fig. 3.13. The vertical lines mark the distance traveled by notch and edge reflected waves. 52

4.1 Representation of the TR procedure. (a) Schematic representation of a generic waveguide. (b) Block diagram of the TR procedure (from the top left side and cloackwise): (i) apply a generic tone burst excitation $U_D(t)$ in A; (ii) record the forward wave $U_{acq}(t)$ in B; (iii) emit the time-reversed wave $U_{acq}(-t)$ from B back to A; (iv) pick up the wave in A as the reconstructed wave $U_{D,r}(-t)$. . . 56

4.2 Schematic representation of the FE model involved into the two step TR procedure. Please note the different scale in the x and y-direction. 58

4.3 Different snapshots of the wave propagation phenomenon in the forward wave propagation. Deformation scale factor was assumed equal to 10^7 in order to highlight the waves behaviour. 59

4.4 Different snapshots of the wave propagation phenomenon in the time-reversal reconstruction. Deformation scale factor was assumed equal to 10^7 in order to highlight the waves behaviour. Please note the dispersion compensation occurring in the TR reconstruction. 60

4.5 Reconstructed wave using a 2-count 100 kHz tone burst excitation in simulation of two-mode Lamb wave time-reversal. 61

4.6 Schematic overview of the proposed technique for the impact localization: (a) scanning area; (b) *Training data* set acquisition; (c) actual impact event; (d) actual impact Impulse response function (OPV). 62

4.7 Correlation values for the numerical case between each signal of the scanned area $g_i(t)$ and the signal of the actual impact point $f(t)$. (a) If time reversibility is not exploited, correlation is coarse and more than one point can be assumed as the impact position. (b) When time reversibility is taken into account, identification procedure is much more precise. 63

4.8 A schematic representation of the specimen. (a) xy plane view and (b) its cross-section. The drawings, for sake of clarity, are not to scale. Measures are given in millimetres. The light grey rectangle indicates the scanning area. 65

4.9 (a) Eccentrically stiffened aluminium plate finite element model. (b) Snapshot in terms of Von Mises stresses of guided waves propagating in the specimen 30 ms after the impact occurred. It is worth noticing that the stiffeners waveguide the wave absorbing a lot of energy due to its high rigidity. 66

4.10 Excitation pulse: the excitation signal has been designed as a sharp square pulse in order to be a good representative of actual impact event. 67

4.11 Numerical results. (a,c,e) Correlation values between each signal of the scanned grid points and the signal of the actual impact points (1-D plot); the estimated point of impact is highlighted; (b,d,f) 2-D visualization of the estimated impact points. The black dots denote the scanning points, the red circle the acquisition point, the green spot the real impact position and the blue cross the estimated one. 68

4.12 Schematic diagram of the experimental set-up. A scanning measurement head is connected to a data acquisition system and steering circuit. A synchronisation cable connects the digital generator with the steering circuit through the amplifier that feeds the inducing signal to the piezoelectric element. Additionally, a signal from the generator is fed into the data acquisition system. A computer system integrated with the data acquisition system and steering circuit provides communication with the user and allows measurements to be processed. 69

4.13 Illustration of the tested specimen. The red circle represents the position of both the PZT transducer used as actuator for the data training acquisition and of the SLDV acquisition point after the impact occurred. The testing region (768 mm × 803 mm), represented as the yellow rectangular box, is made of 93 × 91 acquisition equispaced points. The unknown impact points - $\#1 = (494, 433)$, $\#2 = (424, 354)$ and $\#3 = (392, 150)$ - are represented by means of black stars and chosen within the area delimited by the stiffeners. 70

4.14 Experimental results. (a,c,e) Correlation values between each signal of the scanned grid points and the signal of the actual impact points (1-D plot); the estimated point of impact is highlighted; (b,d,f) 2-D visualization of the estimated impact points. The black dots denote all the scanning points, the red circle the acquisition point, the green spot the real impact position and the blue cross the estimated one. 72

4.15 (a) Acquired signal for the first impact case. (b) For simplicity in the experiment the PZT actuator and the laser-vibrometer acquisition were synchronized so that the zero time acquisition point coincides with the excitation time. 73

4.16 A posteriori modification of the actual registered signal and impact localization results for the first impact case. (a) The original signal has been lengthened by adding 1.765e μs of idle time and (c) shortened by removing 0.3 μs of the original signal. (b,d)In both cases results are still accurate. 74

5.1 A crystalline solid. (a) A Bravais lattice: all the atoms are arranged periodically. (b) A non-Bravais lattice. 81

5.2 Vectors $\mathbf{a}$ and $\mathbf{b}$ are basis vectors of the lattice. Vectors $\mathbf{a}$ and $\mathbf{b}'$ form another set of basis vectors. Shaded and hatched areas are unit cells corresponding to first and second set of basis vectors, respectively. 81

5.3 Area S_1 is a primitive unit cell; area S_2 is a non-primitive unit cell. 83

5.4 Simple-cubic direct lattice (a) and its reciprocal lattice (b). The primitive vectors of both lattices are also indicated. 84

5.5 The Wigner-Seitz cell for a two-dimensional Bravais lattice. The sides of the cell bisect the lines joining the central points to its nearest neighbouring points (shown in blue lines). In two dimensions the Wigner-Seitz cell is always a hexagon unless the lattice is rectangular. 85

5.6 (a) The first three Brillouin zones of the reciprocal lattice of the 2D square Bravais lattice. The dots indicate reciprocal lattice points, the solid lines indicate Bragg planes, and the digits indicate the order of the corresponding Brillouin zone. (b) The first Brillouin zone with the two high-symmetry directions commonly referred to as $\Gamma - X$ and $\Gamma - M$. 86

5.7 Lattice periodicity and geometrical dimensions based classification of PMs. The “P” letter refers to the lattice periodicity, meanwhile the “D” letter defines the dimensionality of structure. 88

5.8 (a) Finite elements discretization and (b-d) proper boundary conditions of the unitary cell. 92

6.1 Wave propagation plane in an ordinary (a) and in a phononic (b) plate under 2D plane strain assumption. Schematic representation of several coupled periodic elements joined together end-to-end in the ordinary (c) and phononic (d) waveguide. Ordinary (e) and phononic (f) unitary cell with geometric dimensions and prescribed boundary conditions. 97

6.2 Comsol script flowchart. 101

6.3 Dispersion curves for both ordinary and phononic waveguides. Band diagram is plotted in the $k^* \in [0, 1]$ reduced wavenumber range, corresponding to the symmetry direction $\Gamma{-}X$ of the first Brillouin zone. Ordinary plate band diagram is extracted both via Comsol and via SAFE. Perfect agreement is found. Dispersion curves for the phononic plate (extracted via Comsol) are also provided. The light grey rectangle emphasizes the position of the band gap. . . . 102

6.4 (a) Dispersion curves in the case of phononic waveguide are distorted if compared to the ordinary aluminium plate. Detailed behaviours of: (b) 2^{nd} and 3^{rd} bands between $k^* = 0.7245$ and $k^* = 0.7247$; (c) 4^{th} and 5^{th} bands between $k^* = 0.429$ and $k^* = 0.431$; (d) 4^{th} and 5^{th} bands between $k^* = 0.5275$ and $k^* = 0.5295$. 103

6.5 Schematic representation of the FE model exploited to evaluate the influence of the phononic region length on the transmission coefficient. 104

6.6 Dispersion curves for the symmetry direction $\Gamma - X$ of the first Brillouin zone for the Tungsten-vacuum phononic waveguide. . . . 104

6.7 Time and frequency representation of the excitation signal. 105

6.8 Von Mises stress field (snapshots at 28 μs) for the waveguide presented in Fig. 6.5 consisting of a central portion containing the finite PC sandwiched between two homogeneous regions. From the bottom to the top the number of unit cells is increased from 0 to 4. 105

6.9 Von Mises stress field (snapshots at 36 μs) for the waveguide presented in Fig. 6.5 consisting of a central portion containing the finite PC sandwiched between two homogeneous regions. From the bottom to the top the number of unit cells is increased from 0 to 4. 106

6.10 Influence of the number of periodic cells on the transmission coefficient α_T. The grey regions delimit the full band gap for the infinite PC. From the top: $n \in [1, 3]$-periodic-long phononic plate. 106

6.11 Influence of the number of periodic cells on transmission coefficient α_T. The grey regions delimit the full band gap for the infinite PC. From the top: $n \in [4, 7]$-periodic-long phononic plate. 107

6.12 FE results showing the effect of prestrain on A_0 mode phase velocity in a 1-mm thick aluminium plate. Phase velocity is normalized w.r.t. to the bulk transverse shear wave speed in aluminium. Tensile strains tend to increase the natural frequencies, while compressive strains tend to decrease them. 110

6.13 Phononic plate dispersion diagram for different levels of applied prestrain. The main effect of the prestrain field is to shift towards higher/lower frequencies dispersion curves. 111

6.14 Prestrain effects on the 1^{st} mode for the considered phononic plate. 112

6.15 (a) Schematics of the epoxy/steel phononic plate with square lattice constant $a = 0.008$ m and filling fraction $f = 0.4418$. (b) The first irreducible Brillouin zone $M - \Gamma - X$. 113

6.16 Band structure of the steel/epoxy PC with square lattice. Only complete band gaps are highlighted by means of light grey rectangles. Note the existence of a low-dispersive single pass band separating the second and third complete band gaps. Letters denote normal modes associated to particular reduced wavevector and frequency values. 114

6.17 Band structure of the steel/epoxy PM with square lattice. Complete band gaps (light grey) and stop bands (dark grey) are highlighted. 116

6.18 Displacement fields (magnitude) of eigenmodes in the $M-\Gamma$ direction of propagation. (a) $\mathbf{k}=(3.92, 3.92)$ m^{-1}, $f=62.59$ kHz corresponding to the point A of Fig. 6.16; (b) $\mathbf{k}=(196.35, 196.35)$ m^{-1}, $f=66.71$ kHz corresponding to the point B of Fig. 6.16; (c) $\mathbf{k}=(392.69, 392.69)$ m^{-1}, $f=86.15$ kHz corresponding to the point C of Fig. 6.16; (d) $\mathbf{k}=(3.92, 3.92)$ m^{-1}, $f=239.00$ kHz corresponding to the point D of Fig. 6.16. 117

6.19 Displacement fields (magnitude) of eigenmodes in the $\Gamma-X$ direction of propagation. (a) $\mathbf{k}=(3.92, 0)$ m^{-1}, $f=1.24$ kHz corresponding to the point E of Fig. 6.16; (b) $\mathbf{k}=(196.35, 0)$ m^{-1}, $f=80.94$ kHz corresponding to the point F of Fig. 6.16; (c) $\mathbf{k}=(392.69, 0)$ m^{-1}, $f=72.38$ kHz corresponding to the point G of Fig. 6.16; (d) $\mathbf{k}=(196.35, 0)$ m^{-1}, $f=273.07$ kHz corresponding to the point H of Fig. 6.16. 118

6.20 Displacement fields (magnitude) of eigenmodes in the $X-M$ direction of propagation. (a) $\mathbf{k}=(0, 3.92)$ m^{-1}, $f=42.27$ kHz corresponding to the point I of Fig. 6.16; (b) $\mathbf{k}=(0, 3.92)$ m^{-1}, $f=221.39$ kHz corresponding to the point L of Fig. 6.16; (c) $\mathbf{k}=(0,)$ m^{-1}, $f=72.38$ kHz corresponding to the point G of Fig. 6.16; (d) $\mathbf{k}=(196.35, 0)$ m^{-1}, $f=273.07$ kHz corresponding to the point H of Fig. 6.16. 119

6.21 FE model exploited for the transmission spectra evaluation. Red and green dots denote excitation and acquisition points, respectively. 120

6.22 (a) Time and frequency representation of the imposed displacement used to excite modes up to 400 kHz in the PM. (b) PC band structure together with normalized transmission power spectrum (TPS) measured after 10 periodic cells at A (see fig. 6.21). TPS clearly shows a almost complete attenuation in the complete band gap zones. 121

6.23 Single unit cell for the considered sonic crystal system. Periodic boundary conditions are applied to the borders of the unit cell in terms of pressure distribution. 122

6.24 Band structures of the acoustic phononic crystal made of aluminium cylinders immersed in air. 123

6.25 Unit cell ($a = 200$ mm) for the analysed acoustic metamaterials: (a,b) air-aluminium interaction, (c,d) air-PVC interaction ($R = 80$ mm). 125

6.26 Band structures for (a,b) air-aluminium interaction, (c,d) air-PVC interaction. 126

6.27 Finite element model implemented in Comsol Multiphysics to compute the pressure fields at different frequencies inside and outside BGs. The model consists of 3.2 mm thick hollow PVC cylinders immersed in air. A plane wave radiation boundary condition is set to the left side of the system. Sound hard boundaries (SHB) have been assigned to the PVC cylinders, as well as to the external domain boundaries. 127

6.28 A comparison of finite element computed band structure in the $\Gamma - X$ direction against the FE computed frequency spectra for sound pressure level. 129

6.29 Pressure maps for hollow PVC cylinders placed in air via finite element computation at: (a) 480, (b) 800 and (c) 1280 Hz, respectively. 130

6.30 Finite element model implemented in Comsol Multiphysics exploited to compute the pressure maps and the sound insulation index. The model consists of hollow PVC cylinders ($R = 80$ mm and $t = 3.2$ mm) immersed in air. A plane wave radiation boundary condition is set to the left side of the system, while the remaining are air impedance matching boundaries. Sound pressure levels are measured at positions $M - P1$, $M - P2$ and $M - P3$, $L_M = 0.25$ m away from the last row of cylinders and spaced apart 5 cm. The phononic region is $L_{PhR} = n \cdot a$ wide, where n is the number of unitary cells and $a = 0.2$ m. The first row of cylinders is set $L_{Ls} = 1$ m away from the radiation boundary. Sound hard boundaries have been assigned to the PVC cylinders, as well. . . . 131

6.31 Influence of the number of unitary cells compounding the phononic region. Pressure maps for hollow PVC cylinders placed in air via finite element computation for 1, 2, 3 and 4 unitary cells, respectively. 133
6.32 Influence of the number of unitary cells compounding the phononic region. Sound insulation index for hollow PVC cylinders placed in air is calculated via finite element computation for different configurations. 134
6.33 Unit cell for the phononic material made of cross-like cylindrical holes in aluminium matrix: (a) geometry description; (b) periodic boundary condition along x-direction (PBCx); (c) periodic boundary condition along y-direction (PBCy); free boundary condition along z-direction (FBCz). 136
6.34 Band structures of cross-like cylindrical holes embedded in an isotropic elastic solid slab in a square lattice. 137
6.35 (a) Mesh discretization for the unit cell and (b-d) vibration modes (VM) in the first Brillouin zone: (b) VM belonging to the $\Gamma - X$ path, characterized by $\mathbf{k} = (157, 0)$ m^{-1}, $f = 9.061$ kHz; (c) VM belonging to the $X - M$ path, characterized by $\mathbf{k} = (0, 157)$ m^{-1}, $f = 4.099$ kHz; (d) VM belonging to the $M - \Gamma$ path, characterized by $\mathbf{k} = (157, 157)$ m^{-1}, $f = 19.18$ kHz. 138
6.36 Schematic representation of the PM unit cell (circular steel cylinders embedded into a background epoxy matrix) and set boundary conditions: (a) geometry description; (b) periodic boundary condition along x-direction (PBCx); (c) periodic boundary condition along y-direction (PBCy); free boundary condition along z-direction (FBCz). 139
6.37 Dispersion curves for a PM made of circular cylindrical inclusions in an epoxy matrix. (a) 2D model under plane strain assumption; (b) 3D model with $t_r = 0.125$, (c) 3D model with $t = 0.25$. (d) 3D model with $t_r = 0.5$. 140
6.38 Schematics of the phononic system composed of an ordinary PVC plate hosting a phononic region screening a specific region. Excitation point (E) and receiving points (A and B) are highlighted. . 141

6.39 (a) Isometric and (b) in-plane view of the unitary cell composing the phononic part of the system. 141

6.40 Dispersion map for the unit cell presented in Fig. 6.39. 142

6.41 Excitation displacements: (a) 50 kHz centred pulse of 2 sinusoidal cycles modulated by a Hanning window and (b) 27.5 kHz centred pulse of 21 sinusoidal cycles modulated by a Hanning window. . . 143

6.42 Simulated Von Mises stress for cross-rounded holes phononic plate. Frequency excitation was centred at 50 kHz (therefore covering frequencies even outside the band gap). Snapshots are taken at: (a) $t = 1.2 \cdot 10^{-}4$ s, (b) $t = 2.4 \cdot 10^{-}4$ s, (c) $t = 3.6 \cdot 10^{-}4$ s, (d) $t = 4.8 \cdot 10^{-}4$ s, (e) $t = 6 \cdot 10^{-}4$ s and (f) $t = 12 \cdot 10^{-}4$ s. 144

6.43 Simulated Von Mises stress for cross-rounded holes phononic plate. Frequency excitation was centred at 27.5 kHz (therefore covering frequencies even outside the band gap). Snapshots are taken at: (a) $t = 3 \cdot 10^{-}4$ s, (b) $t = 4.8 \cdot 10^{-}4$ s, (c) $t = 6.6 \cdot 10^{-}4$ s, (d) $t = 8.4 \cdot 10^{-}4$ s, (e) $t = 10 \cdot 10^{-}4$ s and (f) $t = 20 \cdot 10^{-}4$ s. 145

6.44 Normalized displacement u_1 at points A and B versus time (left) and its Fourier spectrum (right). The complete band gap is also highlighted as the light grey region. 146

6.45 Normalized displacement u_2 at points A and B versus time (left) and its Fourier spectrum (right). The complete band gap is also highlighted as the light grey region. 146

6.46 Normalized displacement u_3 at points A and B versus time (left) and its Fourier spectrum (right). The complete band gap is also highlighted as the light grey region. 147

7.1 In-plane view of the phononic plate constituted of 160 hollow rounded cross-cylinder inclusions drilled into a $1000 \times 500 \times 12$ mm^3 Polyvinyl chloride (PVC) matrix: (a) experimentally tested specimen and (b) numerical model. Emitting/Receiver transducers are also visible. . 151

7.2 (a) Isometric and (b) in-plane view of the unitary cell constituting the phononic region of the plate. 152

7.3 Example of time history for a 21 cycles sine pulse, its Hanning modulation and its frequency content. The probing pulse is centred at 27.5 kHz. 153

7.4 Measurement setup adopted in the PZT pitch-catch experiment to extract the transmission coefficient in the PVC phononic plate. . . 154

7.5 (a) Time waveforms (RF signals) detected by the sensors at 15 kHz. (b) Power spectrum of the excitation and acquired signals. . 155

7.6 (a) Time waveforms (RF signals) detected by the sensors at 27.5 kHz. (b) Power spectrum of the excitation and acquired signals. . 156

7.7 (a) Time waveforms (RF signals) detected by the sensors at 42.5 kHz. (b) Power spectrum of the excitation and acquired signals. . 157

7.8 (a) Time waveforms (RF signals) detected by the sensors at 51 kHz. (b) Power spectrum of the excitation and acquired signals. . 158

7.9 Top and bottom panels present time waveforms for a 21 cycles Hanning modulated pulse centred at 42.5 kHz propagating through the ordinary PVC plate and through the phononic region, respectively. A significant time delay can be observed when the wave propagates in the phononic region of the plate. 159

7.10 Transmission power spectrum as a function of the frequency. The y axis is normalised w.r.t. the input signal energy content. The light grey rectangular box denotes the numerical predicted band gap width. 160

7.11 Representation of the experimental setup. A scanning measurement head is connected to a data acquisition system and steering circuit. A synchronisation cable connects the digital generator with the steering circuit through the amplifier that feeds the inducing signal to the piezoelectric element. Additionally, a signal from the generator is fed into the data acquisition system. A computer system integrated with the data acquisition system and steering circuit provides communication with the user and allows measurements to be processed. 161

7.12 Measured out-of-plane velocity maps for cross-rounded holes phononic plate. Frequency excitations were centred at: (a) 15 kHz, i.e. outside the band gap and (b) 27.5 kHz, i.e. inside the band gap. . . . 162

7.13 (a) Numerical model and experimental set-up for the (b) 2-period long and (c) 4-period long specimen consisting of hollow circular cylinders arrays. Scatterers are 3 m long with an external radius $R_e = 80$ mm and a thickness of 3.2 mm. The acoustic wave generator and acquisition microphones are also visible. 164

7.14 (a) Experimental response for the free-field measurement and (b-d) the experimental waveforms at the three acquisition points $M-P1$, $M-P2$ and $M-P3$ for the case of $n = 3$-period long in the y direction barrier. Amplitudes are normalised to the maximum registered value of each signal. 165

7.15 Sound insulation index comparison between numerical and experimental analyses. Results are presented for (a, c, e) 1-period long and (b, d, f 2-period long) phononic barrier for (a, b) $M-P1$, (c, d) $M-P2$ and (e, f) $M-P3$ acquisition points, respectively. . . 167

7.16 Sound insulation index comparison between numerical and experimental analyses. Results are presented for (a, c, e) 3-period long and (b, d, f 4-period long) phononic barrier for (a, b) $M-P1$, (c, d) $M-P2$ and (e, f) $M-P3$ acquisition points, respectively. . . 168

8.1 Phononic bandgaps. An elastic wave is incident on the surface of a two-dimensional PM made of cylinders arranged in a triangular lattice. (a) When the frequency of the incoming wave is not inside the BG, the wave is transmitted through the structure (top). If the elastic wave has a frequency within the gap, its propagation is not permitted any more within the PM and it is reflected backwards (bottom). (b) Numerical calculation showing an ultrasonic wave propagating within the periodic metallic composite made of pure aluminium (right) and aluminium-mercury ultrasonic materials (left). The vertical line indicates the boundary between the two regions. The mercury cylinders are indicated by superimposed circles. 174

8.2 Schematic illustration of the metamaterial barrier protecting a strategic building from seismic waves. 176

8.3 (a) Top view of the infinite pile-soil system. (b) First Brillouin zone and irreducible Brillouin zone. 177

8.4 Periodic boundary conditions for periodic materials. 178

8.5 Dispersion curves for infinite periodic panels made of steel cylinders embedded into a rubber coating hosted into a square concrete matrix. Results are in perfect agreement with available literature. 179

8.6 Dispersion curves for soil/rubber/steel arrangement with the following geometrical properties: $a = 1$ m, $R_{hcm} = 0.25a = 0.25$ m and $R_{sm} = 0.45a = 0.45$ m. 180

8.7 Influence of the filling fraction on dispersion modes in a soil/rubber/concrete PM: (a) $R_{hmc} = 0.09a$ (b) $R_{hmc} = 0.018a$, (c) $R_{hmc} = 0.27a$, (d) $R_{hmc} = 0.36a$. 183

8.8 Influence of the filling fraction on dispersion modes in a soil/rubber/concrete PM: (a) $R_{sm} = 0.30a$ (b) $R_{sm} = 0.35a$, (c) $R_{sm} = 0.40a$, (d) $R_{sm} = 0.45a$. 184

8.9 Lower bound frequency (LBF), upper bound frequency (UBF) and width of attenuation zone (WAZ) for different filling fraction of the soil/rubber/concrete PM. 185

8.10 Lower bound frequency (LBF), upper bound frequency (UBF) and width of attenuation zone (WAZ) for different values of elastic modulus, Poisson ratio and density for the hosting material. . . . 186

8.11 Influence of the hosting material elastic modulus E on the first 15 dispersion modes in a soil/rubber/concrete PM: (a) $E_{hm} = 1$ MPa (b) $E_{hm} = 85$ MPa, (c) $E_{hm} = 170$ MPa, (d) $E_{hm} = 255$ MPa. . . 187

8.12 Lower bound frequency (LBF), upper bound frequency (UBF) and width of attenuation zone (WAZ) for different values of elastic modulus, Poisson ratio and density for the hard material core. . . 188

8.13 Lower bound frequency (LBF), upper bound frequency (UBF) and width of attenuation zone (WAZ) for different values of elastic modulus, Poisson ratio and density for the soft material coating. . 189

8.14 (a) Schematic representation of the giant acoustic metamaterial constituting the earthquake-proof barrier. Hosting material is the ground itself, considered as a loose sandy soil. Inclusions are made of steel. (b) Dispersion map for the giant acoustic metamaterial. . 190

8.15 Four-storey frame structure built above an earthquake-proof barrier (left side) and on an ordinary loose sandy soil without isolation capabilities (right side). 191

8.16 Imposed displacement time history for an artificially created horizontal elastic wave. It consists of a 21 cycles modulated Hanning signal with a 7 Hz central frequency. 192

8.17 Snapshot of the wave propagation phenomenon at 1.25 s. Excitation wave time history is reported in Fig. 8.16. 192

8.18 Snapshot of the wave propagation phenomenon at 2.5 s. Excitation wave time history is reported in Fig. 8.16. 193

8.19 Snapshot of the wave propagation phenomenon at 5 s. Excitation wave time history is reported in Fig. 8.16. 193

8.20 Snapshot of the wave propagation phenomenon at 7.25 s. Excitation wave time history is reported in Fig. 8.16. 194

8.21 Time history and energy content of for the monitoring points. . . 194

8.22 Zoom of the displacement field of the four-storey frame built above a loose sandy soil with phononic isolation capabilities (a) and above the same soil without any PM barrier (b). 195
8.23 Time history and energy content for the El Centro earthquake. . . 196
8.24 Energy content of the monitored point $M_{g,2}$ for an ordinary loose sandy soil without isolation capabilities and the same soil with an embedded PM barrier for the El Centro earthquake. 196

Chapter 1

Introduction

In the last decades elastic waves have shown great potentials in different application fields. In particular, the present thesis focuses on a specific class of elastic waves, the so called guided waves (GWs), in the framework of non-destructive evaluation (NDE) and structural health monitoring (SHM), as well as on the study of waves propagation in metamaterials (artificial periodic materials).

Generally speaking, elastic waves are particle disturbances of a medium (solid or fluid) associated with volume and/or shape deformation caused by an external source. For small disturbances, the energy of elastic deformation associated to the wave propagation is transferred in the absence of matter transport. Elastic waves are generally classified according to the motion of individual particles with respect to the propagation direction (plane, spherical, or cylindrical wave front) and to the eventual restrictions imposed to the elastic medium (bulk, surface and guided waves[1]).

Elastic waves can be fully described by defining the amplitude and vibration frequency of the particles of the medium, its wavelength, phase and group velocities, and the law governing the distribution of displacements and stresses over the wave front [1].

---

[1] Examples of elastic waves include the waves generated in the Earth's crust during earthquakes and sonic and ultrasonic waves in solids and fluids.

1.1 Introduction to GWs-based NDE

In recent years, the interest in non-destructive (NDE) and non-invasive evaluation techniques based on guided waves is increasing in many fields including civil, industrial and medical engineering and geophysical science.

Guided waves are stress waves that propagate along elongated structures with one (such as plates and shells) or two (such as pipes and rods) dimensions much smaller than the remaining. The name derives from the fact that the geometry of the structure "guides" the stress waves along the length of the structure itself.

Guided waves (GWs) can be classified according to the boundary conditions of the structure: (i) surface waves propagating in a semi-infinite medium with a stress free surface give rise to Rayleigh waves; (ii) Lamb waves exist in a thin infinite plate with stress free boundaries; (iii) Love waves exist at an interface between a thin layer and a semi-infinite medium, while, (iv) Stoneley waves propagate at the interface of two semi-infinite mediums. Further details of wave propagation can be found in reference literature [1, 2, 3, 4].

Guided waves SHM systems use waves propagating in structures to determine the health state of the structural component. Compared to traditional bulk waves, guided waves are of interest because they provide larger monitoring ranges and the complete coverage of the waveguide cross-section. Furthermore, guided waves often allow to reach hidden areas that are generally difficult to inspect by traditional methods.

For example, water and oil transportation industry widely exploits GWs-based techniques for the detection of defects in pipelines. In the rail-road industry they are used to monitoring the conditions of rails, with the aim to prevent failures that can cause disservices or compromise safety. In the aerospace industry, they are largely employed for the quality assessment of adhesively-bonded components. In the civil engineering field, guided waves have proven to be effective in the damage detection of bridge cables, inspections of foundation piles, weld inspections and characterization of the material constants in composite structural components.

However, to fully exploit the potentials of GWs for NDE purposes in the aforementioned applications, an accurate knowledge of their complex multi-modal and dispersive behaviour is needed. In fact, the structural geometry and wave propagation phenomenon interaction give rise to the well known concept of waves dispersion, which denotes a variation of the behaviour of GWs as a function of the frequency [5]. Phase velocity, group/energy velocity and attenuation are the fundamental dispersive parameters describing the process. Phase and group velocities denote the rate at which the crests of a particular guided mode propagate along the waveguide at a certain frequency and the rate at which packets of waves at infinitely close frequencies move along the waveguide, respectively. Attenuation, instead, expresses the wave amplitude decay per unit of travelled distance.

These features give an indication about how much dispersion occurs for a signal generated in a certain frequency range, i.e. how much the shape of the signal is distorted while it propagates along the waveguide [6].

Such complexities are strictly related to the geometrical and mechanical properties of the waveguide cross-section which, generally, affects wavelength, group velocity, attenuation and wave-structure of propagating multiple mechanical waves.

1.2 Introduction to metamaterials

Wave propagation through periodic structures is a subject of interest for several branches of science and technology, such as water, seismology, acoustics and electromagnetism. The most important common property of such systems is perhaps the presence of the so called "band gaps", i.e. frequency ranges in which wave propagation is inhibited. Many interesting physical phenomena arise from this property such as wave localization, excitation of evanescent waves, as well as relevant applications concerning filtering, focusing and waveguiding [7].

Historically, the first dealing with metamaterials was the Russian physicist Victor Veselago, who published a visionary paper predicting a medium with simultaneously negative permittivity and magnetic permeability characterized by a negative refractive index in 1967 [8]. However this negative index medium remained as an academic curiosity for almost thirty years, until Pendry et al. [9] proposed the designs of artificial structured materials which would have effectively negative permeability and permittivity. In next years, the interest focused whether designing metamaterial for other kind of waves, for example, acoustic wave, was possible. At the end of last millennium, the development of phononic materials for the control of vibrational waves underwent a great growth. In particular the group of Ping Sheng, at the University of Hong-Kong provided the first numerical and experimental evidence of a localized resonant structure for elastic wave propagating in three-dimensional arrays of thin coated spheres [10]. This work paved the way towards phonons, sound, and other waves to be manipulated and controlled.

However, before dwelling in the technical aspects of metamaterials, the meaning of the word metamaterial itself shall be first defined.

So, what are Metamaterials ? The prefix "meta"- comes from Greek $\mu\epsilon\tau\acute{\alpha}$ and originally has been used in the sense of "spring" of new properties from a special combination of materials exhibiting conventional behaviours. Nowadays, however, the most common meaning given to the prefix "meta" in metamaterials is "beyond", "above", "over", as in the word metaphysics. Following this latter interpretation, the word metamaterials, then, indicates a particular class of artificial materials that exhibit properties commonly not found in nature. The therm has been introduced in 2000 by Rodger M. Walser who gave the following definition:

"Metamaterials are defined as macroscopic composites having a man-made, three dimensional, periodic cellular architecture designed to produce an optimized combination, not available in nature, of two or more responses to a specific excitation" [11].

Since then, other definitions have been suggested in the scientific literature, such as:

"A class of artificial materials exhibiting surprising and anomalous properties that cannot be found in natural materials" [12].

"Metamaterials are typically man-made and have properties that are not found in nature" [13].

All definitions above share the ideas that metamaterials (i) are not present in nature and (ii) their resulting properties are not observed in the single constituents.

Despite the aforementioned more traditional definitions, in the present thesis another description is preferred in order to provide a general standpoint valid for several areas of physics: acoustics, mechanics, electro-magnetics and so on:

> "A metamaterial is a composite material characterized by an artificially designed structure such that the emerging effective macroscopic response of the system to a given excitation is not readily encountered in nature".

From the above discussion, it emerged that a universally accepted definition of metamaterial does not exist yet. Nevertheless, the whole scientific community agrees that it owes much to crystallography, a specific branch of Solid State Physics. This branch of physics deals with the arrangement of atoms in solids, studying how the large-scale properties of solid materials result from their atomic-scale properties.

Following from recent developments of this field, the idea behind metamaterials is that as electrons in a semiconductor can only occupy certain energy bands, a metamaterial allows waves to travel through via the pass band only in specific frequency ranges, whilst other frequencies are inhibited by the so called "frequency band gaps" (BGs)[1]. The core concept of BGs is driven directly from Bragg reflections and metamaterials consist in replacing the "atoms" composing matter with man-made structures, viewed then as "artificial atoms" on a scale comparable (ordinary elastic metamaterials) or much smaller (locally resonant elastic metamaterials) than the relevant wavelength involved in the propagation phenomenon.

This addressed scientists in restless designing new artificial materials which offer a way to dramatically manipulate light (photonic materials), elastic waves

---

[1] It is well known from quantum mechanics that the energy of an electron in an atom assumes discrete values. However, when the atomic orbitals overlap as the atoms come close together in a solid, the energy levels of the electrons broaden and form continuous regions, also known as energy bands. At the same time, because of the periodicity of the crystal structure, the electronic wave functions undergo strong Bragg reflections at the boundaries of the Brillouin zones. The destructive interference of the Bragg-scattered wave functions gives rise to the existence of energy regions in which no electronic energy levels exist. Since these regions are not accessible by the electrons, they are also known as forbidden bands.

(phononic materials - PMs) as well as both of them (phoxonic materials). These materials exhibit a rich variety of physical properties of interest to theoretical and applied research [14], as the huge available literature on the topic confirms [15].

In this thesis, the interest is mainly focused on phonons, sound, and elastic waves control and manipulation, therefore on phononic materials (PMs).

1.3 Thesis outline

The present work focuses on elastic waves behaviour in ordinary structures as well as in acousto-elastic metamaterials via numerical and experimental applications.

In particular, Chapter 1 provides a brief introduction on: (i) the behaviour of elastic guided waves in the framework of non-destructive evaluation (NDE) and structural health monitoring (SHM) and (ii) the study of elastic waves propagation in acousto-elastic metamaterials.

Afterwards, in Chapter 2, dispersion curves for thin walled beams and arbitrary cross-section waveguides are extracted via Semi-Analytical Finite Element (SAFE) methods. After complex multi-modal and dispersive behaviour for such geometries is predicted, in Chapter 3 a novel strategy tackling signal dispersion to locate defects in the case of irregular waveguides is proposed and numerically validated. Finally, in Chapter 4 a time-reversal and laser vibrometry based procedure for impact location is numerically and experimentally tested on a flat aluminium plate reinforced by two unidirectional eccentric stiffeners.

For what concerns the second part of the thesis, Chapter 5 provides a general introduction and a brief review of the basic definitions necessary to describe elastic and acoustic metamaterials is provided. In addition, a numerical approach to extract dispersion properties in such structures is highlighted. In Chapter 6, solid-solid and solid-fluid phononic systems are discussed via numerical applications. In particular, band structures and transmission power spectra are predicted for 1P-2D, 2P-2D and 2P-3D phononic systems. In addition, Chapter 7 provides an experimental investigation on attenuation bands in the ultrasonic as well as in the sonic frequency regimes. In the experimental validation, PZTs in a pitch-catch configuration and laser vibrometric measurements are performed on a PVC phononic plate in the ultrasonic frequency range and sound insulation index is computed for a 2P-3D phononic barrier in the sonic frequency range. In both cases the comparison between numerical and experimental results confirms the existence of the numerical predicted band gaps.

Finally, in Chapter 8 the feasibility of an innovative passive isolation strategy based on giant elastic metamaterials is numerically proved to be practical for civil structures. In particular, attenuation of seismic waves is demonstrated via finite elements analyses. Further, a parametric study shows that depending on the soil properties, such an earthquake-proof barrier could lead to significant reduction of the superstructure displacement.

Part I

Elastic guided waves

Chapter 2

Dispersion properties prediction

2.1 Introduction

The non-destructive evaluation of structural integrity is a very important task in present-day industry. Recently, the interest to ultrasonic guided waves has considerably increased. Compared to classical bulk waves based inspections, the use of ultrasonic guided waves has many advantages such as longer inspection range, higher sensitivity to small flaws and larger versatility. Furthermore, guided waves often allow to reach hidden areas that are generally difficult to inspect by traditional methods.

In general, guided waves develop in waveguides like plates, rods, pipes or elongated structures, after several reflections and refractions of the original incident wave. Multiple guided waves can propagate, the majority of which are dispersive, i.e. their principal features, known as phase and group velocity, attenuation, wavestructure and wavelength, are frequency dependant [5].

However, to fully exploit the potentials of guided waves for NDE purposes, their complex multi-modal and dispersive behaviour must be predicted. In this thesis, such complexities are unveiled by means of Semi-Analytical Finite Element (SAFE) formulations modelling guided waves in plates, cylinders, arbitrary cross-section and thin-walled beams waveguides.

To date numerous SAFE formulations have been proposed for modelling guided waves in plates, cylinders [16], helical wires [17] and arbitrary cross-section waveguides [18, 19, 20].

While for first two classes of waveguides geometrical symmetries allow exploiting mono-dimensional finite elements, with enormous computational cost savings, for arbitrary cross-section waveguides planar bi-dimensional finite elements have been generally employed. The use of such elements type becomes computationally onerous when the waveguide cross-section has thin walls. In this case, in fact, the number of planar elements can be prohibitive. To avoid such a problem, ad-hoc SAFE formulations based on low order structural theories have been proposed [21, 22, 23].

In what follows, dispersion curves for some of the aforementioned types of waveguides are extracted by means of different SAFE approaches, which proved to be fast and reliable.

2.2 Dispersion curves extraction in thin walled beams structures

Computation of the complex behaviour of mechanical waves in thin walled beam-like structures by means of a SAFE formulations is here presented. SAFE formulations have been recently used to predict guided waves in thin-walled waveguides [22, 23]. In particular, these formulations, being based on mono-dimensional shell elements, allow to model each thin-wall of the waveguide cross-section by using only one or few finite elements developed combining the in-plane and out-of-plane behaviour of the thin-wall lamina.

In this section the formulation in Ref. [22] is extended to linear viscoelastic materials by exploiting the approach proposed in Refs. [19, 24].

A SAFE element shell that combines the plane strain in-plane and out-of-plane behaviour of the lamina is developed. By formulating the governing equation in the frequency domain, linear viscoelastic rheological constitutive relations are introduced at the element level. The guided wave equation for viscoelastic waveguides with arbitrary thin-walled cross-section is built by simply interpolating the cross-section mid line. As a result, the guided waves attenuation dispersive spectrum can be obtained.

The proposed formulation is applied to model the mechanical guided waves in waveguides with simply and multiply connected cross-section. It is shown that for increasing frequencies the waveguide with simply connected cross-section presents more guided waves compared to the multiply connected section.

2.2.1 Mathematical formulation

A SAFE shell element is used to build the guided wave equation. The waveguide cross-section is subdivided into n_{el} elements. Each element is defined with respect to a local reference system xyz, as shown in Fig. 2.1. The element is assumed to have an infinite length in the axial direction, x, a finite width, L_u, in the y-direction and a constant thickness, t, in the z-direction. A global reference coordinates system (X, Y, Z) is assumed such that X coincides with x, and the y-axis makes an angle ϑ with the global XY plane as shown in Fig. 2.1a. The element is formulated by combining the in-plane and the out-of-plane behaviour of the shell. The in-plane response (u, v) of the shell is modelled by means of a 3 node SAFE element in plane stress, while its out-of-plane kinematic (w, ϑ) is represented by two quadratic SAFE elements with 2 nodes per element. This approach was used to have an inter-element continuous description of the strain [22].

2.2.1.1 In-plane problem

For the in-plane problem, at the generic point $\mathbf{x} \equiv (x, y, z)$ the displacement $\mathbf{u}$, the stress $\boldsymbol{\sigma}$ and the strain $\boldsymbol{\varepsilon}$ vectors with components $\mathbf{u} = \begin{bmatrix} u & v \end{bmatrix}^{\mathrm{T}}$, $\boldsymbol{\sigma} = \begin{bmatrix} \sigma_{xx} & \sigma_{yy} & \sigma_{xy} \end{bmatrix}^{\mathrm{T}}$, $\boldsymbol{\varepsilon} = \begin{bmatrix} \varepsilon_{xx} & \varepsilon_{yy} & \varepsilon_{xy} \end{bmatrix}^{\mathrm{T}}$, where the T superscript means transposition, are considered. Taking into account a 3 node shell element of length L_u, the displacement at a point within the generic $i-th$ element is approximated as:

$$\mathbf{u}_h(x, y, t) = \mathbf{N}^u(y)\mathbf{q}(x, t) \tag{2.1}$$

where $\mathbf{N}^u(y)$ is a 2×12 matrix containing the element quadratic shape functions, the upper-script u denotes the in-plane behaviour and $\mathbf{q}(x, t)$ is the assumed

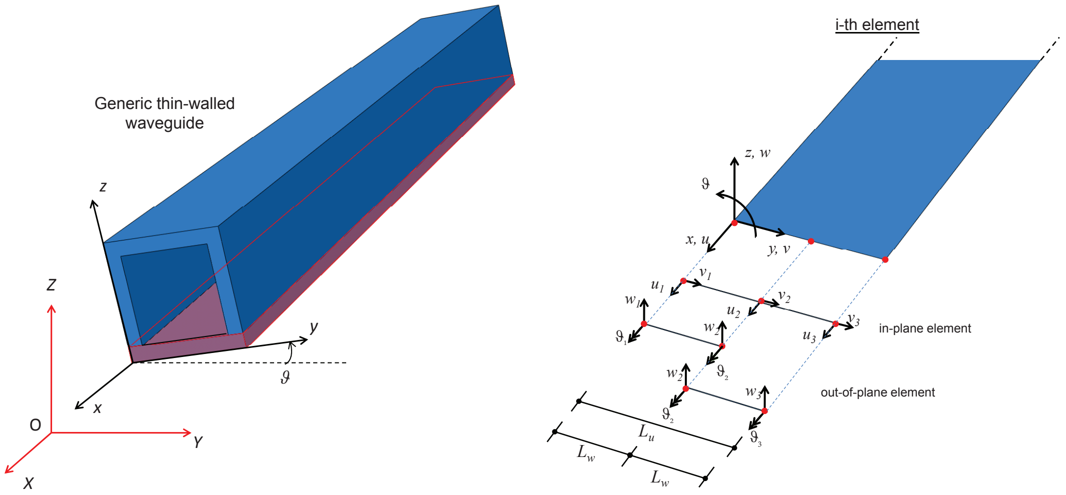

(a) (b)

Figure 2.1: Schematic representation of the waveguide (a) and generic element (b).

vector of nodal displacements:

$$\mathbf{q} = \begin{bmatrix} u_1 & v_1 & w_1 & \vartheta_1 & u_2 & v_2 & w_2 & \vartheta_2 & u_3 & v_3 & w_3 & \vartheta_3 \end{bmatrix}^{\mathrm{T}} \tag{2.2}$$

The approximated strain vector is written as:

$$\boldsymbol{\varepsilon}_h(x, y, t) = \mathbf{B}_x \frac{\partial \mathbf{q}}{\partial x} + \mathbf{B}_y \mathbf{q} \tag{2.3}$$

where $\mathbf{B}_x = \mathbf{L}_x \mathbf{N}^u$ and $\mathbf{B}_y = \mathbf{L}_y \frac{\partial \mathbf{N}^u}{\partial y}$ and the $\mathbf{L}_i$ operators are defined as:

$$\mathbf{L}_x = \begin{bmatrix} 1 & 0 & 0 \\ 0 & 0 & 1 \end{bmatrix}^{\mathrm{T}}, \qquad \mathbf{L}_y = \begin{bmatrix} 0 & 0 & 1 \\ 0 & 1 & 0 \end{bmatrix}^{\mathrm{T}} \tag{2.4}$$

At a given frequency ω, the kinetic and potential energies are respectively:

$$T_h = \frac{1}{2}\omega^2 \int\int \rho t \mathbf{u}_h^T \mathbf{u}_h \mathrm{d}x\mathrm{d}y, \qquad \Pi_h = \frac{1}{2} \int\int \boldsymbol{\varepsilon}_h^T \tilde{\mathbf{D}}^u(\omega)\, \boldsymbol{\varepsilon}_h \mathrm{d}x\mathrm{d}y \tag{2.5}$$

where ρ is the material density, t is the element thickness and $\tilde{\mathbf{D}}^u(\omega) = t\tilde{\mathbf{D}}$. $\tilde{\mathbf{D}}$ is the frequency dependent complex linear viscoelastic operator for plane-stress defined as:

$$\tilde{\mathbf{D}} = \begin{bmatrix} \tilde{D_{11}} & \tilde{D_{12}} & 0 \\ \tilde{D_{21}} & \tilde{D_{22}} & 0 \\ 0 & 0 & \tilde{D_{66}} \end{bmatrix} \tag{2.6}$$

where the coefficients $\tilde{D_{ij}}$ depend on the assumed rehological behaviour of the material.

After some algebraic manipulations, that include the Fourier transformation of the x-dependence into the wavenumber domain (ξ), the element governing equations can be written in the form:

$$-\xi^2 \mathbf{k}_1 \mathbf{q} + \mathrm{i}\xi \mathbf{k}_2 \mathbf{q} - \mathbf{k}_3 \mathbf{q} + \omega^2 \mathbf{m}_u \mathbf{q} = \mathbf{0} \tag{2.7}$$

where:

$$\mathbf{k}_1 = \int_0^{L_u} \mathbf{B}_x^{\mathrm{T}} \tilde{\mathbf{D}}^u \mathbf{B}_x \mathrm{d}y, \qquad \mathbf{k}_2 = \int_0^{L_u} \left(\mathbf{B}_y^{\mathrm{T}} \tilde{\mathbf{D}}^u \mathbf{B}_x - \mathbf{B}_x^{\mathrm{T}} \tilde{\mathbf{D}}^u \mathbf{B}_y \right) \mathrm{d}y, \tag{2.8}$$

$$\mathbf{k}_3 = \int_0^{L_u} \mathbf{B}_y^{\mathrm{T}} \tilde{\mathbf{D}}^u \mathbf{B}_y \mathrm{d}y, \qquad \mathbf{m}_u = \int_0^{L_u} \rho t \left(\mathbf{N}^u\right)^{\mathrm{T}} \mathbf{N}^u \mathrm{d}y \tag{2.9}$$

2.2.1.2 Out-of-plane problem

For the out-plane problem, at the generic point $\mathbf{x} \equiv (x, y, z)$ the displacement $\mathbf{u}$ presents only the displacement component w, while the stress $\boldsymbol{\sigma}$ and the curvature $\boldsymbol{\kappa}$ vectors are defined as $\boldsymbol{\sigma} = \begin{bmatrix} \sigma_{xx} & \sigma_{yy} & \sigma_{xy} \end{bmatrix}^{\mathrm{T}}$, $\boldsymbol{\kappa} = \begin{bmatrix} -\frac{\partial^2 w}{\partial x^2} & -\frac{\partial^2 w}{\partial y^2} & -2\frac{\partial^2 w}{\partial x \partial y} \end{bmatrix}^{\mathrm{T}}$. The displacement at a point within the generic $i-th$ element can be approximated as:

$$w_h^{\alpha}(x, y, t) = \mathbf{N}^w(y) \mathbf{q}(x, t) \qquad \alpha = 1, 2 \tag{2.10}$$

where $\mathbf{N}^w(y)$ is a 1×12 vector containing the cubic element shape functions in positions 3, 4, 7 and 8, the upper-script w denotes the out-of-plane and $\alpha = 1, 2$ indicates the first and the second element, respectively (see Fig. 2.1b). The approximated strain vector is written as:

$$\boldsymbol{\kappa}_h(x,y,t) = -\mathbf{a}_\alpha\mathbf{q} - \mathbf{b}_\alpha\frac{\partial\mathbf{q}}{\partial x} - \mathbf{c}_\alpha\frac{\partial^2\mathbf{q}}{\partial x^2} \tag{2.11}$$

where $\mathbf{a}_\alpha, \mathbf{b}_\alpha$ and $\mathbf{c}_\alpha$ are defined as:

$$\mathbf{a}_1 = \begin{bmatrix} 0 & 0 & 0 & 0 & 0 & 0 & 0 & 0 & 0 & 0 & 0 & 0 \\ 0 & 0 & \frac{\partial^2 N_1^w}{\partial y^2} & \frac{\partial^2 N_2^w}{\partial y^2} & 0 & 0 & \frac{\partial^2 N_3^w}{\partial y^2} & \frac{\partial^2 N_4^w}{\partial y^2} & 0 & 0 & 0 & 0 \\ 0 & 0 & 0 & 0 & 0 & 0 & 0 & 0 & 0 & 0 & 0 & 0 \end{bmatrix} \tag{2.12}$$

$$\mathbf{b}_1 = \begin{bmatrix} 0 & 0 & 0 & 0 & 0 & 0 & 0 & 0 & 0 & 0 & 0 & 0 \\ 0 & 0 & 0 & 0 & 0 & 0 & 0 & 0 & 0 & 0 & 0 & 0 \\ 0 & 0 & 2\frac{\partial N_1^w}{\partial y} & 2\frac{\partial N_2^w}{\partial y} & 0 & 0 & 2\frac{\partial N_3^w}{\partial y} & 2\frac{\partial N_4^w}{\partial y} & 0 & 0 & 0 & 0 \end{bmatrix} \tag{2.13}$$

$$\mathbf{c}_1 = \begin{bmatrix} 0 & 0 & N_1^w & N_2^w & 0 & 0 & N_3^w & N_4^w & 0 & 0 & 0 & 0 \\ 0 & 0 & 0 & 0 & 0 & 0 & 0 & 0 & 0 & 0 & 0 & 0 \\ 0 & 0 & 0 & 0 & 0 & 0 & 0 & 0 & 0 & 0 & 0 & 0 \end{bmatrix} \tag{2.14}$$

for $\alpha = 1$ and where $\mathbf{a}_2, \mathbf{b}_2$ and $\mathbf{c}_2$ can be obtained from matrices $\mathbf{a}_1, \mathbf{b}_1$ and $\mathbf{c}_1$, respectively, by moving the columns 3, 4, 7 and 8 in positions 7, 8, 11 and 12.

The expressions of the kinetic and potential energies for the out-of-plane problem are:

$$T_h = \frac{1}{2}\omega\int\int \rho t w_h^{\mathrm{T}} w_h \mathrm{d}x\mathrm{d}y, \qquad \Pi_h = \frac{1}{2}\int\int \boldsymbol{\kappa}_h^{\mathrm{T}}\tilde{\mathbf{D}}^w(\omega)\,\boldsymbol{\kappa}_h \mathrm{d}x\mathrm{d}y \tag{2.15}$$

where $\tilde{\mathbf{D}}^w(\omega) = t^3/12\tilde{\mathbf{D}}$.

The equations governing the element out-of-plane problem becomes:

$$-\xi^4\mathbf{e}_1^\alpha\mathbf{q} + \xi^2\mathbf{e}_2^\alpha\mathbf{q} - \mathbf{e}_3^\alpha\mathbf{q} + \omega^2\mathbf{m}_b^\alpha\mathbf{q} = \mathbf{0} \tag{2.16}$$

where:

$$\mathbf{e}_1^{\alpha} = \int_0^{L_w} \mathbf{d}_{\alpha}^{\mathrm{T}} \tilde{\mathbf{D}}^{w} \mathbf{d}_{\alpha} \mathrm{d}y, \qquad \mathbf{e}_2^{\alpha} = \int_0^{L_w} \left(\mathbf{d}_{\alpha}^{\mathrm{T}} \tilde{\mathbf{D}}^{w} \mathbf{a}_{\alpha} - \mathbf{b}_{\alpha}^{\mathrm{T}} \tilde{\mathbf{D}}^{w} \mathbf{b}_{\alpha} + \mathbf{a}_{\alpha}^{\mathrm{T}} \tilde{\mathbf{D}}^{w} \mathbf{d}_{\alpha} \right) \mathrm{d}y, \tag{2.17}$$

$$\mathbf{e}_3^{\alpha} = \int_0^{L_w} \mathbf{a}_{\alpha}^{\mathrm{T}} \tilde{\mathbf{D}}^{w} \mathbf{a}_{\alpha} \mathrm{d}y, \qquad \mathbf{m}_b^{\alpha} = \int_0^{L_w} \rho t \left(\mathbf{N}^{w} \right)^{\mathrm{T}} \mathbf{N}^{w} \mathrm{d}y \tag{2.18}$$

where L_w is the out-of-plane element length.

Combining the in-plane and out-of-plane problems, the element dynamic equation can be written in the local coordinates as:

$$-\xi^4 \mathbf{s}_1 \mathbf{q} - \xi^2 \mathbf{s}_2 \mathbf{q} + \mathrm{i}\xi \mathbf{s}_3 \mathbf{q} - \mathbf{s}_4 \mathbf{q} + \omega^2 \mathbf{m} \mathbf{q} = \mathbf{0} \tag{2.19}$$

where:

$$\begin{gathered} \mathbf{s}_1 = \mathbf{e}_1^1 + \mathbf{e}_1^2, \qquad \mathbf{s}_2 = \mathbf{k}_1 - \mathbf{e}_2^1 - \mathbf{e}_2^2, \\ \mathbf{s}_3 = \mathbf{k}_2, \qquad \mathbf{s}_4 = \mathbf{k}_3 + \mathbf{e}_3^1 + \mathbf{e}_3^2, \qquad \mathbf{m} = \mathbf{m}_u + \mathbf{m}_b^1 + \mathbf{m}_b^2 \end{gathered} \tag{2.20}$$

Applying standard procedures for finite elements yields to a system of M equations representing the wave equation of the waveguide:

$$\left[-\xi^4 \mathbf{S}_1 - \xi^2 \mathbf{S}_2 + \xi \hat{\mathbf{S}}_3 - \mathbf{S}_4 + \omega^2 \mathbf{M} \right] \mathbf{Q} = \mathbf{0} \tag{2.21}$$

where $\hat{\mathbf{S}}_3 = \mathbf{T}^{\mathrm{T}} \left(\mathrm{i}\xi \mathbf{S}_3 \right) \mathbf{T}$ and $\mathbf{T}$ is a diagonal matrix with its elements corresponding to the u degrees of freedom equal to the imaginary unit while those corresponding to the other degrees of freedom are equal to 1.

2.2.1.3 Solution method

The dispersive properties of guided waves can be found by solving the eigenvalue problem in eq. (2.21). Such problem can be solved for a given real ξ in the unknown ω. Even if the $\mathbf{S}_1$ matrix is singular, the problem remains well posed, but some predicted eigenvalues will be infinite; these solutions will simply be ignored. However, to capture damped waves eq. (2.21) must be solved in the wavenumber ξ for given ω. By reordering eq. (2.21) in the following $4M \times 4M$ linear system:

$$\left(\begin{bmatrix} \mathbf{0} & -\mathbf{I} & \mathbf{0} & \mathbf{0} \\ \mathbf{0} & \mathbf{0} & -\mathbf{I} & \mathbf{0} \\ \mathbf{0} & \mathbf{0} & \mathbf{0} & -\mathbf{I} \\ (\mathbf{S}_4 - \omega^2\mathbf{M}) & -\hat{\mathbf{S}}_3 & \mathbf{S}_2 & \mathbf{0} \end{bmatrix} - \xi \begin{bmatrix} -\mathbf{I} & \mathbf{0} & \mathbf{0} & \mathbf{0} \\ \mathbf{0} & -\mathbf{I} & \mathbf{0} & \mathbf{0} \\ \mathbf{0} & \mathbf{0} & -\mathbf{I} & \mathbf{0} \\ \mathbf{0} & \mathbf{0} & \mathbf{0} & -\mathbf{S}_1 \end{bmatrix}\right) \begin{bmatrix} \mathbf{Q} \\ \xi\mathbf{Q} \\ \xi^2\mathbf{Q} \\ \xi^3\mathbf{Q} \end{bmatrix} = \begin{bmatrix} \mathbf{0} \\ \mathbf{0} \\ \mathbf{0} \\ \mathbf{0} \end{bmatrix} \tag{2.22}$$

all the $4M$ wavenumbers $\xi^m = \xi^m_{\Re} + i\xi^m_{\Im}$ and waveshapes $\mathbf{Q}^m$ existing at the given frequency ω can be obtained solving the associated eigenvalue problem.

In order to avoid numerical instabilities in computing the eigenvalues of eq. (2.22), the elements of the identity matrix $\mathbf{I}$ were multiplied by $10e^9$.

Whereas in elastic medium, by using this method, real, purely imaginary and complex eigenvalues corresponding to wave numbers of propagating and evanescent waves, respectively, are obtained, when viscoelasticity is introduced all the modes assume a complex wavenumber and such a type of distinction is no longer possible. In such case the real part of the wavenumber describes the wave spatial frequency in the x-direction, while its imaginary part expresses the wave amplitude decay.

From each ξ^m, the phase velocity [m s^{-1}] and the attenuation [Np m^{-1}] of the $m-th$ wave are computed as:

$$c^m_{ph} = \frac{\omega}{\xi^m_{\Re}}, \qquad att^m = \xi^m_{\Im} \tag{2.23}$$

where an attenuation of one Neper per meter means that a wave of unit amplitude is reduced to an amplitude of $e^{-\xi^m_{\Im}}$ after travelling one meter. Mode attenuation in Decibel per meter [dB m^{-1}] can be easily obtained since Decibel and Neper have a fixed linear ratio to each other: 1 dB $= ln\,(10)\,/20$ Np.

The $m-th$ wave group velocity can be computed as:

$$c^m_g = \frac{\partial\omega}{\partial\xi^m_{\Re}} = \frac{(\mathbf{Q}^m)^{\mathrm{T}}\left[-4\,(\xi^m_{\Re})^3\,\mathbf{S}_1 - 2\xi^m_{\Re}\mathbf{S}_2 + \hat{\mathbf{S}}_3\right]\mathbf{Q}^m}{2\omega\,(\mathbf{Q}^m)^{\mathrm{T}}\,\mathbf{M}\mathbf{Q}^m} \tag{2.24}$$

From these relations the phase/group velocity and attenuation can be evaluated for each solution (ω, ξ^m) and the dispersion curves traced.

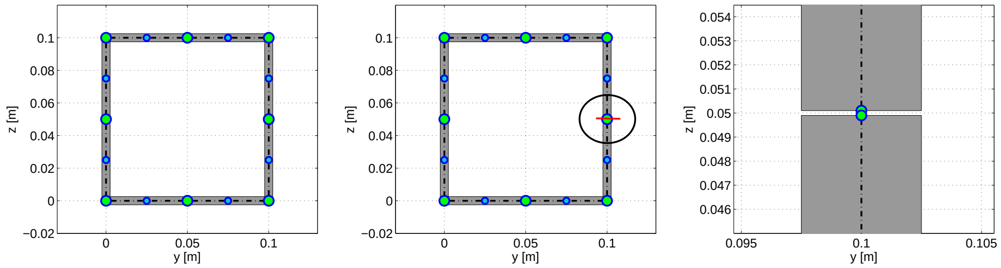

(a) (b) (c)

Figure 2.2: (a) Multiply connected cross-section (8 elements, 16 nodes, 64 dofs); (b) simply connected cross-section (8 elements, 17 nodes, 68 dofs); (c) zoom for the line cut.

2.2.2 Numerical applications and discussions

A hollow waveguide with square cross-section characterized by a 100 mm side and a 5 mm thickness is considered. Two cases are examined: a closed hollow quadratic section (see Fig. 2.2a) and a simply connected case where a cut of neglecting depth has been considered (see Fig. 2.2b). The location of the cut is emphasised in Fig. 2.2c.

The material is steel, with the following nominal properties: longitudinal bulk wave speed $c_L = 6020$ m s^{-1}, shear bulk wave speed $c_S = 3217$ m s^{-1}, longitudinal bulk attenuation $\kappa_L = 0.003$ Np m^{-1}, shear bulk wave attenuation $\kappa_S = 0.008$ Np m^{-1} and density $\rho = 7800$ kg m^{-3}. Assuming a hysteretic rehological model, the complex Young's modulus $\tilde{E} = E_{\Re} + \mathrm{i}E_{\Im} = 209.9 - \mathrm{i}0.463$ GPa and complex Poisson's ratio $\tilde{\nu} = \nu_{\Re} + \mathrm{i}\nu_{\Im} = 0.3001 + \mathrm{i}0.0004$ can be obtained by well known formulae [19] and the coefficients of the constitutive operator defined:

$$\tilde{D_{11}} = \tilde{D_{22}} = \frac{\tilde{E}}{1-\tilde{\nu}^2}, \qquad \tilde{D_{12}} = \tilde{D_{21}} = \frac{\tilde{\nu}\tilde{E}}{1-\tilde{\nu}^2}, \qquad \tilde{D_{66}} = \frac{(1-\tilde{\nu})\,\tilde{E}}{2\,(1-\tilde{\nu}^2)} \tag{2.25}$$

The dispersive curves in terms of phase, attenuation and group velocity are

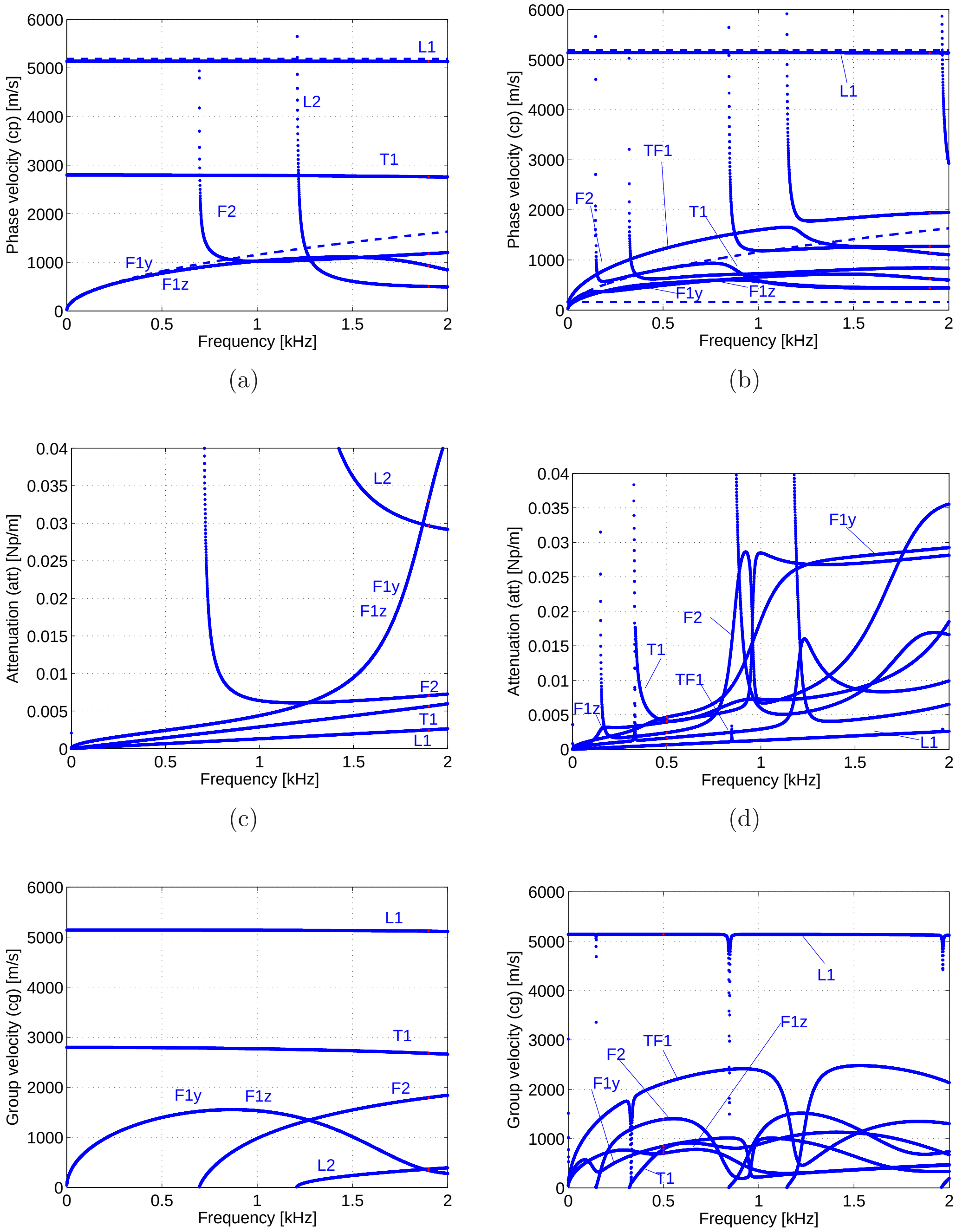

(a) (b)

(c) (d)

(e) (f)

Figure 2.3: Phase, Attenuation and Group velocity curves for the multiply connected section (a, c, e) and for the simply connected section (b, d, f).

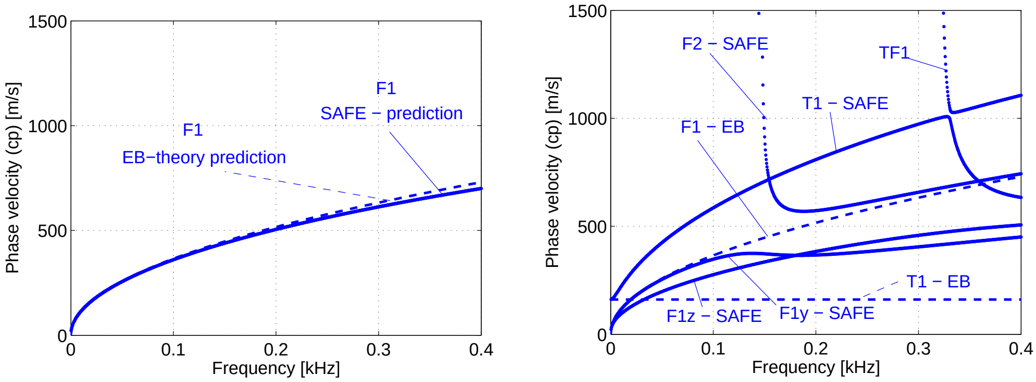

(a) (b)

Figure 2.4: Differences emphasize between the Euler-Bernoulli EB beam theory and the $SAFE$ theory predictions in the $0-0.4$ kHz frequency range.

represented in Fig. 2.3 for both waveguides. For the multiply connected cross-section (see Fig. 2.3a, c and e) in the $0-2$ kHz frequency range up to six waves exist. In particular two longitudinal waves $(L1, L2)$, three flexural waves $(F1y, F1z, F2)$ and a torsional wave $(T1)$ were recognized also by means of the waveshape representations (see Fig. 2.5).

At low frequency, the $L1$ and $T1$ waves have a very low dispersive behaviour in agreement with the longitudinal and rotational waves for an Euler-Bernoulli beam, represented in Fig. 2.3 and 2.4 with dashed lines:

$$c_{ph}^{L1} = \frac{\omega}{\xi^{L1}} = \sqrt{\frac{\tilde{E}_{\Re}}{\rho}} \cong 5187 \quad ms^{-1}, \qquad c_{ph}^{T1} = \frac{\omega}{\xi^{T1}} = \sqrt{\frac{\tilde{G}_{\Re} J_t}{\rho I_p}} \cong 2782 \quad ms^{-1} \tag{2.26}$$

where $\tilde{G}_{\Re} = \tilde{E}_{\Re}/(2(1+\tilde{\nu}_{\Re}))$, J_t is the Saint-Venant torsion constant and $I_p = I_y + I_z$ is the sum of the area moments about the principal $y-$ and $z-$ axis of the cross-section. However, while the $T1$ wave has a phase speed almost coincident with the one predicted by the Euler beam theory, contrary the $L1$ wave has a phase speed slightly smaller than that predicted by the Euler beam theory. As it can be seen from the waveshape $L1$ in Fig. 2.5, in fact, the $L1$ wave besides a main extensional behaviour shows an out-of-plane deformation of the cross-section. Due to such deformation the cross-section results more flexible and the

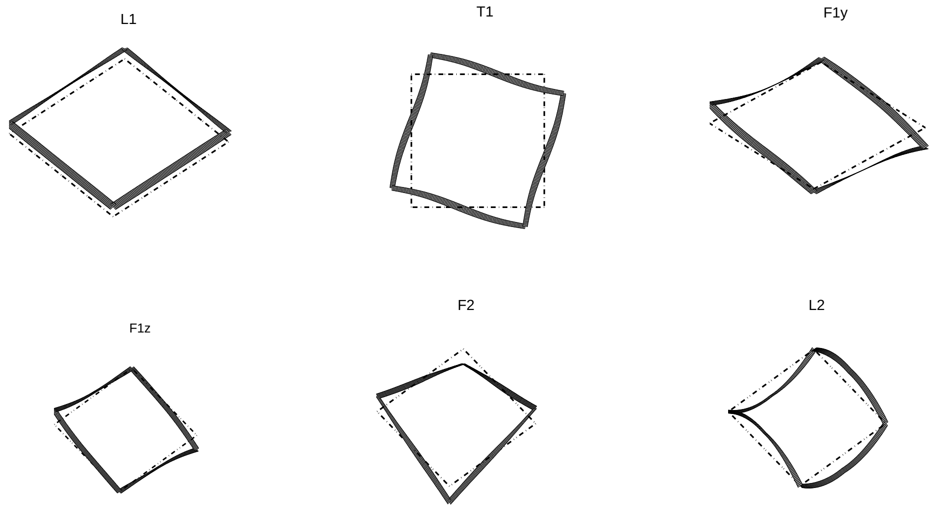

Figure 2.5: Wavestructures for the multiply connected cross-section calculated at 2 kHz frequency.

speed of the longitudinal wave smaller than 5187 m s^{-1}.

In addition to the $T1$ and $L1$ waves, two fundamental flexural waves, with identical dispersive behaviour exist. Such waves are labelled as $F1y$ and $F1z$, since they present a global rotation of the cross-section with respect the principal $y-$ and $z-$axis, as it can be noted from Fig. 2.5. In agreement with the Euler-Bernoulli theory, such waves start propagating at zero frequency with a dispersive behaviour for increasing frequency:

$$c_{ph}^{F1y} = \frac{\omega}{\xi^{F1y}} = \sqrt[4]{\frac{\tilde{E}_{\Re} I_y}{\rho A}\omega^2}, \qquad c_{ph}^{F1z} = \frac{\omega}{\xi^{F1z}} = \sqrt[4]{\frac{\tilde{E}_{\Re} I_x}{\rho A}\omega^2} \tag{2.27}$$

where A is the cross-section area.

Finally, the two more waves labelled $F2$ and $L2$, with cut-off frequency around 0.7 kHz and 1.2 kHz, respectively, show distorted wavestructures that cannot be described by Euler-Bernoulli beam theory. By observing also the attenuation curves it can be inferred that in the considered frequency range the $T1$ and $L1$ waves have very low attenuation and therefore can be chosen as potential

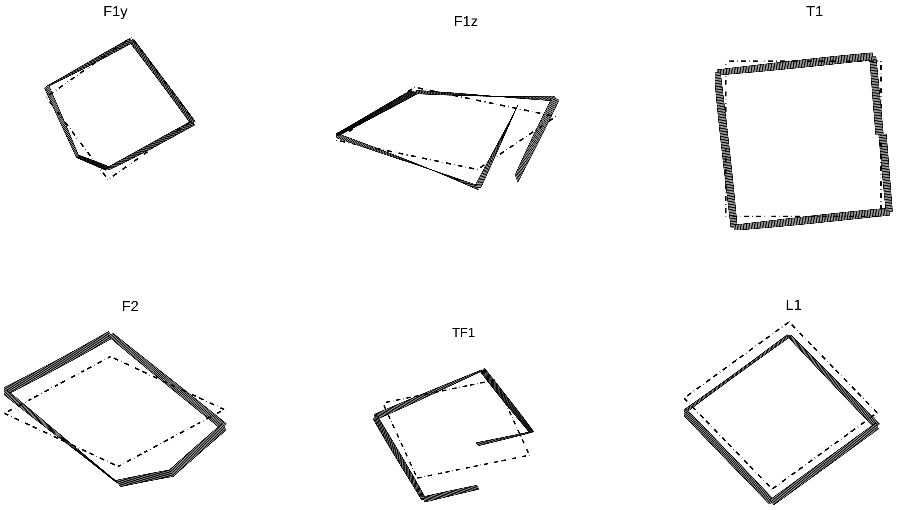

Figure 2.6: Wavestructures for the simply connected cross-section calculated at 0.5 kHz frequency.

candidates for the long range inspection of such waveguides.

In the simply connected cross-section, see Fig. 2.3b, d and e, more waves exist in the same frequency range. From the curves comparison at very low frequencies, it appears that the longitudinal $L1$ wave, characterized by the highest speed among the propagative waves, doesn't differ much in the two cases. Longitudinal waves, in fact, are driven by the axial stiffness of the cross-section that is practically identical for the multiply and the simply connected cross-section.

On the other hand, since the torsional stiffness for the simply connected section is much lower than the torsional stiffness for the multiply connected section, the formerly $T1$ wave is not any more supported by the simply connected cross-section. The dispersion curves of the guided torsional $T1$ wave for the simply connected section, with wave shape highlighted in Fig. 2.6, in fact, shows a smaller and dispersive phase and group velocities.

It can also be noted that for the simply connected cross-section the two fundamental flexural waves assume a different dispersive behaviour, since their waveshapes behave differently, as can be seen in Fig. 2.6. For increasing frequencies more waves with coupled behaviour appear. For instance, the $TF1$ wave, with torsional and flexural behaviour coupled has been highlighted. Such wave with coupled motion, as many others in the same frequency range, exists due to the fact that the mass centre of the cross-section does not coincide to its shear centre.

2.3 Dispersion curves extraction in waveguides with arbitrary cross-section

This section investigates dispersion curves in waveguides characterized by arbitrary cross-sections. A semi-analytical finite element (SAFE) formulation based on a 3-node triangular constant strain elements with both linear or quadratic shape functions is used to set the guided wave equation.

Besides, how an open internal crack running along the cross section of a straight pipe affects the dispersion curves is examined. This allows to highlight the guided waves phase velocity sensitivity to various depths of the open crack and to define some modes, being particularly sensitive to the defect, as good candidates for the non-destructive detection of the crack depth.

2.3.1 Mathematical formulation

A semi-analytical finite element formulation is used to extract the principal guided wave features. Such formulation requires a bi-dimensional finite element mesh over the waveguide cross-section only, here generated by using the *"pdetool"* of Mtalab.

Figure 2.7 shows a schematic representation of the infinitely long considered waveguide[1]. The waveguide cross-section belongs to the $x-y$ plane and the z axis coincides with the longitudinal axis of the waveguide. The structure is considered to be in vacuum. The wave propagates along z direction. The problem variables at the general point $\mathbf{x} \equiv (x, y, z)$ of the waveguide are the displacement $\mathbf{u}$, the

---

[1] It's worth noticing that even if the examined case consists of a circular pipe, the routine is still valid for arbitrary cross-section waveguides.

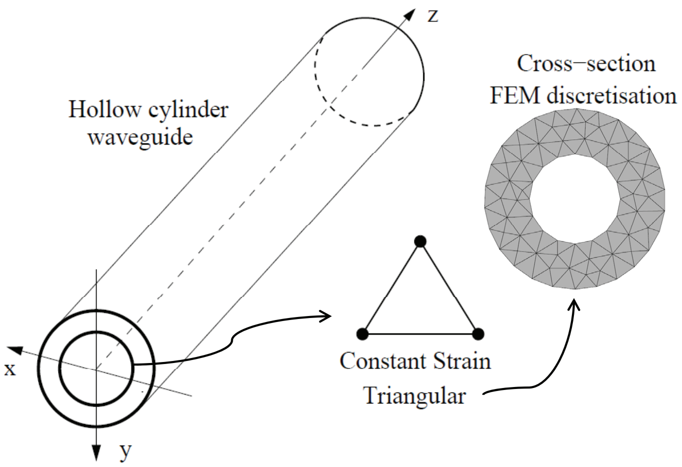

Figure 2.7: Schematic representation of the waveguide and the cross-section bidimensional finite element mesh.

stress $\boldsymbol{\sigma}$ and the strain $\boldsymbol{\epsilon}$ vectors with components:

$$\begin{gathered}\mathbf{u} = \left[u_x \quad u_y \quad u_z\right]^T, \quad \boldsymbol{\sigma} = \left[\sigma_{xx} \quad \sigma_{yy} \quad \sigma_{zz} \quad \sigma_{yz} \quad \sigma_{xz} \quad \sigma_{xy}\right]^T, \\ \boldsymbol{\epsilon} = \left[\epsilon_{xx} \quad \epsilon_{yy} \quad \epsilon_{zz} \quad \gamma_{yz} \quad \gamma_{xz} \quad \gamma_{xy}\right]^T\end{gathered} \tag{2.28}$$

where the T superscript means transposition. The structure cross-section is discretized by constant strain triangular (CST) elements, with 3 dofs per node associated to the displacement u_x, u_y and u_z. The generic displacement vector at a point within the generic $e-th$ element can be approximated as:

$$\mathbf{u}_h(\mathbf{x}, t) = \mathbf{N}(x, y)\mathbf{q}(z, t) \tag{2.29}$$

with $\mathbf{N}(x, y)$ shape functions matrix and $\mathbf{q}(z, t)$ vector with the $e-th$ element nodal displacements. Similarly, it is possible to write the approximated strain vector as:

$$\boldsymbol{\epsilon}(\mathbf{x}, t) = \mathbf{B}_{xy}\mathbf{q} + \mathbf{B}_z\frac{\partial \mathbf{q}}{\partial z} \tag{2.30}$$

where $\mathbf{B}_{xy} = \mathbf{L}_x \frac{\partial \mathbf{N}_x}{\partial x} + \mathbf{L}_y \frac{\partial \mathbf{N}_y}{\partial y}$, $\mathbf{B}_z = \mathbf{L}_z \mathbf{N}$, and the $\mathbf{L}_i$ operators are defined as:

$$\mathbf{L}_x = \begin{bmatrix} 1 & 0 & 0 \\ 0 & 0 & 0 \\ 0 & 0 & 0 \\ 0 & 0 & 0 \\ 0 & 0 & 1 \\ 0 & 1 & 0 \end{bmatrix}, \qquad \mathbf{L}_y = \begin{bmatrix} 0 & 0 & 0 \\ 0 & 1 & 0 \\ 0 & 0 & 0 \\ 0 & 0 & 1 \\ 0 & 0 & 0 \\ 1 & 0 & 0 \end{bmatrix}, \quad \mathbf{L}_z = \begin{bmatrix} 0 & 0 & 0 \\ 0 & 0 & 0 \\ 0 & 0 & 1 \\ 0 & 1 & 0 \\ 1 & 0 & 0 \\ 0 & 0 & 0 \end{bmatrix} \tag{2.31}$$

By using Hamilton's principle, the waveguide Lagrangian reads:

$$\mathcal{L} = \frac{1}{2} \bigcup_{e=1}^{n_{el}} \int_{-\infty}^{+\infty} \int_{\Omega_e} \left[\rho^e \dot{\mathbf{u}}_h^T \dot{\mathbf{u}}_h - \boldsymbol{\epsilon}_h^T \mathbf{C}^e \boldsymbol{\epsilon}_h \right] dxdydz \tag{2.32}$$

where ρ^e is the element mass density, $\mathbf{C}^e$ is the viscoelastic operator [25]. Those quantities are considered to be constant over Ω_e. After some algebraic manipulations the guided wave equation is obtained from Eq. (2.32):

$$[\mathbf{A} - \xi \mathbf{B}]_{2H} \mathbf{Q} = \mathbf{0} \tag{2.33}$$

where H is the total number of degrees of freedom of the cross-section mesh.

The solution of the wave equation is found using the *"eig"* command of Matlab [26], for a given frequency in input ($\omega = 2\pi f$). Then all the complex wavenumbers ξ^m and waveshapes $\mathbf{Q}^m$ exsisting at that frequency, where $m = 1, 2, 3, ..., 2H$, are obtained. Finally, phase velocity is calculated from these modal properties by means of simple formulae. Dispersion curves are traced repeating this procedure for all the frequencies of interest.

Mathematical steps are discussed in details in the Ref. [19].

2.3.2 Numerical applications and discussions

A hollow cylinder is considered. Inner and outer radius are $R_i = 10$ cm and $R_e = 20$ cm, respectively. The material is steel, with the following nominal properties: longitudinal bulk wave speed $c_L = 5875.1$ m/s, shear bulk wave speed

$c_S = 3140.4$ m/s, density $\rho = 7800$ kg/m^3. Steel is modelled as an isotropic elastic material.

Case	D0	D1	D2	D3
Defect semi diameters lengths	$a = 0$ cm $b = 0$ cm	$a = 2$ cm $b = 2$ cm	$a = 4$ cm $b = 2$ cm	$a = 6$ cm $b = 2$ cm

Table 2.1: Analysed cross-section denomination and defect description.

Four cases are considered: the pristine hollow cylinder and three damaged cases with an elliptical notch of increasing depth. The notch is characterized by its semi-diameters lengths a and b (see Table 2.1). The location of the notch is identical for all the cases considered (see Fig. 2.8). The mesh around the crack location is refined in order to obtain a more accurate solution.

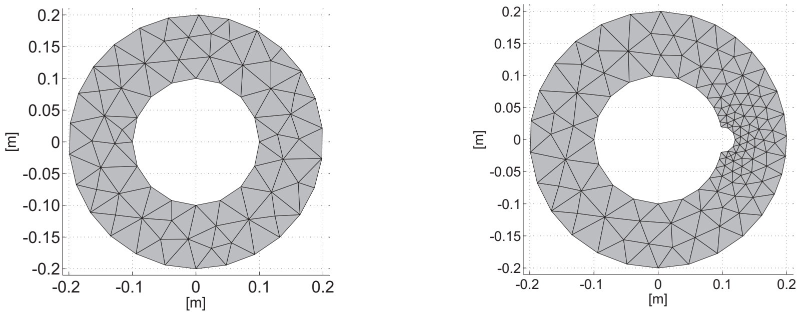

(a) D0 (b) D1

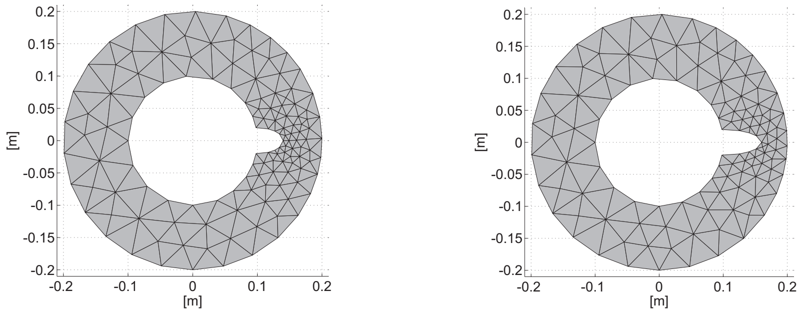

(c) D2 (d) D3

Figure 2.8: Analysed cases: from a pristine cross-section (a) to damaged cross-sections (b,c,d).

The phase velocity dispersion curves for the pristine cylinder are represented in Fig. 2.9. It can be noted that in the 0-8000 Hz range several dispersive waves exist. Larger slope of the curves denotes higher dispersion: in those zones, called *high dispersive zones*, waves are more distorted with propagating distance.

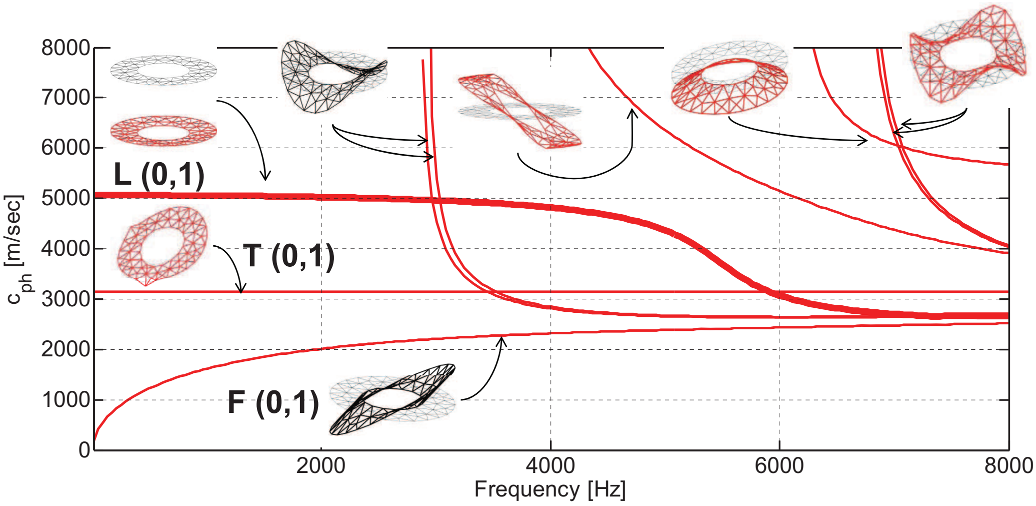

Figure 2.9: Phase velocities curves and waveshapes for the pristine case.

Normalised waveshapes for each mode are also reported in Fig. 2.9. It appears that below 3000 Hz three guided modes exist: a flexural one (F), a torsional one (T) and a longitudinal one (L). The F-mode and the L-mode are dispersive; the T-mode is non-dispersive. For upper frequency values, new dispersion curves exist.

A fundamental aspect in the inspection procedure is related to the sensitivity that each propagating wave shows with respect to the target defect. In this study, sensitivity is defined as the difference between the phase velocity for the intact case (chosen as a reference curve) and the phase velocity for the damaged cases (see Fig. 2.10). As it can be seen, the longitudinal mode shows potential for detection of this kind of defect. The above results indicate that the phase velocity of the L(0,1) mode in the 4000 - 8000 kHz frequency range decreases for increasing crack depths. In conclusion, this wave-phase velocity shift could be potentially used for detecting the presence of an internal open elliptical crack on pipes.

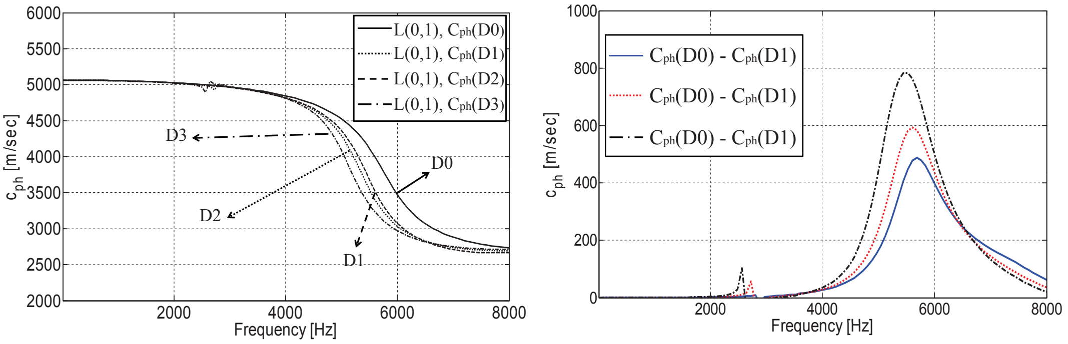

(a) (b)

Figure 2.10: (a) L(0,1) phase velocity dispersion curves for the four considered cases. (b) L(0,1) sensitivity curves for the elliptical notch.

2.4 Conclusions

Different semi-analytical finite element (SAFE) formulations have been presented to study guided waves in cylinders, arbitrary cross-section and thin-walled waveguides having infinite length in the wave propagation direction.

Plane strain (arbitrary cross-section waveguides) and plane stress (thin-walled beams) assumptions have been made according to the analysed cases. Numerical examples illustrate good accuracy for the lowest modes and the general applicability of the methods.

The formulations can be useful in constructing the elastodynamic Green's function as well as for solving boundary-value problems of such structures. However, it must be remembered that while the group velocity computation hold for undamped media, when material attenuation is accounted, as for some of the considered cases, the energy velocity should be computed as in Ref. [19].

However, for frequency independent constitutive relations and low attenuation values, the group velocity can still be accepted to predict the speed of propagation of mechanical guided pulses.

Further efforts will be toward the implementation and testing of the energy velocity.

Chapter 3

Dispersion compensation for defect detection and localization

3.1 Introduction

In recent years, ultrasonic Guided Waves (GWs) have received a great deal of attention among the nondestructive testing and structural health monitoring (NDT/SHM) scientific community mainly thanks to the ability to travel long distances without substantial attenuation as well as to the versatile multimode/frequency examination for defects detection, classification and sizing. Among the various applications based on GWs, numerous approaches have been proposed to detect and locate defects in pipes [27, 28], cables [29], rails [25, 30] as well as in plates-like structures [5, 31, 32, 33, 34].

Operating in pulse echo mode, generally, a defect is revealed within the received signal by means of unexpected waves generated (scattered) by the interaction of the incident wave/waves with the defect. These unexpected waves are next utilized to locate the defect. In this step, the use of GWs dispersion compensation procedures is of great benefit. In fact, such procedures exploit the dispersive properties of GWs, that can be computed once the waveguide material and geometrical properties are known, to extract from the received signal the distance of propagation of the scattered waves. Once this information has been obtained, the defect can be located straightforwardly in mono-dimensional waveguides (cables, pipes, rails, etc.) or by means of triangulation based procedures in bi-dimensional structures (plates).

GWs signal compensation is not an easy task since several dispersive modes might simultaneously appear in the received signal. The modes, in fact, overlap in both time and frequency domains and simple Fourier analysis techniques are not able to separate them. To such purpose, recent works in the area of time-frequency representations (TFRs) have been proposed [35, 36, 37, 38].

Nevertheless, even in the time-frequency domain, fast identification and separation of guided modes is a challenging step in the process of damage detection and localization. This task is even more difficult in waveguides (irregular) composed by segments with (i) different material properties, (ii) different cross-section, (iii) tapered geometry, as well as (iv) different radii of curvature (for instance a bent pipe in a pipeline). The waves propagating in these segments, in fact, are characterized by a different dispersive behavior thus complicating further the final received signal. In such cases, dispersion compensation procedures designed to operate in waveguides with constant dispersive properties [39, 40] fail.

In this chapter a novel strategy to tackle signal dispersion in case of irregular waveguides is proposed and validated numerically on simulated waveforms. In particular, once a so called reference portion (RP) of the irregular waveguide has been assumed, and within which the defect is sought, a two-step signal processing strategy is applied. In the first step, the Warped Frequency Transform (WFT) [41] is exploited to compensate the acquired signal for the dispersion experienced by the guided wave propagating along the reference portion (RP). The second step is aimed at removing the additional group delay produced by the remaining segments, i.e. the irregular portion (IP) of the waveguide, which are characterized by dispersive patterns different from the one of the regular portion (RP).

The above processing, applied to a received signal, reveals immediately the distance traveled by the defect-reflected wave in the regular portion (RP), allowing thus to locate the defect in an irregular waveguide.

The potential of the proposed procedure is shown by means of some examples in which guided waves signals are obtained via accurate Finite Elements simulations. In particular, plate waves propagating in waveguides composed by uniform, tapered and curved segments are considered. It is shown that the dispersion compensated signals detect immediately the distance traveled by the waves, thus allowing to precisely localize defects in irregular plate waveguides.

It is worth noticing that the low computational cost of WFT, which is comparable with that of the Fast Fourier Transform, makes the new tool suitable for real time applications. In addition, the procedure can be extended to arbitrary cross-section waveguides.

3.2 Group delay computation

The group delay can be considered as a measure of the time delay introduced in each frequency component of a dispersive signal by the distance of propagation. For a given distance, such time delay depends on the dispersive pattern of the waves for the given waveguide. If the waveguide is composed by multiple segments with different dispersive properties, i.e. if the waveguide is irregular, the group delay will depend on the dispersive patterns of all the segments traveled by the wave. As well known, for a waveguide segment with homogeneous material properties, as those that will be considered in this work, the dispersive pattern only depends on its cross-section geometry.

The group delay of a GW propagating in an irregular waveguide is computed by using the approach previously presented in [42], and concisely summarized hereinafter. An irregular waveguide is assumed as composed of a sequence of N segments each with a well defined dispersive pattern. Thus, the group delay of the M-th guided wave propagating for a distance $D = \sum_{i=1}^{N} \Delta x_i$, can be computed as:

$$\tau_D^M(f) = \sum_{i=1}^{N} \tau_{\Delta x_i}^M(f) \tag{3.1}$$

where $\tau_{\Delta x_i}^M$ is the group delay that the wave experiences in the i-th segment of length Δx_i. For instance, referring to the case of Fig. 3.1, the group delay for the M-th wave traveling from point A to point G reads:

$$\tau_{D_{AG}}^M(f) = \tau_{D_{AB}}^M(f) + \tau_{D_{BC}}^M(f) + \tau_{D_{CD}}^M(f) + \tau_{D_{DE}}^M(f) + \tau_{D_{EF}}^M(f) + \tau_{D_{FG}}^M(f) \tag{3.2}$$

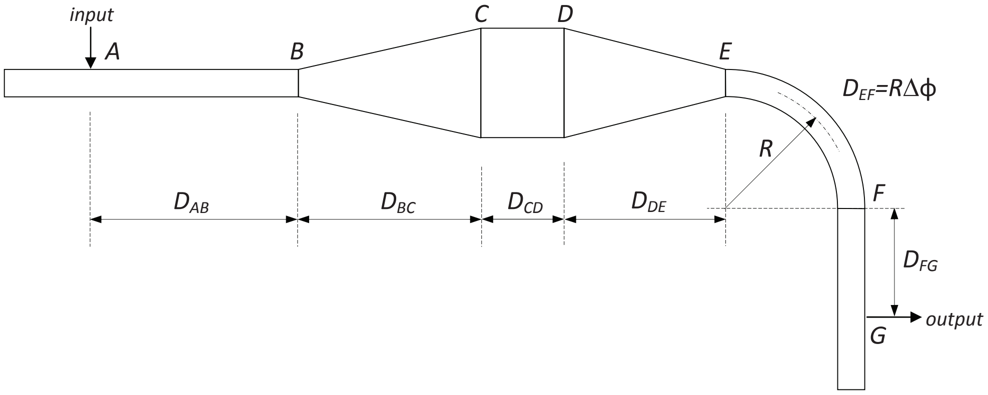

Figure 3.1: Schematic representation of an irregular waveguide composed by uniform ($\bar{AB}$, $\bar{CD}$ and $\bar{FG}$), tapered ($\bar{BC}$ and $\bar{DE}$) and curved ($\bar{EF}$) segments.

As well known, a guided wave crossing two segments with different cross-section and/or traveling along tapered waveguides may experience wave reflection [43] and mode conversion [44]. However, as long as the attention is not on the wave energy that is reflected or converted in different guided modes but on the behavior that a specific GW undergoes while traveling along an irregular waveguide, Eq. (3.1) is acceptable for the computation of its group delay [43, 45, 46]. Obviously, this requires that the GW considered in each portion for the computation of the group delay is generated by the incoming wave that has been considered in the previous segment of waveguide.

3.2.1 Segments with uniform cross-section

The group delay of the M-th GW propagating for a distance D in a straight segment with uniform cross-section is defined as:

$$\tau_D^M(f) = \frac{D}{cg^M(f,\Omega)} \tag{3.3}$$

where $cg^M(f,\Omega)$ is the M-th wave group velocity while f and Ω denote the frequency and the waveguide cross-section, respectively. The above equation holds also for curved segments with uniform cross-section and constant radius of curvature. In such case, the distance of propagation can be computed as

$D = R\Delta\phi$, where R is the mean radius and $\Delta\phi$ is the angle subtended by the first and last cross-section of the curved waveguide.

3.2.2 Tapered segments

The group delay computation in Eq. (3.3) can be extended to the case of a segment with moderately and continuously varying cross-section, tapered, by computing the following integral [42]:

$$\tau_D^M(f) = \int_0^D \frac{dx}{cg^M(f, \Omega(x))} \tag{3.4}$$

where $cg^M(f, \Omega(x))$ is the M-th wave group velocity curve at the cross-section $\Omega(x)$, and x is a coordinate along the segment axis. It can be observed that Eq. (3.4) simplifies to Eq. (3.3) when applied to a waveguide segment with uniform cross-section Ω.

For the numerical computation of such integral, it was shown in [42] that a proper group delay can be calculated as a summation of group delays that the wave ideally experiences propagating in a sequence of N_U short waveguides with uniform cross-section, used to approximate the tapered waveguide, as:

$$\tau_D^M(f) = \sum_{i=1}^{N_U} \frac{\Delta x_i}{cg^M(f, \Omega_i)} \tag{3.5}$$

where Δx_i is the length of the i-th portion with uniform cross-section Ω_i for which the wave has a group velocity $cg^M(f, \Omega_i)$, and $D = \sum_{i=1}^{N_U} \Delta x_i$ is the total length of the tapered waveguide (see Fig. 3.2).

Such procedure was successfully applied to predict the group delay of longitudinal waves propagating in tapered steel rods and of symmetric Lamb-type waves propagating in aluminum tapered plates [42], as well as to other different waveguides by different authors [47, 48, 49].

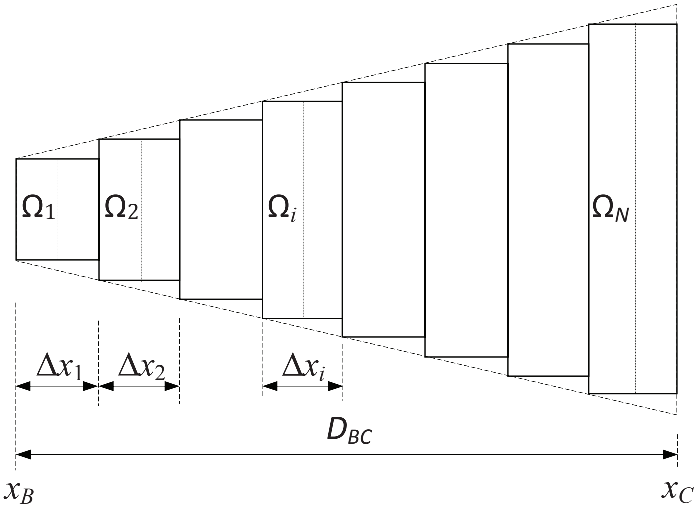

Figure 3.2: Sketch of a waveguide segment with varying cross-section $\Omega_1 \rightarrow \Omega_N$.

3.2.3 Group-delay of the reference (RP) and irregular (IP) portions

The group delay $\tau^M_{D_{AG}}(f)$ in Eq. (3.2), and in general the one of a GW propagating in an irregular waveguide, can be rewritten as:

$$\tau^M_D(f) = \tau^M_{D_R}(f) + \tau^M_{D_I}(f) \tag{3.6}$$

where $\tau^M_{D_R}(f)$ is the group delay that the wave experiences while traveling in the reference portion (RP) of the waveguide, and $\tau^M_{D_I}(f)$ takes into account the group delay of the GW gained while traveling along all the remaining waveguide segments characterized by different dispersive properties with respect to that of the reference portion (RP). Such part of the waveguide is termed as irregular portion (IP). Defects placed at unknown positions within the reference portion (RP) of the waveguide can be localized by the proposed strategy.

As it will be shown later, in fact, the proposed procedure is capable of extracting the unknown distance traveled by a GW in a waveguide with constant dispersive properties (RP) once the group delay of the waveguide irregular part (IP), in which the distance traveled by the wave is known, has been computed.

Thus, the reference portion of the waveguide can be composed by one or more uniform cross-section segments with identical dispersion properties.

For instance, for a wave traveling from point A to point G in the scheme of Fig. 3.1, both (or only one of them) segments $\bar{AB}$ and $\bar{FG}$, characterized by equal dispersive properties, can be assumed as the reference portion (RP) of the waveguide, i.e. $\tau^M_{D_R}(f) = \tau^M_{D_{AB}}(f) + \tau^M_{D_{FG}}(f)$, while the tapered segments $\bar{BC}$ and $\bar{DE}$, the segment $\bar{CD}$ (characterized by a constant cross-section but different from that of the reference portion) as well as the curved segment $\bar{EF}$ as the irregular portion (IP), i.e. $\tau^M_{D_I}(f) = \tau^M_{D_{BC}}(f) + \tau^M_{D_{CD}}(f) + \tau^M_{D_{DE}}(f) + \tau^M_{D_{EF}}(f)$.

3.3 Signal dispersion compensation

3.3.1 The Warped Frequency Transform (WFT)

The WFT is a unitary time-frequency transformation that produces a flexible sampling of the time-frequency domain. Given a generic signal $s(t)$ which frequency representation is $S(f) = \mathbf{F}\{s(t)\}$, being $\mathbf{F}$ the Fourier Transform operator, the Frequency Warping operator $\mathbf{W}_w$ reshapes the periodic frequency axis by means of a proper warping map $w(f)$, such as:

$$\begin{aligned} s_w(t) &= \mathbf{W}_w\{s(t)\} \\ \mathbf{F}\{s_w(t)\} &= \sqrt{\dot{w}(f)} \cdot S(w(f)) \end{aligned} \tag{3.7}$$

where $s_w(t)$ is the warped signal, and $\dot{w}(f)$ represents the first derivative of $w(f)$. $w(f)$ must be an odd function, i.e. $w(f) = -w(-f)$, and in order to preserve invertibility, $w(f)$ must map f axis on itself, i.e. $w^{-1}[w(f)] = f$.

The WFT can be exploited to compensate a received signal from the dispersion generated by a traveling GW (see [41]). To such aim, the warping map $w(f)$ can be defined, through its functional inverse, as:

$$K \frac{\mathrm{d}w^{-1}(f)}{\mathrm{d}f} = \frac{1}{cg^M(f,\Omega)} \tag{3.8}$$

where K is a normalization parameter selected so that $w^{-1}(0.5) = w(0.5) = 0.5$

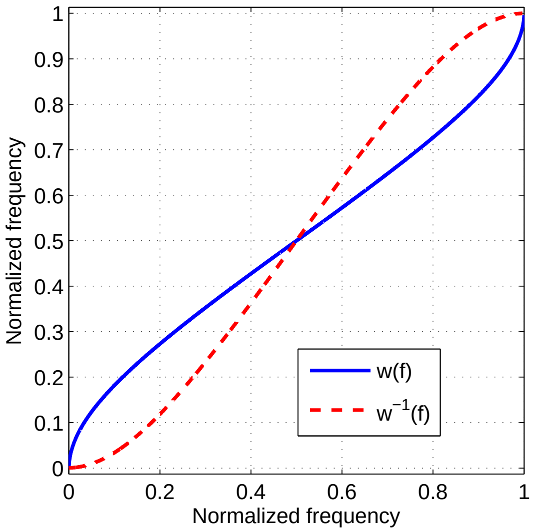

Figure 3.3: Warping map $w(f)$ for A_0 wave dispersion compensation and its functional inverse $w^{-1}(f)$ designed according to Eq. (3.8).

and $cg^M(f, \Omega)$ is the group velocity of the GW which dispersive effect has to be compensated.

For instance, a sample warping map is depicted in Fig. 3.3 along with its functional inverse. It was computed according to Eq. (3.8) by considering the group velocity curve of the Lamb A_0 mode for a $\Omega = 1$ mm-thick aluminium plate with Young modulus $E = 69$ GPa, Poisson's coefficient $\nu = 0.33$ and density $\rho = 2700$ kg/m^3, represented in Fig. 3.4. These Lamb waves group velocity curves were obtained by using a free tool [50] based on the Semi-Analytical Finite Element (SAFE) formulation proposed in [19]. The number of SAFE elements used for the computation was set according to the accuracy criterion given in [24].

3.3.2 Step 1: compensation of dispersion due to the reference portion (RP) of the waveguide

Let us suppose that operating in pulse-echo mode a dispersive M-th GW is excited by means of an impulsive waveform $s(t, x)$, starting at position $x = 0$, in a uniform cross-section waveguide with cross-section Ω_R. In this context such

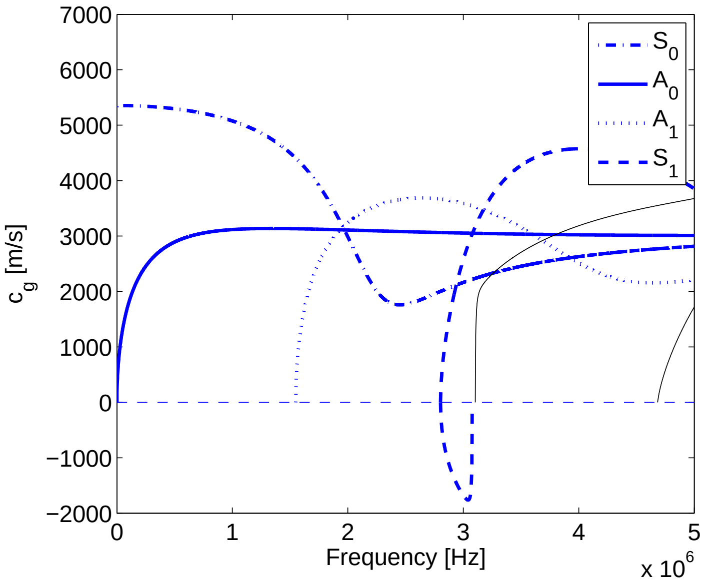

Figure 3.4: Group velocity dispersion curves $cg(f,h)$ for the Lamb waves propagating in an aluminium $h = 1$ mm thick-plate (Young modulus $E = 69$ GPa, Poisson's coefficient $\nu = 0.33$, density $\rho = 2700\ kg/m^3$).

waveguide could represent the reference portion (RP) of an irregular waveguide. The response at a distance $x = D_R$, indicated as $s(t, D_R)$, can be modelled in the frequency domain as:

$$S(f, D_R) = S(f, 0) \cdot e^{-j2\pi \int_0^f \tau_{D_R}^M(\alpha)\mathrm{d}\alpha} \tag{3.9}$$

where $S(f, 0)$ is the Fourier Transform of the exciting pulse in the point of actuation and $\tau_{D_R}^M(f)$ is the group delay of the wave component of frequency f. In force of Eqs. (3.3) and (3.8) the right hand term of Eq. (3.9) can be rewritten as:

$$\begin{aligned} S(f, D_R) &= S(f, 0) \cdot e^{-j2\pi D_R \int_0^f \frac{1}{cg^M(\alpha,\Omega_R)}\mathrm{d}\alpha} \\ &= S(f, 0) \cdot e^{-j2\pi w^{-1}(f) K D_R} \end{aligned} \tag{3.10}$$

in which a signal dispersive distortion results from the nonlinear phase term.

At this point, the application of the warping operator $\mathbf{W}_w$ to $s(t, D_R)$ leads to a new signal whose frequency transform is:

$$\mathbf{FW}_w\{s(t, D_R)\} = [\sqrt{\dot{w}(f)}S(w(f), 0)] \cdot e^{-j2\pi f K D_R} \tag{3.11}$$

Now, the phase term in Eq. (3.11) presents a linear dependence on warped frequencies. Therefore, the inverse Fourier Transform ($\mathbf{F}^{-1}$) of Eq. (3.11) yields to a warped signal $s_w(t) = s_w(Kx)$ that peaks in correspondence of KD_R and so directly related to the distance traveled by the wave D_R (please see Figure 3 of Ref. [41]).

The above signal processing is perfectly suited for active localization of defects in uniform mono-dimensional waveguides (similar approaches have been proposed in Refs. [39, 40]). In fact, processing a received guided wave, that has been generated at a known location and reflected from a defect positioned at an unknown location, will yield to the distance traveled by the wave and thus to the defect position. Similarly, such procedure has been used in a triangulation approach to locate defects in plate-like structures [51].

3.3.3 Step 2: compensation of dispersion due to the irregular portion (IP) of the waveguide

A signal processing as the one proposed in Eq. (3.11) is not sufficient in case the M-th GW propagates for a distance $D = D_R + D_I$ along an irregular waveguide, as the one represented in Fig. 3.1, where D_R is the path length traveled over the reference portion (RP) of the waveguide and D_I is the distance traveled along the irregular portion (IP). In such a case, in fact, the response $s(t, x)$ in $x = D$ can be modeled in the frequency domain as:

$$S(f, D) = S(f, 0) \cdot e^{-j2\pi \int_0^f \tau_{D_R}^M(\alpha) \mathrm{d}\alpha} \cdot e^{-j2\pi \int_0^f \tau_{D_I}^M(\alpha)\, \mathrm{d}\alpha} \tag{3.12}$$

It follows that, by applying the warping operator and Fourier transforming the warped signal, the following distortion in the phase term is obtained:

$$\mathbf{FW}_w\{s(t, D)\} = [\sqrt{\dot{w}(f)}S(w(f), 0)] \cdot e^{-j2\pi f K D_R} \cdot e^{-j2\pi \int_0^f \hat{\tau}_{D_I}^M(\alpha)\, \mathrm{d}\alpha} \tag{3.13}$$

where:

$$\hat{\tau}_{D_I}^M(f) = \frac{\mathrm{d}\int_0^f \tau_{D_I}^M(w(f))\,\mathrm{d}w(f)}{\mathrm{d}f} = K\tau_{D_I}^M(w^{-1}(f)) \cdot cg^M(w^{-1}(f), \Omega_R) \qquad (3.14)$$

is the group delay for the M-th wave induced by the irregular portion (IP) of the waveguide. Such group delay can be easily removed from the warped signal in Eq. (3.13) by forcing an opposite term $-\hat{\tau}_{D_I}^M(f)$ in its phase spectrum as:

$$\begin{aligned} S_w^{\text{comp}}(f, D) &= \mathbf{FW}_w\{s(t, D)\} \cdot e^{j2\pi \int_0^f \hat{\tau}_{D_I}^M(\alpha)\,\mathrm{d}\alpha} \\ &= [\sqrt{\dot{w}(f)} S(w(f), 0)] \cdot e^{-j2\pi f K D_R} \end{aligned} \qquad (3.15)$$

By doing so, a dispersion compensation of the actuated pulse suitable to extract the distance traveled by the M-th GW in the regular portion (RP) of the irregular waveguide, i.e. D_R, is obtained. In fact, the signal $s_w^{\text{comp}}(Kx_R) = \mathbf{F}^{-1} S_w^{\text{comp}}(f, D)$, where x_R denotes a coordinate along the regular portion (RP) of the waveguide, peaks in correspondence of KD_R. It follows that defects located in the regular portion (RP) of the irregular waveguide at unknown positions, as long as they reflect part of the M-th wave, can be located by the proposed approach.

3.4 Numerical validation

The procedure has been tested on different irregular waveguides composed by straight and curved plate portions, both symmetric and anti-symmetric tapered segments, and different locations/type of defects. In particular, the following cases have been considered: (i) a waveguide composed by two flat plates with different thickness and a symmetric tapered segment in between, (ii) a similar one but with an anti-symmetric tapered segment, (iii) one with both a symmetric and an anti-symmetric tapered segments positioned within three uniform straight plates (see Fig. 3.5), and finally, (iv) a more complex waveguide with two straight segments, two tapered segments and a curved segment (see Fig. 3.6).

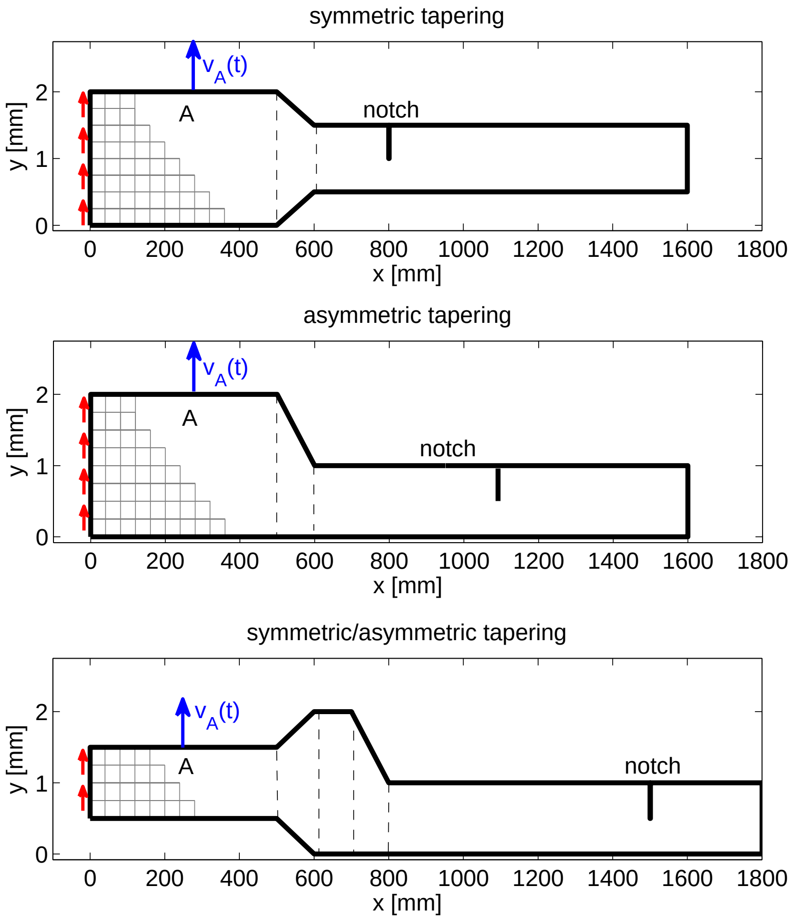

Figure 3.5: Schematic representation of the three straight irregular plate waveguides considered as cases (i), (ii) and (iii). Please note the different scale in the x and y-direction.

In all these examples, the propagation of guided waves was simulated by means of Finite Element (FE) analyses using the commercial package Abaqus explicit [52]. For all the FE simulations, some common features apply and are here recalled:

- a linear elastic aluminium with Young modulus $E = 69$ GPa, Poisson's coefficient $\nu = 0.33$ and density $\rho = 2700$ kg/m^3, was considered;
- only the $x - y$ propagation plane of the waveguide is modeled as a bi-dimensional body in plane strain condition by using linear (4-nodes) plate

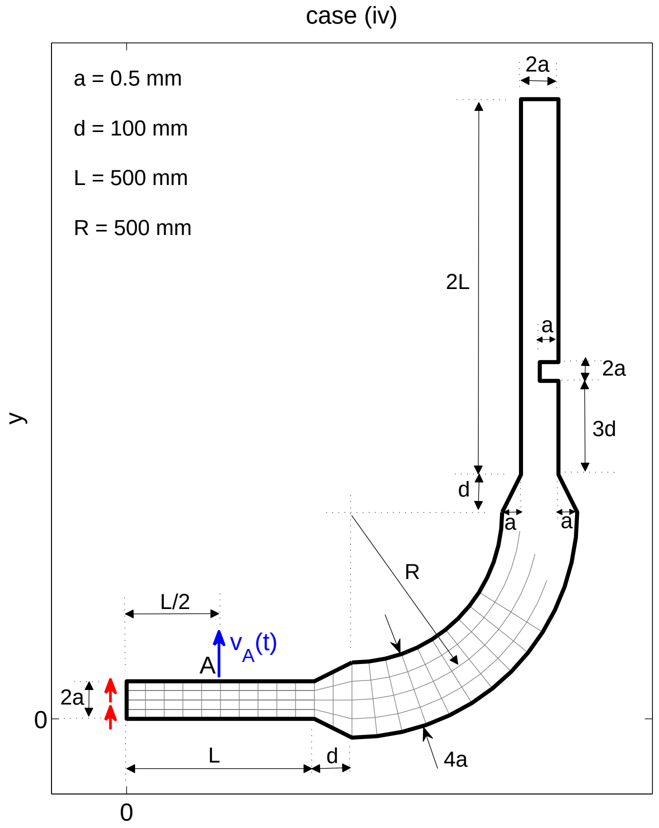

Figure 3.6: Schematic representation of the irregular waveguide considered as case (iv).

elements (CPE4R);

- to mainly excite flexural waves the waveguide has been excited at its left edge ($x = 0$) by imposing an impulsive out-of-plane (y direction) displacement $v(t)$;

- the imposed displacement is shaped in time as a triangular window with a maximum amplitude of 1 nm and a total duration of 10 μs in order to excite consistent guided waves up to 100 kHz (see Fig. 3.7);

- to ensure accuracy to the time-transient finite element simulations [53] the plate domain was discretized with elements of maximum side length $L_{max} = 0.125$ mm and the time integration step was kept $\Delta t < 1e - 8$ s.

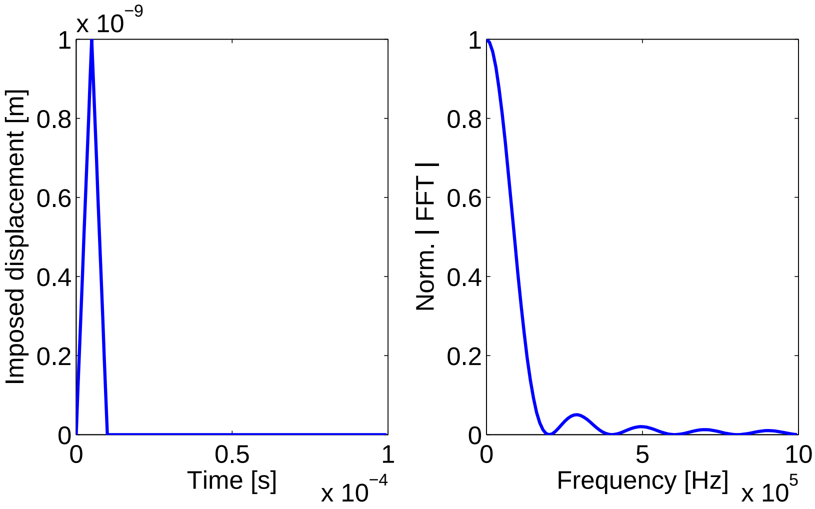

Figure 3.7: Time and frequency representation of the imposed displacement used to mainly excite the A_0 mode in the irregular waveguides.

It must be remarked that because of the assumed plane strain condition of the propagation plane, that is the waveguide cross-section in the $x - y$ plane, neither wave reflections generated by plate edges in z-direction nor geometrical attenuation due to wave radiation in the z-direction, that might be present in real cases, are modelled. Nevertheless, for the purpose of validating the proposed signal processing approach, the assumed plane strain condition is sufficient since it allows to the applied pulse to fully develop signal dispersion in the different considered segments.

In addition, also for plates with finite dimension along the z-axis, the actuation can be designed to focus the wave energy along the y-axis with minimal radiation in the z-direction and the plane strain assumption can be reasonably used to model the waveguide response.

3.4.1 Straight waveguides with symmetric and antisymmetric tapering

For cases (i), (ii), and (iii), as shown in Fig. 3.5, notches of width b= 1 mm and depth a=0.5 mm (y-direction) were placed on the top side of the waveguides at x= 800 mm, x= 1100 mm, and x= 1500 mm, respectively.

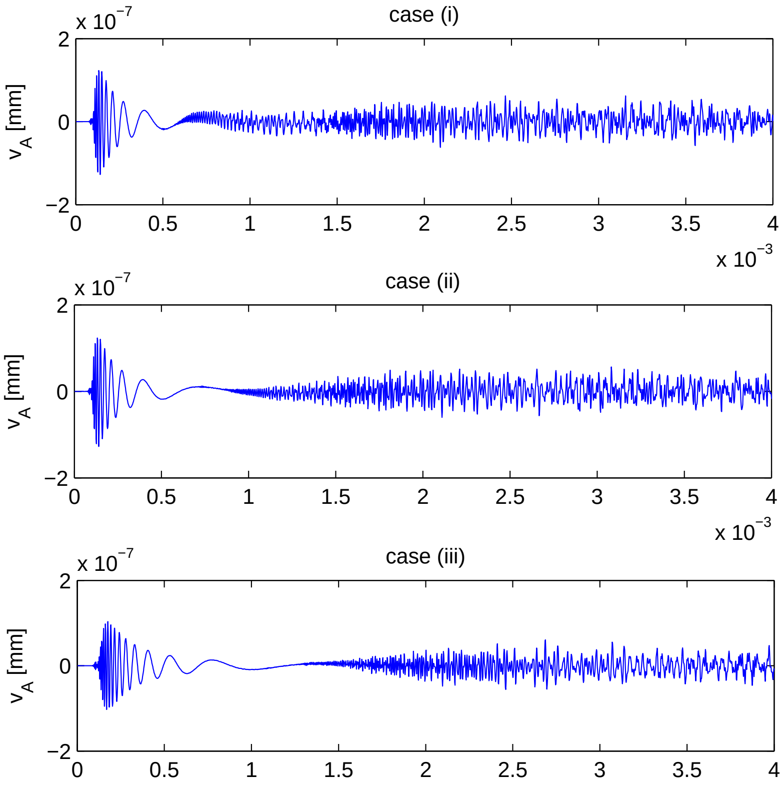

Figure 3.8: Time-transient responses $v_A(t)$ acquired at x=250 mm for the three cases (i), (ii) and (iii) represented in Fig. 3.5.

The out-of-plane time-transient responses in the y-direction $v_A(t)$ were recorded at x=250 mm (see Fig. 3.8). As can be seen from Fig. 3.8, the incipient A_0 mode is clearly visible in the responses within 0.5×10^{-3} s, but nothing can be inferred on the defects from the remaining portions of the signals. Wave reflections can be clearly seen in the spectrogram of $v_A(t)$ for case (i) represented in Fig. 3.9(a). On such plot, the A_0 group delay curves for the different wave paths depicted in Fig. 3.9(b) and denoted as W1, W2a, W2b, W3a and W3b, are overimposed. In particular, W1 refers to the incipient A_0 wave, W2a and W3a denote the A_0 waves reflected from the defect and from the right edge of the waveguide, respectively, while W2b and W3b include the further A_0 reflection from the left edge of the waveguide. The group delay curves have been computed as described in Section 3.2 by using the SAFE based tool proposed in Ref. [50].

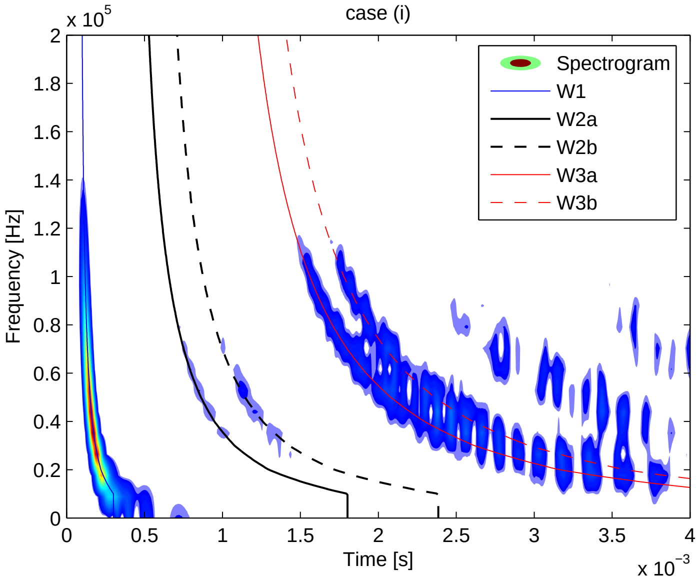

(a)

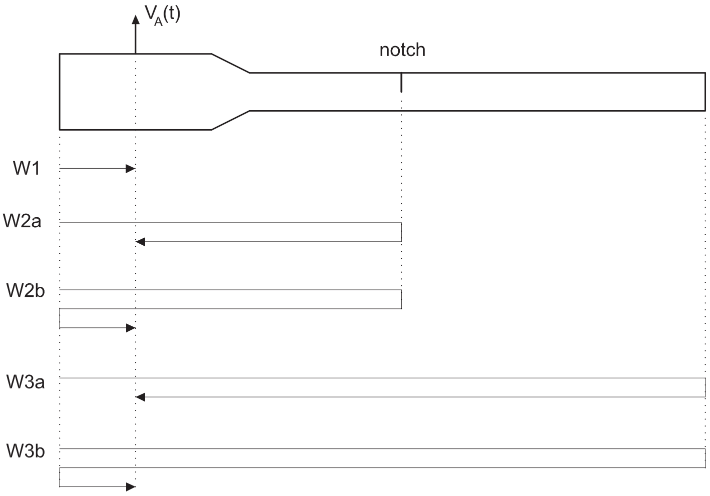

(b)

Figure 3.9: (a) Spectrogram of the time-transient response $v_A(t)$ for case (i) represented in Fig. 3.8. The group delay curves for the A_0 wave computed with the proposed procedure considering different paths are overimposed: incipient wave (W1), notch and right edge reflections (W2a and W3a, respectively), left edge reflections (W2b and W3b). (b) Schematic representation of the different paths.

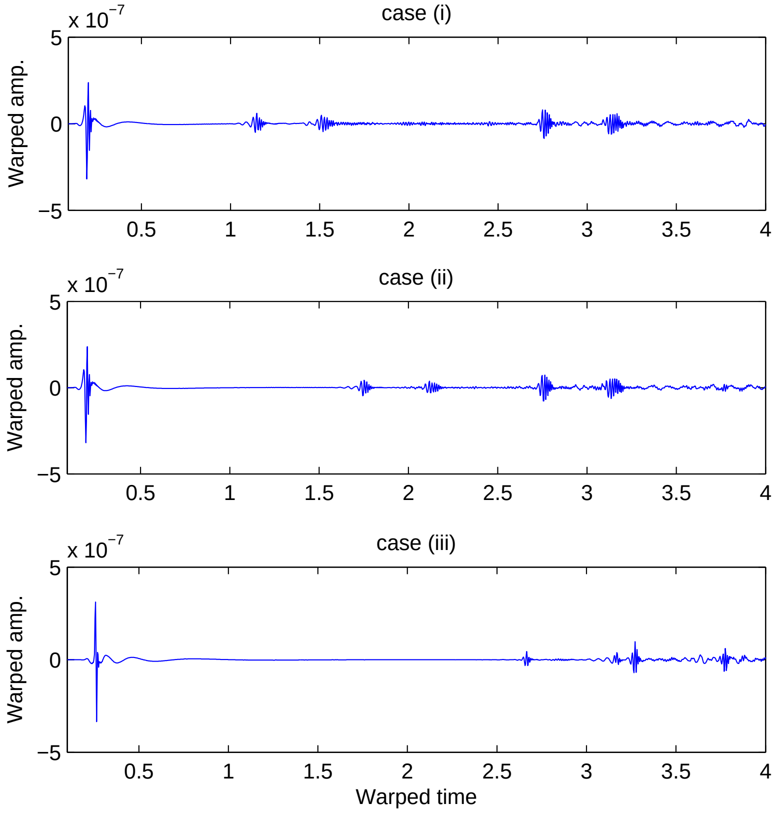

Figure 3.10: Warped version of the time-transient signals $v_A(t)$ represented in Fig. 3.8 for the three cases (i), (ii) and (iii).

As can be seen, the group delay curves perfectly overlap the energy content of the incipient, scattered (from the defect) and reflected (from the edges) A_0 modes within the signal. Therefore, this confirms the reliability of the adopted group delay computation for irregular waveguides that will be exploited for the purpose of detecting/locating a defect at an unknown position by means of the proposed dispersion compensation strategy.

First the WFT operator must be defined. The three considered irregular waveguides, i.e. cases (i), (ii) and (iii), have an identical reference portion (RP) consisting in a 1 mm thick plate. The group velocity curve for the fundamental antisymmetric A_0 mode for such a plate was thus selected as M-th wave to design

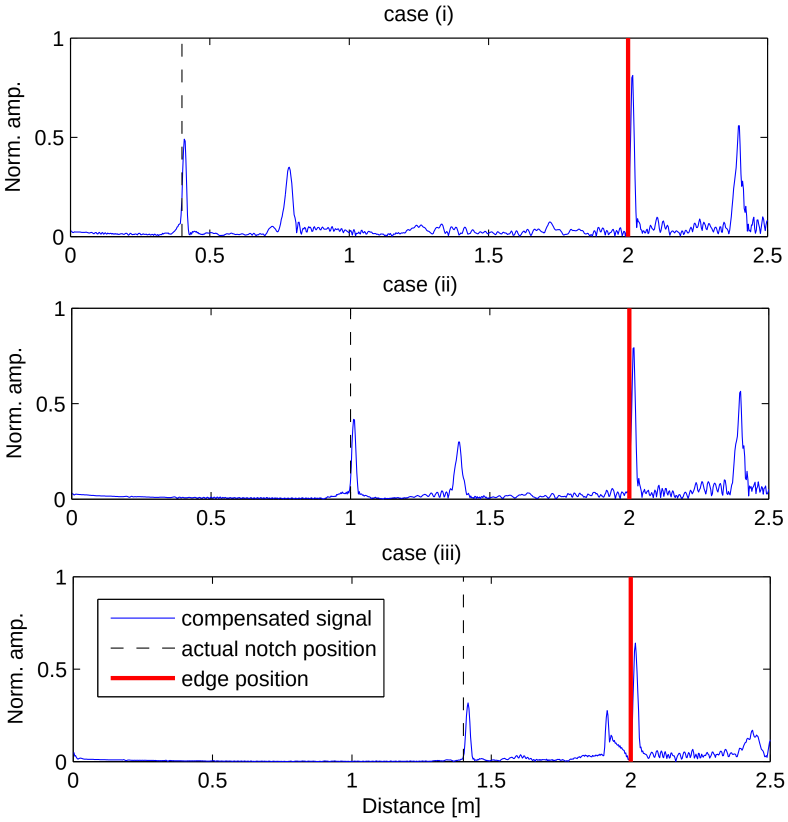

Figure 3.11: Normalized H_{env} of the signals depicted in Fig. 3.10. The vertical lines mark the distance traveled by notch and edge reflected waves.

the WFT operator. Processing the time-waveforms represented in Fig. 3.8 by the designed operator, leads to the warped signals shown in Fig. 3.10.

As it can be noted, in the warped domain, due to the removal of the group delay dependency on distance in $\tau^M_{D_R}(f)$, i.e. compensating the dispersion due to D_R, the pulses energy is confined in smaller spots. Such pulses are related to the direct, scattered from the defect and reflected from the waveguide edges A_0 waves within the signals $v_A(t)$.

However, a further processing step is needed to compress the remaining frequency modulation due to the group delay introduced by the irregular part of the waveguide $\tau^M_{D_I}(f)$. The effect of such processing leads to the new signals

$S_w^{\text{comp}}(f, D)$, along with their inverse Fourier Transforms $s_w^{\text{comp}}(Kx_R)$, which resulting envelopes H_{env} are shown in Fig. 3.11 after normalization. Envelopes are computed as the absolute value of the Hilbert Transform, i.e. $H_{env} = |H(s_w^{\text{comp}}(Kx_R))|$, where H denotes the Hilbert operator.

It is worth noticing that the energy of the processed signals is now concentrated near the actual distance traveled by the waves in the reference portion of the waveguide. In particular, the signals peak at 400 mm, 1000 mm and 1400 mm, for the case (i), (ii) and (iii), respectively, i.e. at exactly twice the distance from the left edge of the reference portion (RP) and the defect. The spurious contributions in Fig. 3.11 (due to further reflections from the plate edges) could be easily removed, for example, by combining the results of multiple acquisitions at different locations (for instance by using classical delay-and-sum beamforming procedures).

3.4.2 Irregular waveguide with straight, curved and tapered segments

The waveguide considered in this example is shown in Fig. 3.6. A notch of width b= 1 mm and depth a=0.5 mm was placed on the straight portion after the curved segments at 300 mm from the end of the second tapering. The time-transient response $v_A(t)$ at x=250 mm along the y-direction, was recorded and plotted in Fig. 3.12, along with the related spectrogram. In the time-frequency plane, the predicted group delay curves of the incipient pulse (W1), notch (W2a) and right edge reflections (W3a) are highlighted. Notch and edge reflections are further reflected by the left edge of the waveguide (W2b and W3b). For the curved portion, the anti-symmetric type Lamb wave group velocity curve was computed by using the analytical formulation provided in Ref. [54] for circumferential guided waves. In particular, the curves were obtained by searching for null values of the secular equation using a bi-section method. As it can be noted, the signal dispersion induced by the irregular waveguide complicates the detection of notch reflections.

To localize the unknown position of the defect the signal processing steps detailed in sec. 3.3 have to be applied. At first, dispersion compensation for the

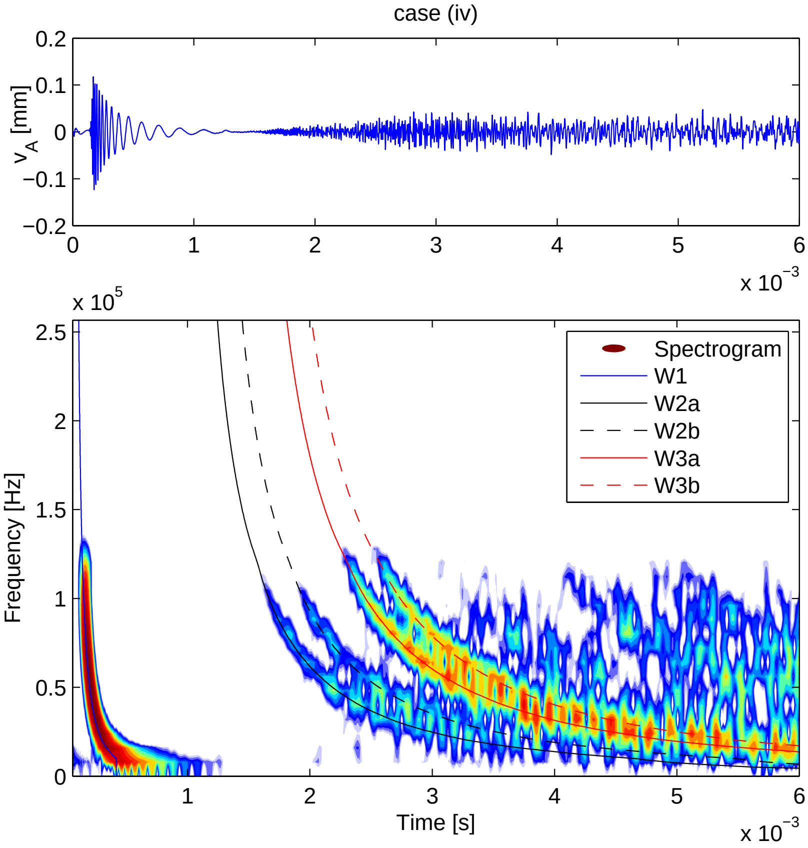

Figure 3.12: Time-transient response $v_A(t)$ for case (iv) along with its spectrogram. In the spectrogram the group delay curves for the incipient pulse (W1), notch and right edge reflections (W2a and W3a, respectively), W2a and W3a reflections from the left edge (W2b and W3b), have been overimposed. Group delays are estimated according to Eq. (3.5).

reference portion of the waveguide (a straight plate 1 mm thick) is performed, considering the A_0 mode to shape the WFT operator. By warping the acquired response the signal shown in Fig. 3.13 along with its spectrogram is obtained. Then, the group delay $\tau_{D_I}^{M}$ introduced by the irregular part of the waveguide (the two tapered segments and the curved segment) is computed and transposed in the warped domain through Eq. (3.14). Finally, the group delay $\hat{\tau}_{D_I}^{M}$ is subtracted to the warped signal.

The resulting envelope H_{env} is shown in Fig. 3.14. In this figure, it is possible to evaluate the combined effect of the WFT and of the group delay compensation procedure. It is worth noticing how the abscissa value corresponding to envelope maxima are directly related to the distances traveled by the waves scattered by the defect and reflected by the right edge of the waveguide. There is also a significant spurious contribution which is due to the reflections of the same waves from the left edge. However, the contribution of W2a and W3a is higher and more picky, because the compensation was explicitly designed to enhance the defect localization in the thinner portion of the waveguide.

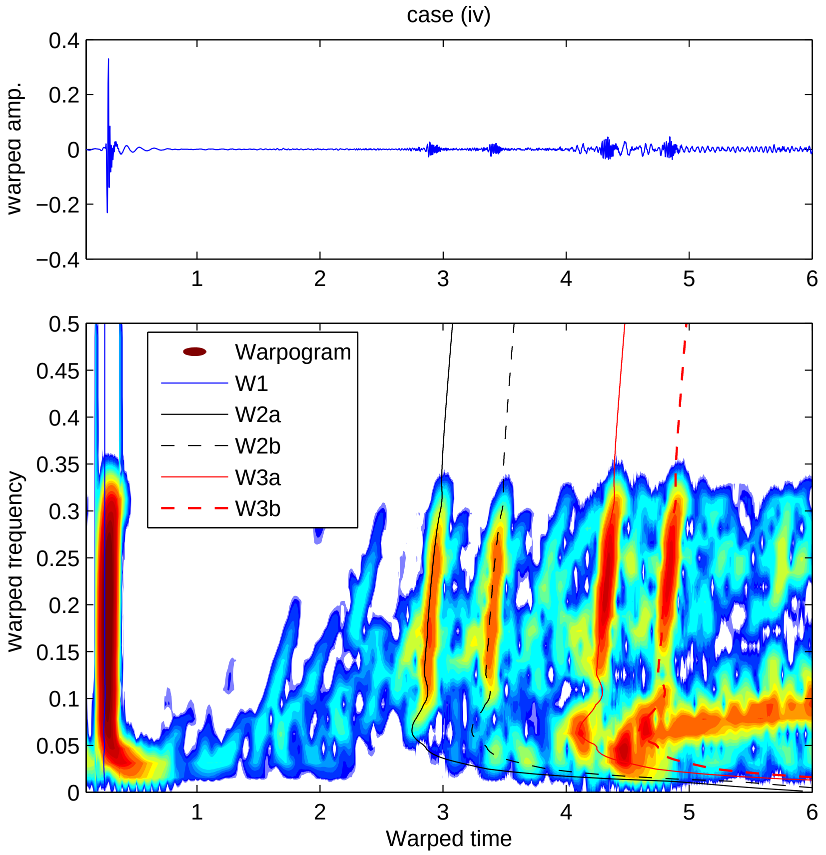

Figure 3.13: Warped version of $v_A(t)$ represented in Fig. 3.12 along with the spectrogram of the warped signal. In such plot the warped group delays of incipient pulse (W1), notch and right edge reflections (W2a and W3a, respectively), W2a and W3a reflections from the left edge (W2b and W3b), have been overimposed.

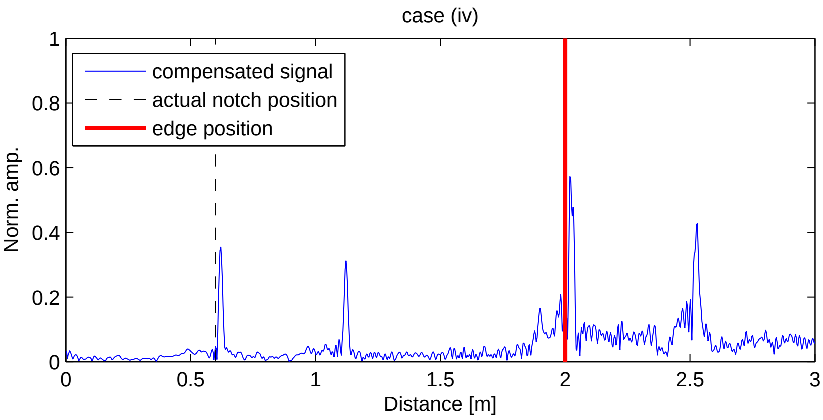

Figure 3.14: Normalized H_{env} of the signal depicted in Fig. 3.13. The vertical lines mark the distance traveled by notch and edge reflected waves.

3.5 Conclusions

In this chapter, a signal processing strategy aimed at locating defects in plates by analysing plate-type waves is proposed. The method is suitable for tapered and irregular waveguides, and it is based on a two-step procedure applied to the acquired signals. The implemented signal processing directly reveals the distance traveled by the waves, thus overcoming the difficulties associated to wave arrival time detection in dispersive media. In particular, by exploiting the dispersion compensation properties of the WFT, waveforms characterized by a unique time-frequency pattern are obtained. The remaining time-frequency modulation is compressed in a subsequent processing step. This step is based on the estimation of the group delay in tapered, curved or irregular portions of the waveguide. The reported spectrograms showed that the adopted method has an excellent accuracy in group delay calculation. Such accuracy can be conveniently exploited for wave distance of propagation estimation, as shown by several numerical examples.

Thanks to its unique potential the developed tool could lead to a new class of procedures to locate defects in waveguides.

Chapter 4

Time-reversal and laser-vibrometry based impact location

4.1 Introduction

Assessment of the integrity of structural components is of great importance for aerospace vehicles and systems, land and marine transportation, civil infrastructures, oil industry as well as other biological and mechanical applications. It is well known that accidental impacts may generate hidden damage in structures, that can develop under cyclic load, until it endangers the integrity of the whole structure. In some case, undetected damages can be the cause of the structure collapse. One of the most known failure case is the one occurred when the composite tile on the leading edge of the wing of the Space Shuttle Columbia fractured due to impact. It led to catastrophic failure of the whole vehicle on February 1, 2003.

In order to prevent such incidents the capability to identify impacts and then to monitor eventual damage evolution in the neighbourhood of the impact is of crucial importance. To this aim, the use of guided waves (GWs) driven by a network of piezoelectric transducers[1] has attracted several researchers interest in

---

[1] PZTs sensors can be used both in *active* or *passive* monitoring modes. Under the active

recent decades.

For isotropic plates, various impact localization techniques have been proposed over the years, the majority of which locate the point of impact after detecting the acoustic emission signal (generated by the impact phenomenon) by at least three sensors and applying standard triangulation techniques [41].

Contrary, when the isotropy assumption is removed in monitored plates standard triangulation technique fails. Therefore, among the others, alternative methods have been proposed for anisotropic [55] and inhomogeneous plate-like [56] structures.

However, one difficulty associated with this type of algorithms is that they are very sensitive to the time of detection and a small error in the measurement of the time of flight at a sensor can result in a large error in the impact location prediction. Furthermore, because of the presence of noise in the received signals, there is always some error in the time of flight measurement that results in a large uncertainty in the predicted location of the impact point.

In order to overcome these difficulties, recently, a new impact localization algorithm based on time reversal and scanning laser Doppler vibrometer (SLDV) was proposed [57]. This technique is shown to be very powerful particularly in complex structures because it does not require the knowledge of the wave velocity or the structural geometry. Its main advantages over the existing techniques are: (a) it can be applied to complex structures with additional structural features such as ribs, stringers, stiffeners, spars, and rivet connections; (b) only simple correlation calculations are required for impact localization, making it attractive for real-time automated monitoring; (c) a high spatial resolution of impact localization is achieved using SLDV for sensing.

However, to nowadays, while the time-reversal procedure (TRP) for non-dispersive body waves has been well-established, the study of the TRP for Lamb waves is still relatively new. Historically, Ing and Fink first adapted the TRP to Lamb waves[1] in order to compensate for their dispersive behaviour to detect

---

mode, acoustic actuators generate ultrasonic signals; under passive mode monitoring, the impact of foreign objects (or crack initiation) acts as the acoustic source. Ultrasonic sensors are placed in critical areas of the structure to efficiently receive ultrasonic signals and monitor its condition [41].

[1] Broadly speaking, researches focused on the spatial focusing of TR Lamb waves can be

defects in a pulse-echo mode [58]. Afterwards time-reversal has been extensively used both to focus Lamb wave energy for damage detection in plates [59, 60, 61] and for impact localization [57, 62].

In what follows, first, the mechanism of time-reversal applied to Lamb waves in plates is elucidated through numerical simulations and then the time-reversal based procedure is applied to a flat aluminium plate reinforced by two unidirectional L-shaped eccentric stiffeners.

4.2 A time-reversal based procedure for impact location

4.2.1 Time-reversal basic principles

Time-reversal was introduced by the acoustics community and applied to many fields such as lithotripsy, ultrasonic brain surgery, active sonar and underwater communications, medical imaging, hyperthermia therapy, bioengineering, and non-destructive testing (NDT).

Its basic physics states that in a non-dissipative medium, for every burst of sound that diverges from a source, a set of waves that would precisely retrace the path of the sound back to the source exists.

The procedure to obtain such a converging wave [58] is shown in Fig. 4.1: (i) apply a generic tone burst excitation $U_D(t)$ in A; (ii) record the forward wave $U_{acq}(t)$ in B; (iii) emit the time-reversed wave $U_{acq}(-t)$ from B back to A; (iv) pick up the wave in A as the reconstructed wave $U_{D,r}(-t)$.

---

divided into two categories depending on equipment used in the TR process. One is to use the time reversal mirror (TRM) being a sophisticated probe carefully designed through integrating tens to hundreds of piezoelectric transducers. Dispersive characteristics of Lamb waves get the spatial focusing enhanced when using the TRM. However, the TRM requires very expensive equipment which can conduct actuation and reception simultaneously through numerous piezoelectric transducers. The other category is to use a chaotic cavity which makes the spatial focusing possible using a small number of transducers. In the chaotic cavity, an incident wave emitting from the arbitrary location should cover the entire cavity at least one time due to reflections as time passes by. Draeger et al. (1999) have realized the spatial focusing of TR Lamb waves at the original input source using only one-channel sensor on a chaotic cavity made of a silicon wafer.

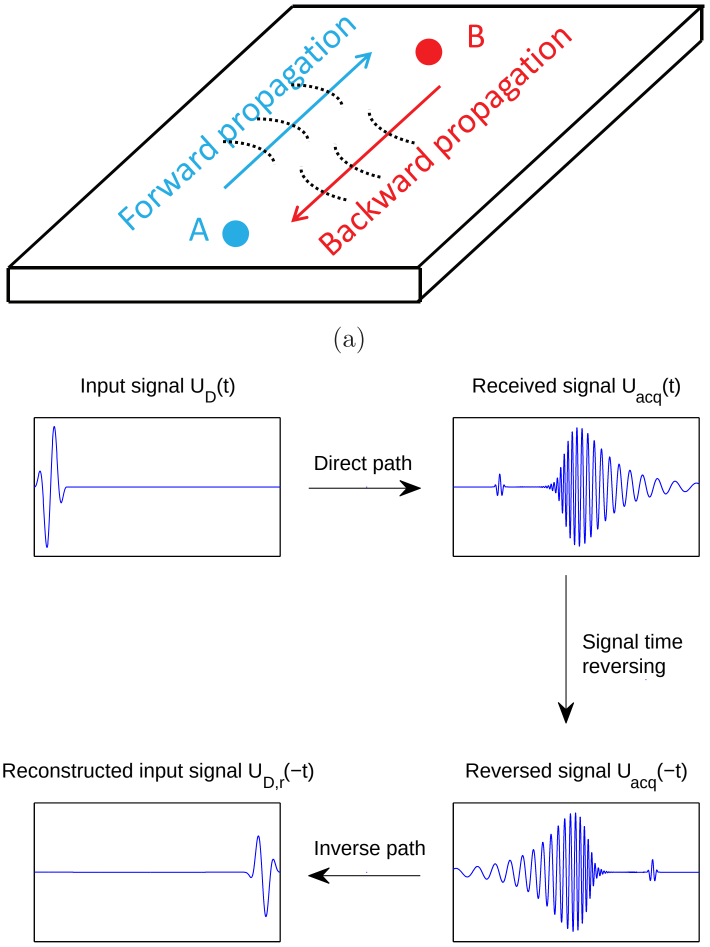

(a)

(b)

Figure 4.1: Representation of the TR procedure. (a) Schematic representation of a generic waveguide. (b) Block diagram of the TR procedure (from the top left side and cloackwise): (i) apply a generic tone burst excitation $U_D(t)$ in A; (ii) record the forward wave $U_{acq}(t)$ in B; (iii) emit the time-reversed wave $U_{acq}(-t)$ from B back to A; (iv) pick up the wave in A as the reconstructed wave $U_{D,r}(-t)$.

In fact, in the range of sonic or ultrasonic frequencies, where adiabatic processes dominate, the acoustic pressure field is described by a scalar $p(\mathbf{r}, t)$ that, within a heterogeneous propagation medium of density $\rho(\mathbf{r})$ and compressibility $\kappa(\mathbf{r})$, satisfies the equation:

$$(L_r + L_t)p(\mathbf{r}, t) = 0 \tag{4.1}$$

where:

$$L_r = \nabla \cdot \left(\frac{1}{p(\mathbf{r}, t)} \nabla \right), \qquad L_t = -\kappa \left(\mathbf{r} \partial_{tt} \right) \tag{4.2}$$

This equation is time-reversal invariant because: (i) L_t contains only second-order derivatives with respect to time and (ii) L_r satisfies spatial reciprocity, since interchanging the source and the receiver does not alter the resulting fields [63]. In a non-dissipative medium, Eq. (4.1) guarantees that for every wave propagating from a source and possibly reflected, refracted, or scattered, a set of waves that precisely retraces all of these complex paths and converges in synchrony at the original source, as if time was going backward, in theory exists. This fact remains true even if the propagation medium is inhomogeneous with variations of density and compressibility which reflect, scatter, and refract the acoustic waves. If the source is point like, time reversal allows focusing back to the source whatever the medium complexity [64, 65, 66]. Spatial reciprocity is not broken by velocity dispersion, multiple scattering, mode conversion, anisotropy, refraction nor attenuation, as long as the attenuation is linear with wave amplitude. Contrary, non linear elastic effects may break spatial reciprocity. Similarly, spatial reciprocity is also broken if the medium's velocity structure changes in the direct and inverse propagation paths. An example is a medium that experiences changes in temperature, altering then its wave velocity [67].

4.2.2 Time-reversal for Lamb waves

Lamb waves are extensively involved in plate structure non invasive inspection because of their guided nature. However, their dispersive nature often limits their use because of the large time duration and the complex waveform of signals. In fact, pulses will distort due to variation in modal group velocities. Because of this, the received signals are often difficult to interpret.

This issue makes the time-reversal an attractive tool to overcome the GWs dispersion problem. In fact it only requires a little prior knowledge of the monitored structures and does not need any knowledge of the propagating medium [59, 61].

In the following a description of how the TRP works for Lamb waves in plates is examined by means of dynamic transient finite element (FE) simulations. To this purpose, an aluminium 1 mm-thick plate is considered, as shown in figure 4.2.

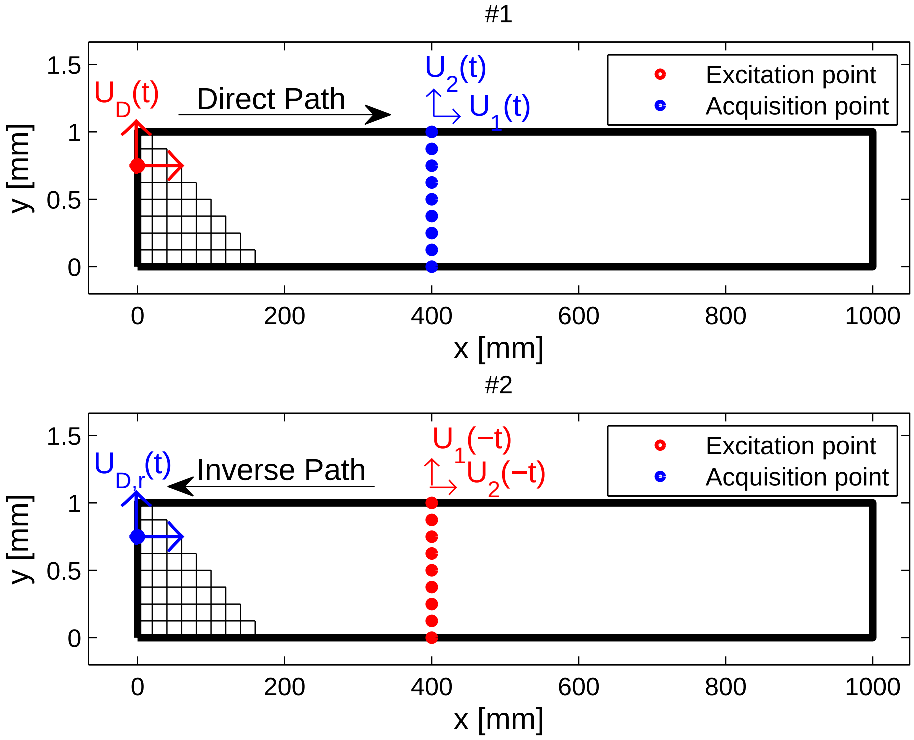

Figure 4.2: Schematic representation of the FE model involved into the two step TR procedure. Please note the different scale in the x and y-direction.

First, a source emits waves with time-history $U_D(t)$, with generic components $U_{1D}(t)$ and $U_{2D}(t)$. Such waves propagate through and are distorted by the waveguide. In-plane $U_1(t)$ and out-of-plane $U_2(t)$ displacements are detected and stored along all the nodes discretizing the transversal cross-section after waves travelled 400 mm. Afterwards, each stored signal $U_1(t)$ and $U_2(t)$ is reversed - $U_1(-t)$ and $U_2(-t)$ - and played back in synchrony with the others.

Due to the time invariance and spatial reciprocity[1] of linear wave Eq. (4.1), the original wave is re-created travelling backward, thus retracing its passage back

---

[1] Paths traversed by a pulse from point A to point B, including reflected paths, will also be traversed if the same pulse is sent from point B to point A.

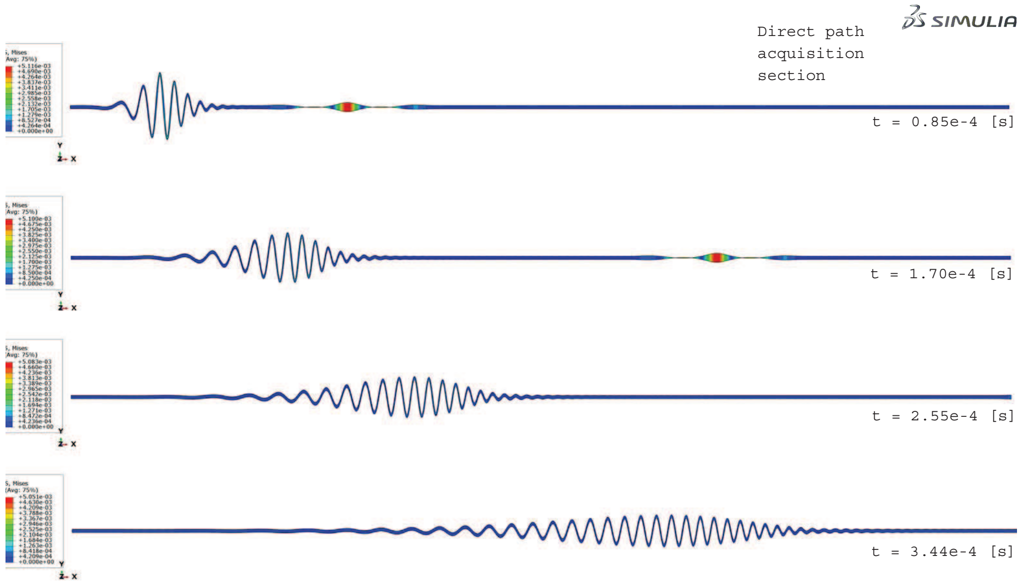

Figure 4.3: Different snapshots of the wave propagation phenomenon in the forward wave propagation. Deformation scale factor was assumed equal to 10^7 in order to highlight the waves behaviour.

through the medium, untangling its distortions and refocusing on the original source point (compare Fig. 4.3 and Fig 4.4). Fig. 4.5 shows the source $U_D(t)$ reconstruction as $U_D(-t)$ in the time domain. After the time-reversal procedure, the two signal are similar unless than a scale factor [68].

Guided waves propagation shown in Figs. 4.3 and 4.4 is simulated by means of the commercial package Abaqus/Explicit [52]. For the FE simulations, some common features apply and are here recalled:

i) a linear elastic aluminium with Young modulus $E = 69$ GPa, Poisson's coefficient $\nu = 0.33$ and density $\rho = 2700$ kg/m^3, was considered;

ii) only the xy propagation plane of the waveguide is modelled as a bi-dimensional body in plane strain condition by using linear (4-nodes) plate elements (CPE4R);

iii) the imposed displacement is shaped in time as a sinusoidal n-cycles Hanning windowed toneburst with a maximum amplitude of 1 nm and central

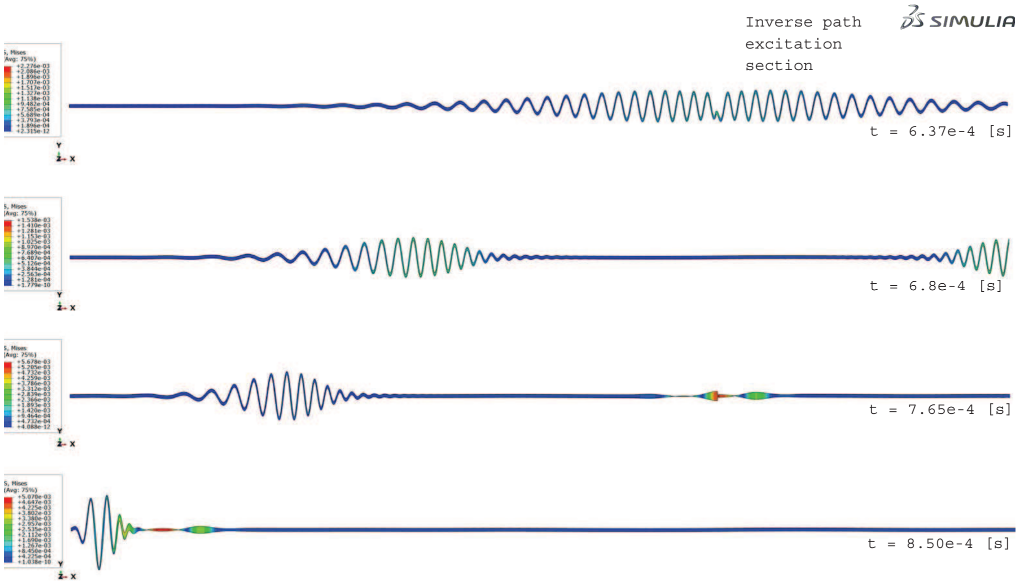

Figure 4.4: Different snapshots of the wave propagation phenomenon in the time-reversal reconstruction. Deformation scale factor was assumed equal to 10^7 in order to highlight the waves behaviour. Please note the dispersion compensation occurring in the TR reconstruction.

frequency equal to 100 kHz (where n depends on the application);

iv) to ensure accuracy to the time-transient finite element simulations the plate domain was discretized with elements of maximum side length $L_{max} = 0.1$ mm and the time integration step was kept $\Delta_t = 1e-8$ s.

The waveguide has been excited at its left edge($x = 0$) by imposing a generic impulsive displacement $\mathbf{U}_D(t)$.

It must be remarked that even if assuming the propagation plane in plane strain condition does not allow to account for geometrical attenuation, it permits to the applied pulse to fully develop signal dispersion representing in full the TRP process.

Unlike the time-reversal using bulk waves, time-reversal of Lamb waves is complicated by the dispersion and multi-mode characteristics of Lamb waves themselves. Anyway, it has been proved that from a numerical point of view

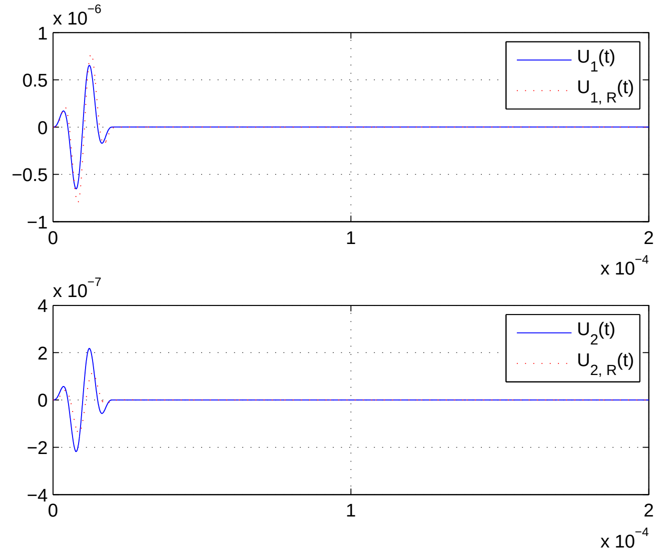

Figure 4.5: Reconstructed wave using a 2-count 100 kHz tone burst excitation in simulation of two-mode Lamb wave time-reversal.

Lamb wave is fully time reversible even under the circumstances of multiple-mode excitation/extraction.

4.2.3 Procedure description

Fig. 4.6 overviews the impact procedure, originally proposed by Park et al. [57]:

- a pulse input is generated by a surface-mounted PZT transducer (red circle) and the corresponding out-of-plane velocity $V_2(t)$ is measured (OPV) by Scanning Laser Doppler Vibrometer (SLDV) at a single point (one of the black dots) within the target scan area (bounded by the red dashed lines). The shape of the pulse input is adjusted so to approximate that of an expected real impact event (Fig. 4.6a).

- The same pulse excitation is repeated by the PZT transducer and additional OPVs are obtained by scanning the entire target scan area. Responses are stored in a data set called *Training data*: $g_1(t)$, ..., $g_m(t)$ (Fig. 4.6b).

- An impact occurring in any point within the scanned area is simulated by means of a PZT sensor (Fig. 4.6c).

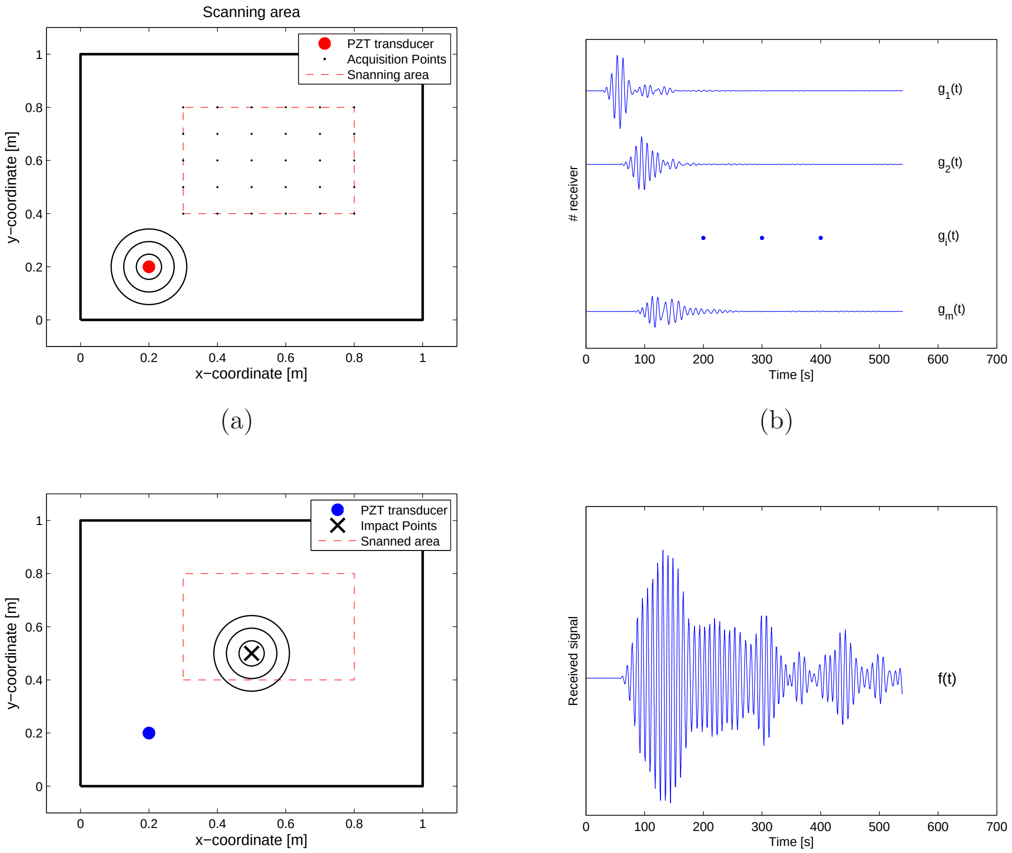

(a) (b)

(c) (d)

Figure 4.6: Schematic overview of the proposed technique for the impact localization: (a) scanning area; (b) *Training data* set acquisition; (c) actual impact event; (d) actual impact Impulse response function (OPV).

- The response $f(t)$ is recorded at the red circle point by the SLDV (Fig. 4.6d).

At this point, correlations between the actual impact response $f(t)$ and the OPVs in the training data $g_i(t)$ are computed. Because of the dispersive nature of Lamb waves, without any numerical manipulation correlations result very poor (the signals are completely different), as shown in fig. 4.7a. Contrary, if correlations between the actual impact response $f(t)$ and the OPVs in the training data $g_i(t)$ are computed exploiting time reversibility of Eq. (4.1), the $g_i(t)$ with maximum correlation to the actual impact response $f(t)$ can be much preciser

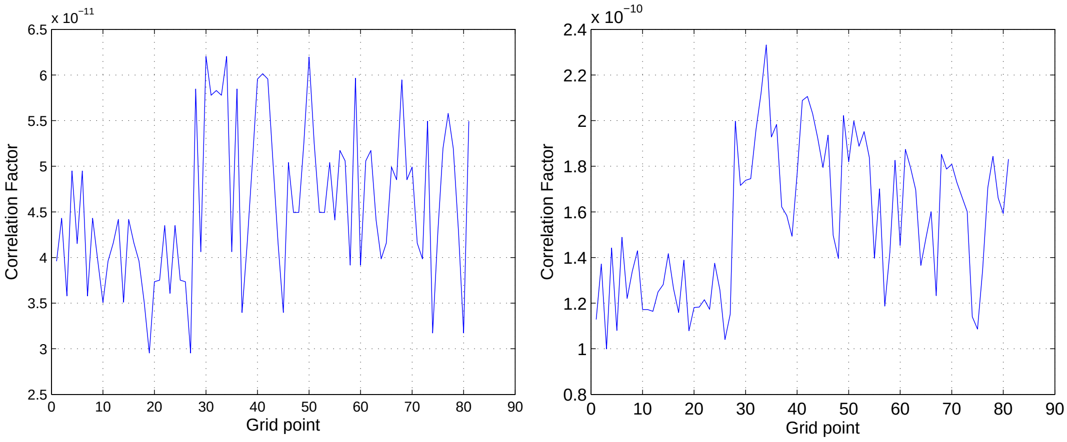

(a) (b)

Figure 4.7: Correlation values for the numerical case between each signal of the scanned area $g_i(t)$ and the signal of the actual impact point $f(t)$. (a) If time reversibility is not exploited, correlation is coarse and more than one point can be assumed as the impact position. (b) When time reversibility is taken into account, identification procedure is much more precise.

identified as the most likely related to the impact location (Fig. 4.7b).

Let $f(t)$ and $g(t)$ represent actual and one of the training OPVs, respectively. The correlation between the two OPVs is defined as follows:

$$(f \star g)(\tau) = \int_{-\infty}^{+\infty} f(t)g(\tau + t)\mathrm{d}t \tag{4.3}$$

where $\star$ denotes the correlation operation. On the other hand, the convolution of two functions is defined as:

$$(f \otimes g)(\tau) = \int_{-\infty}^{+\infty} f(t)g(\tau - t)\mathrm{d}t \tag{4.4}$$

where $\otimes$ is the convolution operation. Comparison of equations (4.3) and (4.4) reveals that the correlation and convolution are related to each other as follows:

$$(f \star g)(\tau) = f(-t) \otimes g \tag{4.5}$$

Equation (4.5) shows that the correlation between two OPVs is mathematically equivalent to the convolution between one OPV and the time-reversed version of the other OPV.

Because the computation of convolution is typically time consuming, its computation is often performed in the frequency domain based on the convolution theorem. By applying the Fourier transform, the convolution in the time domain is transformed into a simple multiplication in the frequency domain:

$$\mathcal{F}\{f \otimes g\} = \mathcal{F}\{f\} \cdot \mathcal{F}\{g\} \tag{4.6}$$

where $\mathcal{F}$ denotes the Fourier transform operator. The convolution is reconstructed by taking the inverse Fourier transform of equation (4.6):

$$f \otimes g = \mathcal{F}^{-1}\{\mathcal{F}\{f\} \cdot \mathcal{F}\{g\}\} \tag{4.7}$$

Since this new formula involves only Fourier and inverse Fourier transforms and point-wise multiplications, the correlation or convolution can be computed effectively:

$$f \star g = f(-t) \otimes g = \mathcal{F}^{-1}\{\mathcal{F}\{f(-t)\} \cdot \mathcal{F}\{g\}\} \tag{4.8}$$

The maximum correlation value, obtained using equation (4.8) is designated as the most likely impact point.

A fully detailed description of the impact localization technique can be found in Ref. [57].

4.3 Impact localization: numerical and experimental results

4.3.1 Description of the tested element

The reviewed impact localization technique has been applied to a reinforced aluminium plate, schematically presented in Fig. 4.8. The tested article is 1000 mm in length and 1000 mm in width. It is composed of a flat aluminium 1-mm thick plate reinforced by two unidirectional eccentric stiffeners with L cross-section. Width of both the web and the flange of the stiffeners is 3 mm. The stiffeners are parallel to the rectangular edge and are connected to the plate along their full length. The area supposed to be scanned is indicated by the light grey rectangle in Fig. 4.8a.

The article tested in the experimental analysis has been provided by the Laboratory of Department of Mechanics of Intelligent Structures of the Institute of Fluid-Flow Machinery, Polish Academy of Science. Material properties are the following: Young modulus $E = 68$ GPa, Poisson ratio 0.32 and density $\rho = 2700$ kg/m^3.

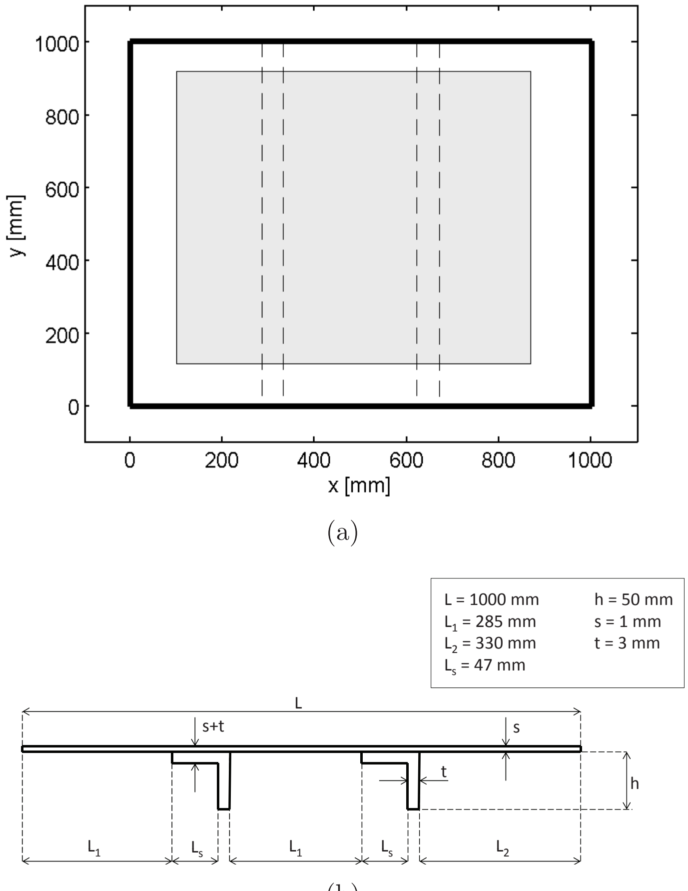

(a)

(b)

Figure 4.8: A schematic representation of the specimen. (a) xy plane view and (b) its cross-section. The drawings, for sake of clarity, are not to scale. Measures are given in millimetres. The light grey rectangle indicates the scanning area.

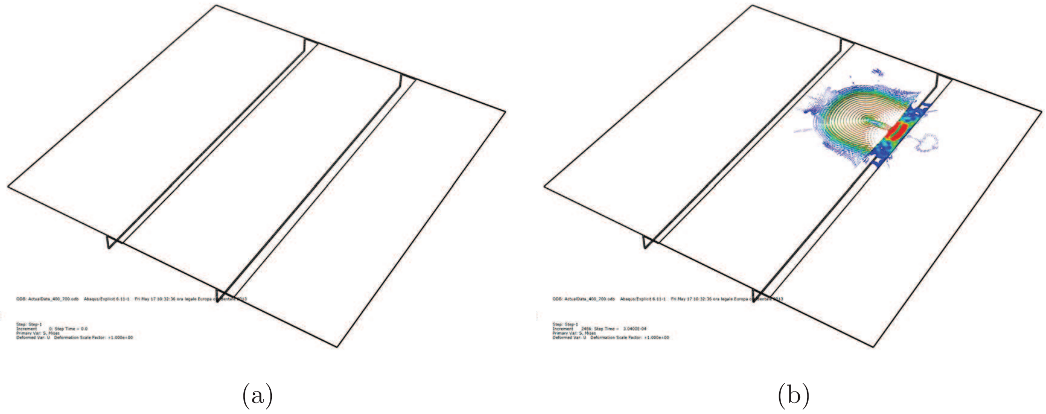
(a) (b)

Figure 4.9: (a) Eccentrically stiffened aluminium plate finite element model. (b) Snapshot in terms of Von Mises stresses of guided waves propagating in the specimen 30 ms after the impact occurred. It is worth noticing that the stiffeners waveguide the wave absorbing a lot of energy due to its high rigidity.

4.3.2 Numerical application

Reliability of the proposed technique has been first tested numerically by means of Finite Element (FE) analyses simulating the propagation of guided waves in the aforementioned specimen. The commercial package Abaqus Explicit [52] has been used. Fig. 4.9a shows the implemented 3D FE model. Main features used in the FE simulations are here recalled:

- full $3D$ propagation field is simulated by using linear hexahedral brick elements of type C3D8R. Total number of nodes is $2,686,684$.
- to ensure accuracy to the time-transient finite element simulations the plate domain was discretized with elements of maximum side length $L_{max} = 1$ mm and the time integration step was kept $t_{int} \leq 1e-8$ s [69].

It must be remarked that both wave reflections, generated by plate edges and stiffeners, and geometrical attenuation, due to wave radiation, are taken into account.

Fig. 4.9b sows a snapshot of guided waves propagation in terms of Von Mises stress 30 ms after the simulated impact has been applied. Impact was simulated

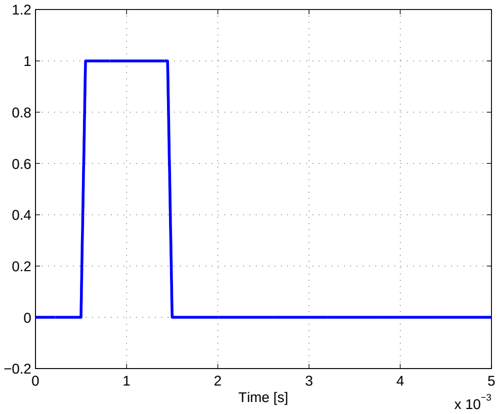

Figure 4.10: Excitation pulse: the excitation signal has been designed as a sharp square pulse in order to be a good representative of actual impact event.

by imposing an out-of-plane displacement shaped in time as a sharp square pulse of 1 nm and a total duration of 10 μs (see fig. 4.10).

In the FE analyses only 81 scanning points covering a square scanning area of 900 × 900 mm have been considered. The following impact cases are presented:

i) impact point corresponding to a grid point, Figs. 4.11a, 4.11b;

ii) impact point corresponding to a random point within the area delimited by the stiffeners, Figs. 4.11c, 4.11d;

iii) impact point corresponding to an equispaced point between four grid points, Figs. 4.11e, 4.11f;

Corresponding responses are collected for 32 ms at a 512 kHz sampling frequency and processed as explained in Section 4.2.3. Results presented in Fig. 4.11 confirm the methodology reliability. Furthermore, it was found that, when the impact point coincides with an acquisition point (Figs. 4.11b), the correlation presents a higher value (Fig. 4.11a) than for a random point (Figs. 4.11c and 4.11e) and predicting the impact location is extremely accurate (Fig. 4.11b).

Therefore, it can be inferred that the farther is the impact point from a scanning point, generally the lower the correlation value is. The minimum is achieved when an impact occurs in an equispaced position between more scanning points (Figs. 4.11e and 4.11f).

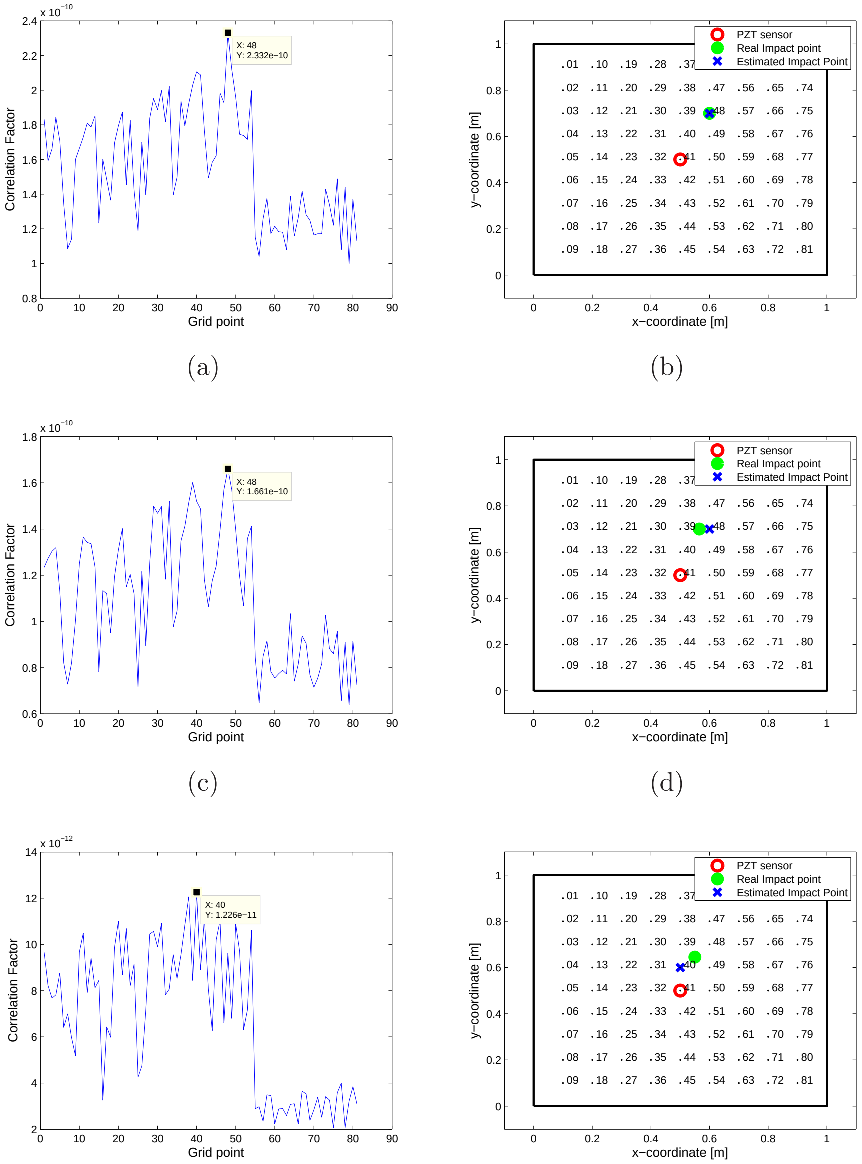

(a) (b)

(c) (d)

(e) (f)

Figure 4.11: Numerical results. (a,c,e) Correlation values between each signal of the scanned grid points and the signal of the actual impact points (1-D plot); the estimated point of impact is highlighted; (b,d,f) 2-D visualization of the estimated impact points. The black dots denote the scanning points, the red circle the acquisition point, the green spot the real impact position and the blue cross the estimated one.

4.3.3 Experimental application

Fig. 4.12 presents a scheme of the experimental set-up. A scanning measurement head is connected to a data acquisition system and steering circuit. A synchronisation cable connects the digital generator with the steering circuit through the amplifier that feeds the inducing signal to the piezoelectric element. Additionally, a signal from the generator is fed into the data acquisition system. A computer system integrated with the data acquisition system and steering circuit provides communication with the user and allows measurements to be processed.

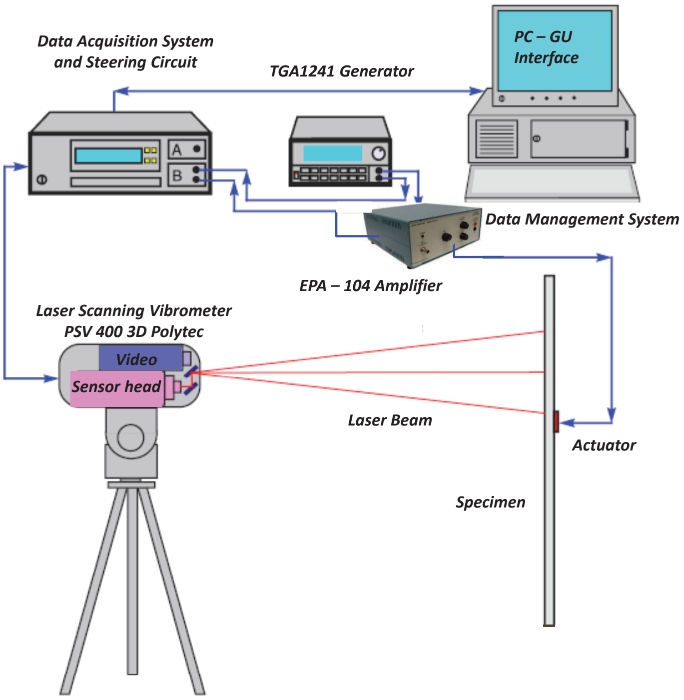

Figure 4.12: Schematic diagram of the experimental set-up. A scanning measurement head is connected to a data acquisition system and steering circuit. A synchronisation cable connects the digital generator with the steering circuit through the amplifier that feeds the inducing signal to the piezoelectric element. Additionally, a signal from the generator is fed into the data acquisition system. A computer system integrated with the data acquisition system and steering circuit provides communication with the user and allows measurements to be processed.

In particular, elastic guided waves were induced using a ceramic piezoelectric disk of diameter 10 mm made of Sonox® by CeramTec® glued to the surface

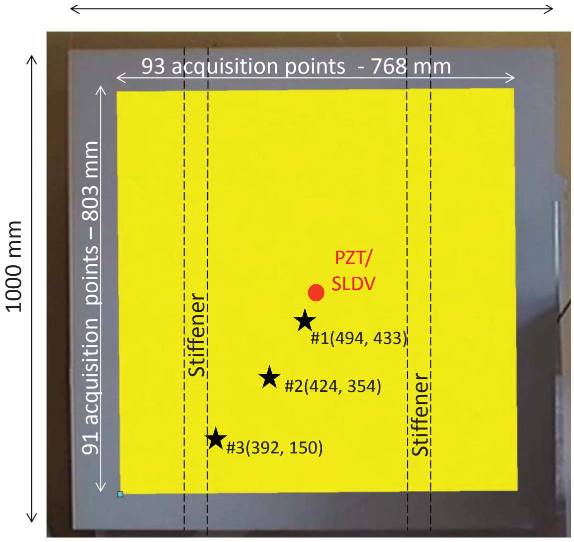

Figure 4.13: Illustration of the tested specimen. The red circle represents the position of both the PZT transducer used as actuator for the data training acquisition and of the SLDV acquisition point after the impact occurred. The testing region (768 mm × 803 mm), represented as the yellow rectangular box, is made of 93×91 acquisition equispaced points. The unknown impact points - $\#1 = (494, 433), \#2 = (424, 354)$ and $\#3 = (392, 150)$ - are represented by means of black stars and chosen within the area delimited by the stiffeners.

of the investigated sample using commercial super-glue. A 3D laser scanning vibrometer PSV 400 3D by Polytec® was used to perform the out-of-plane measurements of the velocities over the target area. The pulse excitation was fed from a TGA1241 generator by Thurlby Thandar Instruments through an EPA-104 amplifier by Piezo Systems® Inc, inducing a 20 V_{pp} signal. In order to improve measurements accuracy the investigated specimen was covered with self-adesive retroreflective film by ORALITE®. This was aimed at improving the laser vibrometer signal level in each measurement point regardless of the angle of incidence of the measurement beam on the surface being measured [1].

Impacts have been simulated into 3 different random points chosen within the area delimited by the stiffeners to verify experimentally the reliability of the proposed technique (see fig. 4.13). The training process has been realized by means of a pulse excitation with a duration of 1 ms applied to the PZT transducer. For each scanning point, 16,384 samples are collected over 8 ms by the SLDV at a sampling rate of 256 kHz, and 100 time signals are averaged to improve the signal-to-noise ratio. Approximately, 50 ms intervals are provided between two consecutive pulse excitations to allow signals to decay close to a background noise level before a new data collection. Measurement of all time signals from $8,463$ scanning points takes approximately 8 hours.

The results for the 3 experiments are shown in Fig. 4.14. As it can be seen accuracy is very high for all the examined cases regardless the impact position.

4.3.4 Further considerations on the acquired signals

In this section how the proposed procedure is capable to efficiently work in a passive way is highlighted. Fig. 4.15a shows the acquired signal for the first examined impact point. For simplicity in the experiment the PZT actuator and the laser-vibrometer acquisition were synchronized so that the zero time acquisition point coincides with the excitation time. In real impacts the time of actuation is unknown. Therefore, to recreate such a situation, the acquired signal has been a posteriori modified by adding or removing some idle time to the registered signals (Figs. 4.16a and 4.16c).

Localization results for these modified signals are represented in Figs. 4.16b and 4.16d: the procedure still properly identifies the impact positions, even if the arrival times of the original and modified waves are quite different. This confirms the good reliability and robustness of the procedure to work in a passive manner as well, making the technique a promising approach for real time impact location.

4.4 Conclusions

This chapter dealt with an impact localization procedure based on time-reversal and laser-vibrometry acquisition. The central idea was to locate an impact events simply by comparing an impact response with OPVs obtained from a grid of training points. The method revealed to be suitable for irregular wave-guide, potentially regardless of the geometric complexity of the specimen or additional structural features attached to it. The proposed technique revealed to be a promising approach for real time impact location.

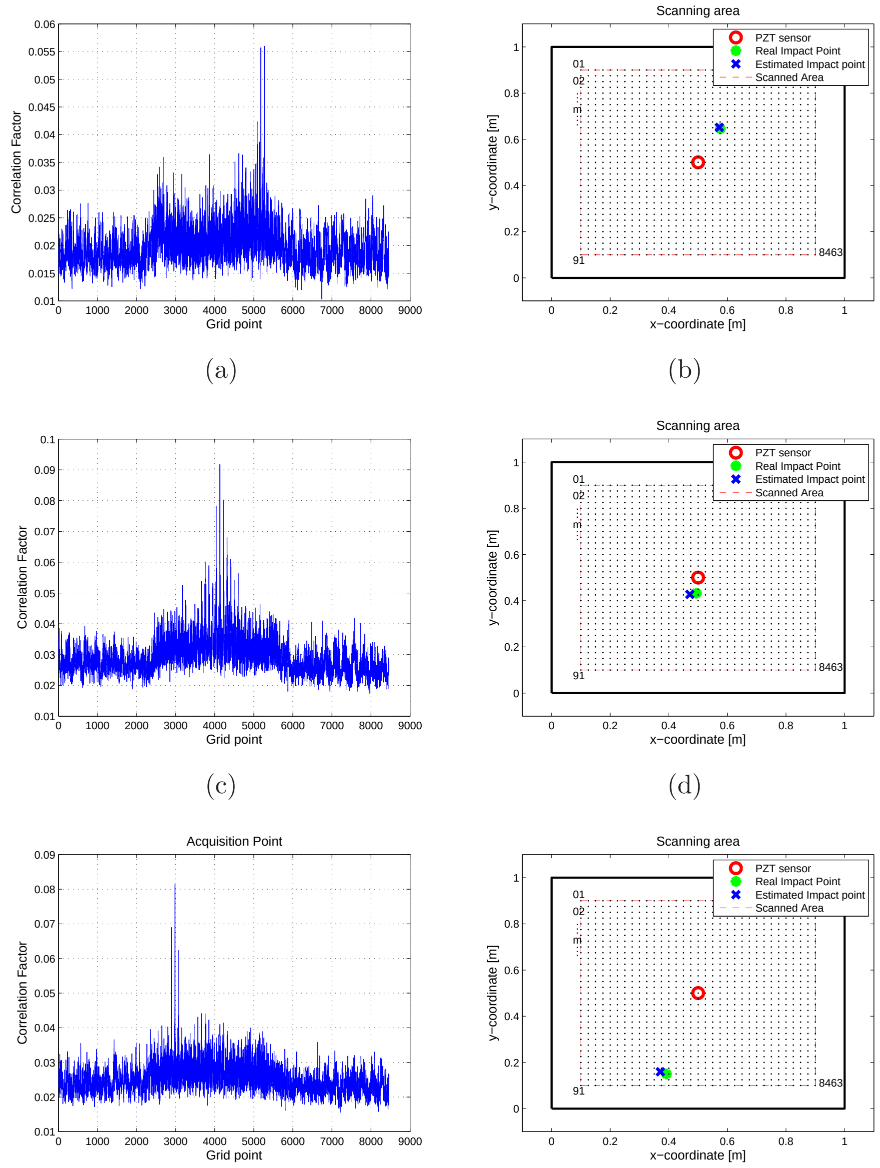

(a) (b)

(c) (d)

(e) (f)

Figure 4.14: Experimental results. (a,c,e) Correlation values between each signal of the scanned grid points and the signal of the actual impact points (1-D plot); the estimated point of impact is highlighted; (b,d,f) 2-D visualization of the estimated impact points. The black dots denote all the scanning points, the red circle the acquisition point, the green spot the real impact position and the blue cross the estimated one.

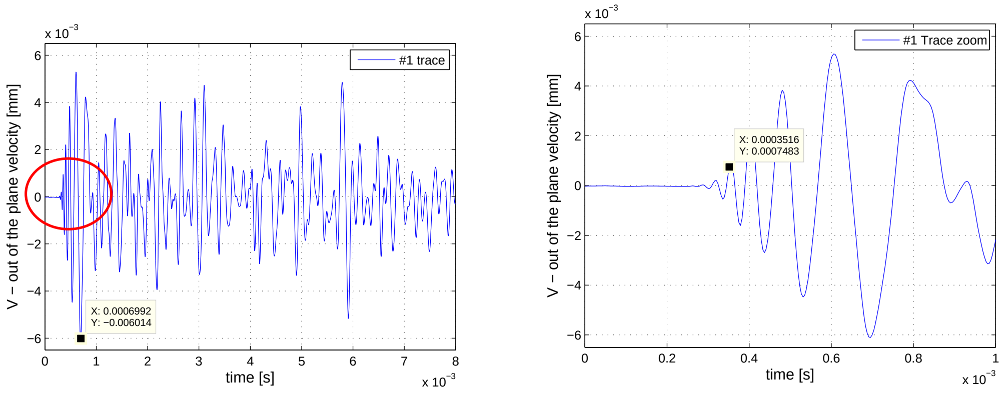

(a) (b)

Figure 4.15: (a) Acquired signal for the first impact case. (b) For simplicity in the experiment the PZT actuator and the laser-vibrometer acquisition were synchronized so that the zero time acquisition point coincides with the excitation time.

Both numerical and experimental results confirmed the methodology capability to identify unknown impact positions without a prior knowledge of the tested specimen. The so far described procedure is validated using only a single acquisition point. Actually, multiple acquisition points can be performed on the target structure. This will enhance the localization performance, although it is not a necessary requirements for the proposed technique.

The effectiveness of the proposed localization technique is examined using the data obtained from a stiffened aluminium plate. It has been demonstrated that the locations of test impacts are successfully identified regardless of the impact position (near to the sensor, far from the sensor, near to a plate edge, near to a stiffener). However, a special surface treatment with retro-reflective tapes is necessary to obtain strong laser return signals for SLDV measurement.

Future developments involve additional tests in order to examine the robustness of the proposed localization technique under temperature variations.

Although many methods are already available, thanks to its unique potential to treat in the same manner different kind of wave-guides (isotropic as well as anisotropic, homogeneous as well inhomogeneous, simple or irregular geometries) the developed tool allows to locate unexpected impacts regardless of the complexity of the material as well as the mechanical properties.

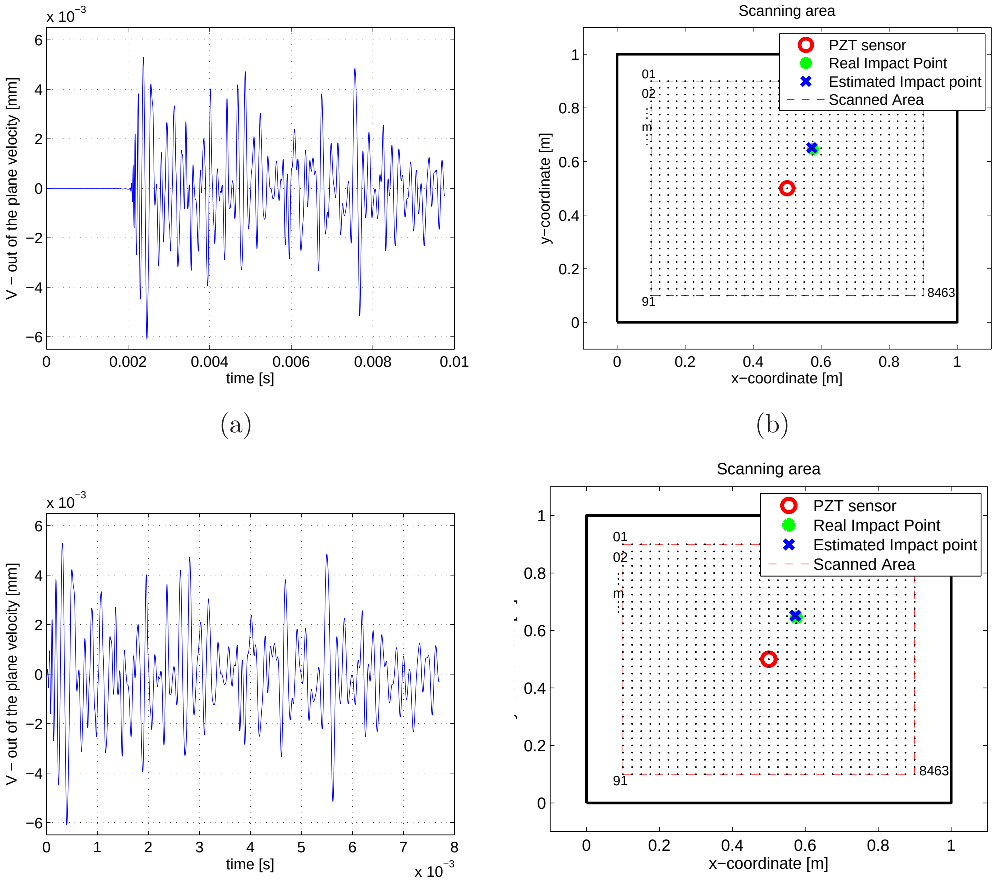

(a) (b)

(c) (d)

Figure 4.16: A posteriori modification of the actual registered signal and impact localization results for the first impact case. (a) The original signal has been lengthened by adding 1.765*e* μs of idle time and (c) shortened by removing 0.3 μs of the original signal. (b,d)In both cases results are still accurate.

Results also show the robustness of the method working in a passive manner, making the technique suitable for real time applications.

4.5 Funding

This study was supported by the Spinner Consortium of University of Bologna.

4.6 Acknowledgements

The author would like to thank the Laboratory of Department of Mechanics of Intelligent Structures of the Institute of Fluid-Flow Machinery, Polish Academy of Science for providing the test article and professional assistance during the experiments.

Part II

Acoustic metamaterials

Chapter 5

Elastic and acoustic metamaterials

5.1 Introduction

Over the past years, metamaterials have shown tremendous potential in many disciplines of science and technology. The prefix meta- comes from Greek $\mu\epsilon\tau\acute{\alpha}$ and means beyond, above, over. The word metamaterials, then, indicates a particular class of artificial materials that exhibits properties commonly not found in nature.

Although a universally accepted definition of acoustic metamaterials does not exist yet, there is no doubts that they owe much to crystallography, a specific branch of Solid State Physics. This branch of physics deals with the arrangement of atoms in solids, studying how the large-scale properties of solid materials result from their atomic-scale properties.

Following from recent developments of this field, the idea behind metamaterials is that as electrons in a semiconductor can only occupy certain energy bands, a metamaterial allows elastic and/or electromagnetic waves in specific frequency ranges to travel through via the “pass bands” meanwhile the other frequencies are inhibited by the so called “frequency band gaps”.

Therefore, the keen interest of scientists in metamaterials is mainly due to their capacity of manipulating light as well as elastic waves replacing the “atoms” composing matter with man-made structures, viewed then as “artificial atoms”.

These innovative properties make metamaterials of great interest from both theoretical and applied research viewpoint [14], as the increasing available literature on the topic confirms.

In this thesis, the interest is mainly focused on phonons, sound, and elastic waves control and manipulation, therefore on phononic crystals.

5.2 Basic definitions

It is convenient to introduce few basic definitions that apply to one-, two- and three-dimensional crystals. It’s worth noticing that concepts discussed in this section are of general nature and can be applied to any periodic system without being limited to atomic crystals [15].

5.2.1 Crystal lattice

To the naked eye, a solid appears as a continuous body. Experiments have proved, however, that all solids are composed of discrete basic units: atoms. These atoms are not distributed randomly, but they are arranged in a highly ordered manner relative to each other. Such a group of ordered atoms is typically referred to as a *crystal*[1]. Therefore, a solid is said to be a *crystal* if the atoms are arranged in such a way that their positions are *exactly periodic*. Fig. 5.1a illustrates the concept for the 2-D case. The distance between any two nearest neighbours along the x and y directions is a and b, respectively (x and y axes are not necessarily orthogonal). A *perfect* crystal maintains this periodicity in both x and y directions from $-\infty$ to $+\infty$. It follows from the periodicity that the atoms A, B, C, etc. are *equivalent*. In other words, to an observer located at any of these atomic sites, the crystal lattice appears exactly the same. Depending on the geometry of the atomic arrangement the physical properties of the solid change.

There are two classes of lattices: the *Bravais* lattice and the *non-Bravais* lattice. In a Bravais lattice, all lattice points are equivalent, and hence by necessity all atoms in the crystal are of the same kind. On the other hand, in a non-Bravais

---

[1] Crystallography is the science focused on the geometrical pattern of the matter.

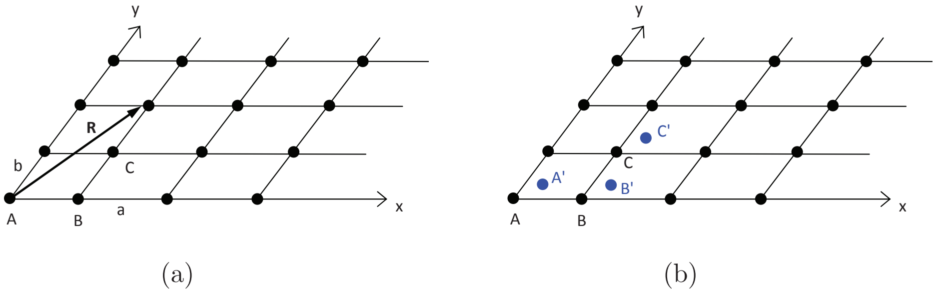

(a) (b)

Figure 5.1: A crystalline solid. (a) A Bravais lattice: all the atoms are arranged periodically. (b) A non-Bravais lattice.

lattice, some of the lattice points are non-equivalent. Fig. 5.1b shows it clearly. Here the lattice sites A, B, C are equivalent to each other, and so are the sites A', B', C' among themselves, but the two sites A and A' are not equivalent to each other, as can be seen by the fact that the lattice is not invariant under a translation by AA'.

5.2.2 Basis vectors

Consider the lattice shown in Fig. 5.2 and choose the origin of coordinates at the lattice point A.

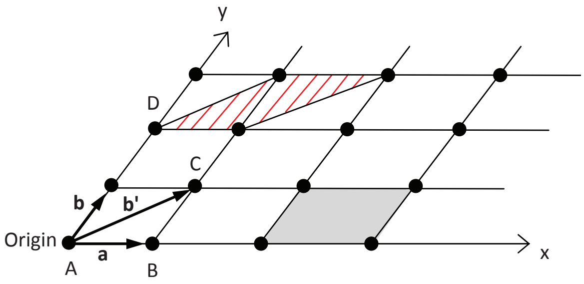

Figure 5.2: Vectors **a** and **b** are basis vectors of the lattice. Vectors **a** and **b**′ form another set of basis vectors. Shaded and hatched areas are unit cells corresponding to first and second set of basis vectors, respectively.

The position vector of any lattice point can be written as:

$$\mathbf{R} = n_1\mathbf{a} + n_2\mathbf{b} \tag{5.1}$$

where **a**, **b** are the two vectors shown and (n_1, n_2) is a pair of integers which values depend on the lattice point[1]. Thus, it occurs that for the point D, $(n_1, n_2) = (0, 2)$ and for the point B, $(n_1, n_2) = (1, 0)$.

The two vectors **a** and **b** (which must be non co-linear) form a set of *basis vectors* for the lattice, in terms of which the positions of all lattice points can be conveniently expressed by the use of Eq. (5.1). The set of all vectors expressed by this equation is called the *lattice vectors*. It is possible also to say that the lattice is invariant under the group of all the translations expressed by (5.1), i.e. crystals have *translational symmetry*, meaning that if the crystal is translated by any vector joining two atoms, say **R** in Fig. 5.1a, the crystal appears exactly the same as it did before the translation.

The choice of basis vectors is not unique. Thus one could equally take the vectors **a** and $\mathbf{b}'(= \mathbf{a} + \mathbf{b})$ as a basis (Fig. 5.2). Other possibilities are also evident. The choice is usually dictated by convenience.

5.2.3 The unit cell

The area of the parallelogram the sides of which are the basis vectors **a** and **b** is called *unit cell* of the lattice (Fig. 5.2) if translating such a cell by all the lattice vectors of Eq. (5.1) the area of the *whole* lattice is covered once and only once. The unit cell is usually the *smallest* area which produces this coverage. Therefore the lattice may be seen as composed of a large number of equivalent unit cells placed side by side, like a mosaic.

The choice of the unit cell is not unique. The following remarks may be helpful.

i. All unit cells have the same area. Thus the cell formed by **a**, **b** has the area $S = |\mathbf{a} \times \mathbf{b}|$, as the one formed by **a**, $\mathbf{b}'$ has the area $S' = |\mathbf{a} \times \mathbf{b}'| = |\mathbf{a} \times (\mathbf{a} + \mathbf{b})| = |\mathbf{a} \times \mathbf{b}| = S$, where the result $\mathbf{a} \times \mathbf{a} = 0$ has been used. Therefore the area of the unit cell is unique, even though the particular shape is not.

---

[1] All the previous statements can be extended to three dimensions in a straight-forward manner. In that case, the lattice vectors become three-dimensional and can be expressed by $\mathbf{R} = n_1\mathbf{a} + n_2\mathbf{b} + n_3\mathbf{c}$, where **a**, **b** and **c** are three *non co-planar* vectors joining the lattice point at the origin to its near neighbours; n_1, n_2 and n_3 are a triplet of integers.

ii. The unit cell formed by $\mathbf{a} \times \mathbf{b}$ has four points at its corners, but each of these points is shared by four adjacent cells. Hence each unit cell has only one lattice point.

5.2.4 Primitive versus non-primitive cells

The unit cell discussed above is called *primitive cell*. It is sometimes more convenient to deal with a unit cell which is larger and exhibits the symmetry of the lattice more clearly. The idea is illustrated by the Bravais lattice in Fig. 5.3. Clearly, the vectors $\mathbf{a_1}$, $\mathbf{b_1}$ can be chosen as a basis set, in which case the unit cell is the parallelogram S_1. However, the lattice may also be regarded as a set of adjacent rectangles, where the vectors $\mathbf{a_2}$ and $\mathbf{b_2}$ are taken as basis vectors. The unit cell is then S_2. It has one lattice point at its center, in addition to the points at the corner. This cell is *non-primitive* unit cell.

The reason for the choice of the non-primitive cell S_2 is that it shows the rectangular symmetry most clearly.

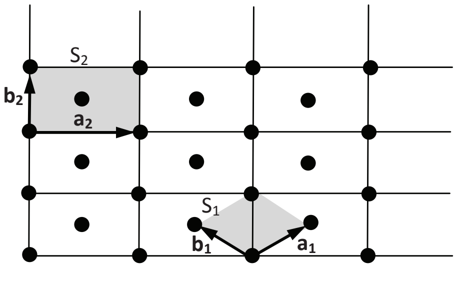

Figure 5.3: Area S_1 is a primitive unit cell; area S_2 is a non-primitive unit cell.

5.2.5 Reciprocal lattice

The reciprocal lattice plays a fundamental role in most analytic studies of periodic structures. Consider a set of points $\mathbf{R}$ constituting a Bravais lattice, and a plane wave $e^{\imath \mathbf{k} \cdot \mathbf{r}}$. For general $\mathbf{k}$, such a plane wave will not, of course, have the periodicity of the Bravais lattice, but for certain special choices of wave vector it will. *The set of all wave vectors* $\mathbf{k}$ *that yield plane waves with the periodicity of*

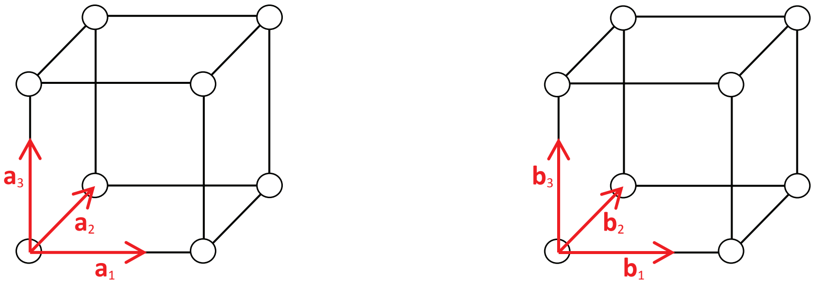

(a) (b)

Figure 5.4: Simple-cubic direct lattice (a) and its reciprocal lattice (b). The primitive vectors of both lattices are also indicated.

a given Bravais lattice is known as its reciprocal lattice. Analytically, **k** belongs to the reciprocal lattice of a Bravais lattice of points **R** if the following relation:

$$e^{\imath\mathbf{k}\cdot(\mathbf{r}+\mathbf{R})} = e^{\imath\mathbf{k}\cdot\mathbf{r}} \tag{5.2}$$

holds for any **r** and for all **R** in the Bravais lattice. Factoring out $e^{\imath\mathbf{k}\cdot\mathbf{r}}$, the reciprocal lattice can be characterized as the set of wave vectors **k** satisfying:

$$e^{\imath\mathbf{k}\cdot\mathbf{R}} = 1 \tag{5.3}$$

for all **R** in the Bravais lattice.

Note that a reciprocal lattice is defined with reference to a particular Bravais lattice. The Bravais lattice that determines a given reciprocal lattice is often referred to as the *direct lattice*, when viewed in relation to its reciprocal [70].

For example, considering a 3-D lattice, as the shown in Fig. 5.4a, defined by a basis vectors: $\mathbf{a}_1$, $\mathbf{a}_2$ and $\mathbf{a}_3$, a new set of basis vectors $\mathbf{b}_1$, $\mathbf{b}_2$ and $\mathbf{b}_3$ can be defined according to the following relations:

$$\begin{aligned}
\mathbf{b}_1 &= 2\pi\frac{\mathbf{a}_2 \times \mathbf{a}_3}{\boldsymbol{\Omega}} \\
\mathbf{b}_2 &= 2\pi\frac{\mathbf{a}_3 \times \mathbf{a}_1}{\boldsymbol{\Omega}} \\
\mathbf{b}_3 &= 2\pi\frac{\mathbf{a}_1 \times \mathbf{a}_2}{\boldsymbol{\Omega}}
\end{aligned} \tag{5.4}$$

where $\mathbf{\Omega} = \mathbf{a}_1 \cdot \mathbf{a}_2 \times \mathbf{a}_3$ is the volume of the unit cell. Now it is possible to exploit the vectors $\mathbf{b}_1$, $\mathbf{b}_2$ and $\mathbf{b}_3$ as a basis for a new lattice, the vectors of which are given by:

$$\mathbf{G} = n_1\mathbf{b}_1 + n_2\mathbf{b}_2 + n_3\mathbf{b}_3 \tag{5.5}$$

where n_1, n_2 and n_3 are any set of integers. The lattice just defined is known as the *reciprocal lattice*, and $\mathbf{b}_1$, $\mathbf{b}_2$ and $\mathbf{b}_3$ are called the *reciprocal basis vectors*.

5.2.6 Wigner-Seitz primitive cell

Among the possibles choices available for a primitive cell, the most common is the *Wigner-Seitz cell*. The Wigner-Seitz cell about a lattice point is the region of space that is closer to that point than to any other lattice point. Because of the translational symmetry of the Bravais lattice, the Wigner-Seitz cell, when translated through all lattice vectors, will just fill space without overlapping; i.e., the Wigner-Seitz cell is a primitive cell.

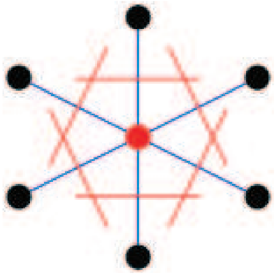

Figure 5.5: The Wigner-Seitz cell for a two-dimensional Bravais lattice. The sides of the cell bisect the lines joining the central points to its nearest neighbouring points (shown in blue lines). In two dimensions the Wigner-Seitz cell is always a hexagon unless the lattice is rectangular.

The Wigner-Seitz cell in the reciprocal space is known as the first Brillouin zone (BZ). In 2D, the first BZ is always a hexagon (see Fig. 5.5) unless the lattice possess rectangular symmetry, as shown in Fig. 5.6. It can also be defined as the set of all points in k-space that can be reached from the origin without crossing any Bragg plane[1]. The BZs of higher orders also exist, with the n-th BZ defined

---

[1] A Bragg plane for two points in a lattice is the plane which is perpendicular to the line

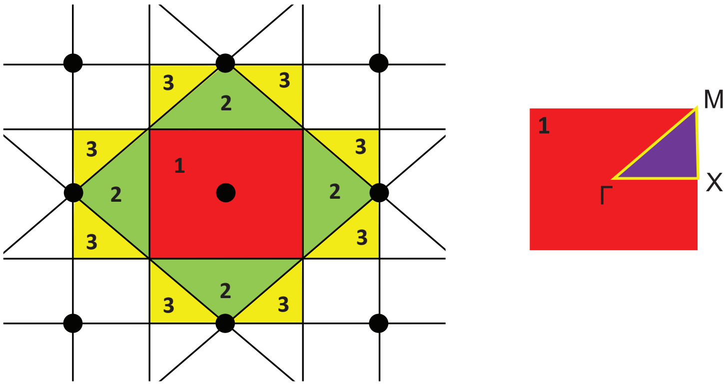

(a) (b)

Figure 5.6: (a) The first three Brillouin zones of the reciprocal lattice of the 2D square Bravais lattice. The dots indicate reciprocal lattice points, the solid lines indicate Bragg planes, and the digits indicate the order of the corresponding Brillouin zone. (b) The first Brillouin zone with the two high-symmetry directions commonly referred to as $\Gamma - X$ and $\Gamma - M$.

as the set of points that can be reached from the origin by crossing $(n-1)$ Bragg planes. The first BZ is of great importance in the theory of solids with periodic structures, since the periodicity of the structure allows the description of the properties of the solids within the first BZ. Figure 5.6 shows the first three BZs of the 2D square Bravais lattice. The first BZ has a shape of a square with two high-symmetry directions, which are commonly referred to as $\Gamma - X$ and $\Gamma - M$.

5.3 Phononic materials

The concept of phonon was introduced by Russian physicist Igor Tamm. The name phonon comes from the Greek word $\varphi\omega\nu\eta$ (phonè), which translates as sound, voice, as long-wavelength phonons give rise to sound. In physics, a phonon is a quasi-particle representing the quantization of a special type of vibrational motion, in which a lattice uniformly oscillates at the same frequency. In classical mechanics these are known as normal modes[1]. These modes are important

---

between the two points and passes through the bisector of that line.

[1] While normal modes are wave-like phenomena in classical mechanics, they have particle-like properties in the wave-particle duality description of quantum mechanics.

because any arbitrary lattice vibration can be considered as a superposition of these elementary vibrations.

Phononic materials (PMs) are composite materials with a periodic distribution of elastic properties and mass density according to a particular lattice symmetry. They are made, for instance, by periodically distributed elastic scatterers embedded in a matrix with high impedance contrast of mass densities and/or elastic properties[1]. This can give rise to new acoustic dispersion band structures if compared to the traditional dispersion maps [71].

As well known, PMs are characterized by the existence of band gaps (BGs), i.e. frequency ranges in which they do not support the propagation of elastic waves. This property makes PMs suitable for several applications such as sound isolators, acoustic filters, acoustic mirrors, acoustic resonators, seismic shields, among others [72, 73, 74, 75, 76].

Since the pioneering work of Kushwaha [77], that explored the concept of phononic materials in 1993, and the one of Martinez et al. [78], who confirmed the existence of acoustic band gaps in the famous periodic sculpture by Eusebio Sempere, elastic band gaps in one-dimension [79, 80, 81, 82], two-dimension [83] and three-dimension [84] PMs, have been extensively studied for solid-solid, fluid-fluid and mixed solid-fluid composite systems.

A coarse classification of PMs can be made on the base of lattice periodicity and geometrical dimensions. Fig. 5.7 depicts the possible arrangements, where the letter “P” refers to the lattice periodicity, while the letter “D” defines the dimensionality of the structure.

Generally speaking, PMs can be classified into two categories: acoustic phononic materials (APMs) characterized by a fluid matrix, and elastic phononic crystals (EPMs) with an elastic solid matrix.

In past years, much efforts were dedicated to the band structure calculation and its mechanism of formation [14, 76, 85, 86, 87]. To this end, several calculation methods have been proposed and adopted in order to compute PMs dispersion band structure. Among them, plane wave expansion (PWE) method, finite-difference time-domain (FDTD) method, finite element (FE) method and transfer

---

[1] Generally speaking, matrix and scatterers need to be composed of different materials, however holes drilled in the matrix material can work as well.

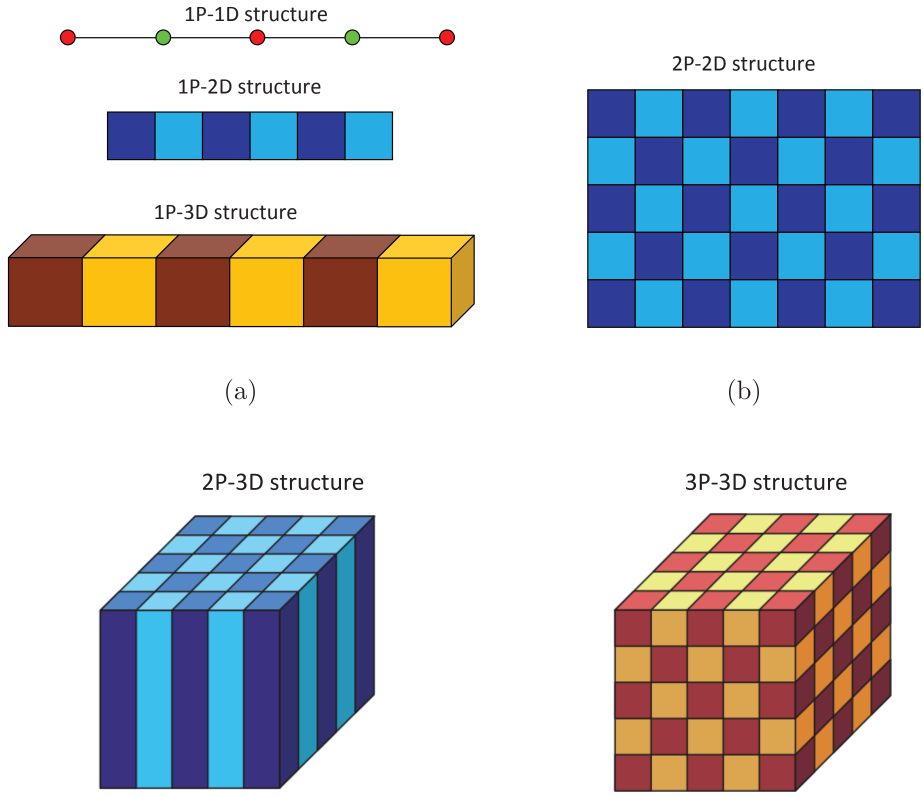

(a)

(b)

(c)

Figure 5.7: Lattice periodicity and geometrical dimensions based classification of PMs. The “P” letter refers to the lattice periodicity, meanwhile the “D” letter defines the dimensionality of structure.

matrix (TM) method are the most popular [88, 89].

Researchers predicted theoretically the existence of absolute band gaps in two-dimensional phononic crystals [14, 77] prior to being demonstrated experimentally.

Theoretical models of two-dimensional [90, 91, 92] and three-dimensional [93] phononic materials have shown that the width of the acoustic band gaps strongly depends on: (i) a large contrast in physical properties such as density and speeds of sound between the inclusions and the matrix, and (ii) a sufficient filling factor of inclusions. Several classes of phononic materials differing in the physical nature of the inclusions as well as of the matrix have been intensively investigated. Among them, solid-solid, fluid-fluid and mixed solid-fluid[1] composite systems have been considered [87].

5.4 Dispersion properties

A phononic material consists at least of two different materials A and B characterized by different rheological properties, as the key requirement is that the elastic wave scattering on the inclusions is very efficient. To describe the governing wave equations, consider a phononic material made of a material A (inclusions) embedded in an infinite elastic matrix B.

The density and elastic properties, ρ_A and $\mathbf{C}^A$ for the inclusions and ρ_B and $\mathbf{C}^B$ for the matrix are periodic functions of the position $\mathbf{r}$. This allows to identify a unitary cell characterized by lattice parameters a_i, ($i = 1, 2$ or 3 depending on the space dimension of the material) and a ratio between inclusion and matrix, also known as filling fraction, denoted by f. In force of such a periodicity, it is possible to write material density ρ and elastic properies $\mathbf{C}$ as Fourier series [87]:

$$\rho(\mathbf{r}) = \sum_{\mathbf{G}} \rho(\mathbf{G}) e^{(\imath \mathbf{G} \mathbf{r})} \tag{5.6}$$

and:

$$\mathbf{C}(\mathbf{r}) = \sum_{\mathbf{G}} \mathbf{C}(\mathbf{G}) e^{(\imath \mathbf{G} \mathbf{r})} \tag{5.7}$$

where $\mathbf{r}$ is the position vector and $\mathbf{G}$ is the reciprocal lattice vector. Similarly, the time t dependent wave displacement field $\mathbf{u}$ can be represented as:

$$\mathbf{u}(\mathbf{r}, t) = e^{\imath(\mathbf{k} \cdot \mathbf{r} - \omega t)} \sum_{\mathbf{G}} \mathbf{u}_{\mathbf{k}} \mathbf{G} e^{(\imath \mathbf{G} \cdot \mathbf{r})} \tag{5.8}$$

where $\mathbf{k}$ is the wavevector, ω is the wave circular frequency and $\mathbf{u}_{\mathbf{k}}$ is the wave amplitude. Under these conditions, the dispersion properties of the system can be fully investigated exploiting Bloch theorem considering a unitary cell only.

---

[1] In mixed composites, the fluid can be either a condensed liquid or a gas

The Fourier coefficients in Eq. (5.6) take the form:

$$\rho(\mathbf{G}) = \frac{1}{V}\int \mathrm{d}^3\mathbf{r}\rho(\mathbf{r})e^{(-\imath\mathbf{G}\mathbf{r})} \tag{5.9}$$

where the integration is performed over the unit cell of volume V. For $\mathbf{G} = \mathbf{0}$, Eq. (5.9) gives the average density:

$$\rho(\mathbf{G}=\mathbf{0}) = \bar{\rho} = \rho^A f + \rho^B(1-f) \tag{5.10}$$

For $\mathbf{G} \neq \mathbf{0}$, Eq. (5.9) may be written as:

$$\rho(\mathbf{G}\neq\mathbf{0}) = (\rho^A - \rho^B)F(\mathbf{G}) \tag{5.11}$$

where $F(\mathbf{G})$ is the structure factor given by:

$$F(\mathbf{G}) = \frac{1}{V}\int \mathrm{d}^3\mathbf{r}e^{(-\imath\mathbf{G}\mathbf{r})} \tag{5.12}$$

In Eq. (5.12), the integration is only performed on material A. In an analogously way, Eq. (5.7) gives:

$$\mathbf{C}(\mathbf{G}=\mathbf{0}) = \bar{\mathbf{C}} = \mathbf{C}^A f + \mathbf{C}^B(1-f) \tag{5.13}$$

and:

$$\mathbf{C}(\mathbf{G}\neq\mathbf{0}) = (\mathbf{C}^A - \mathbf{C}^B)F(\mathbf{G}) = (\Delta\mathbf{C})F(\mathbf{G}) \tag{5.14}$$

Considering small amplitude waves propagating in a linear elastic metamaterial, compatibility, constitutive and equilibrium equations, in absence of body forces, read:

$$\begin{aligned} \boldsymbol{\varepsilon} &= \frac{1}{2}\left[(\nabla\mathbf{u})^{\mathrm{T}} + \nabla\mathbf{u}\right] \\ \boldsymbol{\sigma} &= \mathbf{C}\boldsymbol{\varepsilon} \\ \nabla\cdot\boldsymbol{\sigma} + \rho\omega^2\mathbf{u} &= \mathbf{0} \end{aligned} \tag{5.15}$$

where $\boldsymbol{\varepsilon}$ is the strain vector, $\boldsymbol{\sigma}$ is the Cauchy stress tensor.

Substituting Eqs. (5.6)-(5.8) into Eqs. (5.15) and applying proper periodic boundary conditions, the equations of motion can be described taking into account a unitary cell only.

5.4.1 Finite Element discretization

In this study, the finite element method (FEM) has been used to approximate the equation of motion. The unit cell is first divided into an arbitrary number of discrete finite elements, as shown in Fig. 5.8a. Within each finite element a polynomial formulation is assumed for the displacement field, which is related to the displacements of node points defining each element. By considering the equilibrium equations, the material constitutive relations, the strain-displacement relations and the boundary conditions, the general equation of motion results:

$$\mathbf{M}\ddot{\mathbf{u}} + \mathbf{K}\mathbf{u} = \mathbf{F} \tag{5.16}$$

where $\mathbf{M}$ is the structural mass matrix, symmetric and positive definite, $\mathbf{K}$ is the structural stiffness matrix, symmetric and positive or semipositive definite, $\mathbf{F}$ is the vector of applied loads, and $\mathbf{u}$, $\ddot{\mathbf{u}}$ are the displacement and acceleration vectors, respectively.

The global vector of nodal displacements contains degrees of freedom corresponding to:

- nodes belonging to the x-axis normal boundaries ($\mathbf{U}_{BCx+}$ and $\mathbf{U}_{BCx-}$ in Fig. 5.8b);
- nodes belonging to the x-axis normal boundaries ($\mathbf{U}_{BCy+}$ and $\mathbf{U}_{BCy-}$ in Fig. 5.8c);
- nodes belonging to the x-axis normal boundaries ($\mathbf{U}_{BCz+}$ and $\mathbf{U}_{BCz-}$ in Fig. 5.8d),

as well as all the other internal nodes, $\mathbf{U}_i$. Thus, the vector of nodal displace-

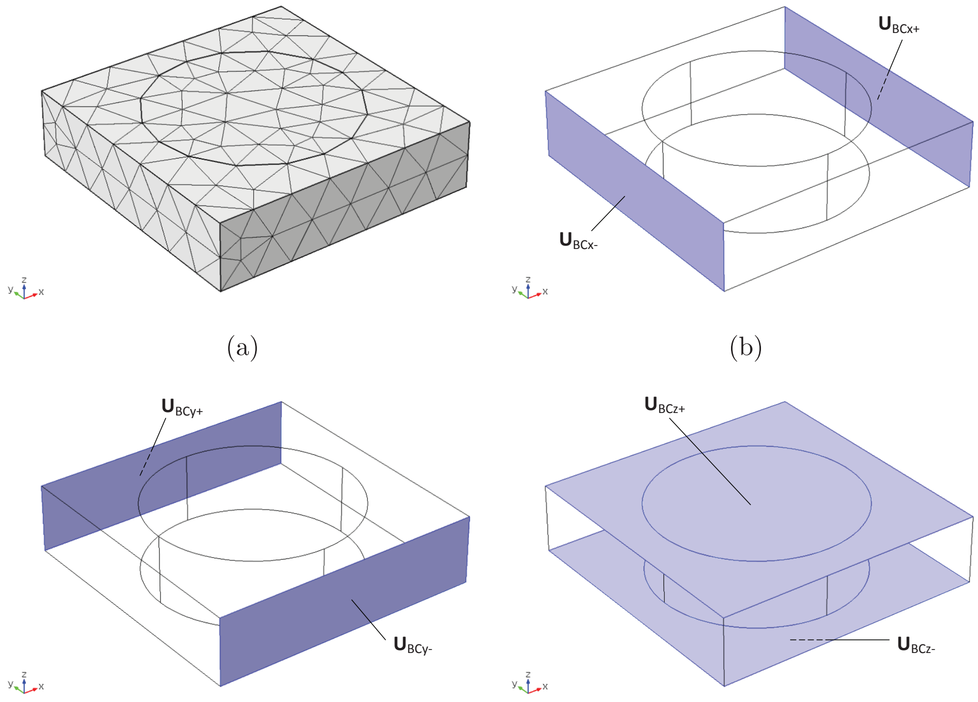

(a) (b)

(c) (d)

Figure 5.8: (a) Finite elements discretization and (b-d) proper boundary conditions of the unitary cell.

ments, and similarly, the force vector for the cell are:

$$\mathbf{U} = \begin{Bmatrix} \mathbf{U}_{BCx+} \\ \mathbf{U}_{BCy+} \\ \mathbf{U}_{BCz+} \\ \mathbf{U}_{i} \\ \mathbf{U}_{BCx-} \\ \mathbf{U}_{BCy-} \\ \mathbf{U}_{BCz-} \end{Bmatrix}; \qquad \mathbf{F} = \begin{Bmatrix} \mathbf{F}_{BCx+} \\ \mathbf{F}_{BCy+} \\ \mathbf{F}_{BCz+} \\ \mathbf{F}_{i} \\ \mathbf{F}_{BCx-} \\ \mathbf{F}_{BCy-} \\ \mathbf{F}_{BCz-} \end{Bmatrix} \tag{5.17}$$

When the periodic cell vibrates harmonically, with circular frequency ω, according to the partition of Eq. (5.17), and assuming a displacement field of the form:

$$\mathbf{u} = \mathbf{U}_0 e^{\imath(\mathbf{k}\cdot\mathbf{r}-\omega t)} \tag{5.18}$$

where $\mathbf{U}_0$ is the wave amplitude, the equation of motion Eq. (5.16) becomes:

$$(\mathbf{K} - \omega^2\mathbf{M})\mathbf{U} = \mathbf{F} \tag{5.19}$$

where the symmetric nature of the stiffness and mass matrices was outlined. When a free wave propagates through an infinite structure, $\mathbf{F}_i = \mathbf{0}$, whilst the nodal forces at the end nodes of the cell, $\mathbf{F}_{BC+}$ and $\mathbf{F}_{BC-}$, are not zero, since these forces are responsible for transmitting the wave motion from one cell to the next. According to Bloch's theorem [94], the ratio between corresponding displacements in adjacent cells of the model is equal to e^{μ}, where μ is the complex propagation constant. For instance, for a propagating wave along x-direction, $\mu = \imath k_x L_x$, where L_x denotes the periodic distance in the x direction. Similarly nodal displacements along boundaries $BCx+$ and $BCx-$ are separated by the same periodic distance L_x. Thus, if the degrees of freedom on boundary $BCx+$ is identical to that on boundary $BCx-$, the nodal displacements are related by:

$$\mathbf{U}_{BCx-} = e^{\imath k_x L_x}\mathbf{U}_{BCx+} \tag{5.20}$$

Similarly, equilibrium between adjacent sections implies that nodal forces and moments at the boundaries are related by:

$$\mathbf{F}_{BCx-} = e^{\imath k_x L_x}\mathbf{F}_{BCx+} \tag{5.21}$$

Further details can be found in Refs.[95, 96, 97].

Chapter 6

Numerical modelling of stress waves in metamaterials

6.1 Introduction

In this Chapter, solid-solid and solid-fluid phononic systems are discussed via numerical applications. Generally, first band structures are derived and then transmission power spectra are investigated. The influence of the number of repeated unitary cells compounding the metamaterial is illustrated. Effects of prestrain/prestress on BGs is also taken into account in a 1P-2D phononic slab. Finally, the plane strain assumption is removed and the effects of the thickness in a 2P-3D PM is investigated by means of FEM wave propagation analyses.

6.2 1P-2D phononic materials

Although from a theoretical point of view, PMs are supposed to be infinite along three dimensions in real space, recently, properties of plate-mode waves in 1P[1]-2D[2] phononic slabs have been studied because of their potential technological applications [98] ranging from acoustic filters to ultrasonic silent blocks, focus lens and non-destructive evaluation [90].

---

[1] 1P refers to the periodicity of the lattice. In this case, lattice repeats only in one direction.

[2] 2D refers to the dimensionality of the modelled structure.

Generally speaking, PMs studied for the plate-mode waves are taken to be a finite size system in at least one direction. It has been shown that Lamb waves can be supported in 2D phononic plate both with the slab surfaces perpendicular or parallel to the axis of periodicity [81].

In this study, characteristics of Lamb waves in a phononic plate consisting of a row or more of square cylinders placed periodically in the hosting material as shown in Fig. 6.1 are investigated.

In particular, first the dispersion properties for an ordinary isotropic plate are computed and compared to literature results to validate the followed procedure. Next, the effect of prestress is introduced. Finally, the influence of the phononic region length (number of unitary cells) on the transmitted energy is studied.

6.2.1 Dispersion properties of phononic materials

Since Lamb waves are of interest in this study, only the propagation plane in 2D plane strain condition, see Fig. 6.1a-b, is considered to build numerical models. Both ordinary and phononic plates can be seen as periodic in the x-direction [94], allowing their dispersion features to be extracted by analysing a unitary cell only.

For the ordinary plate, a unitary cell $a \times a$ is considered. For the phononic waveguide, the unitary cell ($a \times a$) embeds a square cylinder (denoted by B) of side length m, as shown in Fig. 6.1. The inclusion is located at the square lattice centre and the thickness of the slab h equals the lattice spacing a. This allows to define the filling rate as $f = (m^2)/(a^2)$. The structure is assumed to be infinitely long in the out of plane direction, along the which axes of the cylinders inclusions are placed, as well as the periodicity of the elementary cell, repeating in the x-direction.

Figs. 6.1e-f illustrate the schematics of the cross-section of a single unit cell considered for the FE calculation both for the ordinary and phononic plate. Materials A and B represent aluminium and vacuum, respectively. Aluminium rheological properties used in the calculations are as follows: density $\rho = 2699$ kg/m^3, Young's modulus $E = 70.3$ GPa and Poisson's ratio $\nu = 0.3436$ (refer to Tab. 6.1 for further details).

Band structures of the Lamb wave modes are computed using Comsol Multi-

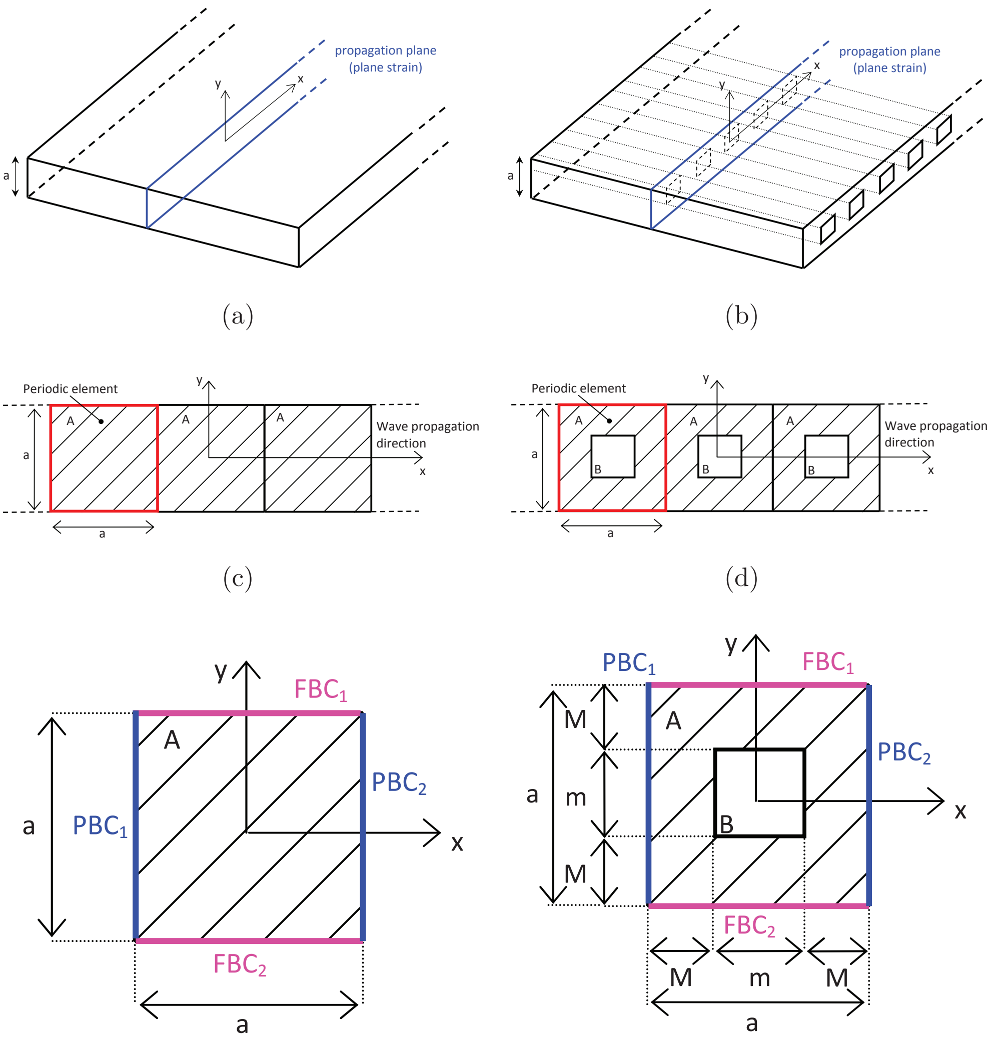

(a) (b)

(c) (d)

(e) (f)

Figure 6.1: Wave propagation plane in an ordinary (a) and in a phononic (b) plate under 2D plane strain assumption. Schematic representation of several coupled periodic elements joined together end-to-end in the ordinary (c) and phononic (d) waveguide. Ordinary (e) and phononic (f) unitary cell with geometric dimensions and prescribed boundary conditions.

Table 6.1: Mechanical properties of the materials used in the analyses. Depending on the material, density ρ, Young modulus E, Poisson ratio ν and longitudinal, c_L, and transverse, c_S, wave velocities are given.

Material	ρ [kg m^{-3}]	E [Pa]	ν [/]	c_L [m s$^-$1]	c_S [m s$^-$1]
W	19200	$404 \cdot 10^9$	0.287	5231	2860
Al	2699	$70.3 \cdot 10^9$	0.3436	6378	3113
Steel	7850	$210 \cdot 10^9$	0.3	6001	3207
PVC	1430	$3 \cdot 10^9$	0.40	2120	865
Epoxy	1180	$4.44 \cdot 10^9$	0.399	2830	1160
Pb	10760	$21.5 \cdot 10^9$	0.384	1960	850
Concrete	2500	$30 \cdot 10^9$	0.3	4020	2148
Soil	1750	$0.340 \cdot 10^9$	0.25	482	278
Rubber	1300	$1.37 \cdot 10^5$	0.463	22	6
Water	1000	/	/	1490	/
Air	1.25	/	/	343	/

physics [99]. The FE model is based on the Bloch-Floquet theorem [73], which allows to express waves in the periodic structure as:

$$\mathbf{u}(\mathbf{r}, t) = e^{i(\mathbf{k}\cdot\mathbf{r}-\omega t)}\mathbf{u}_\mathbf{k}(\mathbf{r}) \tag{6.1}$$

where $\mathbf{u}$ and $\mathbf{r}$ are the displacement and position vectors, respectively, t is the time, $\mathbf{k}$ is the reduced wave vector within the first irreducible Brillouin zone of the considered 1P-2D PM and ω is the circular frequency. Due to the periodic property of material constants, the Fourier expansion is taken into consideration:

$$\begin{aligned}
&\rho(\mathbf{r}) = \rho(x) = \sum_{\mathbf{G_0}} \rho(\mathbf{G_0}) e^{i\mathbf{G_0}\cdot\mathbf{r}} \\
&C_{ii}(\mathbf{r}) = C_{ii}(x) = \sum_{\mathbf{G}} C_{ii}(\mathbf{G}) e^{i\mathbf{G}\cdot\mathbf{r}}, \qquad i = 1, 4 \\
&\mathbf{u}(\mathbf{r}) = \mathbf{u}(x) = \sum_{\mathbf{G}'} \mathbf{u}^{\mathbf{k}}(\mathbf{G}') e^{i(\mathbf{k}+\mathbf{G}')\cdot\mathbf{r}}
\end{aligned} \tag{6.2}$$

where ρ is the mass density, $C_{11} = \lambda + 2\mu$, $C_{44} = \mu$ with λ and μ the first and second Lamè constants, respectively and $\mathbf{G_0}$, $\mathbf{G}$ and $\mathbf{G}'$ are the reciprocal lattice vectors. The starting point is the motion equation, which reads:

$$\nabla(\lambda + 2\mu)(\nabla \cdot \mathbf{u}) - \nabla\mu \times \nabla \times \mathbf{u} = \rho\ddot{\mathbf{u}} \tag{6.3}$$

As in this case the phononic slab is periodic in the x-direction and finite in the y-direction, a plane elastic wave propagating only along x-direction can be considered. In such a case, the displacement vector $\mathbf{u}$ is independent of y and z coordinates, namely $\mathbf{u}(\mathbf{r}, t) = \mathbf{u}(x, t)$. Therefore, Eq. (6.3) can be decoupled into:

$$\begin{aligned}
\rho(x)\frac{\partial^2 u_x}{\partial t^2} &= \frac{\partial}{\partial x}\left[\lambda(x)\frac{\partial u_x}{\partial x}\right] + \frac{\partial}{\partial x}\left[2\mu(x)\frac{\partial u_x}{\partial x}\right] \\
\rho(x)\frac{\partial^2 u_y}{\partial t^2} &= \frac{\partial}{\partial x}\left[\mu(x)\frac{\partial u_y}{\partial x}\right] \\
\rho(x)\frac{\partial^2 u_z}{\partial t^2} &= \frac{\partial}{\partial x}\left[\mu(x)\frac{\partial u_z}{\partial x}\right]
\end{aligned} \tag{6.4}$$

Inserting Eqs. (6.2) into Eqs. (6.4) and applying standard finite element assembling procedures described in Chap. 5, the discrete form of the eigenvalue equations for the unit cell can be written as:

$$(\mathbf{K} - \omega^2\mathbf{M})\mathbf{u} = \mathbf{0} \tag{6.5}$$

where $\mathbf{K}$ and $\mathbf{M}$ are the stiffness and mass matrices of the discrete system. Periodicity allows to compress calculation in one unit cell applying proper Bloch-Floquet periodic boundary conditions (PBC_1 and PBC_2 in Figs. 6.1e-f) to the sides of the unit cell along the x-direction:

$$u(x + a, y) = u(x, y)e^{\imath(k_x \cdot a)} \tag{6.6}$$

with k_x the only component of Bloch wave vector. On the other hand, free boundary conditions FBC_1 and FBC_2 are applied to the top and bottom surfaces of the unit cell, as shown in Figs. 6.1e-f.

The Comsol "Solid Structures Module" operating under the 2D plane strain hypothesis is chosen for the eigenvalue calculations. The modelled unit cell is meshed by Lagrange linear triangular elements provided by COMSOL. Good convergence for a maximum frequency of 2.5 MHz is obtained when the finite element length is set to $L_{FE}^{max} = 1.25 \times 10^{-4}$ m. The analysis type "Eigenfrequency" is selected as the solve mode and the direct (PARADISO) solver is chosen as the linear system solver. For a given wavenumber k_x^i, a group of corresponding eigenfrequencies and eigenmodes are obtained with the FEM algorithm.

In the case of the phononic plate, dispersion properties are $2\pi/a$ periodic with respect to the wavenumber k_x, i.e. $\omega(k_x) = \omega(k_x + 2\pi/a)$. This property allows to limit the wavenumber values to the first Brillouin zone [94], commonly defined in the wavenumber range $[-\pi/a, \pi/a]$. Therefore, the dispersion diagrams are drawn in the half Brillouin zone, i.e. in the $[0, \pi/a] = [\Gamma, X]$ wavenumber range, as it contains all the relevant information for the phononic plate [100]. Running k_x^i along the boundaries of the first Brillouin zone and repeating the calculation, dispersion curves for the Lamb wave modes are obtained [73, 80]. The overall Comsol flowchart is provided in Fig. 6.2.

Fig. 6.3 reports dispersion curves for both ordinary and phononic aluminium plate in the $[0, 1]$ reduced wavenumber $k^* = k \cdot a/\pi$ range. Comsol procedure reliability to extract dispersion maps is tested via SAFE comparison in the case of ordinary waveguide and by means of literature available results comparison in the case of phononic waveguide. It is worth noticing that dispersion curves in the case of phononic waveguide are distorted if compared to the ordinary ones, as clearly showed in Figs. 6.4. Such distortion allows the band gap nucleation, highlighted in Fig. 6.3 as a light grey rectangle. In this frequency range, wave propagation is theoretically inhibited.

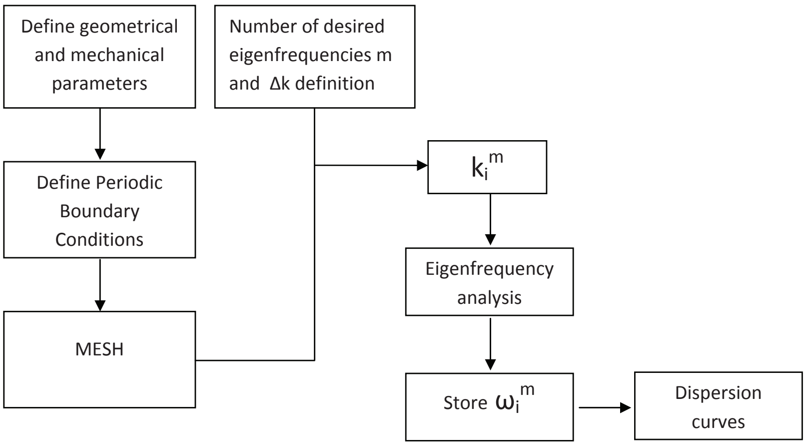

Figure 6.2: Comsol script flowchart.

6.2.2 Effect of phononic region length

In this subsection, filtering properties of the phononic region length towards Lamb waves propagation is investigated. To this end, several FE models with an increasing number of phononic cells have been analysed to evaluate the effect of the phononic region length on the energy transmitted beyond the phononic region. A schematic representation of the considered waveguide consisting of a central finite phononic portion confined by two homogeneous regions is presented in Fig. 6.5. Materials employed in the analyses are tungsten and vacuum, respectively (see Tab. 6.1). Unitary cell repeating in the waveguide phononic portion is the same reported in Fig. 6.1f.

First, the band structure is extracted and reported in Fig. 6.6. Results present good agreement with those published by Chen et al. [90]. Besides, it is worth noticing that the higher rigidity and density of tungsten w.r.t. aluminium enlarged and shifted towards lower frequencies the complete band gap.

After BG frequency range has been located, a wave packet is launched in the whole system along the x-direction at the first homogeneous edge (red arrows in Fig. 6.5). Perfectly Matched Layers (PMLs) are implemented on the right side of the calculation domain [101] to avoid undesired wave reflections. The

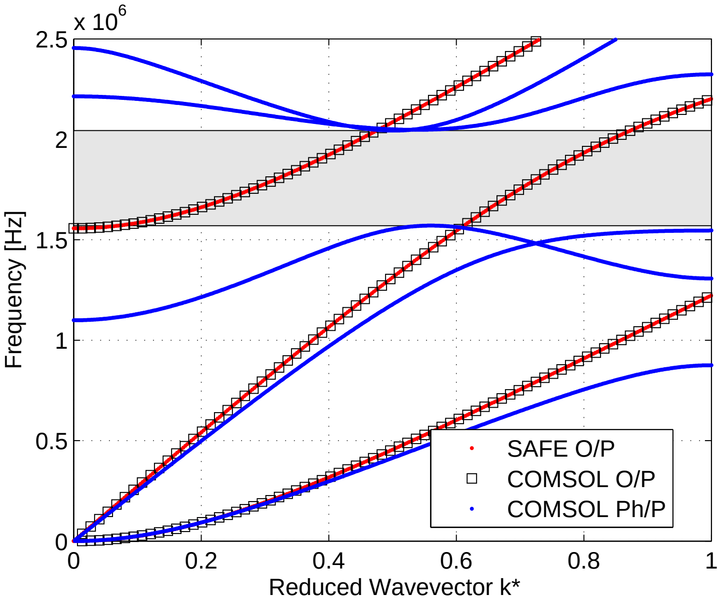

Figure 6.3: Dispersion curves for both ordinary and phononic waveguides. Band diagram is plotted in the $k^* \in [0, 1]$ reduced wavenumber range, corresponding to the symmetry direction $\Gamma - X$ of the first Brillouin zone. Ordinary plate band diagram is extracted both via Comsol and via SAFE. Perfect agreement is found. Dispersion curves for the phononic plate (extracted via Comsol) are also provided. The light grey rectangle emphasizes the position of the band gap.

excitation signal consists of a 13-cycles Hanning modulated sinusoidal toneburst with a central frequency $f_c = 1.55$ MHz and amplitude $A = 1 \cdot 10^{-9}$ m, as shown in Fig. 6.7. The high number of cycles was chosen to generate a low dispersive signal.

Time transient analyses have been conducted by means of the commercial FE package ABAQUS 6.12 [52] and a transmission power spectrum coefficient α_T has been defined to indicate how much energy propagates across the phononic region as a function of frequency. In particular, α_T is here defined as:

$$\alpha_T = \frac{\mathcal{F}\left[u_x^P(t)\right]}{\mathcal{F}\left[\bar{u}_x^P(t)\right]} \tag{6.7}$$

where $u_x^P(t)$ is the displacement along the x-axis acquired at the point P at

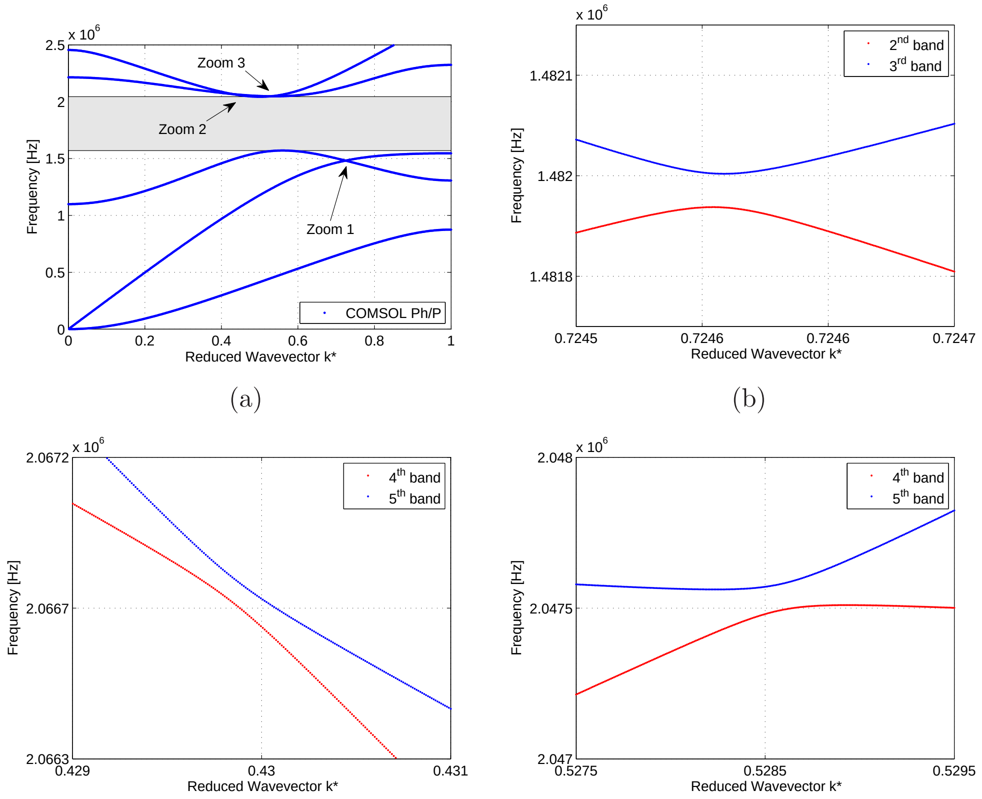

(a) (b)

(c) (d)

Figure 6.4: (a) Dispersion curves in the case of phononic waveguide are distorted if compared to the ordinary aluminium plate. Detailed behaviours of: (b) 2^{nd} and 3^{rd} bands between $k^* = 0.7245$ and $k^* = 0.7247$; (c) 4^{th} and 5^{th} bands between $k^* = 0.429$ and $k^* = 0.431$; (d) 4^{th} and 5^{th} bands between $k^* = 0.5275$ and $k^* = 0.5295$.

$d = 0.6 \cdot L_1$ from the right edge of the plate (see Fig. 6.5), $\bar{u}_x^P(t)$ is the same quantity acquired in the ordinary plate (i.e. with no phononic region) and $\mathcal{F}$ denotes the Fourier Transform operator.

The influence of the number of cells on the wave propagation phenomenon is shown in Figs. 6.8 and 6.9. They present stress fields for the ordinary structure and when additional phononic unit cells are added.

In general, it can be seen that, due to the huge mismatch between the acoustic impedance of the material constituting the PM, the vacuum square cylinders act as very efficient scatterers, so that the acoustic energy after only few cells of

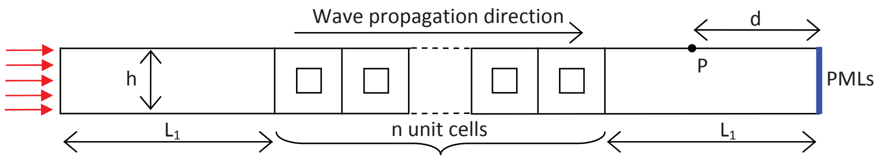

Figure 6.5: Schematic representation of the FE model exploited to evaluate the influence of the phononic region length on the transmission coefficient.

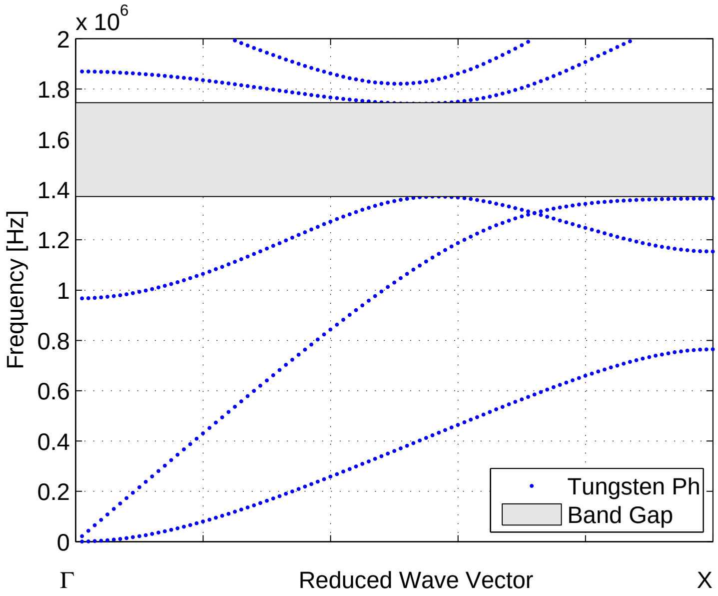

Figure 6.6: Dispersion curves for the symmetry direction $\Gamma - X$ of the first Brillouin zone for the Tungsten-vacuum phononic waveguide.

phononic material does not propagate further in the structure. Figs. 6.10 and 6.11 clearly show this fact in terms of transmission coefficient. In particular, it can be inferred that as the number of periodic cells constituting the phononic region n increases, the transmitted energy decreases (widths of the peaks attenuate). In the case of $n = 4$ almost a complete reduction of the transmitted wave can be observed. Finally, it can be observed that the transitions between the BGs and the transmitting frequency ranges is made sharper by adding more unit cells. This is an interesting property for filtering applications, where it is important to obtain square sharp spectrum [102].

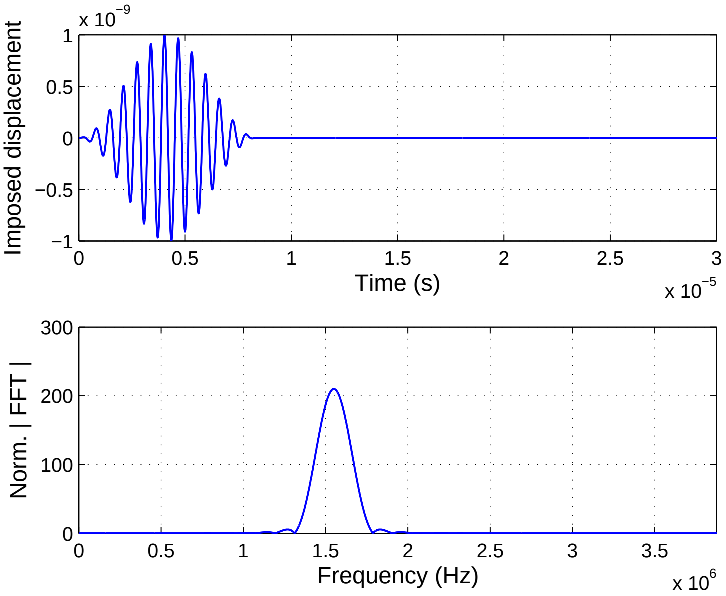

Figure 6.7: Time and frequency representation of the excitation signal.

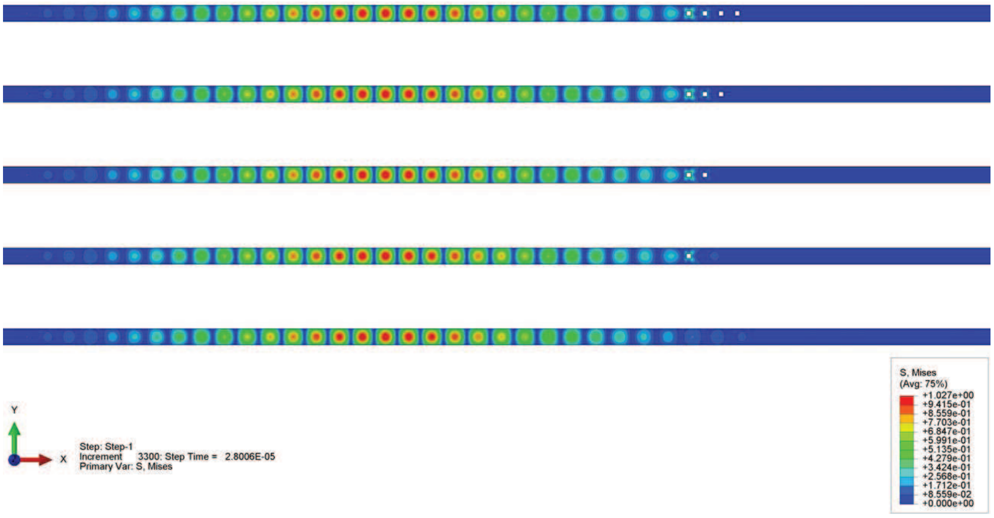

Figure 6.8: Von Mises stress field (snapshots at 28 μs) for the waveguide presented in Fig. 6.5 consisting of a central portion containing the finite PC sandwiched between two homogeneous regions. From the bottom to the top the number of unit cells is increased from 0 to 4.

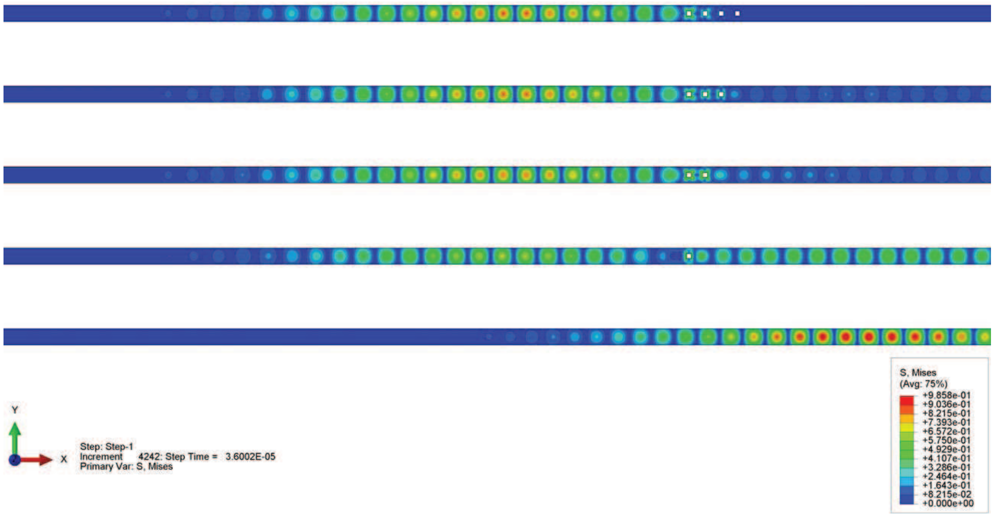

Figure 6.9: Von Mises stress field (snapshots at 36 μs) for the waveguide presented in Fig. 6.5 consisting of a central portion containing the finite PC sandwiched between two homogeneous regions. From the bottom to the top the number of unit cells is increased from 0 to 4.

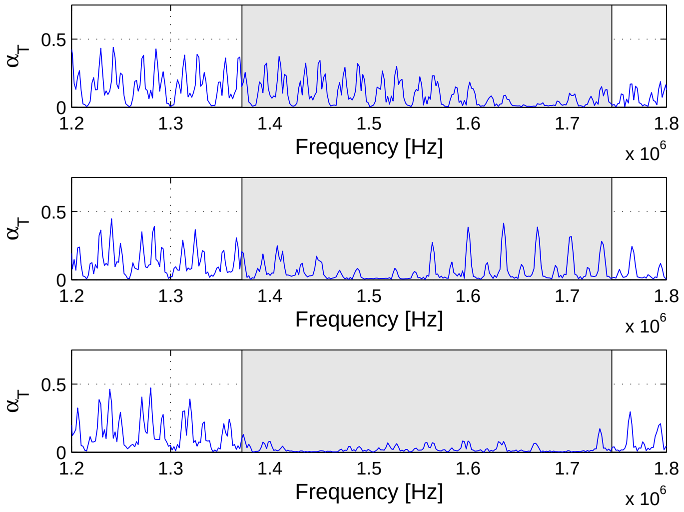

Figure 6.10: Influence of the number of periodic cells on the transmission coefficient α_T. The grey regions delimit the full band gap for the infinite PC. From the top: $n \in [1, 3]$-periodic-long phononic plate.

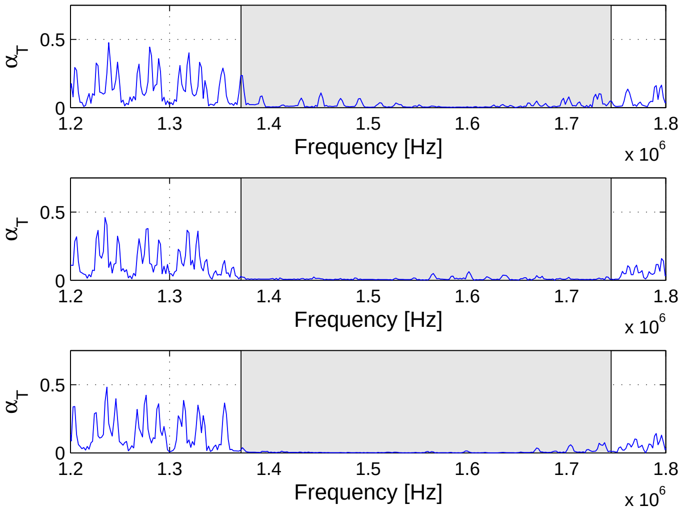

Figure 6.11: Influence of the number of periodic cells on transmission coefficient α_T. The grey regions delimit the full band gap for the infinite PC. From the top: $n \in [4, 7]$-periodic-long phononic plate.

6.2.3 Effect of an applied prestrain/prestress field

The potential of PMs-based applications can be extended by means of methods capable of modifying/controlling (nucleation, shifting and/or annihilation) the band gaps. To such objective, different approaches have been proposed over the years to manipulate BGs [103]. Some researchers have focused on the effect of constitutive parameters, for instance by changing filling fraction and shape of the inclusions [73, 87] or varying the elastic characteristics of the constitutive materials [104, 105, 106]. Different authors proposed the use of electrorheological materials in conjunction with the application of external electric field [107]. Other researchers have considered the effect of temperature [108]. A further way to tune BGs is to superpose to the periodic material an initial field of strain/stress [8, 103, 109]. This approach has a great potential since prestress/prestrain[1] can be easily applied to structures.

In this subsection, the effect of an applied prestrain field on the BGs of Lamb

---

[1] In what follows, the word prestrain will be mainly used as the corresponding prestress can be immediately computed via Hooke's law.

waves propagating in phononic plates is investigated, extending a recent study by Chen et al.[90], in which the effect of the phononic waveguide thickness on the Lamb waves dispersion properties is studied. To account for an initial prestrain/prestress field on BGs of the phononic plate, first a representative unit cell, under 2D plane strain assumption, with boundary conditions imposed according to the Bloch's theorem, is considered. Next, static analyses under the effect of initial strain, including non-linear deformations, are performed. Finally, eigenfrequencies are computed taking into account the non-linear geometric effects by means of proper compatibility relations. Results in terms of dispersion curves obtained by COMSOL MultiPhysics 4.3 [99] show the effects of prestrain on the Lamb waves BG.

The dependence of guided wave velocity on applied prestrain is fundamentally a non-linear effect that can be modelled in COMSOL MultiPhysics by means of a two-step analysis exploiting the module *Prestressed Analysis, Eigenfrequency* [99].

The linearised equations governing the harmonic behaviour of a prestrained linear elastic material, in absence of body forces, read:

$$\begin{aligned}
&\boldsymbol{\varepsilon} = \frac{1}{2}\left[(\nabla\mathbf{u})^{\mathrm{T}} + \nabla\mathbf{u} + (\nabla\mathbf{u})^{\mathrm{T}}\nabla\mathbf{u}\right] \\
&\mathbf{S} - \mathbf{S}_0 = \mathbf{C}\left(\boldsymbol{\varepsilon} - \boldsymbol{\varepsilon}_0\right) \\
&\nabla\cdot\boldsymbol{\sigma} + \rho\omega^2\mathbf{u} = \mathbf{0}
\end{aligned} \tag{6.8}$$

where $\mathbf{u}(\mathbf{r}, t)$ is the time-dependent displacement vector, $\mathbf{r}$ is the position vector, $\boldsymbol{\varepsilon}$ is the Green-Lagrange strain vector, $\boldsymbol{\varepsilon}_0$ is the applied initial strain, $\mathbf{C}$ is the constitutive matrix, $\mathbf{S}$ and $\mathbf{S}_0$ are the actual and initial second Piola-Kirchhoff stress tensors, ρ is the material density and ω is the angular frequency. Considering small displacements the actual second Piola-Kirchhoff stress tensor coalesces with the Cauchy stress tensor $\boldsymbol{\sigma}$.

Material density $\rho\,(\mathbf{r})$ and elastic moduli $\mathbf{C}\,(\mathbf{r})$ expanded in Fourier series as well as the displacement vector for a periodic structure as described in section 6.2.1 drive to the statement of the global governing equations.

Substituting Eqs. (6.2) into the third of Eq. (6.8) and applying proper periodic boundary conditions, a FEM based discretization leads to the global governing equation in the form $[\mathbf{K}(\mathbf{k}) - \omega^2\mathbf{M}]\mathbf{U} = \mathbf{0}$, where $\mathbf{K}$ is the structural stiffness matrix, $\mathbf{M}$ is the structural mass matrix and $\mathbf{U}$ is the generalized vector of nodal displacements [97]. Then, as in the standard case of waveguide without prestrain/prestress applied field, for a given wavenumber $\mathbf{k}_i$ in input, eigensolutions of the global governing equation lead to the dispersion properties of the formulated problem.

6.2.3.1 Lamb waves in ordinary plates under prestrain

In order to validate the approach in COMSOL, the effect of prestrain on Lamb waves existing in a 1-mm thick aluminium plate (see Tab. 6.1 for material properties) is computed and compared with literature results [110]. To this purpose, a single elementary cell of dimensions $a \times a$ ($a = 1$ mm), in plane strain condition (x-y plane), is generated, (see Fig. 6.1e). Next, periodic boundary conditions (PBCs) are imposed on the edges orthogonal to the x-axis. Free boundary conditions (FBCs) are considered on the remaining two edges of the cell.

The unit cell is meshed by means of 4-node quadrilateral Lagrange linear elements of maximum edge size 0.05 mm in order to provide accurate results up to the maximum frequency of interest of 1 MHz. Then, the resulting eigenvalue problem is solved using the PARADISO algorithm [99] for $k_x \in [0, 700]$ m^{-1}.

As in Ref. [110] levels of prestrain ε_0^x corresponding to 0.04%, 0.08% have been considered. In addition, here also the effect of negative (compressional) axial strain has been investigated for ε_0^x equal to -0.04% and -0.08%.

In Fig. 6.12 the A_0 mode phase velocity, normalized w.r.t. the shear bulk wave speed in aluminium, is represented for the different levels of applied prestrain. Results for positive prestrain are in perfect agreement with those of Ref. [110] confirming the reliability of the COMSOL procedure. It can be observed that at low frequencies positive strain, and so tensile stress along the x-axis, tends to increase the natural frequencies, while negative strain, and so compressive stress, tends to decrease them. On the other hand, at relatively high frequencies the effect of load induced by the strain begins to be negligible. At these frequencies the properties of guided wave propagation are governed almost entirely by the

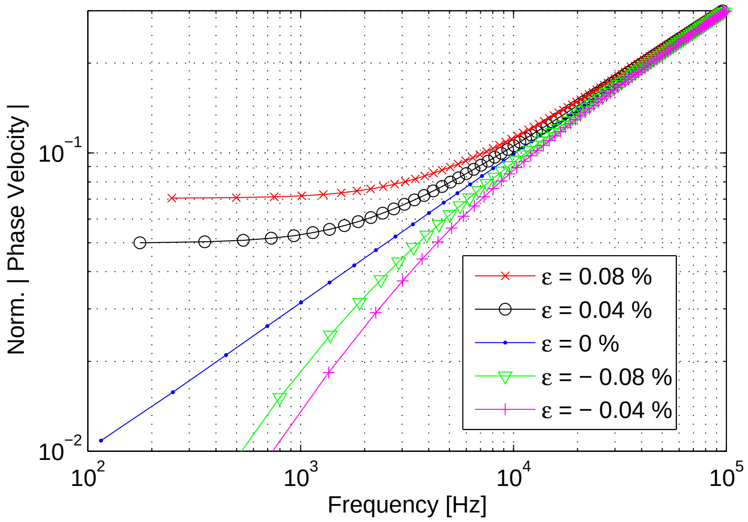

Figure 6.12: FE results showing the effect of prestrain on A_0 mode phase velocity in a 1-mm thick aluminium plate. Phase velocity is normalized w.r.t. to the bulk transverse shear wave speed in aluminium. Tensile strains tend to increase the natural frequencies, while compressive strains tend to decrease them.

material stiffness of the waveguide.

6.2.3.2 Lamb waves in phononic plates under prestrain

Here a 1-mm thick aluminium phononic plate (see Tab. 6.1) is considered. The unitary cell is characterized by a square shaped-hole inclusion (vacuum) located in its centre as shown in Fig. 6.1. In particular, the cell has outer dimensions $a \times a$ ($a = 1$ mm) whereas the square inclusion is $m \times m$ ($m = 0.3$ mm), so that the filling fraction is $f = (m^2)/(a^2) = 0.09$. The unit cell is assumed to be in plane strain condition.

Fig. 6.13 shows the dispersion map in terms of reduced wavenumber $k^* = (k_x a)/\pi$ versus frequency $f = \omega/(2\pi)$ in the $[0 - 2.5]$ MHz frequency range, where 5 modes are visible. Numerical convergence for the maximum frequency of 2.5 MHz was obtained using finite elements of maximum edge length of 0.025 mm. A total band gap between the third and fourth modes and its shifting due to different levels of prestrain can be observed. Comparing the band structures it is possible to note that some bands are lightly affected by the external load while others

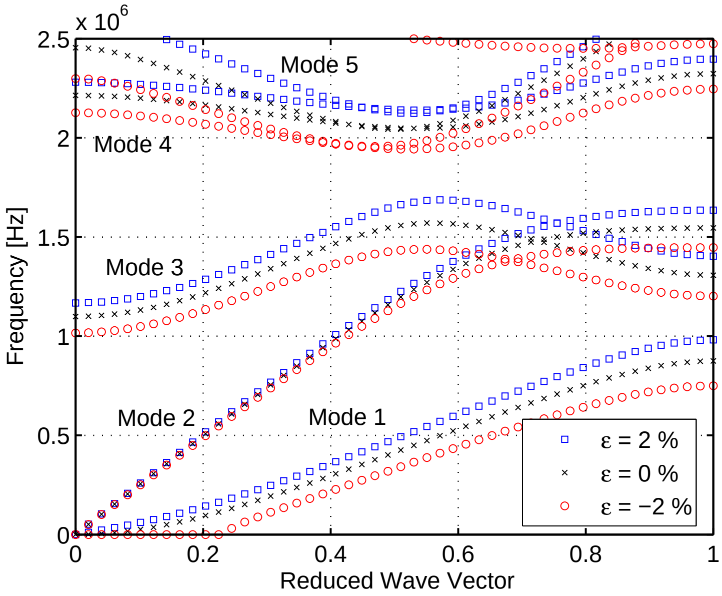

Figure 6.13: Phononic plate dispersion diagram for different levels of applied prestrain. The main effect of the prestrain field is to shift towards higher/lower frequencies dispersion curves.

are more significantly shifted toward higher/lower frequencies. In particular, Fig. 6.14 shows the effects of prestrain on the 1^{st} mode for the considered phononic plate.

6.3 2P-2D phononic materials

Theoretical and experimental works concerning elastic BGs in bi-dimensional structures have been done because of the high technological interest related to them. The most famous experimental attempt to find such a band gap in the audible range was the measurement of sound attenuation by an artistic sculpture (obviously not specially designed for this purpose) which, however, failed to find a full band gap [111].

In this section elastic band structure for 2P-2D phononic materials are presented. Dispersion curves for combinations of different material types (solid/solid, solid/fluid) are calculated, emphasizing the existence of complete band gaps.

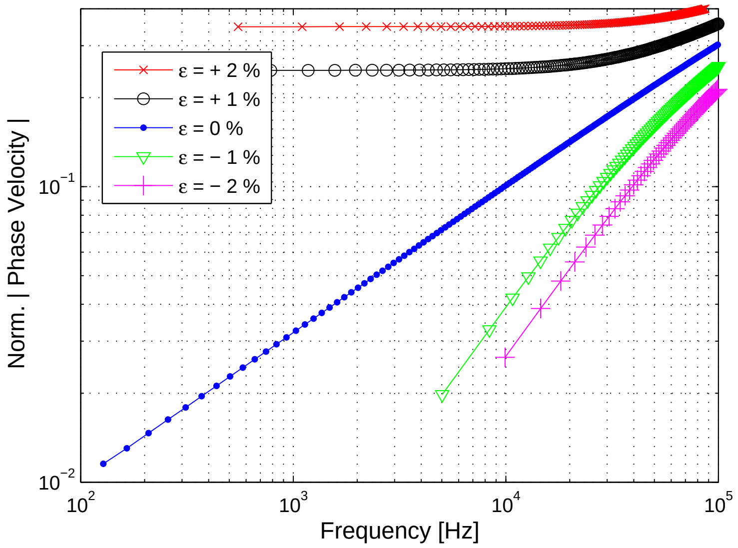

Figure 6.14: Prestrain effects on the 1^{st} mode for the considered phononic plate.

6.3.1 Solid-solid PM

The first investigated model is a square lattice phononic material consisting of steel cylinders embedded in an epoxy matrix. The steel scatterers are denoted by the shaded regions in Fig. 6.15a. The PM lattice constant is $a = 0.008$ m and $R = 0.003$ m is the radius of the cylinder scatterer. The filling fraction for the PM is $f = \pi R^2/a^2 = 0.4418$.

The choice of these materials is based on the mismatch of their densities and elastic constants, $\rho_{steel} = 7850$ kg/m^3, $E_{steel} = 210 \cdot 10^9$ Pa and $\nu_{steel} = 0.3$ for steel, and $\rho^{epoxy} = 1180$ kg/m^3, $E_{Epoxy} = 4.44 \cdot 10^9$ Pa and $\nu_{epoxy} = 0.399$ for epoxy (see Tab. 6.1). To calculate the eigenmodes of acoustic waves in the PM-plate, the unit cell is defined and marked in solid black lines in Fig. 6.15a.

The first irreducible Brillouin zone of the model is also plotted in Fig. 6.15b. Since the Bravais lattice is square-shaped and the materials are isotropic, the representation of the bands along the $M - \Gamma - X - M$ closed path in the first irreducible Brillouin zone contains all relevant information.

Plane strain condition is assumed in order to study the wave propagation confined within the $x - y$ plane (the structure is considered to extend infinitely along the z direction).

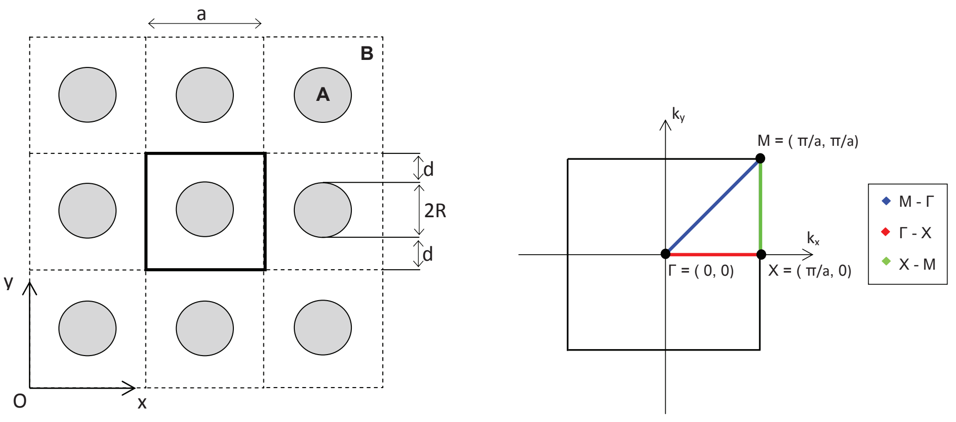

(a) (b)

Figure 6.15: (a) Schematics of the epoxy/steel phononic plate with square lattice constant $a = 0.008$ m and filling fraction $f = 0.4418$. (b) The first irreducible Brillouin zone $M - \Gamma - X$.

Fig. 6.16 presents the band structure for the PM in the three high symmetry directions $M-\Gamma-X$ of the first irreducible 2D Brillouin zone. The horizontal axis is the reduced wavenumber $k^* = ka/\pi$ and the vertical axis reports the frequency values in Hz. Curves are not flat but dispersive and therefore propagating modes are available for most frequencies. However, the existence of a relatively flat band in the band structure is also noticeable ($240 - 250$ kHz range). Flat bands are usually associated with the existence of localized states in the composite material, characterized by very small group velocity [72, 92].

The plot shows unambiguously the existence of 4 complete band gaps in the $0 - 350$ kHz frequency range, i.e. frequency ranges within the propagation of acoustic or elastic waves is inhibited regardless the direction of waves propagation. The largest observed complete band gap appears between 89 kHz and 198 kHz and the other three extend from 229 to 239 kHz, 246 to 250 kHz and 293 to 297 kHz, respectively. On the other hand, when considering waves propagating in a specific direction of the irreducible 2D Brillouin zone ($M - \Gamma$, $\Gamma - X$ or $X - M$), some stop bands (or partial band gaps) may be observed, such as the one occurring from 0 to 42 kHz in the $X - M$ direction, for instance. Other local stop bands appear at higher frequencies in the three directions of propagation (see Table 6.2 and Fig. 6.17 for further details).

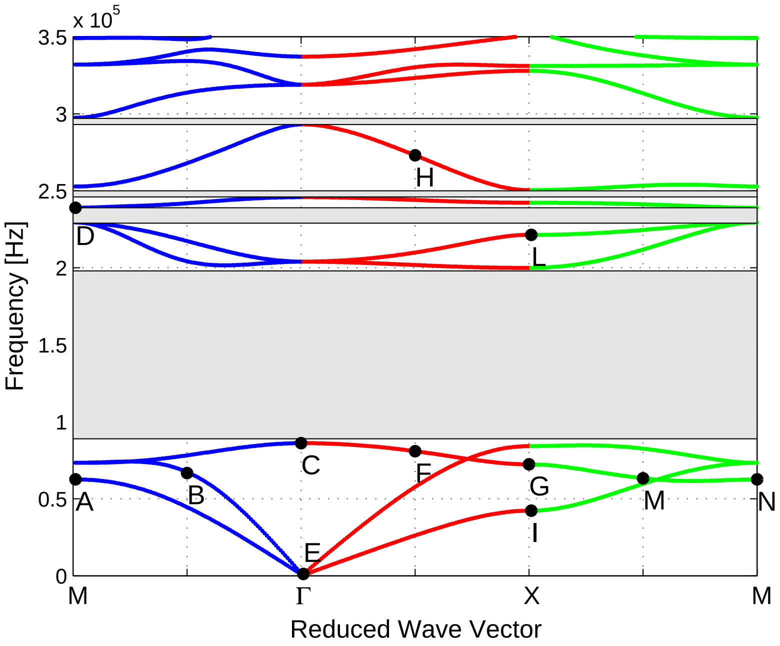

Figure 6.16: Band structure of the steel/epoxy PC with square lattice. Only complete band gaps are highlighted by means of light grey rectangles. Note the existence of a low-dispersive single pass band separating the second and third complete band gaps. Letters denote normal modes associated to particular reduced wavevector and frequency values.

Figs. 6.18 - 6.20 depict the eigenmodes in terms of displacement in the three symmetry directions $M-\Gamma$, $\Gamma-X$ and $X-M$ for particular frequency and reduced wavenumbers values. Modes are clearly coupled and their classification resemble the one used in Lamb waves in the classical plates [93] (flexural antisymmetric, longitudinal symmetric, and transverse shear horizontal waves).

Each mode is uniquely identifiable by means of its wavenumber coordinates and frequency, as shown in Fig. 6.16. For example the first eigenmode (point A of Fig. 6.16) has reduced wave vector $\mathbf{k}^* = (k_x^* = 1, k_y^* = 1)$ and frequency $f = 62.59$ kHz. Besides, Figs. 6.18 - 6.20 show different modes at different frequencies. They all belong to the first band, except modes D, H and L, which belong to the third, forth and second band, respectively.

Table 6.2: Frequency values of the stop bands occurring in specific directions of propagation.

Stop Band	Direction of propagation and frequency range [kHz]		
	$M-\Gamma$	$\Gamma-X$	$X-M$
# 1			0 - 42
# 2	250 - 252		
# 3		221 - 229	
# 4			252 - 293
# 5		297 - 318	
# 6		332 - 337	
# 7			327 - 331
# 8	341 - 348		

6.3.1.1 Transmission spectra

Here, the transmission spectrum of waves crossing the two-dimensional solid-solid PM composed of circular and centred arrays of steel inclusions in an epoxy resin matrix is investigated via FE simulations.

The analyses reproduce a transmission experiment which employs a couple of ultrasonic piezoelectric transducers used as transmitter/receiver transducers. With reference to Fig. 6.21, point A simulates a PZT used as actuator launching the probing waves. B denotes the acquisition point. To launch a broadband wave packet capable to test the complete BGs (therefore involving wavevectors with different combinations of k_x and k_y) as well as examining a wide range of frequencies, a short time pulse (see Fig. 6.22a) was applied at point A. Displacement along the x axis is then recorded at point B. Afterwards, processing the data by means of a Fourier transform, the corresponding transmission power spectrum[1] is obtained and plotted in Fig. 6.22b.

The phononic band structure for an infinite PM are then compared with the transmission power spectrum (TPS) measured numerically in a 10-period-long finite size composite sample in Fig. 6.21.

Measured transmission drops to low levels throughout the frequency intervals in reasonable agreement with the frequency stop bands calculated for the infinite

---

[1] In this case, the transmission power spectrum has not been normalized w.r.t. the wave propagating in the corresponding ordinary plate.

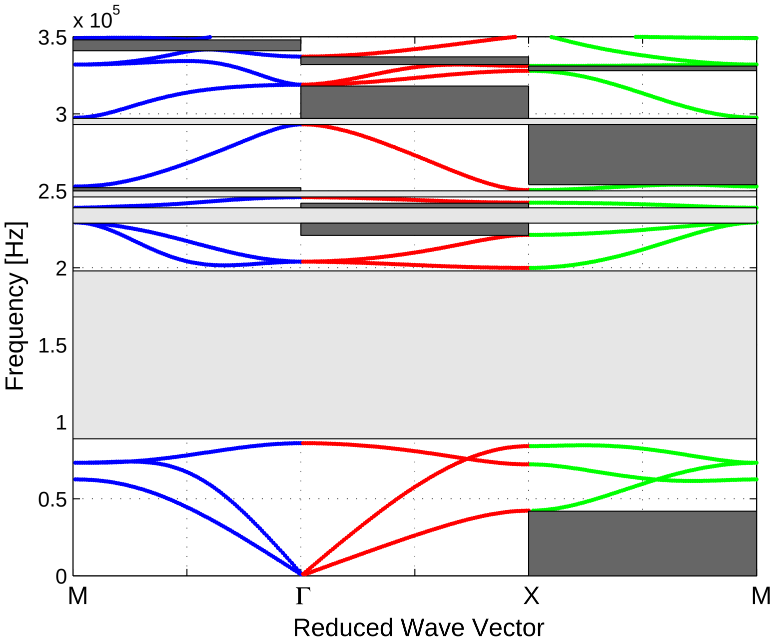

(a)

Figure 6.17: Band structure of the steel/epoxy PM with square lattice. Complete band gaps (light grey) and stop bands (dark grey) are highlighted.

PM (Fig. 6.22b).

6.3.2 Solid-fluid PM

Since first works showed phononic band gaps in elastic composite materials [112, 113], there have been efforts to search wider, lower-frequency and large numbers of band gaps by varying the constituent materials and their configuration arrangement. In recent years a growing interest focused on the propagation of acoustic waves in a particular class of periodic composites, the so called sonic/acoustic crystals, i.e. acoustic metamaterials operating in the audible frequency range (approximately from 20 Hz to 20 kHz).

As in the case of elastic metamaterials the primary phenomena responsible for the band structures of sonic/acoustic crystals are Bragg scattering and local resonance. Because of their large acoustic mismatch or low acoustic impedance, sonic metamaterials (solid/liquid, solid/air or liquid/liquid PMs) proved to achieve

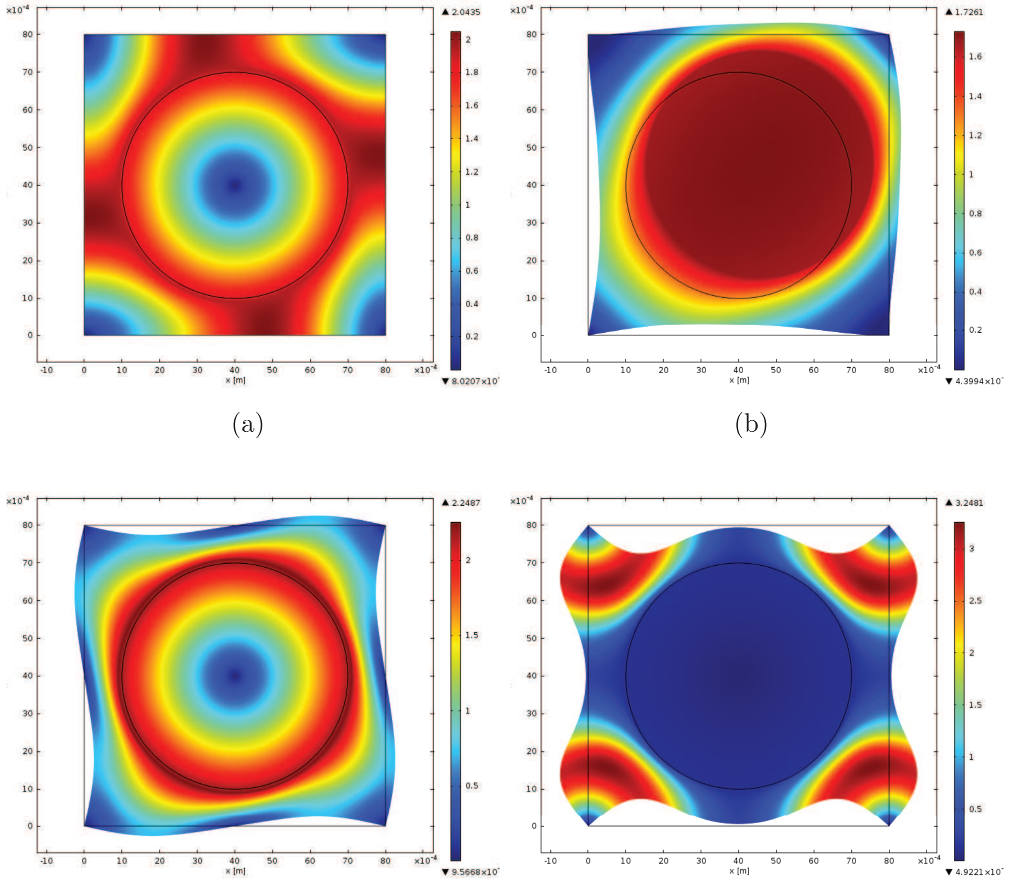

(a) (b)

(c) (d)

Figure 6.18: Displacement fields (magnitude) of eigenmodes in the $M-\Gamma$ direction of propagation. (a) $\mathbf{k}=(3.92, 3.92)$ m^{-1}, $f=62.59$ kHz corresponding to the point A of Fig. 6.16; (b) $\mathbf{k}=(196.35, 196.35)$ m^{-1}, $f=66.71$ kHz corresponding to the point B of Fig. 6.16; (c) $\mathbf{k}=(392.69, 392.69)$ m^{-1}, $f=86.15$ kHz corresponding to the point C of Fig. 6.16; (d) $\mathbf{k}=(3.92, 3.92)$ m^{-1}, $f=239.00$ kHz corresponding to the point D of Fig. 6.16.

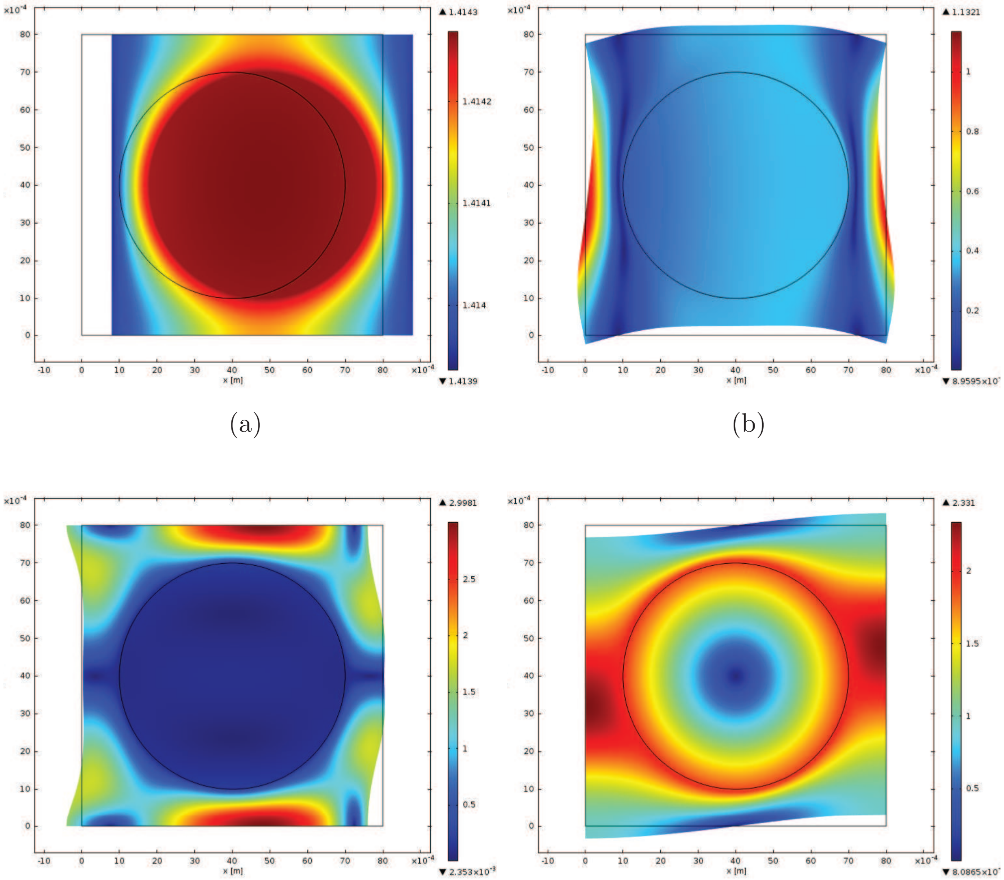

(a) (b)

(c) (d)

Figure 6.19: Displacement fields (magnitude) of eigenmodes in the $\Gamma - X$ direction of propagation. (a) $\mathbf{k} = (3.92, 0)$ m^{-1}, $f = 1.24$ kHz corresponding to the point E of Fig. 6.16; (b) $\mathbf{k} = (196.35, 0)$ m^{-1}, $f = 80.94$ kHz corresponding to the point F of Fig. 6.16; (c) $\mathbf{k} = (392.69, 0)$ m^{-1}, $f = 72.38$ kHz corresponding to the point G of Fig. 6.16; (d) $\mathbf{k} = (196.35, 0)$ m^{-1}, $f = 273.07$ kHz corresponding to the point H of Fig. 6.16.

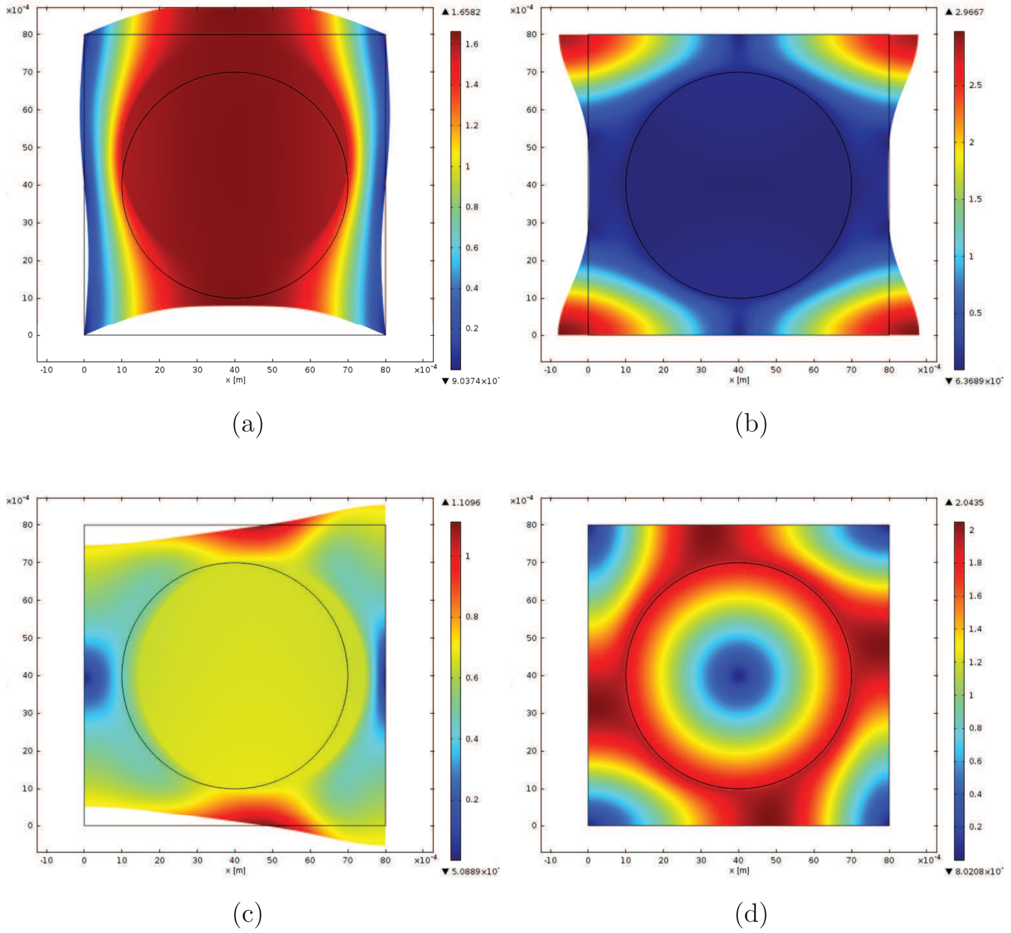

(a) (b)

(c) (d)

Figure 6.20: Displacement fields (magnitude) of eigenmodes in the $X - M$ direction of propagation. (a) $\mathbf{k} = (0, 3.92)$ m^{-1}, $f = 42.27$ kHz corresponding to the point I of Fig. 6.16; (b) $\mathbf{k} = (0, 3.92)$ m^{-1}, $f = 221.39$ kHz corresponding to the point L of Fig. 6.16; (c) $\mathbf{k} = (0,)$ m^{-1}, $f = 72.38$ kHz corresponding to the point G of Fig. 6.16; (d) $\mathbf{k} = (196.35, 0)$ m^{-1}, $f = 273.07$ kHz corresponding to the point H of Fig. 6.16.

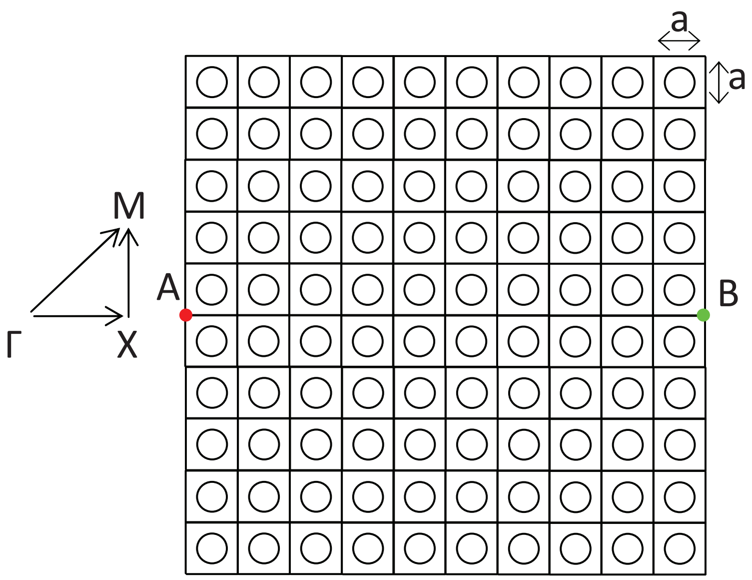

Figure 6.21: FE model exploited for the transmission spectra evaluation. Red and green dots denote excitation and acquisition points, respectively.

larger and/or lower-frequency band gap, if compared to elastic metamaterials. This led to a growing interest in exploiting potentials of sonic crystals as acoustic filters and noise/sound insulators [91].

Recently, studies concerning phononic materials (also known as sonic crystals) used as noise barriers reported sound attenuation up to 25 dB [114, 115]. In particular, the main advantages of employing sonic crystals as sound barriers instead of a traditional solid sound barriers regard (i) the ability to attain peaks of attenuation in a selected frequency range by varying the distance between the scatterers, (ii) the possibility to allow light to pass through and (iii) to have no obstruction to the free flow of air [116].

The relationship between the lattice parameter and operating frequency suggests the required barrier dimensions in order to attenuate the target frequency noise. Locally resonant sonic materials (LRSM) are also well suited to this purpose due to their ability to form band gaps decoupled from the lattice periodicity. However, these BGs are generally characterized by smaller attenuation ranges.

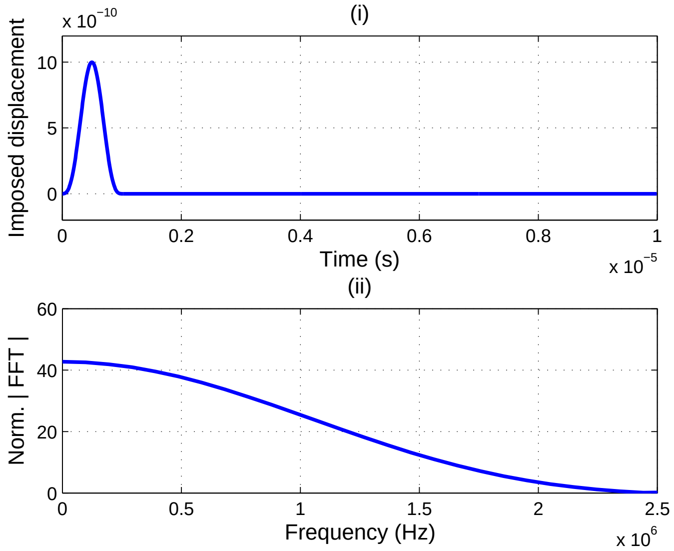

(a)

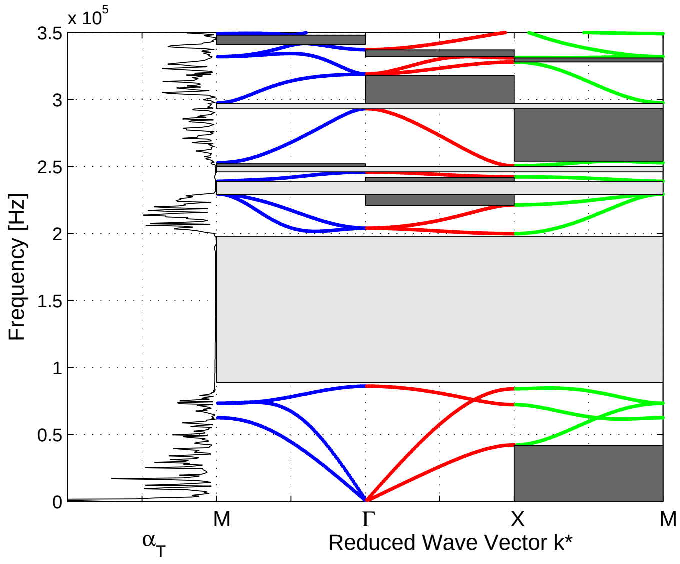

(b)

Figure 6.22: (a) Time and frequency representation of the imposed displacement used to excite modes up to 400 kHz in the PM. (b) PC band structure together with normalized transmission power spectrum (TPS) measured after 10 periodic cells at A (see fig. 6.21). TPS clearly shows a almost complete attenuation in the complete band gap zones.

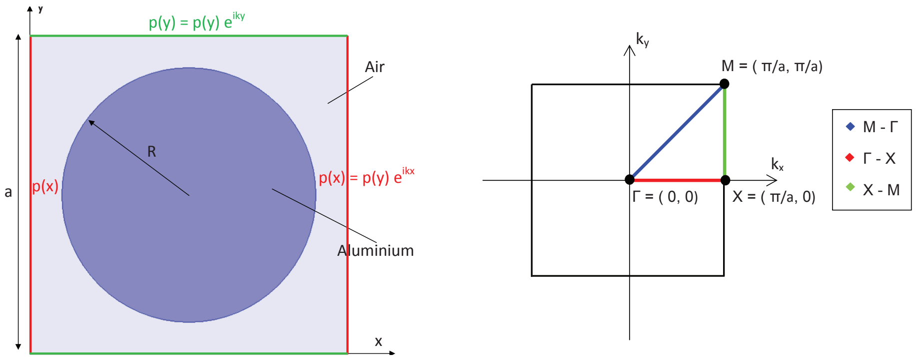

(a) (b)

Figure 6.23: Single unit cell for the considered sonic crystal system. Periodic boundary conditions are applied to the borders of the unit cell in terms of pressure distribution.

6.3.2.1 Band structures in sonic metamaterials

First, an array of infinitely long aluminium cylinders in air [91] is studied[1].

The cylinders are arranged in a two-dimensional square periodic array. The unit cell used as a basis for the calculations is shown in Fig. 6.23a where the light blue indicates the fluid domain (air) and dark blue the solid domain (aluminium). The structure is assumed to be infinite in the out of plane direction and periodic in the x- and y-directions with constant lattice $a = 20$ mm and cylinders radius $R = 8$ mm.

In this case, proper periodic boundary conditions concern pressure distribution p for the nodes lying on the boundary of the unit cell. The aforementioned periodic boundary conditions ensure that the finite simulation space mimics an infinitely periodic crystal both in the x and y directions. As in the case of elastic metamaterials, Bloch wavevector is defined along the edges of the first Brillouin zone (see Fig. 6.23b), i.e.:

i. ΓX path: k_x varies from 0 to π/a, whilst k_y is set equal to 0;

ii. XM path: k_y varies from 0 to π/a, whilst k_x is set equal to π/a;

---

[1] The same methods revised in previous chapters (plane wave expansion method, finite-difference time-domain method, finite element method) can be employed to calculate wave propagation in such materials.

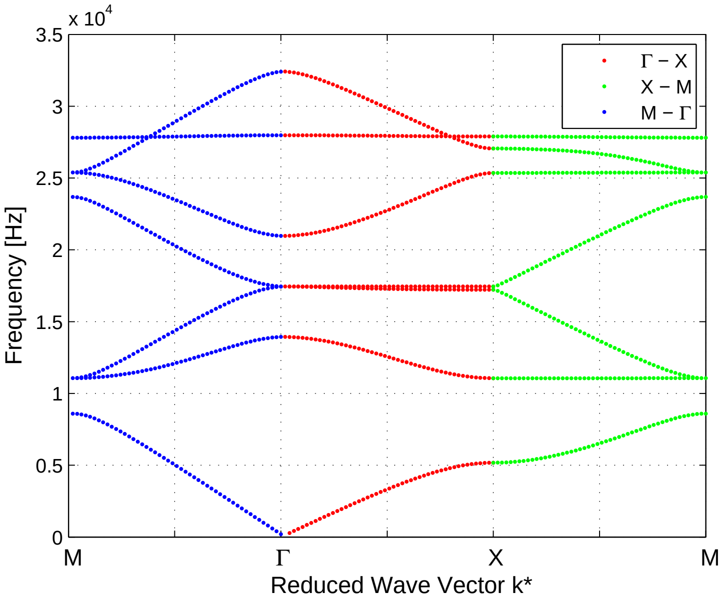

Figure 6.24: Band structures of the acoustic phononic crystal made of aluminium cylinders immersed in air.

iii. $M\Gamma$ path: both k_x and k_y vary from 0 to π/a.

Fig. 6.24 shows the band structure for the described system. Good agreement is found with literature available results [91]. It's worth noticing that outside the complete band gap, which is centred approximately at 10 kHz, waves for most frequencies can propagate. Some waves coalesce at the high symmetry point M outside the BG boundaries, as it occurs between 2^{nd} and 3^{rd} or 5^{th} and 6^{th} curves. However they do not bring to any other total band gap nucleation.

6.3.2.2 Sound barriers

It is possible to exploit acoustic metamaterials for the design of lightweight noise barrier operating at low frequency range as an alternative solution to stiffness-based or dissipation-based solutions (which generally require high areal masses). The idea consists in creating sonic band gaps in order to limit acoustic wave propagation at certain frequencies (for example, create a BG with a central frequency at around 1 kHz, i.e. the main frequency range of the vehicle traffic noise).

Exploiting the BG deriving from the Bragg scattering theory, the target frequency to inhibit sets the scale of spatial periodicity of the phononic structure which needs to be in the order of the target wavelength[1].

In what follows, finite element (FE) models are developed to study mechanical and geometrical properties of the acoustic metamaterials capable of inhibiting the propagation of sound waves in air at around 1 kHz.

To this purpose four metamaterials are considered:

i. a solid aluminium cylinder with radius $R = 80$ mm surrounded by air $a = 200$ mm (Fig. 6.25a);

ii. a hollow aluminium cylinder with outer radius $R = 80$ mm, thickness $t = 3.2$ mm, surrounded by air $a = 200$ mm (Fig. 6.25b);

iii. a hollow Polyvinyl chloride (PVC) cylinder with outer radius $R = 80$ mm, thickness $t = 3.2$ mm, surrounded by air $a = 200$ mm (Fig. 6.25c);

iv. a C-shaped PVC thin wall with external radius $R = 80$ mm and thickness $t = 3.2$ mm (Fig. 6.25d).

In force of the high acoustic mismatch between the solid materials (aluminium and PVC) and air, Neumann boundary conditions have been applied to the solid scatterer surfaces.

Dispersion curves for the above mentioned cases are presented in Fig. 6.26. Comparing Fig. 6.26a and Fig. 6.26b it clearly emerges that more propagating modes exist in the same frequency range $0 - 3000$ Hz for the case of hollow cylinders. However, despite the number of modes the total BG at around 1000 Hz is preserved. The hollow cylinder cases present also an additional band gap as well as the existence of some non-dispersive modes.

Changing the aluminium with PVC produces only a slight shifting towards higher frequencies of the band gaps ($[104 - 145]$ to $[145 - 202]$ for the first BG and $[863 - 1113]$ to $[867 - 1117]$ for the second one) as shown in Fig. 6.25b and Fig. 6.25c.

---

[1] Although this could limit this approach for shielding environmental noise where space is not limited, locally resonant sonic materials (LRSMs) can be used as a viable alternative for low frequency applications when the installation space is limited.

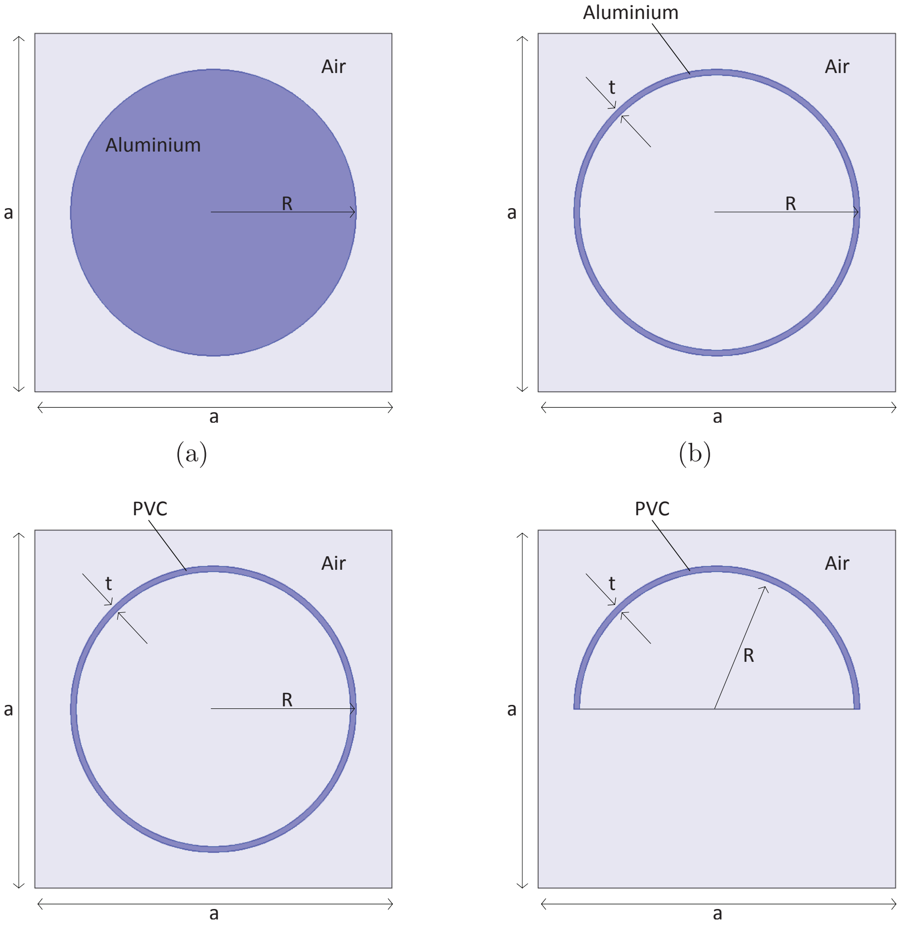

(a) (b) (c) (d)

Figure 6.25: Unit cell ($a = 200$ mm) for the analysed acoustic metamaterials: (a,b) air-aluminium interaction, (c,d) air-PVC interaction ($R = 80$ mm).

Finally, in the case iv (Fig. 6.25d), because of the C-shaped inclusion, dispersion curves appear less dispersive if compared to the other cases. This implies that modes associated with such flatter bands are supposed to have low group velocity and then to exhibit strong spatial localisation. Besides, it is worth noticing that nucleation of new complete BGs is observable.

6.3.2.3 FEM wave propagation analyses

In this section, sound pressure levels for phononic systems are calculated via finite element analyses. First, the existence of predicted directional BGs is highlighted

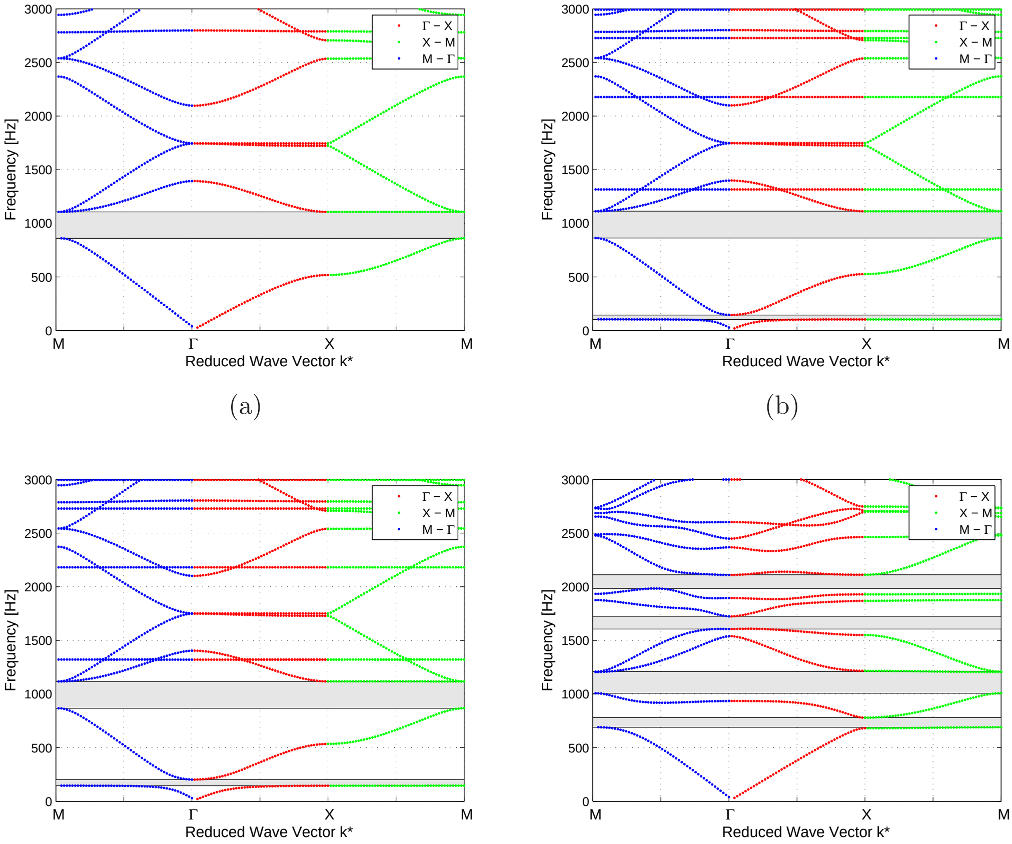

(a) (b)

(c) (d)

Figure 6.26: Band structures for (a,b) air-aluminium interaction, (c,d) air-PVC interaction.

in a 4-period-long phononic system. Afterwards, pressure maps at frequencies inside and outside the BG are shown to emphasizes the screening potentials of the phononic material in the audible frequency range. Finally, the influence of the phononic region length is investigated in order to predict the minimum number of cells needed to reduce the sound pressure level under a desired threshold.

The Comsol Multiphysics software has been adopted to solve the acoustic wave propagation equation in the phononic system:

$$\frac{1}{\rho_0 c^2}\frac{\partial^2 p}{\partial t^2} + \nabla \cdot \left(-\frac{1}{\rho_0} \nabla p \right) = 0 \tag{6.9}$$

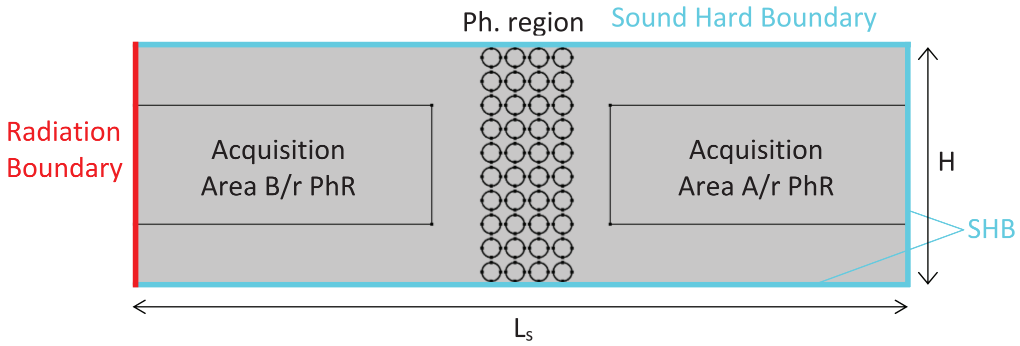

Figure 6.27: Finite element model implemented in Comsol Multiphysics to compute the pressure fields at different frequencies inside and outside BGs. The model consists of 3.2 mm thick hollow PVC cylinders immersed in air. A plane wave radiation boundary condition is set to the left side of the system. Sound hard boundaries (SHB) have been assigned to the PVC cylinders, as well as to the external domain boundaries.

with ρ_0 mass density, p pressure distribution and c speed of sound. This reduces to a Helmholtz equation for a time harmonic pressure wave excitation, $p = p_0 e^{\imath\omega t}$:

$$\nabla \cdot \left(-\frac{1}{\rho_0}\nabla p_0\right) - \frac{\omega^2 p_0}{\rho_0 c^2} = 0 \tag{6.10}$$

where $\omega = 2\pi f$ is the angular frequency. Eq. (6.10) resolution leads to the pressure field [116].

A 2D model in plane strain, $L_s = 6$ m, $H = 2$ m, with a central phononic region made of 4×10 PVC hollow cylinders ($R = 80$ mm and $t = 3.2$ mm) immersed in air, as shown in Fig. 6.27, is analysed. Material properties for PVC and air are presented in Tab. 6.1, and are here reported for sake of clarity: $\rho_{PVC} = 1400$ kg/m^3, $\nu_{PVC} = 0.42$ and $E_{PVC} = 3$ GPa and $\rho_{Air} = 1.25$ kg/m^3 and $c_{Air} = 343$ m/s[1].

In the simulations, a rising tone noise source at the left edge of the domain, from 1 to 3040 Hz, is modelled as a plane wave radiation boundary condition with pressure source set to 1 Pa. The remaining boundaries are modelled as

---

[1] The considerable mismatch between density and mechanical properties of PVC and air allows to apply sound-hard boundary conditions to the PVC cylinders.

sound hard boundaries (SHB) in order to capture the screening power of the only phononic system upon the wave.

Sound pressure levels are measured as the peak values registered within the $3L \times L$ acquisition areas located either before and after the phononic region (see Fig. 6.27). $L = 0.8$ m has been dimensioned to ensure that at least half wavelength develop at all the considered frequencies.

Numerical accuracy is guaranteed choosing a triangular mesh with maximum finite element dimension $L_{FE}^{max} = 10$ mm.

6.3.2.4 Transmission power spectrum and pressure maps in the audible frequency range

Solving the wave equation for a parametric frequency sweep from 1 to 3040 Hz, with a $\Delta f = 80$ kHz, allows to compute the transmission power spectrum for the phononic system (see Fig. 6.28). It can be noted that the first directional BG, extending from 144 to 202 Hz, shows noticeable sound attenuation potential. In addition, all BGs are in good agreement with those of the band structure calculations.

In addition, Fig. 6.29 illustrates pressure maps taken at 480, 800 and 1280 Hz, corresponding to frequencies before, inside and beyond the second directional visible BG (ranging from 534 to 1118 kHz). It is worth noticing that at frequencies outside the BGs, the sonic crystal system behaves as a homogeneous material and acoustic wave propagation is unaltered. This because the lattice parameter is much smaller than the wave wavelength. As the wavelength of the incoming acoustic wave is comparable to the lattice parameter, pressure map clearly shows that wave propagation is severely attenuated due to multiple scattering effects and a shadow zone is formed beyond the sonic crystal. Again, at 1280 Hz, post band gap formation, the wave is free to propagate through the sonic crystal system, as the wavelength of the acoustic wave is smaller than that of the lattice parameter of the sonic crystal system. Pressure maps clearly agree with the predicted band gaps.

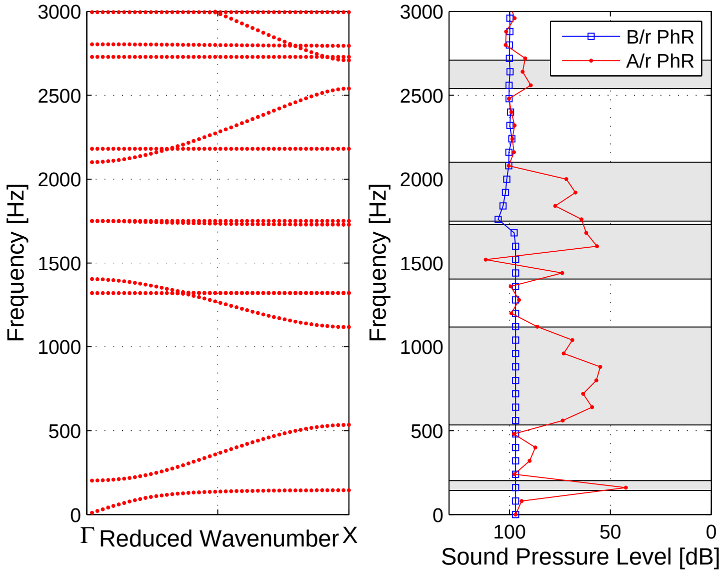

Figure 6.28: A comparison of finite element computed band structure in the $\Gamma - X$ direction against the FE computed frequency spectra for sound pressure level.

6.3.2.5 Influence of the rows number on the PM attenuation

Besides the computation of dispersion properties of a phononic material, from a practical point of view is important to examine the properties of a structure composed by a finite number of periodic unit cells. In the following a parametric study is conducted to evaluate the effect on the PM attenuation potentials w.r.t. the number of periodic cells.

Pressure maps and sound insulation index are chosen as the parameters describing the screening power of the phononic region in order to infer information about the "finiteness" effects on: (i) the frequency band layout, that is, how well the frequency bands match those of the infinite periodic material and (ii) the level of wave attenuation within the BGs. Sound insulation index has been extracted according to the procedure reported in Ref. [117] and here briefly reviewed.

Fig. 6.30 shows a schematic representation of the implemented FE model. A plane wave is set in input at a distance L_{Ls} from the first row of the phononic barrier of length L_{PhR}, whilst air impedance matching boundaries have been set to the remaining edges of the model in order to investigate only the phononic

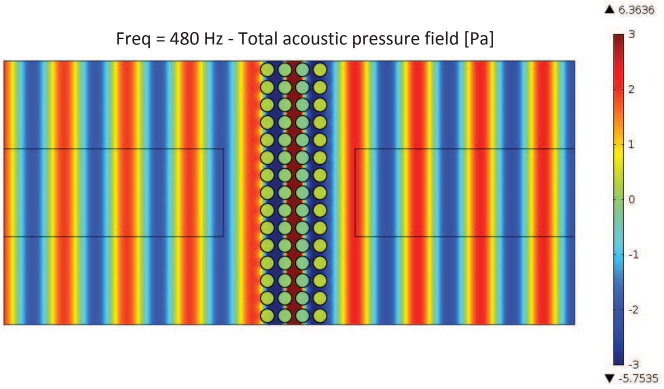

(a)

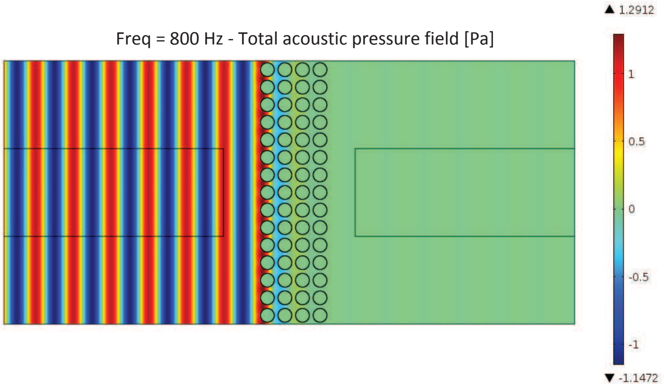

(b)

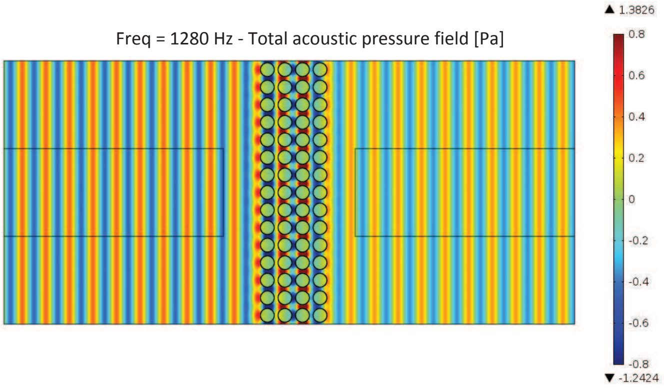

(c)

Figure 6.29: Pressure maps for hollow PVC cylinders placed in air via finite element computation at: (a) 480, (b) 800 and (c) 1280 Hz, respectively.

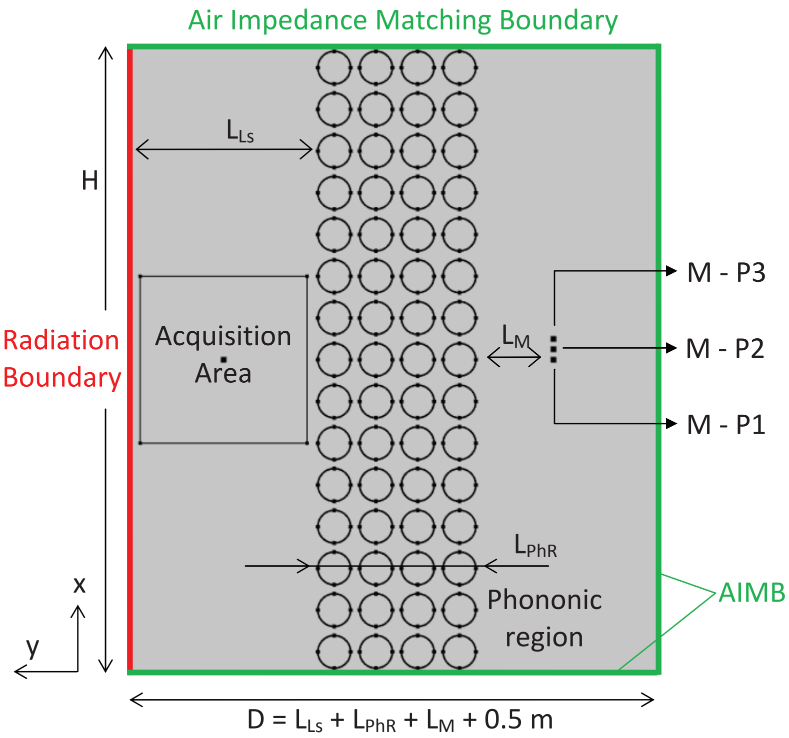

Figure 6.30: Finite element model implemented in Comsol Multiphysics exploited to compute the pressure maps and the sound insulation index. The model consists of hollow PVC cylinders ($R = 80$ mm and $t = 3.2$ mm) immersed in air. A plane wave radiation boundary condition is set to the left side of the system, while the remaining are air impedance matching boundaries. Sound pressure levels are measured at positions $M - P1$, $M - P2$ and $M - P3$, $L_M = 0.25$ m away from the last row of cylinders and spaced apart 5 cm. The phononic region is $L_{PhR} = n \cdot a$ wide, where n is the number of unitary cells and $a = 0.2$ m. The first row of cylinders is set $L_{Ls} = 1$ m away from the radiation boundary. Sound hard boundaries have been assigned to the PVC cylinders, as well.

system screening power. Data are registered at 3 points positioned at a distance L_M from the phononic barrier. In addition, responses at the 3 acquisition points placed at a distance $L_{Ls} + L_{PhR} + L_M$ but without including the phononic region (free-field measurements) are also simulated.

The sound insulation index is computed as:

$$SI = -10\lg\left\{\frac{\sum_{k=1}^{n}\int_{\Delta_{f_j}}\|\mathbf{F}[p_{tk}(t)w_{tk}(t)]\|^2 df\, d_c^2}{n\cdot\int_{\Delta_{f_j}}\|\mathbf{F}[p_i(t)w_i(t)]\|^2 df}\right\} \tag{6.11}$$

where $p_i(t)$ is the reference free-field component, $p_{tk}(t)$ is the transmitted component at the k^{th} scanning point, d_c is a geometrical spreading correction factor, $w_i(t)$ is the time window for the reference free-field component, $w_{tk}(t)$ is the time window for the transmitted component at the k^{th} scanning point, $\mathbf{F}$ is the Fourier transform, Δf_j is the frequency band and n is the number of scanning points [117].

Pressure maps at the frequency of 800 Hz[1] and sound insulation index for various phononic barriers are reported in Figs. 6.31 and 6.32, respectively. In the calculations the number of pipes rows varies from 1 to 4 in the pressure map definition and from 1 to 5 in the sound insulation calculation, respectively.

From the numerical results, it can be inferred that the response of the finite periodic system is still frequency-banded and generally respects the band layout of the infinite periodic material (infinite phononic system BG are reported in Fig. 6.32 as light grey rectangles). This confirms that wave interference mechanisms responsible for the BG nucleation are still achieved within a confined periodic region.

Further, it is worth pointing out that as the phononic region width increases (i.e. a higher number of unit cells are introduced) frequency bands transition are made sharper and, therefore, higher match with the band layout of the infinite periodic material can be observed. On the other hand, if only one cell is used the pressure sound level does not seem to be affected within the BG frequency ranges, especially in the narrower ones. With two unit cells, the transmission power starts to follow the frequency band layout even though a well definite jump in the amplitudes within the BG is not clearly remarkable.

According to the parametric study, a good compromise between sound pressure level attenuation and crystal dimensions can be established in 4 rows of unitary cells, which grantees above 30 dB attenuation on the pressure sound

---

[1] It is worth noticing that this frequency value belongs to the second visible partial BG of Fig. 6.28

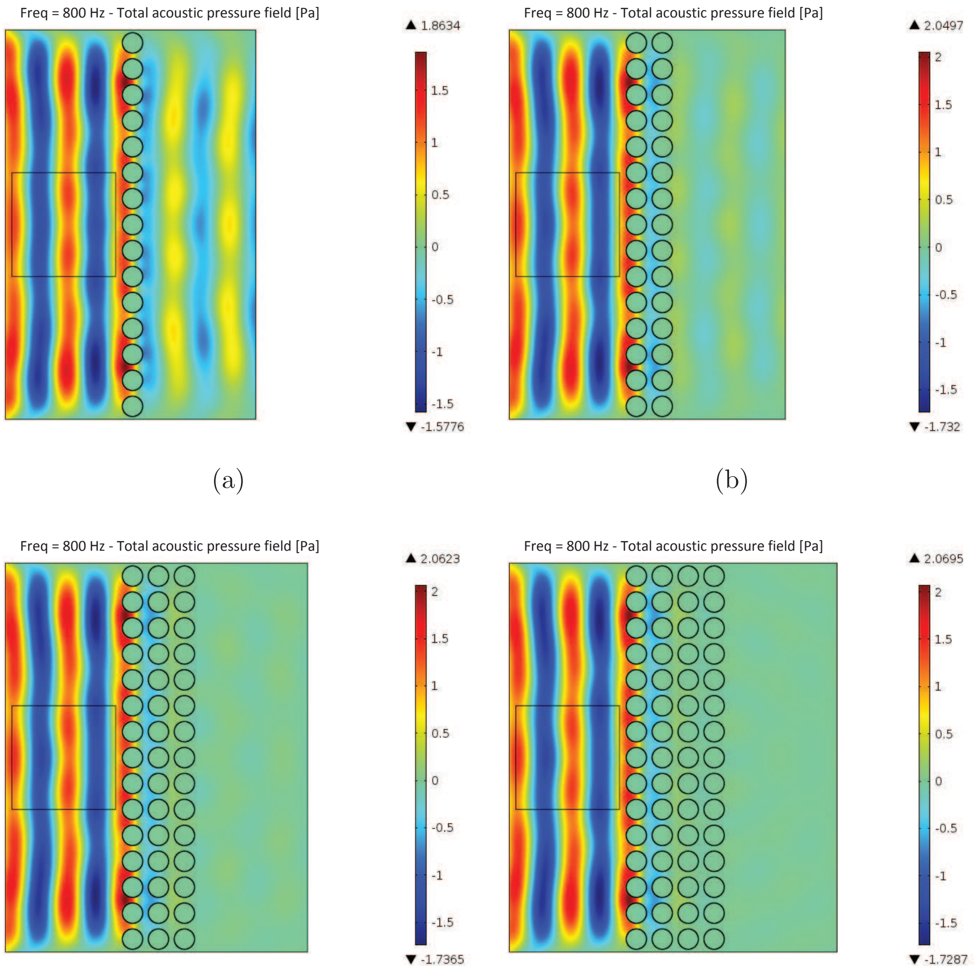

(a) (b)

(c) (d)

Figure 6.31: Influence of the number of unitary cells compounding the phononic region. Pressure maps for hollow PVC cylinders placed in air via finite element computation for 1, 2, 3 and 4 unitary cells, respectively.

level. It is worth noticing that 4 rows of cylinders are sufficient to achieve an insulation power of more than 30 dB inside the predicted BGs.

6.4 2P-3D Phononic materials

In previous sections, the study of phononic materials mainly concerned 1-periodic and 2-periodic systems under plane strain condition which implied the transversal

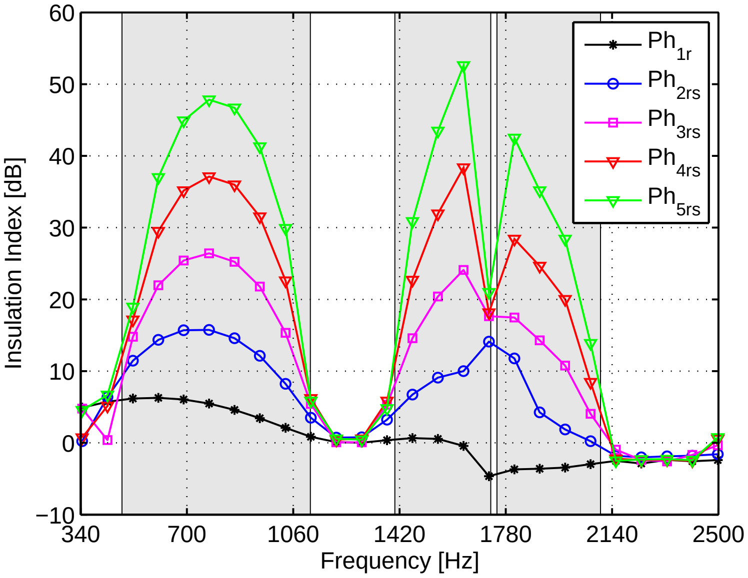

Figure 6.32: Influence of the number of unitary cells compounding the phononic region. Sound insulation index for hollow PVC cylinders placed in air is calculated via finite element computation for different configurations.

dimension to be infinite. However, an increasing attention has been recently pointed on 3D phononic slabs [73, 118, 119, 120], typically formed by etching periodic holes in a solid matrix. In this case, elastic waves are scattered not only by periodically arranged scatterers but also by the free surfaces of the slab itself. This makes such systems naturally well suited for making waveguide in integrated structure as the elastic wave will be confined within the thickness direction and manipulated by the geometry of the structure in the plane of periodicity. Band gaps in such structures are mainly determined by geometric parameters.

In this section, the plane strain assumption is removed and the influence of the out-of-plane finite dimension on band gaps for 2P-3D systems will be investigated via numerical analyses. In particular, in what follows, first, a 2P-3D unitary phononic cell made of periodically arranged cross-holes air inclusions in an aluminium matrix studied numerically by Wang et al. [121] is reviewed. Afterwards, the influence of the slab thickness is investigated in the case of a 3D steel/epoxy phononic system. Finally, the screening power of a 3D aluminium phononic plate is examined.

6.4.1 Dispersion diagram in a phononic slab

Consider a phononic slab consisting of a square lattice of unit cell made of cross-like cylindrical holes embedded in an isotropic elastic matrix, as shown in Fig. 6.33. Be the square lattice characterized by the parameter a and by a finite dimension h in the out-of-plane direction. Be the inclusion geometry defined by two parameters b and c, defining the length and the thickness of the cross arms, respectively. In such a configuration, elastic waves are supposed to propagate along the xy plane, whilst the z-axis is along the slab thickness direction. Elastic parameters used in the calculations are the same used in Ref. [121] and are here reported for sake of clarity: $\rho = 2700$ kg/m^3, $E = 20$ GPa and $\nu = 0.25$.

The FE model and properly applied boundary conditions for the above described phononic unitary cell are depicted in Fig. 6.33, whilst Fig. 6.34 reports its band structure. The existence of the two complete band gaps predicted in Ref. [121] are clearly confirmed. The lower BG extends approximately from 28 to 40 kHz and is located between the 6^{th} and 7^{th} dispersion curves; the upper BG goes from 41.4 to 54 kHz and involves the 7^{th} and 8^{th} curves. It is also worth noticing that the two BGs are almost connected, because the 7^{th} curve is nearly flat, i.e. scarcely dispersive.

Vibration modes are also calculated and reported in Figs. 6.35b-d together with the computation domain discretization (Fig. 6.35a). They allow to infer that the nucleation of the wide low-frequency BGs in the system is due to the local resonance of the resonant elements with large lumps connected by the narrow connectors.

6.4.2 Effects of the slab thickness on dispersion diagram

In this subsection the influence on the band diagram of the ratio $t_r = h/a$ between thickness and lattice constant is investigated. Starting from a 2D plane strain model, dispersion curves for different 3D models characterized by $t_r = 0.125$, $t_r = 0.25$ and $t_r = 0.5$ are investigated. The analysed phononic system is made of circular steel inclusions in an epoxy matrix, as shown in Fig. 6.36a together with its properly applied boundary conditions (Fig. 6.36b-d).

Dispersion diagrams are plotted in Fig. 6.37. In particular, it can be inferred

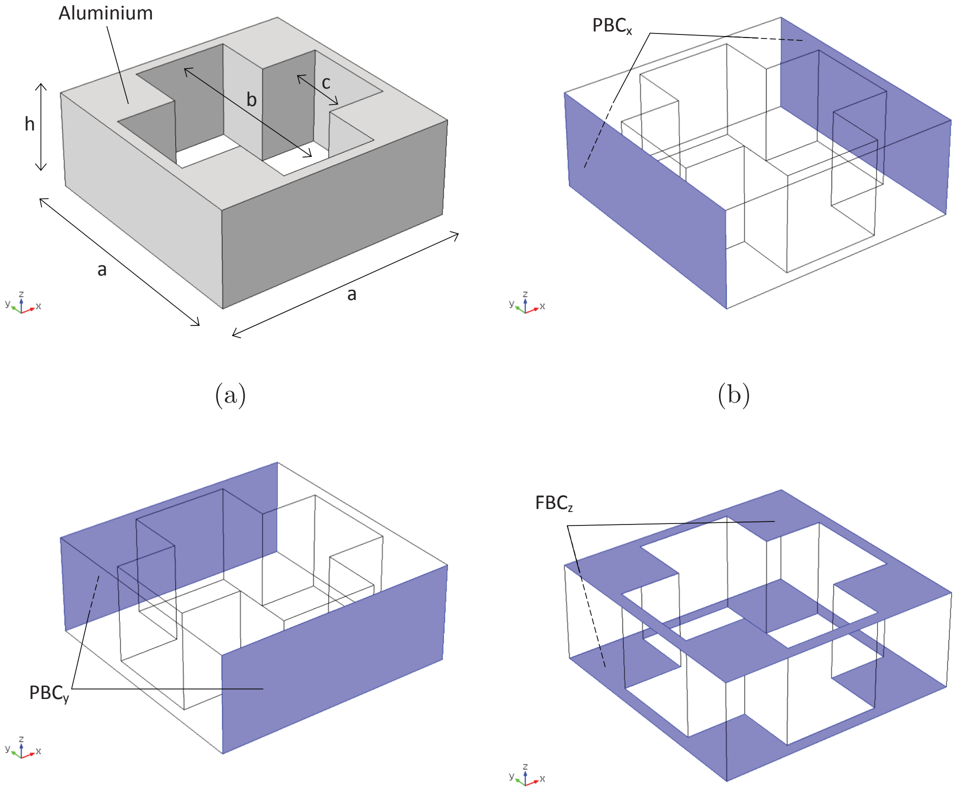

(a) (b) (c) (d)

Figure 6.33: Unit cell for the phononic material made of cross-like cylindrical holes in aluminium matrix: (a) geometry description; (b) periodic boundary condition along x-direction (PBCx); (c) periodic boundary condition along y-direction (PBCy); free boundary condition along z-direction (FBCz).

that under the 2D plane strain assumption, all the modes involving out-of-plane displacements are inhibited (Fig. 6.37a). This allows a large unique band gap approximately ranging from 80 kHz up to 200 kHz. As the third dimension is taken into account, much more modes are visible in the diagram in the same frequency range. In fact, in a 3D model, flexural modes are not inhibited any more. As a consequence, narrower band gaps are distinguishable (Fig. 6.37b-d). Finally, it is worth noticing that increasing the ratio t_r BGs undergo a significant enlargement (see Fig. 6.37c-d) which tends to re-stablish the dispersion diagram of Fig. 6.37a, apart from the almost non-dispersive mode splitting the BG.

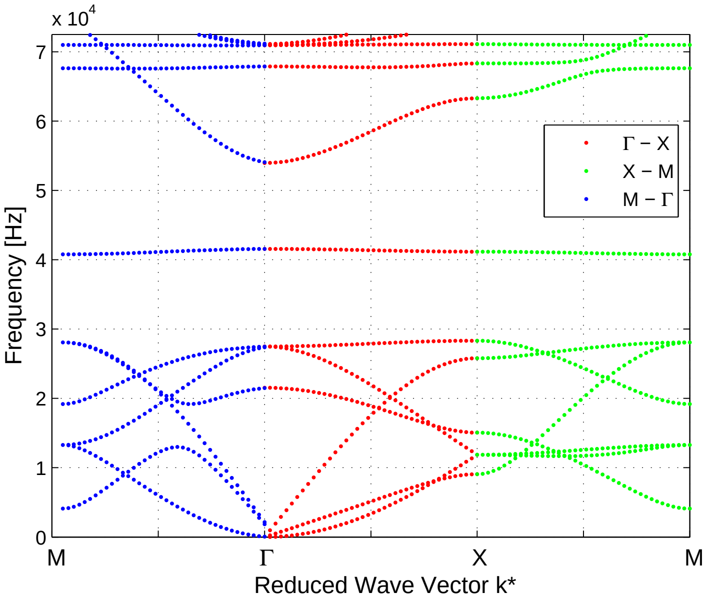

Figure 6.34: Band structures of cross-like cylindrical holes embedded in an isotropic elastic solid slab in a square lattice.

6.4.3 FE wave propagation in a 3D phononic system

Theoretically speaking, the above analyses have shown that perfect filtering properties exist in an infinite, undamped periodic structure. However, in real applications, geometries finiteness must be taken into account also in the in-plane dimensions. To this end a phononic system composed of a PVC plate hosting a phononic region, as shown in Fig. 6.38, in analysed.

The phononic region is made of 2P-3D cross-holes in a specific portion of a $1000 \times 500 \times 12$ mm^3 PVC plate, as shown in Fig. 6.38. A schematic of the unitary cell constituting the phononic region is also reported in Figs. 6.39, where lattice parameter $a = 20$ mm, cylinder radius $c = 3$ mm, cross-length $b = 12$ mm and plate height $H = 12$ mm are also indicated. Material properties are $\rho_{PVC} = 1430$ kg/m^3, $E_{PVC} = 3 \cdot 10^9$ Pa, $\nu_{PVC} = 0.4$ and $\rho_{Air} = 1.25$ kg/m^3, $c_{Air} = 343$ m/s for PVC and air, respectively.

First, BGs for the described unitary cell are computed and presented in Fig. 6.40. The horizontal axis reports the reduced wavenumber $k^* = ka/\pi$ in the three high symmetry directions $M - \Gamma - X$ of the first irreducible Brillouin zone and

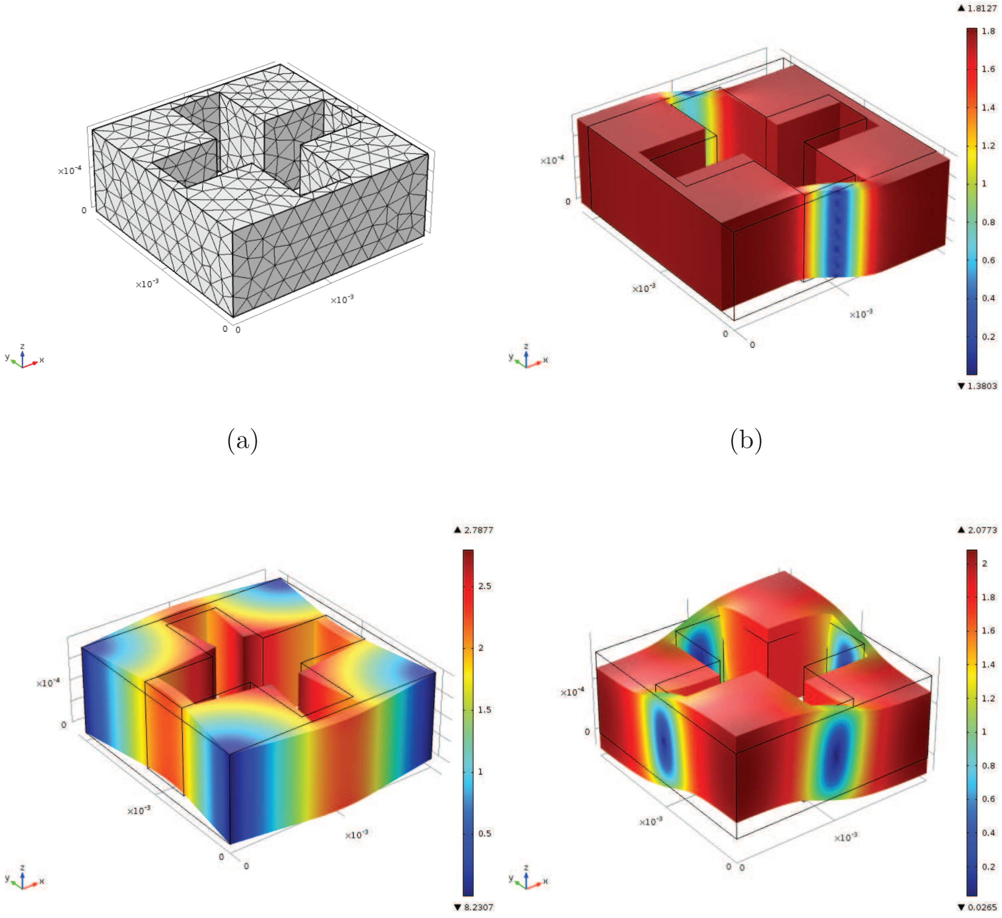

(a) (b)

(c) (d)

Figure 6.35: (a) Mesh discretization for the unit cell and (b-d) vibration modes (VM) in the first Brillouin zone: (b) VM belonging to the $\Gamma - X$ path, characterized by $\mathbf{k} = (157, 0)$ m^{-1}, $f = 9.061$ kHz; (c) VM belonging to the $X - M$ path, characterized by $\mathbf{k} = (0, 157)$ m^{-1}, $f = 4.099$ kHz; (d) VM belonging to the $M - \Gamma$ path, characterized by $\mathbf{k} = (157, 157)$ m^{-1}, $f = 19.18$ kHz.

the vertical axis reports the frequency values in Hz. Curves are dispersive for the majority of the available frequencies. However, the existence of a relatively low-dispersive curve in the band structure is also noticeable at approximately 30 kHz. The plot shows unambiguously the existence of 2 complete BGs in the considered $0 - 50$ kHz frequency range. Directional BG are barely present.

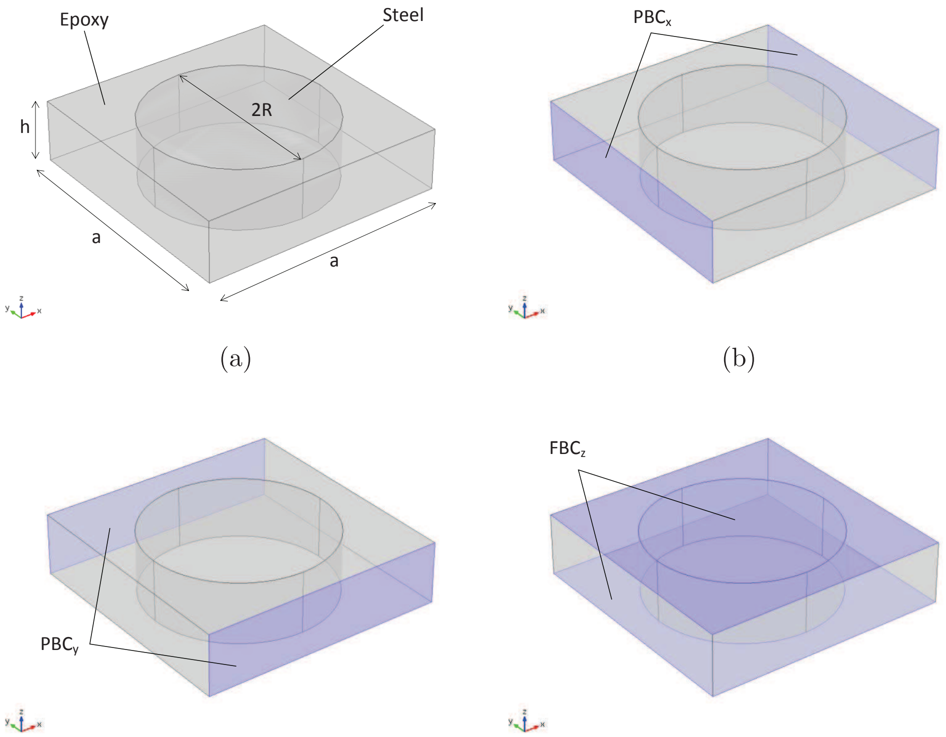

(a) (b)

(c) (d)

Figure 6.36: Schematic representation of the PM unit cell (circular steel cylinders embedded into a background epoxy matrix) and set boundary conditions: (a) geometry description; (b) periodic boundary condition along x-direction (PBCx); (c) periodic boundary condition along y-direction (PBCy); free boundary condition along z-direction (FBCz).

To qualitatively and quantitatively verify the screening power of the predicted BGs, wave propagation is studied in the finite phononic system presented in Fig. 6.38. The basic idea of the analyses is to excite dispersive Lamb waves in the system at point E by means of an imposed displacement (orthogonally to the plate). In-plane as well as out-of-plane displacements are then received at the two acquisition points A and B as functions of time. To have a direct measure of the screening power of the designed phononic region, acquisition points have been set equidistant from the input source E and located in an ordinary portion of the system (point A) as well as inside the screened area (point B). After that, signals are Fourier transformed and their frequency content is compared to highlight the

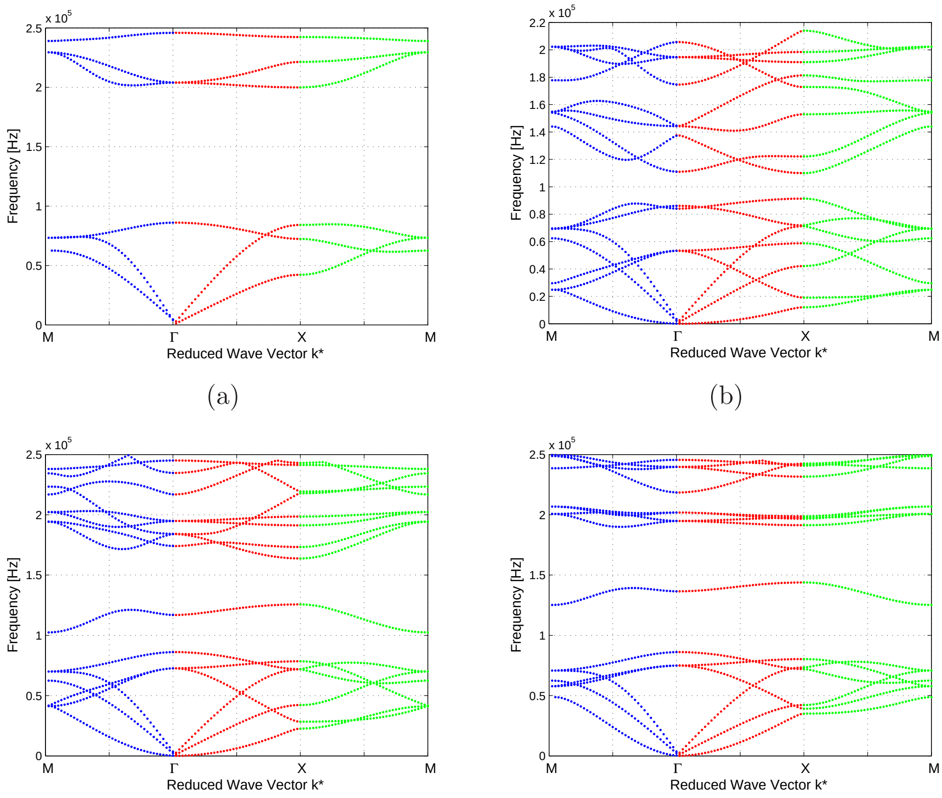

(a)

(b)

(c)

(d)

Figure 6.37: Dispersion curves for a PM made of circular cylindrical inclusions in an epoxy matrix. (a) 2D model under plane strain assumption; (b) 3D model with $t_r = 0.125$, (c) 3D model with $t = 0.25$. (d) 3D model with $t_r = 0.5$.

differences of the two frequency responses.

Two input signals are provided into the simulations, according to the band structure of Fig. 6.40. First, (i) a pulse of 2 sinusoidal cycles centred at 50 kHz and modulated by a Hanning window (Fig. 6.41a) and then (ii) a pulse of 21 sinusoidal cycles centred at 27.5 kHz and modulated by a Hanning window (Fig. 6.41b). Such a typologies of pulses have been chosen in order to highlight the filtering capabilities of the phononic portion, emphasizing the pass-band and band gaps frequency ranges.

Figs. 6.42 and 6.43 show stress (Von Mises) maps for both broad and narrow band excitations. They clearly show that waves with a frequency content falling outside the BG essentially propagate through the phononic region (Fig. 6.42),

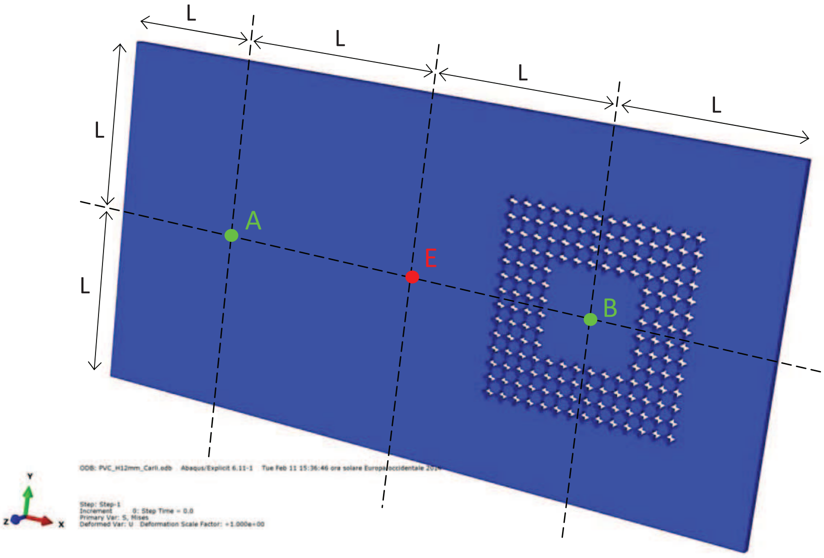

Figure 6.38: Schematics of the phononic system composed of an ordinary PVC plate hosting a phononic region screening a specific region. Excitation point (E) and receiving points (A and B) are highlighted.

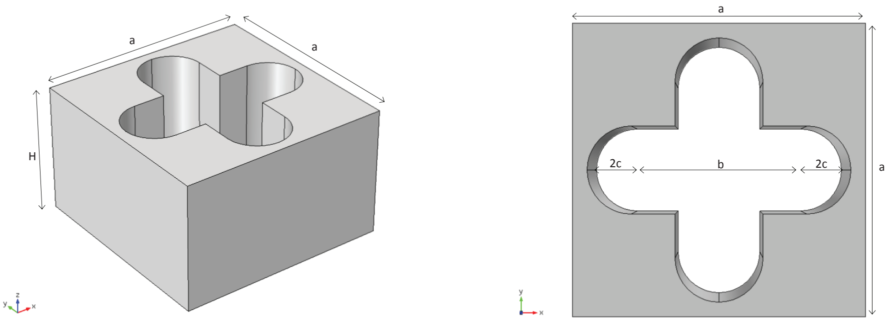

(a)

(b)

Figure 6.39: (a) Isometric and (b) in-plane view of the unitary cell composing the phononic part of the system.

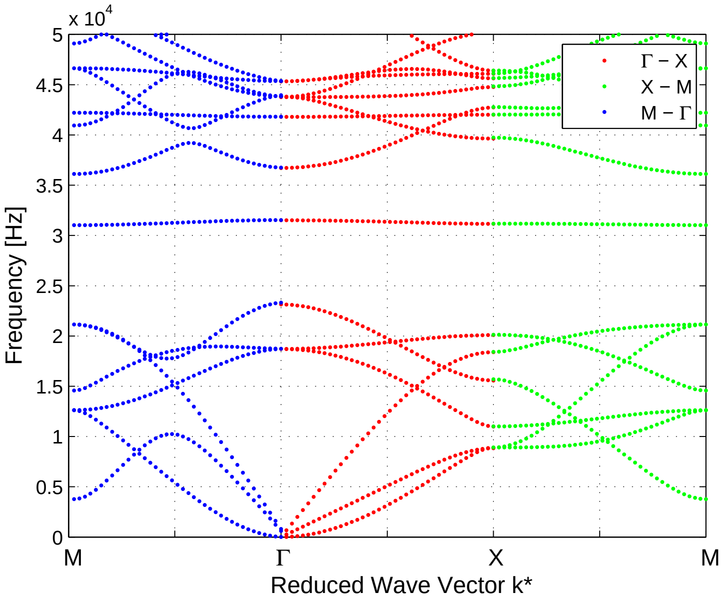

Figure 6.40: Dispersion map for the unit cell presented in Fig. 6.39.

whilst when the frequency content of the wave is centred inside the BG, the phononic region inhibits the wave propagation and a shadow zone ("blind area") is formed behind the periodic inclusions (Fig. 6.43).

To quantify numerically the screening power of the designed phononic system, displacements for the broadband excitation case at points A and B in the $x \equiv 1$, $y \equiv 2$ and $z \equiv 3$ directions, as well as their energy content in the frequency domain are shown in Figs. 6.44 - 6.46. It is worth noticing that at low frequencies (1 - 20 kHz), the phononic system behaves as a homogeneous material and acoustic wave propagation is permitted through the periodic structure. This is due to the lattice parameter being much smaller than the relevant wavelength. As the frequency content of stress waves approaches the BG frequency range, i.e. the wavelength of the incoming wave is comparable to the lattice parameter, the elastic wave is severely attenuated due to multiple scattering effects. Again, at frequencies higher than the BG upper limit, i.e. $f \simeq 36$ kHz, the phononic system lattice parameter is much bigger than the wavelength of the propagating wave which is free to propagate through the phononic system, as the wave see the system as individual scatterers.

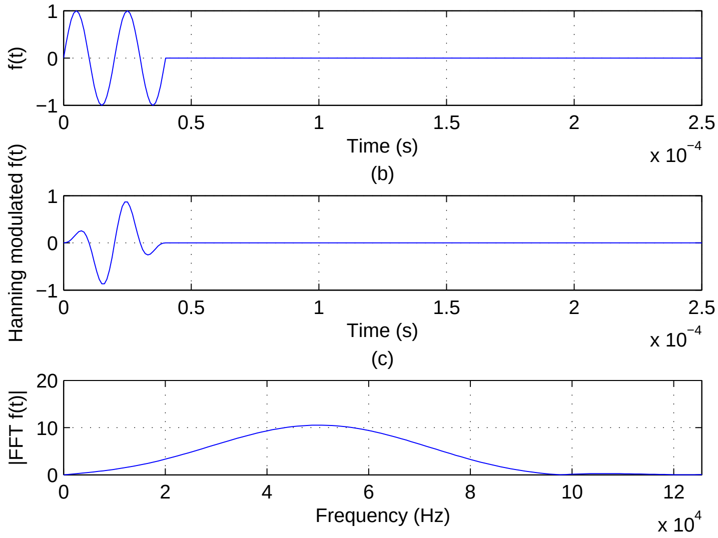

(a)

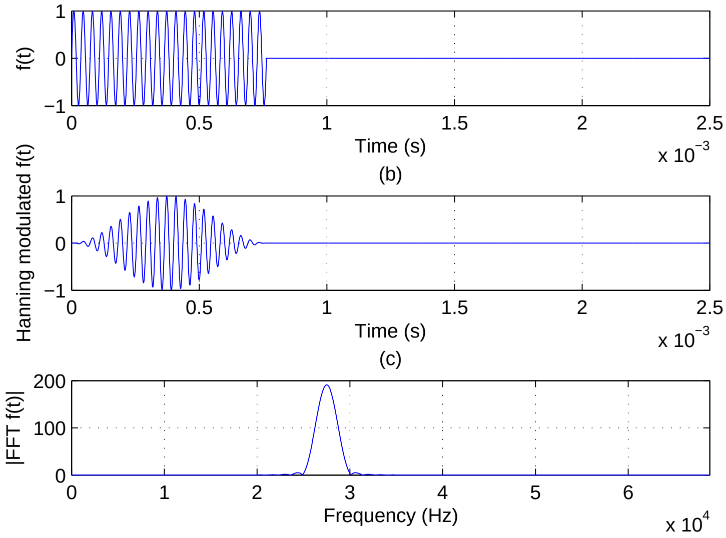

(b)

Figure 6.41: Excitation displacements: (a) 50 kHz centred pulse of 2 sinusoidal cycles modulated by a Hanning window and (b) 27.5 kHz centred pulse of 21 sinusoidal cycles modulated by a Hanning window.

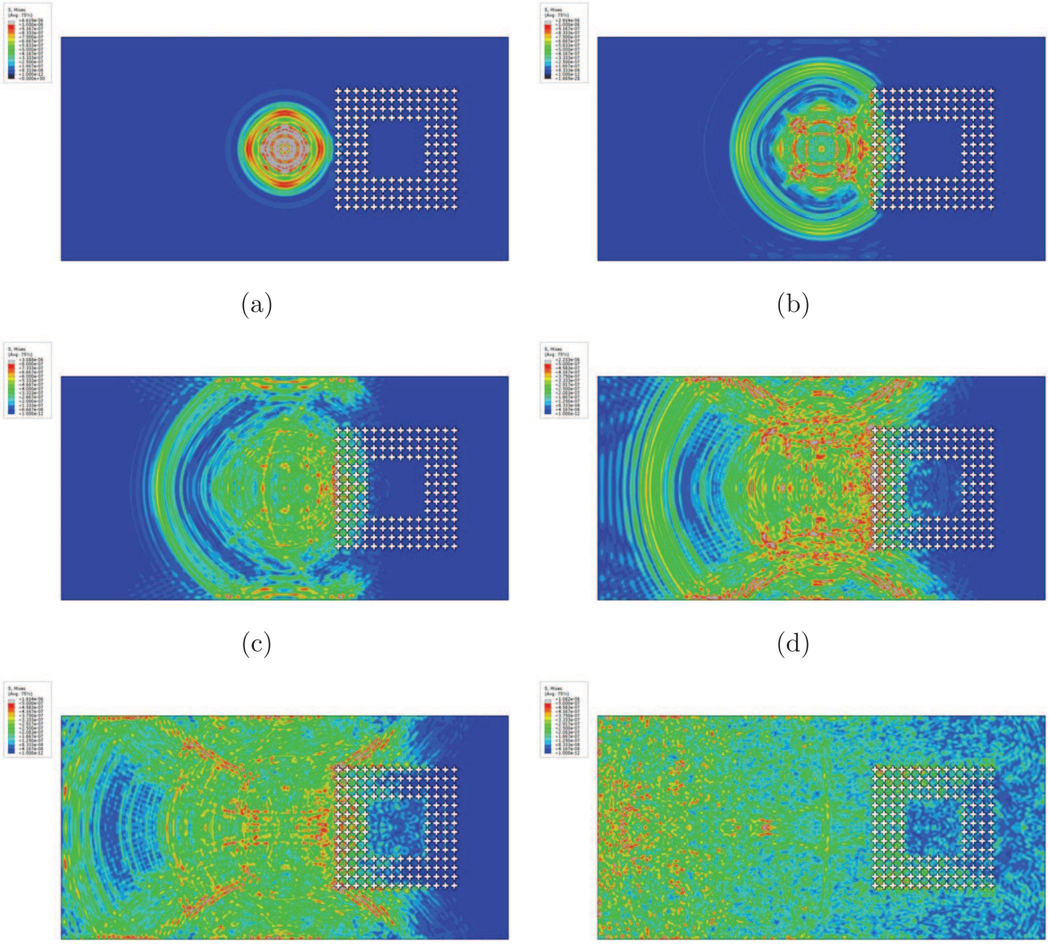

(a) (b) (c) (d) (e) (f)

Figure 6.42: Simulated Von Mises stress for cross-rounded holes phononic plate. Frequency excitation was centred at 50 kHz (therefore covering frequencies even outside the band gap). Snapshots are taken at: (a) $t = 1.2 \cdot 10^{-}4$ s, (b) $t = 2.4 \cdot 10^{-}4$ s, (c) $t = 3.6 \cdot 10^{-}4$ s, (d) $t = 4.8 \cdot 10^{-}4$ s, (e) $t = 6 \cdot 10^{-}4$ s and (f) $t = 12 \cdot 10^{-}4$ s.

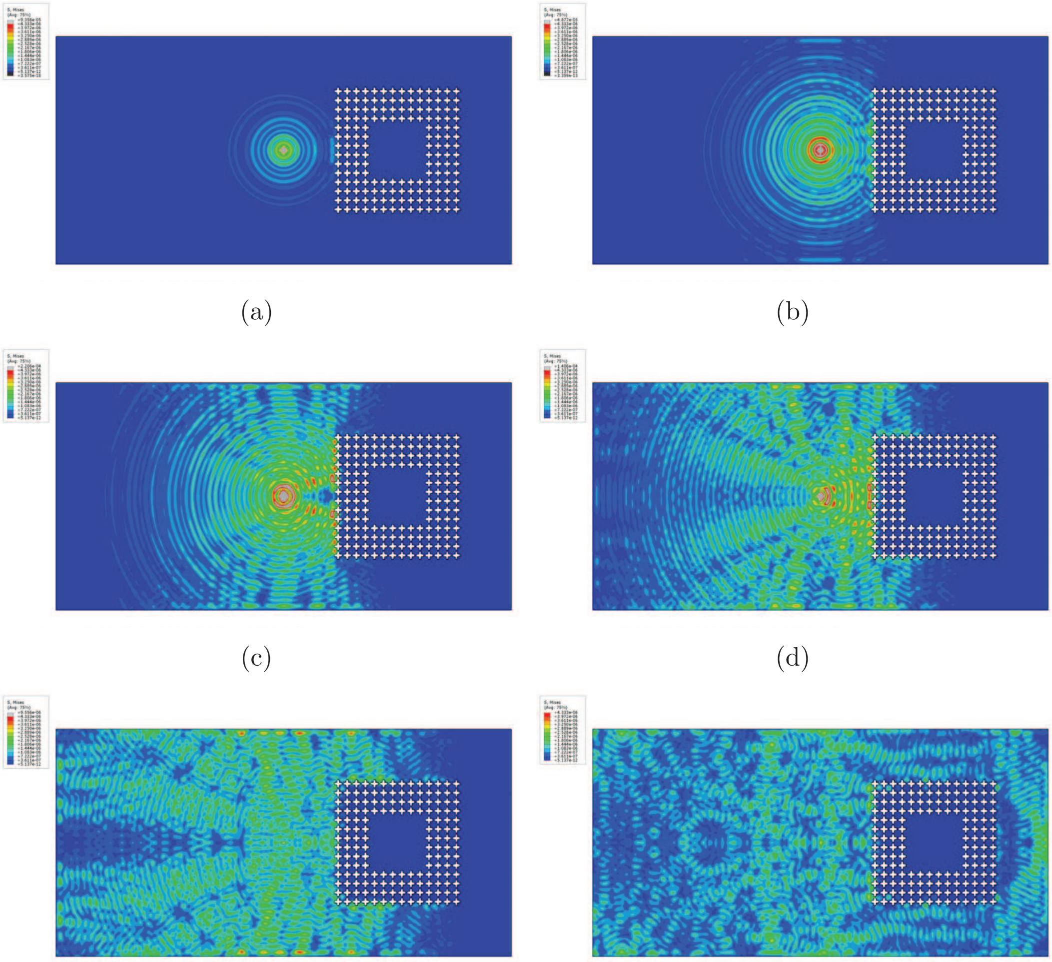
(a) (b) (c) (d) (e) (f)

Figure 6.43: Simulated Von Mises stress for cross-rounded holes phononic plate. Frequency excitation was centred at 27.5 kHz (therefore covering frequencies even outside the band gap). Snapshots are taken at: (a) $t = 3 \cdot 10^{-}4$ s, (b) $t = 4.8 \cdot 10^{-}4$ s, (c) $t = 6.6 \cdot 10^{-}4$ s, (d) $t = 8.4 \cdot 10^{-}4$ s, (e) $t = 10 \cdot 10^{-}4$ s and (f) $t = 20 \cdot 10^{-}4$ s.

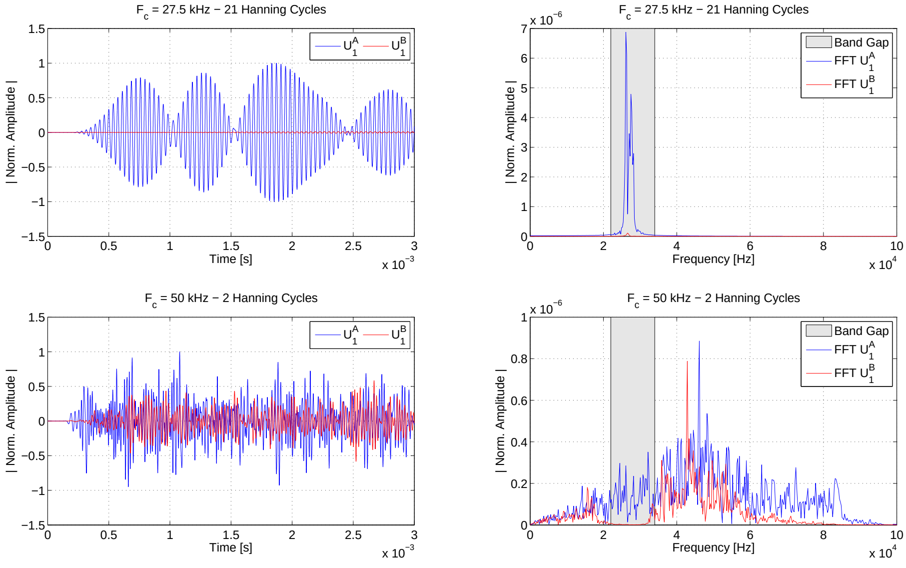

Figure 6.44: Normalized displacement u_1 at points A and B versus time (left) and its Fourier spectrum (right). The complete band gap is also highlighted as the light grey region.

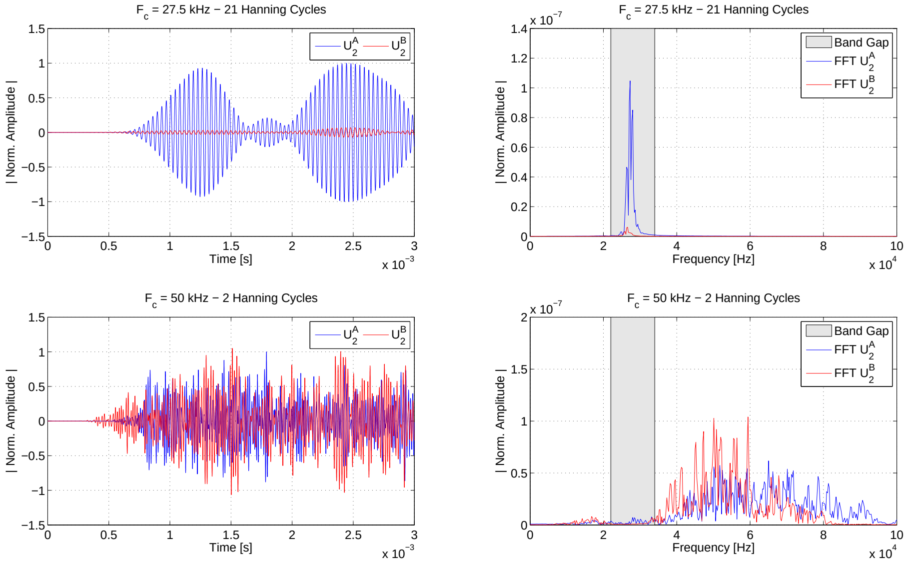

Figure 6.45: Normalized displacement u_2 at points A and B versus time (left) and its Fourier spectrum (right). The complete band gap is also highlighted as the light grey region.

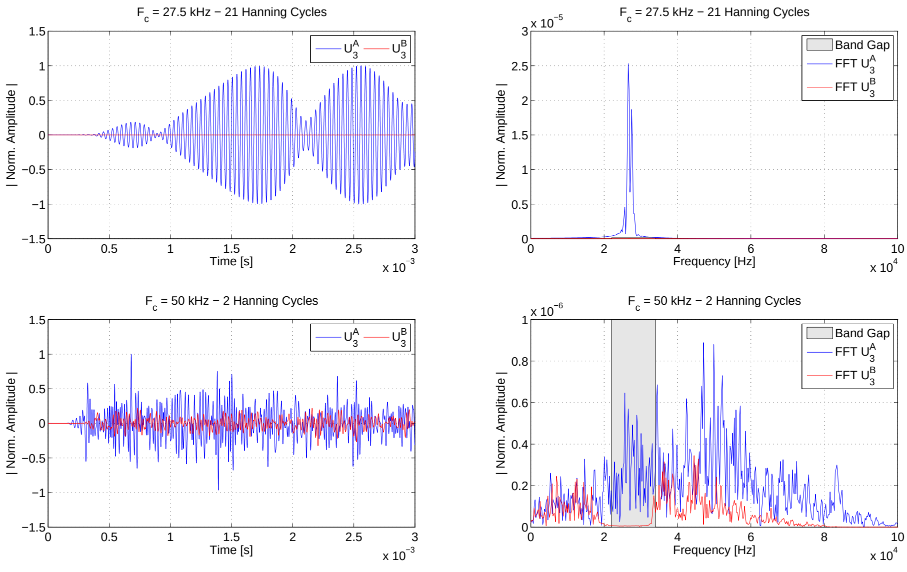

Figure 6.46: Normalized displacement u_3 at points A and B versus time (left) and its Fourier spectrum (right). The complete band gap is also highlighted as the light grey region.

A comparison of the transmission power spectrum against the computed BGs for the infinite phononic system is also made in Figs. 6.44b - 6.46b. In general, the FE calculations give BGs of larger width w.r.t. the infinitely periodic structure. This difference could be attributed to the finite number of scatterers used in the FE models and the subsequent diffraction effects around the edges of the phononic region. However, the BGs overall locations in the frequency domain are in good agreement with those predicted for the infinite PM.

Furthermore, it is useful to remark that numerical simulated measurements of the transmission spectra resulted in the observation of a unique large total band gap extending from 23.32 to 35 kHz instead of two band gaps ranging from 23.5 to 31 kHz and from 31.5 to 35 kHz. This directly derives from the nature of the excitation, which was supposed orthogonal to the plate.

Chapter 7

Experimental applications

7.1 Phononic materials in the ultrasonic range

7.1.1 Introduction

Lamb waves propagation in plate-like phononic structures [76] recently received increasing interest, especially in conjunction with the use of high-frequency piezoelectric transducers (PZTs) [8]. Experimental work in this context has confirmed the existence of directional (partial) as well as complete band gaps for Lamb wave modes in phononic plate structures. In addition, results of these studies proved that phononic plates of finite thickness with only a bi-dimensional periodicity are able to guide elastic waves along desired paths [84].

To date experimental evidence of BGs in phononic plates with lattice constants ranging from millimetre to micrometer scales exists. In this study, complete BGs for Lamb waves with lattice constant of the centimetre order is presented. In particular, a 2P-3D phononic plate with cross-like holes, as the one modelled in Section 6.4.3, is manufactured and experimentally tested.

Ultrasonic and laser vibrometric measurements have been performed and compared to numerically predicted results with a twofold scope, i.e. (i) validating the numerical results and (ii) proving the existence of BGs in the designed sample.

7.1.2 Sample description

A Polyvinyl chloride (PVC) plate of dimensions $1000 \times 500 \times 12$ mm^3 is initially considered. The plate has been subjected to a machining process in which 160 hollow rounded cross-cylinder inclusions have been drilled as shown in Fig. 7.1[1]. The holes are distributed over a square frame of width $4 \times a = 80$ mm (where $a = 20$ mm is the lattice constant). An unaltered area of 120×120 mm^2 is therefore left in the centre of the phononic region. As in the numerical study, the radius of the cylindrical inclusion is $c = 3$ mm and its cross-length $b = 12$ mm, resulting in a filling fraction of approximately $f = 41\%$. For the sake of clarity, the unit cell is schematically reported in Fig. 7.2.

Nominal material properties are $\rho_{PVC} = 1430$ kg/m^3, $E_{PVC} = 3 \cdot 10^9$ Pa, $\nu_{PVC} = 0.4$ and $\rho_{Air} = 1.25$ kg/m^3, $c_{Air} = 343$ m/s for PVC and air, respectively. The choice of PVC and air as constitutive materials derives from the strong contrast in their densities and elastic constants [87].

7.1.3 PZT in pitch-catch configuration

Three PZT PIC-181 transducers (10 mm diameter, 0.63 mm thickness) have been bonded to the plate using Phenylethyl Salilcilate[2] in positions A, B and E, as shown in Fig. 7.1. The inter-distances are set $\bar{AE} = \bar{EB} = 250$ mm. It must be noted that the transducer in position A is placed within the phononic region.

Guided Lamb waves are generated by means of the PZT at position E and received at both PZTs located in A and B.

Sine function with 21-cycle and Hanning[3] modulated, with central frequency ranging from 10 to 80 kHz have been used as the input signals. These kind of pulses have been preferred in order to highlight the filtering capability of the

---

[1] In the practical realization of the specimen, a tolerance of 0.1 mm was respected. Generally speaking, introduction of such irregularities in the lattice lightly alter the acoustic wave propagation, therefore, modifying the band structure of such materials. In some cases further attenuation can be introduced.

[2] Phenylethyl Salilcilate is a white crystalline powder, derived from salicylic acid. Its melting point is around 40° and it recrystallizes as it cools.

[3] The Hanning window, commonly used in ultrasonic non-destructive evaluation (NDE) applications, is applied in order to reduce energy dispersion away from the central excitation frequency.

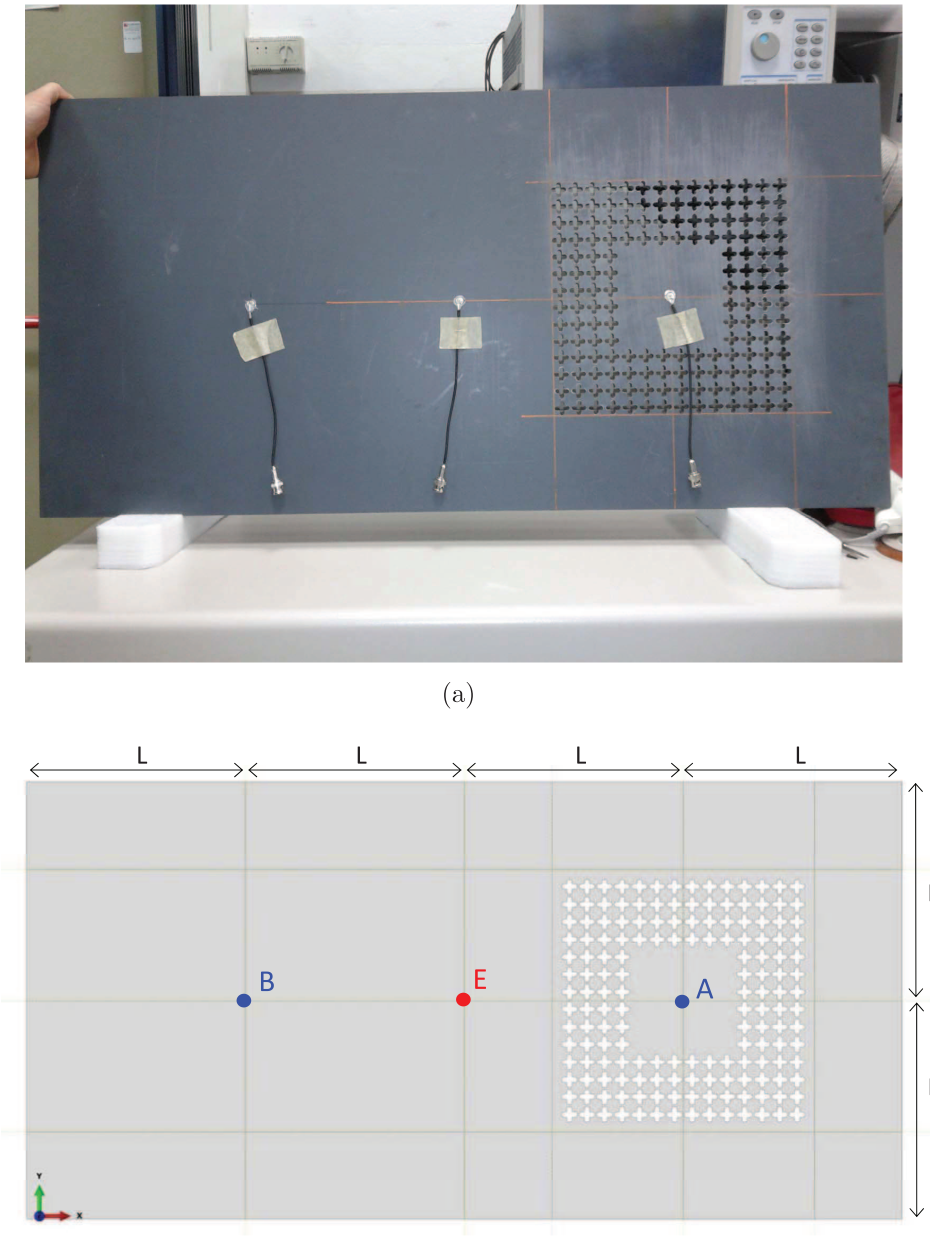

(a)

(b)

Figure 7.1: In-plane view of the phononic plate constituted of 160 hollow rounded cross-cylinder inclusions drilled into a $1000 \times 500 \times 12$ mm^3 Polyvinyl chloride (PVC) matrix: (a) experimentally tested specimen and (b) numerical model. Emitting/Receiver transducers are also visible.

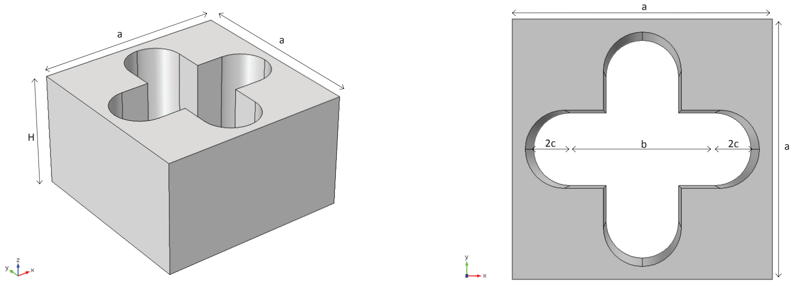

(a) (b)

Figure 7.2: (a) Isometric and (b) in-plane view of the unitary cell constituting the phononic region of the plate.

phononic portion and to avoid energy dispersion due to broadband excitation. As an example, Fig. 7.3 shows time history, Hanning modulation and frequency content of a probing pulse centred at 27.5 kHz.

The experimental apparatus, shown in Fig. 7.4, consists of an arbitrary waveform function generator by Keithley, and a GA-2500A Gated RF amplifier by Ritec used to amplify the input signal up to $V_{pp} = 200$ V. Signals are acquired by a 4-channel LeCroy LC534AL oscilloscope. A personal computer controls the equipment and allows data to be processed.

As the transmitted signals have been measured under the same experimental conditions, a direct comparison between the transmitted intensities can be made. Figs. 7.5 - 7.8 show typical example of actuated (PZT - position E) and detected (PZTs - positions A and B) signals for actuation frequencies centred at 15, 27.5, 42.5 and 51 kHz. Such frequencies correspond to pre-, in- and post-band gap frequencies. In addition, in Figs. 7.5b - 7.8b the signals spectra are provided. Effects on the transmitted pulses of multiple scattering inside the phononic region are clearly visible both in the time and frequency domains. A comparison between the signals allows to infer that: (i) the waves propagating from E to A experience higher amplitude reduction w.r.t. the waves propagating in the ordinary portion of the plate (from E to B); (ii) every kind of wave propagation with a frequency content falling inside the numerically predicted BG is effectively inhibited in the phononc region; (iii) the wave travelling within the phononic region undergoes to a heavier distortion and to a time shift Δt_g if compared to the signal acquired in

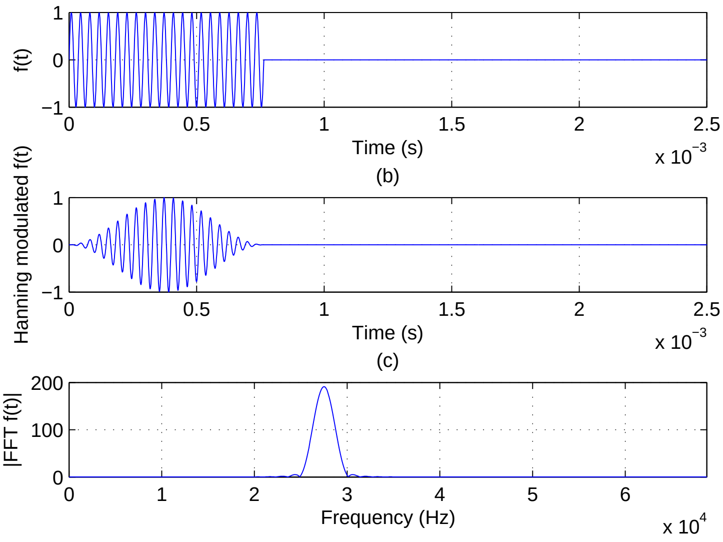

Figure 7.3: Example of time history for a 21 cycles sine pulse, its Hanning modulation and its frequency content. The probing pulse is centred at 27.5 kHz.

the ordinary PVC plate (see Fig. 7.9).

Finally, the maximum of the frequency responses related to actuation pulses driven from 10 to 80 kHz at both A and B positions, normalized w.r.t. the energy content of the input signals, are represented in Fig. 7.10. Thus, the diagram summarizes the screening properties of the phononic region exhibiting a well defined drop in intensity between 22 and 36 kHz (red line with square markers) if compared to the transmission spectrum of the ordinary PVC plate (blue line with circular markers). Indeed, a very good agreement between experimental and numerical results is found. In the BG frequency range only noise level intensity is measured at the sensor located in the screened region. Furthermore, it can be noted as some intensity peaks appear around $42.5, 51$ and 67 kHz in the phononic portion of the plate.

7.1.4 Laser vibrometer experiments

In this test, elastic guided waves were induced using a using a Sonox® ceramic piezoelectric disk, (diameter 10 mm) by CeramTec®. The transducer was glued

Figure 7.4: Measurement setup adopted in the PZT pitch-catch experiment to extract the transmission coefficient in the PVC phononic plate.

to the surface of the investigated sample using commercial super-glue at point E of Fig. 7.1. The actuation signals used both in the numerical simulations (see Section 6.4.3) and in the pitch-catch experiment have been considered.

A 3D laser scanning vibrometer PSV 400 by Polytec® was used to perform the out-of-plane measurements of the velocities over the target area (see Fig. 7.11b). The pulse excitation was fed from a TGA1241 generator by Thurlby Thandar Instruments through an EPA-104 amplifier by Piezo Systems® Inc, inducing a 200 V_{pp} signal. In order to improve measurements accuracy the investigated specimen was covered with self-adesive retroreflective film by ORALITE®. This was aimed at improving the laser vibrometer signal level in each measurement point regardless of the angle of incidence of the measurement beam on the surface being measured [1].

Fig. 7.11 presents a scheme of the experimental apparatus. A scanning mea-

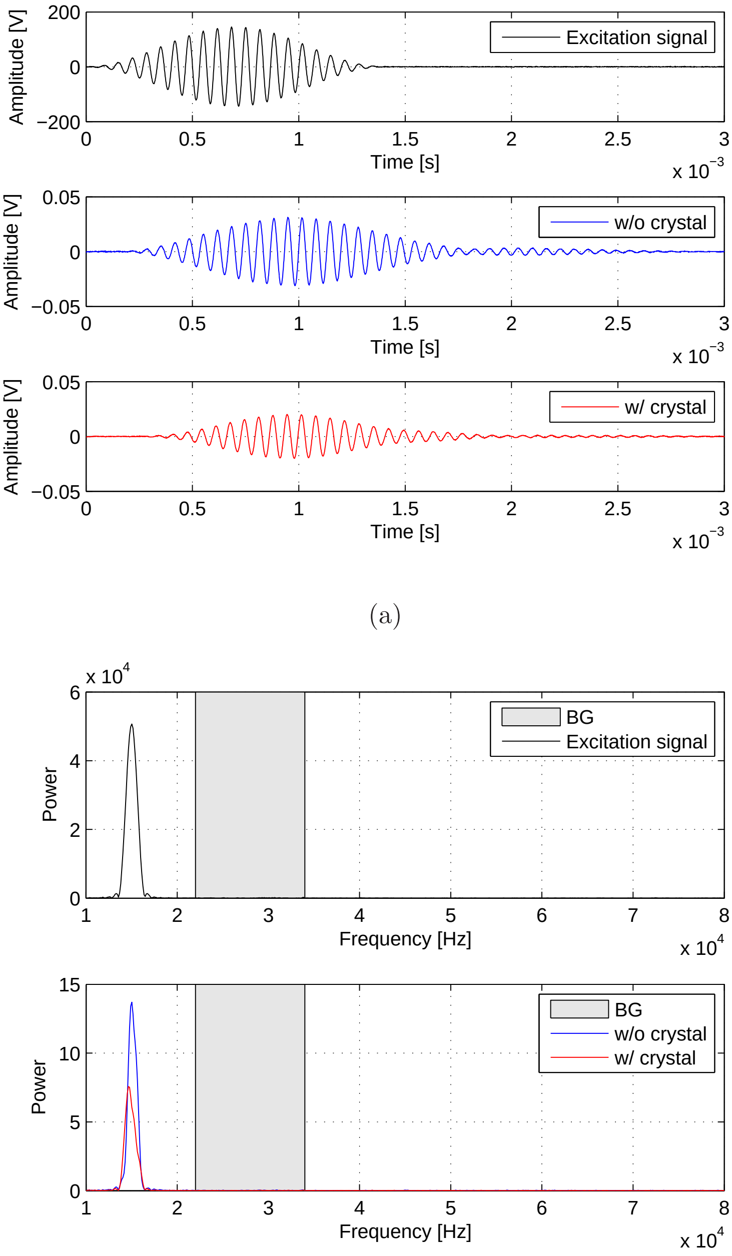

(a)

(b)

Figure 7.5: (a) Time waveforms (RF signals) detected by the sensors at 15 kHz. (b) Power spectrum of the excitation and acquired signals.

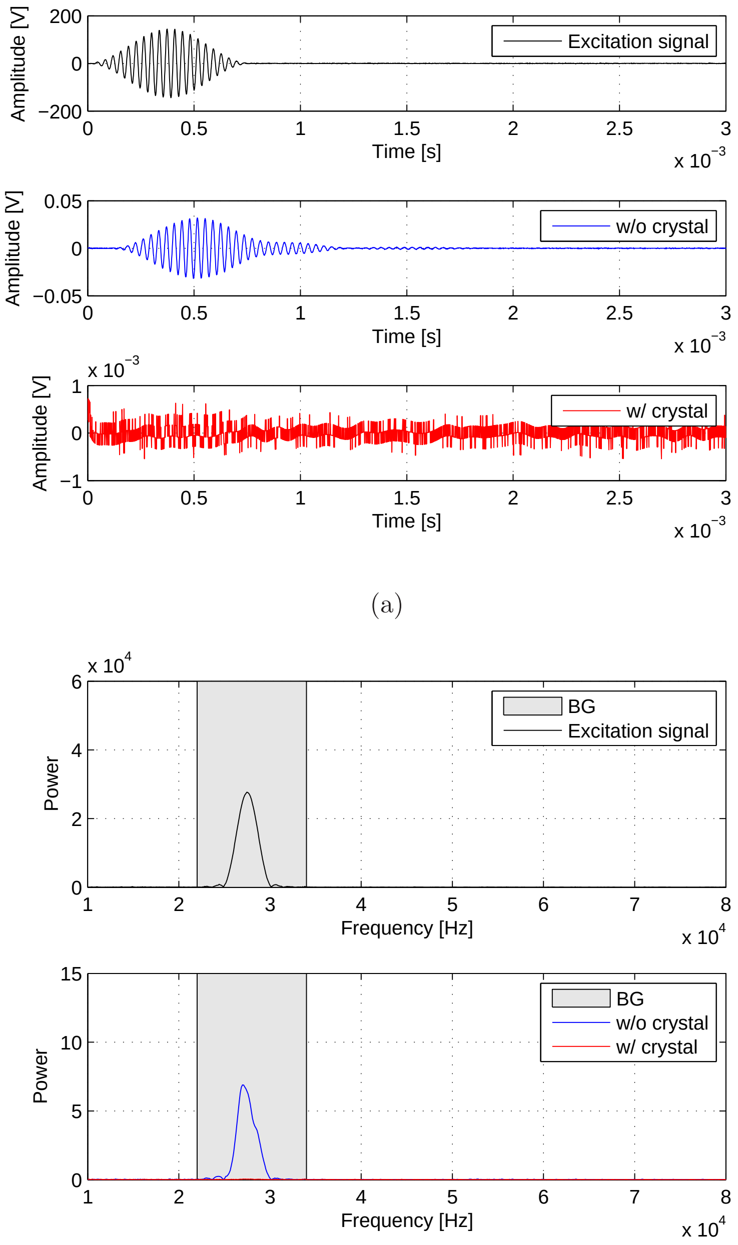

(a)

(b)

Figure 7.6: (a) Time waveforms (RF signals) detected by the sensors at 27.5 kHz. (b) Power spectrum of the excitation and acquired signals.

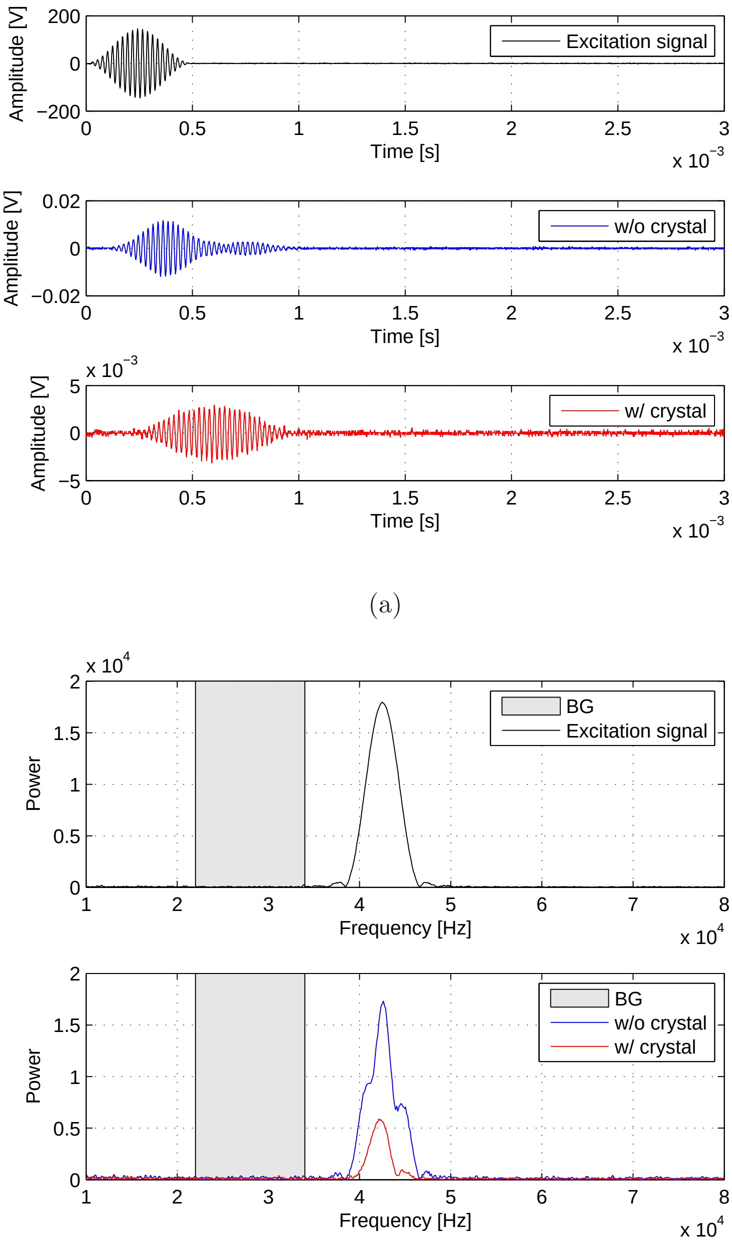

(a)

(b)

Figure 7.7: (a) Time waveforms (RF signals) detected by the sensors at 42.5 kHz. (b) Power spectrum of the excitation and acquired signals.

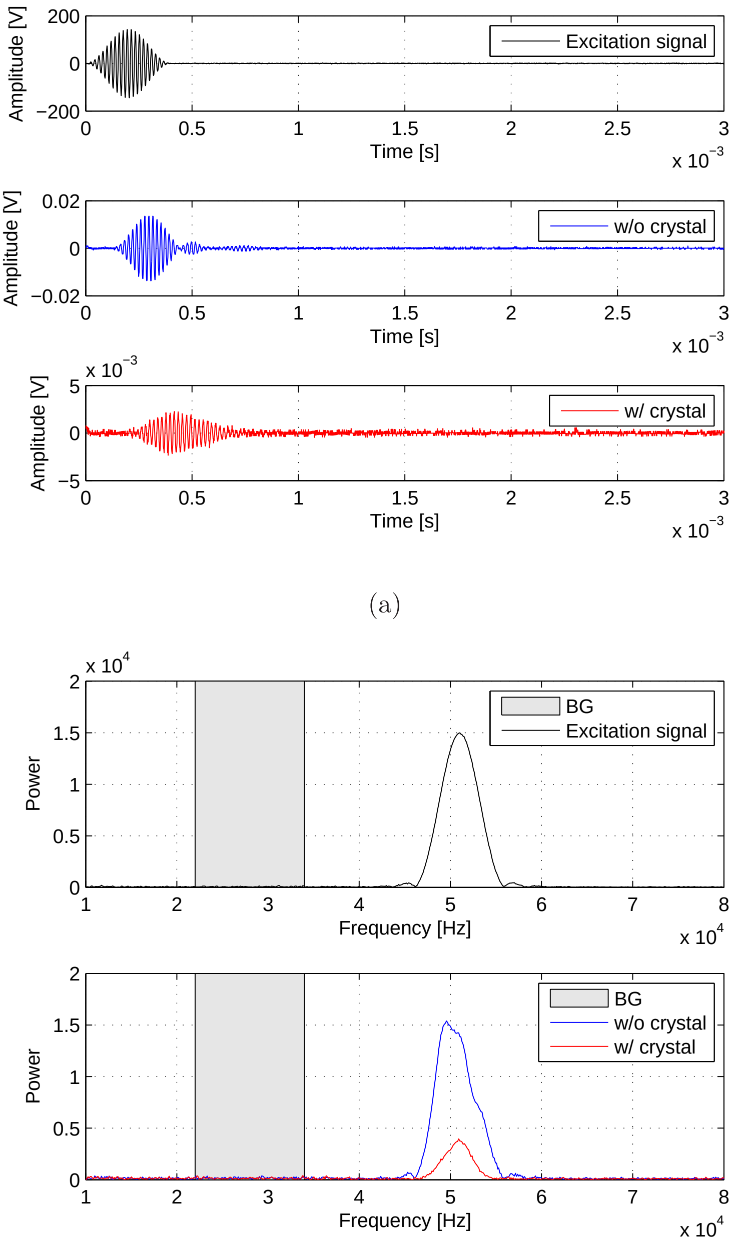

(a)

(b)

Figure 7.8: (a) Time waveforms (RF signals) detected by the sensors at 51 kHz. (b) Power spectrum of the excitation and acquired signals.

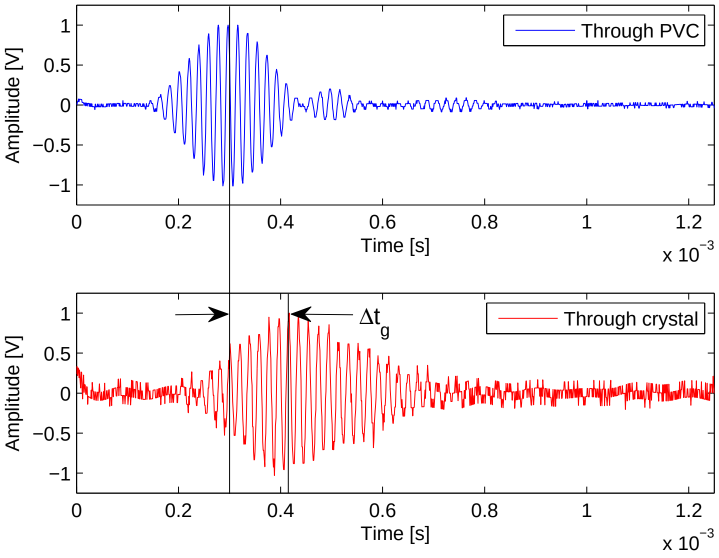

Figure 7.9: Top and bottom panels present time waveforms for a 21 cycles Hanning modulated pulse centred at 42.5 kHz propagating through the ordinary PVC plate and through the phononic region, respectively. A significant time delay can be observed when the wave propagates in the phononic region of the plate.

surement head is connected to a data acquisition system and steering circuit. A synchronisation cable connects the digital generator with the steering circuit through the amplifier that feeds the inducing signal to the piezoelectric element. Additionally, a signal from the generator is fed into the data acquisition system. A computer system integrated with the data acquisition system and steering circuit provides communication with the user and allows measurements to be processed [1].

In the following, out-of-plane velocity maps for exciting pulses with central frequencies corresponding to 15 and 27.5 kHz are presented in Fig. 7.12. As it can be seen, the experimental behaviour reproduces quite well the numerically predicted behaviour. In particular, the expected "blind" area inside the phononic region is clearly visible in Fig. 7.12b.

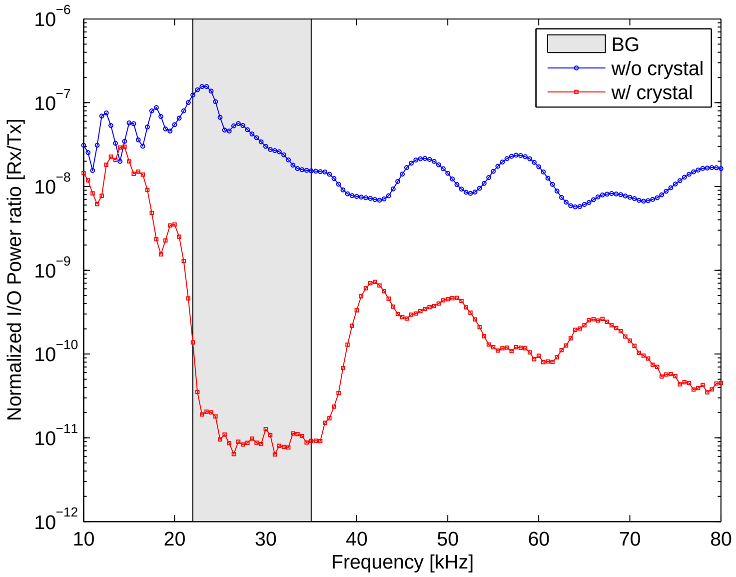

Figure 7.10: Transmission power spectrum as a function of the frequency. The y axis is normalised w.r.t. the input signal energy content. The light grey rectangular box denotes the numerical predicted band gap width.

7.1.5 Results and discussion

Existence of band gap for Lamb waves concerning a phononic plate of finite thickness with rounded cross-like holes recently numerically investigated is here experimentally validated through measurements of the transmission power spectrum. Screening potentials of such a phononic material have been highlighted.

Experimental results are in very good agreement with the numerical ones locating accurately BG frequency range, capturing the dropping trend of the transmission power spectrum. In fact a relatively large complete band gap between 22 and 36 kHz was observed.

It has been also noted that dispersion introduced by the phononic region is very strong, resulting in a dramatic temporal spreading of the incident acoustic pulse, if compared with waves propagating in the ordinary PVC plate.

It could be interesting to extend the experiments to other geometries of practical interest, and especially to weakly disordered phononic materials, in order to improve the understanding of acoustic wave localization.

(a) (b)

Figure 7.11: Representation of the experimental setup. A scanning measurement head is connected to a data acquisition system and steering circuit. A synchronisation cable connects the digital generator with the steering circuit through the amplifier that feeds the inducing signal to the piezoelectric element. Additionally, a signal from the generator is fed into the data acquisition system. A computer system integrated with the data acquisition system and steering circuit provides communication with the user and allows measurements to be processed.

7.2 Phononic materials in the audio range

7.2.1 Introduction

The majority of both theoretical and experimental studies regarding phononic materials concern the ultrasonic transmissions, which effectively involves the easiest frequency range to study and observe the anomalous phenomena of band gaps, due to the highly directive potentials of ultrasounds. [122].

However, Martínez-Sala et al. [78] found that phononic materials tunability allows band gaps nucleation also in the audible frequency range. Since the Eusebio Sempere sculpture, made of a periodic array of acoustic scatterers (solid cylinders) embedded in a homogeneous matrix material (air) proved to exhibit partial band

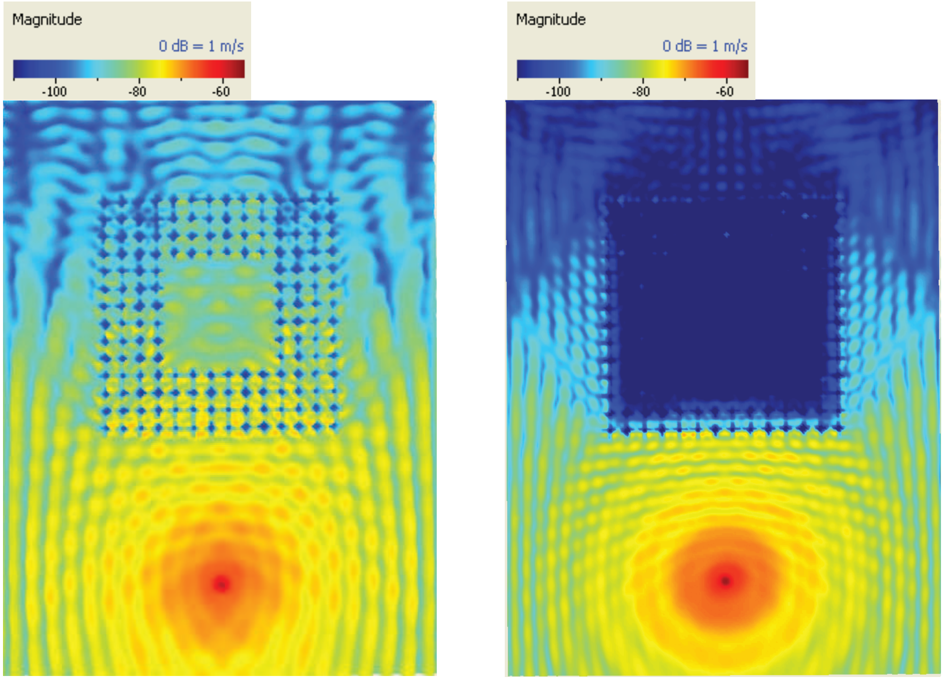

(a) (b)

Figure 7.12: Measured out-of-plane velocity maps for cross-rounded holes phononic plate. Frequency excitations were centred at: (a) 15 kHz, i.e. outside the band gap and (b) 27.5 kHz, i.e. inside the band gap.

gaps also in the acoustic frequency range, a large number of theoretical and experimental investigations have been carried out on the topic [86, 88, 112, 123].

These studies have shown the existence of a pronounced sound attenuation band strongly connected with a large acoustic impedance ratio between the scatterers and the matrix material. The band width and depth vary with the density of the scatterers inside the sonic crystal [7].

The existence of such acoustic band gaps is significant for the design of acoustic wave filters and guides. Usually the goal in the design of sound insulation material is to achieve strong sound attenuation over a large frequency range. However, for application as acoustic filters or noise suppression, materials that impede the propagation of acoustic waves only at selected frequency bands may be desirable, as well [124].

In what follows, evidence of sound attenuation bands in the audible frequency range for a 2P-3D array of hollow cylinders embedded in air are experimentally investigated. Sound insulation index is computed and compared with numerical results for different array geometries in order to validate the numerical predictions.

7.2.2 Sample description

Fig. 7.13 presents both numerical model and tested specimens. The unitary cell of the phononic sample consists of PVC[1] hollow circular cylinder ($R = 80$ mm, $t = 3.2$ mm) immersed in air. Cells are distributed on a square lattice with periodicity $a = 0.2$ m. The phononic system is made of $15 \times n$ cylinders, placed orthogonally to the incident wave (see Fig. 7.13b-c). The n layers extend in the y-direction, resulting into a $n \times a$ m width. Pipes are placed manually within two polystyrene supports (visible at the bottom and top of the cylinders) helping the operators to respect the phononic lattice.

7.2.3 Measurements description

A loudspeaker is placed facing the first row of phononic barrier under test and an array of microphones on the opposite side. The acoustic emitter sends a test sound wave that is partly reflected, partly transmitted, and partly diffracted by the barrier. In particular, the loudspeaker, positioned at a distance $L_{Ls} = 1$ m away from the phononic region[2], generates powerful ultrasonic carrier waves sweeping from $f = 0.2$ up to $f = 3$ kHz frequency range[3]. The microphone, placed at $L_s = 0.25$ m downstream the phononic crystal, receives a signal that, suitably post-processed, gives an overall impulse response. This includes the transmitted component, travelling from the sound source through the noise barrier to the microphone, the component diffracted by the top edge of the screen and other "parasitic" components.

In particular, for the test to be meaningful, the diffraction from the lateral

---

[1] Scatterers are made of PVC in reason of the large impedance contrast between PVC and air, which ensures the hypothesis of infinite rigidity of inclusions w.r.t. the matrix material to be respected.

[2] It is usually accepted that after such a distance, the plane wave nature of the beam is established before the wave-front reach the barrier.

[3] Such a frequency range has been chosen in order to avoid non-linear effects.

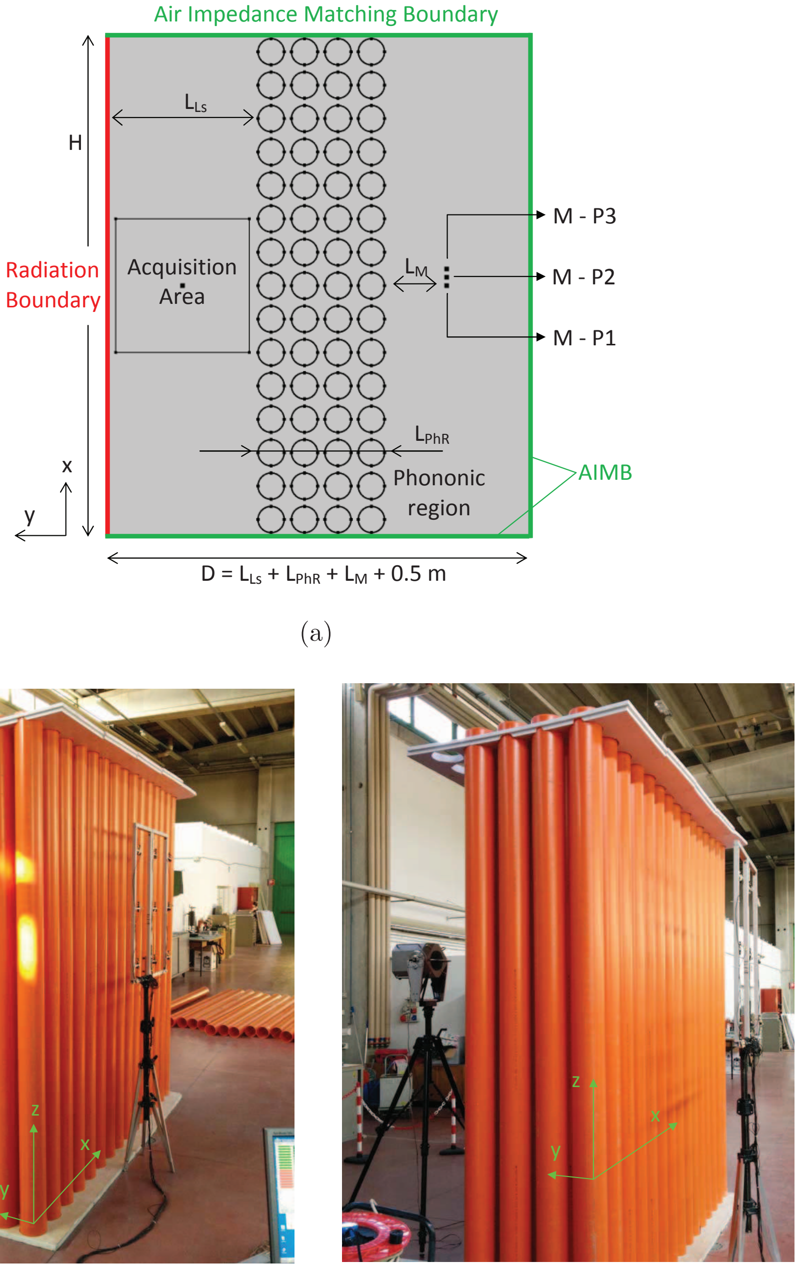

(a)

(b) (c)

Figure 7.13: (a) Numerical model and experimental set-up for the (b) 2-period long and (c) 4-period long specimen consisting of hollow circular cylinders arrays. Scatterers are 3 m long with an external radius $R_e = 80$ mm and a thickness of 3.2 mm. The acoustic wave generator and acquisition microphones are also visible.

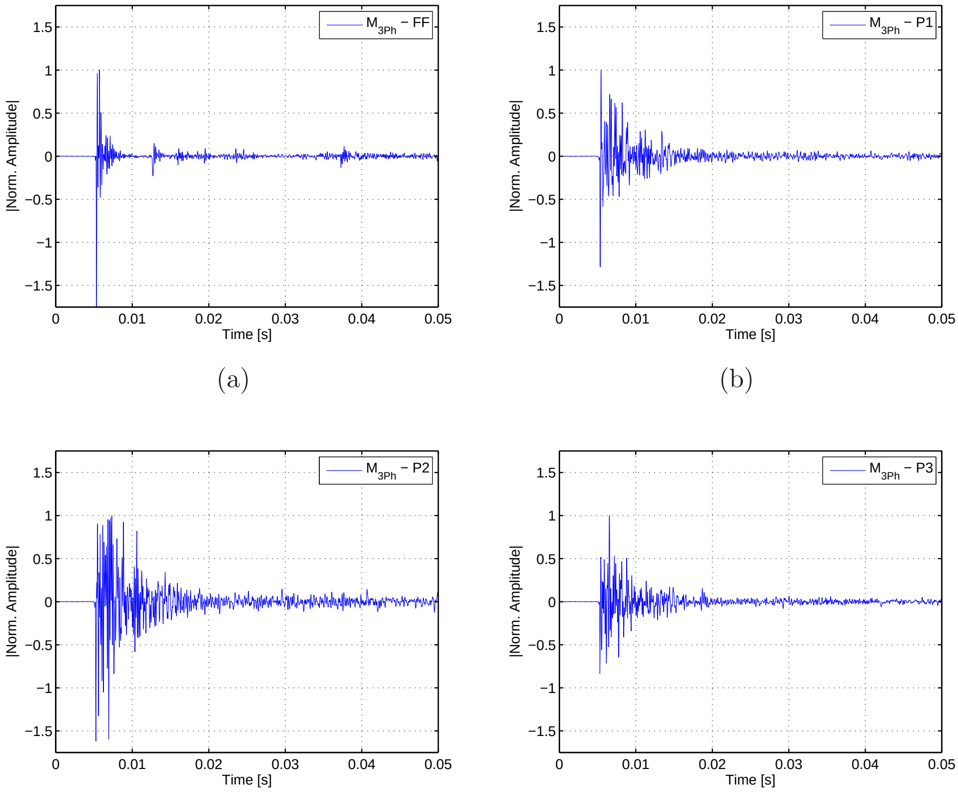

(a) (b)

(c) (d)

Figure 7.14: (a) Experimental response for the free-field measurement and (b-d) the experimental waveforms at the three acquisition points $M-P1$, $M-P2$ and $M-P3$ for the case of $n=3$-period long in the y direction barrier. Amplitudes are normalised to the maximum registered value of each signal.

edges should be sufficiently weak and delayed. The transmitted sound pressure wave is extracted by the global impulse response applying a suitable time window. If the measurement is repeated without the noise barrier between the loudspeaker and the microphone (this is called “free-field” measurement), the direct component alone can be sampled. The power spectra of the direct “free-field” component and the transmitted component, corrected to take into account the path length difference of the two signals, gives the basis for calculating the transmission loss (or sound insulation index, as defined in Section 6.3.2.5).

Four phononic arrangements have been considered varying n from 1 to 4 rows. For each case, measurements are repeated at three points placed on an ideal grid

5 cm horizontally equally spaced ($M - P_i$ scanning points in Fig. 7.13a, with $i = 1, 2, 3$). The final sound insulation index is the logarithmic of the results in the acquisition positions.

7.2.4 Results and discussion

Acoustic pressure time-transient responses are recorded at $L_s = 250$ mm from the last pipes row (see Fig. 7.13) and presented in Fig. 7.14. Incoming waves are clearly visible in the responses within 1.5×10^{-2} s, but nothing can be inferred about the filtering phononic properties.

Therefore, the processing step described in Chapter 6 is exploited to highlight the screening power of the phononic barrier under test. Such a processing leads to the sound insulation indices reported in Figs. 7.15 and 7.16.

Now, the processed signals clearly show the screening power of the phononic barrier. In general, it can be inferred that a good match between numerical predictions and experimental results has been found, especially for what concerns the first directional BG, where at some frequencies a superimposition of the sound insulation index is observed. As numerically predicted, the first BG has a central frequencies approximately of 800 Hz. Finally it is worth remarking that experimental results confirm the numerical prediction of only three rows needed to achieve an insulation index of approximately 30 dB.

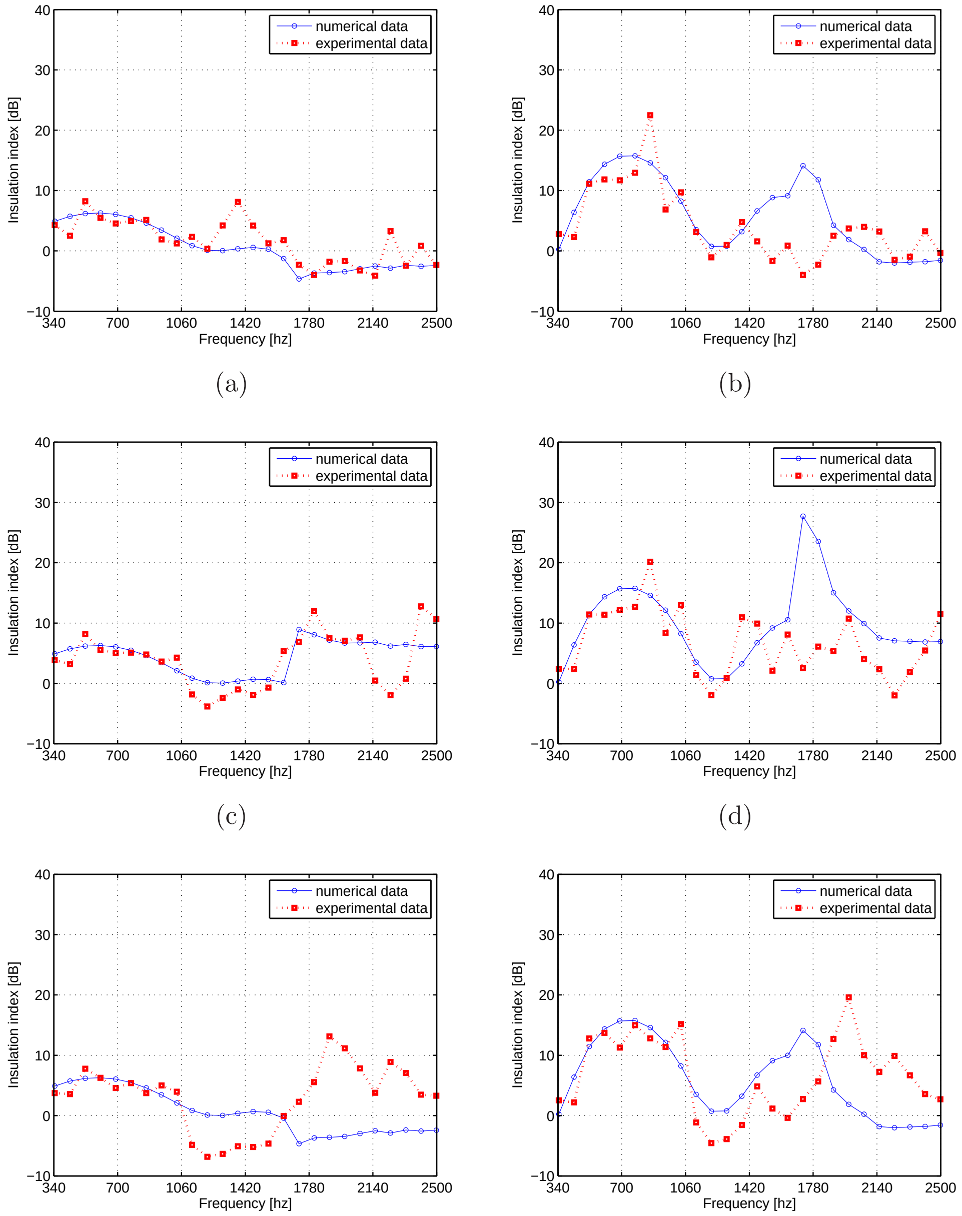

(a) (b)

(c) (d)

(e) (f)

Figure 7.15: Sound insulation index comparison between numerical and experimental analyses. Results are presented for (a, c, e) 1-period long and (b, d, f 2-period long) phononic barrier for (a, b) $M - P1$, (c, d) $M - P2$ and (e, f) $M - P3$ acquisition points, respectively.

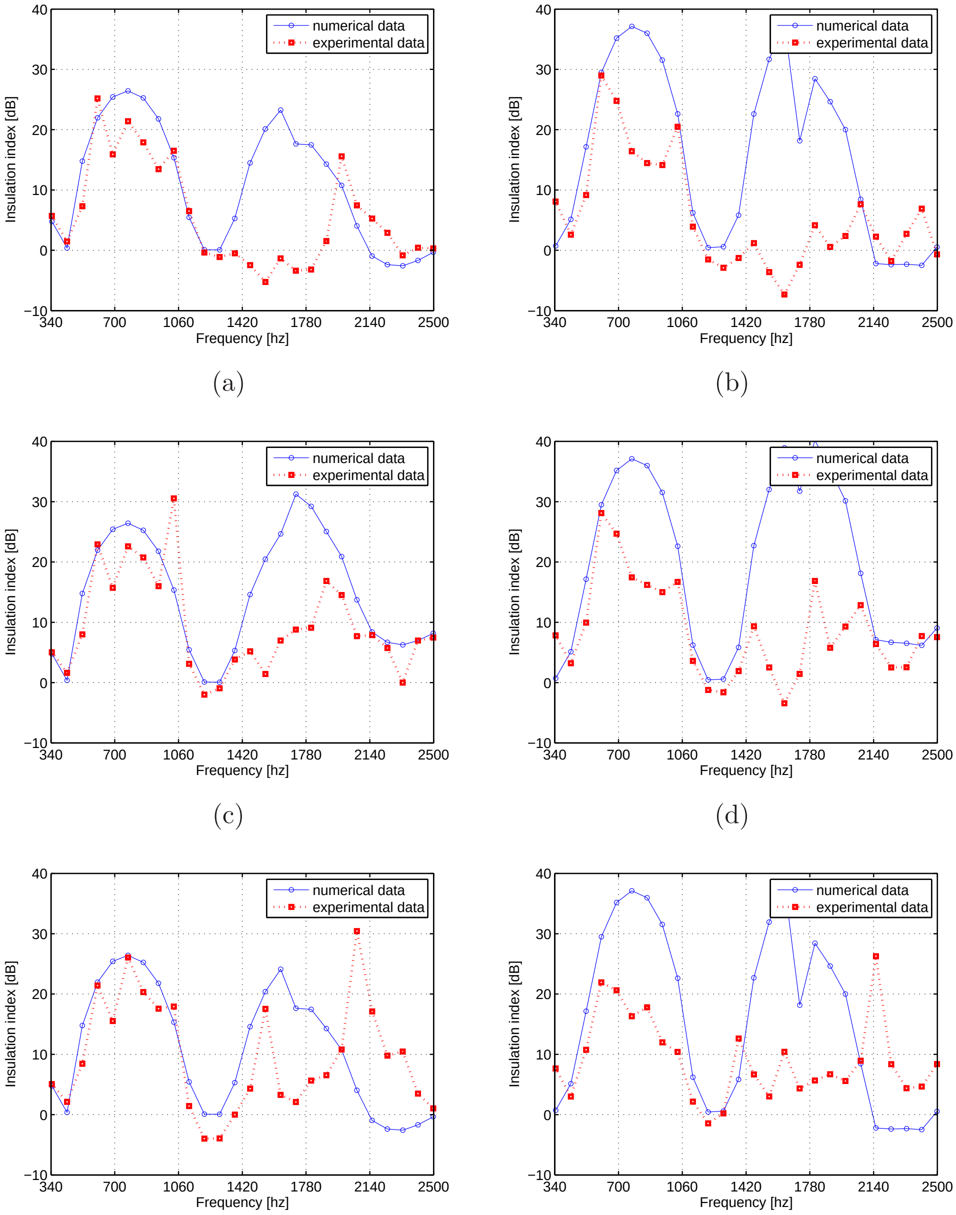

(a) (b) (c) (d) (e) (f)

Figure 7.16: Sound insulation index comparison between numerical and experimental analyses. Results are presented for (a, c, e) 3-period long and (b, d, f 4-period long) phononic barrier for (a, b) $M - P1$, (c, d) $M - P2$ and (e, f) $M - P3$ acquisition points, respectively.

Chapter 8

Seismic shields

8.1 Introduction and state of the art

Reduction or isolation of vibrations for required area enhances structural functionality and safety against natural and man-made induced hazards. This is particularly important in strategic facilities such as hospitals, emergency centres, skyscrapers, energy plants, long span bridges and so on. Therefore engineers and researchers have devoted considerable attention to this topic in the last decades [125].

Elastic waves, including body waves (BWs) and surface waves (SWs), can be generated by several different sources. As examples, some physical sources are indicated in Tab. 8.1 together with the wave typology and its frequency content that such sources produce. Among all the possible natural and man-made causes (trains, tunnels, heavy equipment), certainly earthquakes are the most devastating disasters that can induce building to vibrate. Earthquakes are the result of sudden release of huge amount of energy in the Earth's crust that produces seismic waves with large amplitudes and low frequencies (see Tab. 8.1).

Table 8.1: Waves behaviours and frequency range for various sources.

Physical source	Generated waves	Frequency range [Hz]
Highway/rail	Surface/Body	3 - 40
Buried explosions	Body	1 - 80
Seismic waves	Surface/Body	0.1 - 30

Seismic waves are a kind of inhomogeneous acoustic wave with various wavelengths. Mainly two types of seismic waves exist: body waves, divided into Primary (P) and Secondary (S), and surface waves, Rayleigh (R) and Love (L). Surface waves travel slower than body waves and the amplitudes decrease exponentially with the depth. They travel about $1-3$ km/sec with lots of variety within the depth of a wavelength. The wavelengths are in the order of 100 m and the frequencies are about $10-30$ Hz, that is, low and just below the audible frequency. However, they decay slower than body waves and are most destructive because of their low frequency, long duration, and large amplitude [126].

Rayleigh waves can exist only in an homogeneous medium with a boundary and have transverse motion. Earthquake motions observed at the ground surface are mainly due to R waves. On the other hand, L waves are polarized shear waves guided by an elastic layer. These waves are the main cause of horizontal shifting of the Earth during earthquakes. L waves have both longitudinal and transverse motion and this is what most people feel directly during earthquakes [126, 127].

It is the collapse of bridges, dams, power plants, and other structures that causes extensive damage and loss of life during earthquakes. Therefore, aseismic capabilities are highly relevant to public safety and the design of buildings and other structures capable of withstanding earthquake events has been the focus of research by engineers for many decades. Although a variety of isolation systems have been developed and shown to be effective in tests, some problems still exist with these systems and a commonly accepted method for the design of seismic-resistant buildings and structures has not been developed up to the present time [128].

Traditional strategies commonly accepted by the engineering community as means for decreasing or eliminating the effect of ground vibration on buildings include (i) passive, (ii) active, (iii) hybrid and (iv) semi-active systems.

(i) To nowadays, the most widely diffused isolation strategy is based on passive control devices. The basic idea of a passive control system is to increase the energy dissipation capacity of a structure through dissipative devices placed either within a localized isolation system or diffused over the structure. In such devices reactive forces are imparted to the structure in response to the motion of the structure itself. A passive control system does not require any external power source.

This implies that energy transmitted to the structure cannot be increased by the passive control devices. Passive supplemental strategies can include base isolation systems, viscoelastic dampers, and tuned mass dampers, among the others. Their main drawback is that these passive-device methods are unable to adapt to structural changes and loading conditions. For example, passively isolated structures in one region of Los Angeles that survived the 1994 Northridge earthquake, may well have been damaged severely if they were located elsewhere in the region [129].

(ii) Active control systems are capable to apply forces to the structure in a prescribed manner. These forces can be used to both add and dissipate energy in the structure. Signals sent to the actuators are function of the structure response measured by an active feedback control system by means of physical (optical, mechanical, electrical, chemical, and so on) sensors. Prestressed tendons to stabilize structures, control of tall buildings by cables attached to jacks and use of systems which can provide increased strength to the structure to counter exceptional over-loading are typical examples of active structural control systems [130, 131].

(iii) Afterwards, hybrid control systems are obtained by the combination of active and passive control systems. Because multiple control devices are operating, hybrid control systems can alleviate some of the restrictions and limitations that exist when each system is acting alone. Thus, higher levels of performance may be achieved. Additionally, the resulting hybrid control system can be more reliable than a fully active system, although it is also often more complicated [129]. A structure equipped with distributed viscoelastic damping supplemented with an active mass damper on the top of the structure, or a base isolated structure with actuators actively controlled are examples of hybrid control systems.

(iv) Semi-active control systems have only very recently been considered for structural control applications. A semi-active control system generally originates from a passive control system which has been subsequently modified to allow for the adjustment of mechanical properties. For example, supplemental energy dissipation devices which dissipate energy through shearing of viscous fluid and sliding friction have been modified to behave in a semi-active manner. The mechanical properties of these systems may be adjusted based on feedback from the excitation and/or from the measured response. As in an active control system, a controller monitors the feedback measurements and generates an appropriate command signal for the semi-active devices. As in a passive control system, however, the control forces are developed as a result of the motion of the structure itself. The control forces are developed through appropriate adjustment of the mechanical properties of the semi-active control system. Besides, the control forces in many semi-active control systems primarily act to oppose the motion of the structural system and therefore promote the global stability of the structure. Semi-active control systems are a class of active control systems for which the external energy requirements are orders of magnitude smaller than typical active control systems. Typically, semi-active control devices do not add mechanical energy to the structural system and are often viewed as controllable passive devices [132, 133].

Smart controlled systems (active, semi-active and hybrid control systems) are appealing and have good potential for isolation, but they require sensors and actuators with feedback control loops, which make them more complex than purely passive systems. While research on smart controlled systems is developing, passive isolation systems may be still explored in order to provide a new class of passive isolation system offering higher performance keeping design and implementation simplicity in comparison with active or semi-active systems.

8.2 A potential passive seismic isolation strategy

Based on recent developments in Solid-State Physics, a new idea for passive isolation has been proposed. Differently from the traditional technologies briefly summarized above, this method makes use of phononic materials (PMs) in order to shield structures from seismic waves [14, 87, 92, 94, 134].

In brief, Fig. 8.1 shows how in the same PM if the frequency of an incident wave is outside the BG, the wave propagates through the PM and is transmitted to the other side (Fig. 8.1a - top). In contrast, if the incoming elastic wave frequency is within the BG, it is not allowed to propagate through the PM and the energy is partially trapped and partially reflected (Fig. 8.1a - bottom). Similarly, Fig. 8.1b illustrates wave propagation in both periodic and non-periodic structures from a point source [135]. The source generated wave (and energy), supposed in the BG frequency range, cannot propagate in the periodic structure on the left side meanwhile it can, however, propagate in the homogeneous, non-periodic structure on the right side of the figure [135, 136].

The origin of phononic BGs lies in the multiple scattering of a propagating wave at the interfaces of the inclusions (denoted by circles in Fig. 8.1). The scattering leads to the appearance of secondary waves interfering with each other. Constructive interference results in formation of propagation bands, whereas destructive interference causes BGs. These gaps in the frequencies make PMs acting as elastic reflectors.

When the aforementioned interferences are related to the Bragg scattering [137], these types of periodic panels are named "Bragg-scattering periodic panels".

Scalability of the equations that governs wave propagation allowed researchers to focus their efforts on possible applications of periodic materials to civil engineering structure. In fact, any wave phenomena that appears for a certain range of wavelengths and length scale can be extrapolated to other systems whose order length is scaled up or down with respect to the previous one. In other words, if we halve the length scale we double the energies [138]. From the experimental side, this property allows to work with manageable samples in a laboratory environment.

Driven by the aforementioned developments of metamaterial science, some researchers introduced a new seismic isolation system called periodic foundation (PF). PF, differently from traditional base isolation systems, which cause a shift in the structure fundamental vibrating frequency, reduces the seismic response of the structure by means of frequency BGs. The influence of physical and geometrical parameters such as density and elastic modulus as well as filling fraction of the PF and its materials on the BGs were investigated, and different designs proposed.

Bao et al. [139] studied the dynamic responses of a seven-storey frame structure with three different foundations, including the so-called PFs. Numerical simulations proved that seismic waves are not able to propagate in the periodic foundation without being attenuated when the frequencies of the seismic wave fall

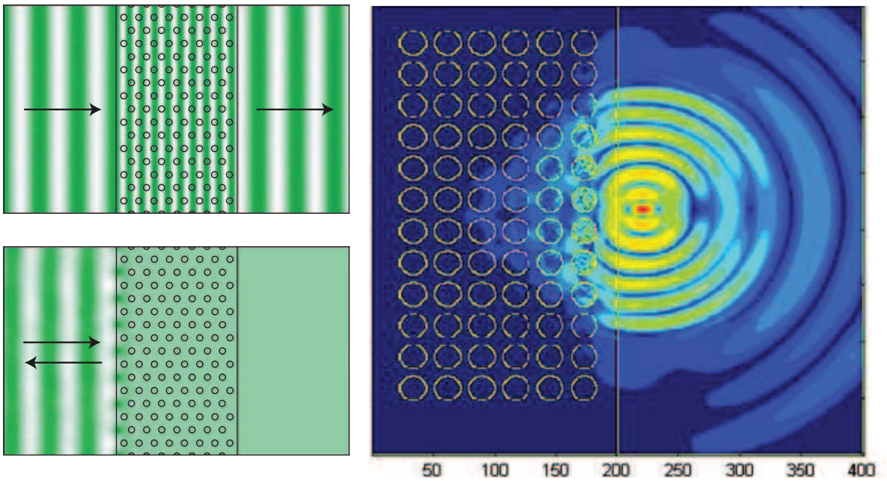

(a) (b)

Figure 8.1: Phononic bandgaps. An elastic wave is incident on the surface of a two-dimensional PM made of cylinders arranged in a triangular lattice. (a) When the frequency of the incoming wave is not inside the BG, the wave is transmitted through the structure (top). If the elastic wave has a frequency within the gap, its propagation is not permitted any more within the PM and it is reflected backwards (bottom). (b) Numerical calculation showing an ultrasonic wave propagating within the periodic metallic composite made of pure aluminium (right) and aluminium-mercury ultrasonic materials (left). The vertical line indicates the boundary between the two regions. The mercury cylinders are indicated by superimposed circles.

within the band of frequency gap of the foundation. Thus, the dynamic responses of the supported structure will be greatly reduced.

Xiang et al. [140], based on previous analytical and numerical results, fabricated a scaled model frame with a periodic foundation and experimentally proved strong harmonic vibration attenuations when the exciting frequencies felt into the BGs, exploiting shake table tests.

Finally, elastic wave attenuation by phononic structure directly built in the ground has been demonstrated both numerically by Alagöz et al. [141] and experimentally by Brûlé et al. [142].

Even though these works demonstrated that periodic materials have a great potential in future applications for seismic isolation, employing the hole-ground structures proposed by Alagöz et al. [141] means involving very large areas, in the order of thousands of meters. On the other hand, Brûlé et al. [142] designed geometries characterized by only partial BG, i.e. for waves propagating in a specific direction, and involved small wave intensities, compared to the earthquake intensities.

The purpose of the present Chapter is to investigate the potential of using PM as seismic barriers. In particular, a parametric study is conducted to achieve a frequency BG in the desired frequency range (1-30 Hz, typical of seismic waves). After that, the benefits of the application of periodic theory in solving the problems of seismic isolation are numerically demonstrated. It is shown that the present findings allow to decrease dramatically the induced seismic displacements to structures (more than 10 times w.r.t. an ordinary structure). For multiple rows of piles, results obtained for both the frequency domain and the time domain show that strong vibration attenuation is found in the range of the calculated BGs. The screening effectiveness of periodic pile barriers and the effect of pile parameters are also discussed.

8.2.1 Strategy overview

In the proposed strategy, the ground is considered the matrix of the PM and it will be referred to as "hosting material". Periodic inclusions are directly built in the ground, just beneath the building foundations, as shown in Fig. 8.2.

Researchers dealing with pile barriers focused their attention on the development of different theoretical as well as numerical methodologies to analyse the performance of discontinuous pile barriers. However, in most cases, only a single row of piles was investigated and even when multiple rows of piles were considered, the periodic nature of rows of piles was not taken into account and the concept of dispersion curves was not properly discussed [143, 144].

Here, the pile-soil system consists of piles arranged in a periodic configuration and referred as "phononic barrier" or "periodic structures". Geometry and mechanical parameters of the inclusions define the dispersion curves for the periodic pile-soil system allowing the calculation of the attenuation zones (AZs) frequency

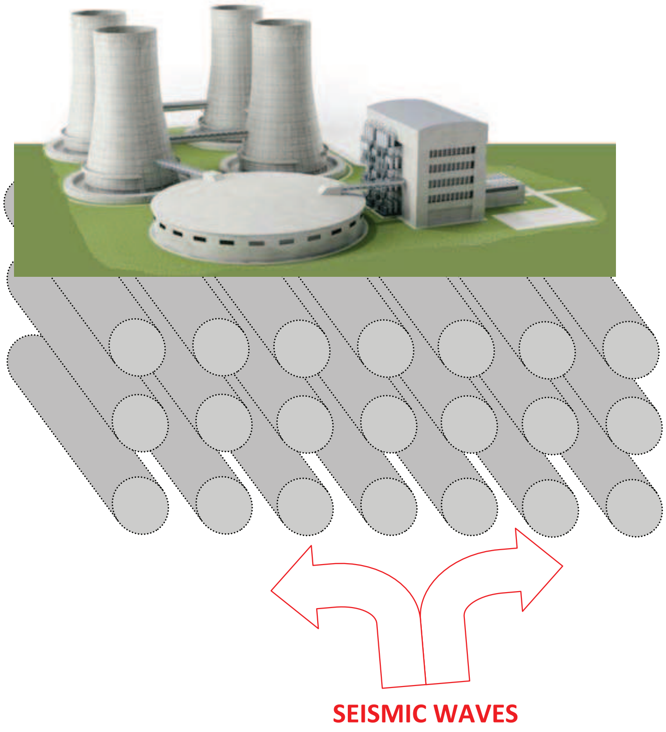

Figure 8.2: Schematic illustration of the metamaterial barrier protecting a strategic building from seismic waves.

range where the elastic waves experience a strong attenuation.

To reveal the inherent properties existing in a complicated system such as a 3D pile soil system, some simplifications and assumptions must be introduced. In the present work, it is assumed that both soil and concrete are homogeneous linearly elastic materials that are perfectly bonded at the interface. In practical engineering, it may be better that the soil is described as inelastic-plastic material. However, goals of this study do not include the estimation of the distribution of stress and strain fields in the ground, which is only modelled to support elastic waves causing structure vibration. Elastic waves are assumed to be plane waves and impacting the periodic piles embedded in the soil from vertical direction. Thus, plane-strain assumption is reasonably introduced [125, 145]. Material mechanical parameters adopted in the present numerical simulation are provided in

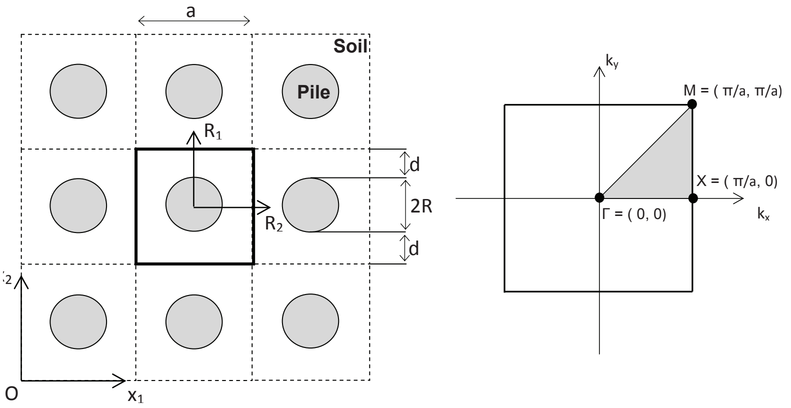

(a) (b)

Figure 8.3: (a) Top view of the infinite pile-soil system. (b) First Brillouin zone and irreducible Brillouin zone.

Tab. 8.2. They are assumed to be constants and stress independent.

Table 8.2: Mechanical properties of the materials used in the analysis. Density ρ, Young modulus E, Poisson ratio ν, longitudinal c_L and transverse c_T speeds of sound are given.

Material	ρ [kg m^{-3}]	E [Pa]	ν [/]	c_L [m $\mathrm{s}^{-}1$]	c_T [m $\mathrm{s}^{-}1$]
Ground	1750	$340 \cdot 10^6$	0.25	482	278
Steel	7850	$210 \cdot 10^9$	0.3	6000	3207
Concrete	2500	$30 \cdot 10^9$	0.25	3794	2190
Rubber	1300	$1.37 \cdot 10^5$	0.463	482	278
Air	1.25	-	-	343	-

Generally speaking, the 2D plane strain model is adopted because this model can reflect some major properties of a pile barrier system in some circumstances. In the present investigation, attention will be focused on the first band of frequency gap, because a low critical frequency for the frequency band is more interesting in civil engineering applications.

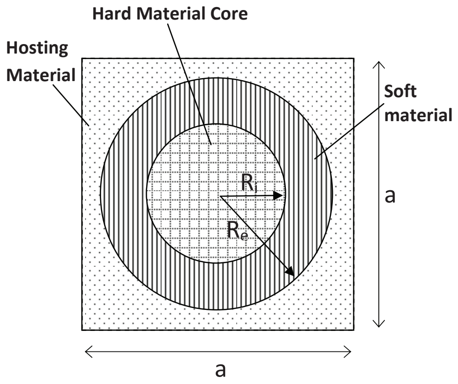

Figure 8.4: Periodic boundary conditions for periodic materials.

8.3 Dispersion relations and attenuation zones

Only a single structural unit of the periodic system is modelled, as shown in Fig. 8.4. It consists of three different materials arranged periodically in a square lattice of constant a. The unit cell is made of: (i) a hard core circular cylinder of radius $R_i = R_{hcm}$; (ii) a soft coating material of thickness $t = R_e - R_i = R_{sm} - R_{hcm}$; (iii) hosting material. Elastic and geometrical properties used in the simulations are listed in Tab. 8.2 and Tab. 8.3, respectively. Parametrically sweeping on wavenumbers, frequency values are extracted by means of an ordinary eigenfrequency solver, under 2D plane strain assumption. The mesh size is set according to the shortest wave length expected among the frequency range, controlled by:

$$\begin{aligned} \lambda_S &= c_S \cdot f_{max} \\ \text{Ł}_{FE} &= \lambda_S / \beta \end{aligned} \tag{8.1}$$

where c_S is the shear wave velocity, f_{max} is the maximum frequency content expected in the propagating wave and β is a coefficient depending on the order of the finite element ($\beta = 10$ for linear elements, $\beta = 4$ for quadratic elements).

First of all, to verify the method used in the present work, dispersion curves for a phononic system made of steel cylinders (hard core material) embedded into a rubber coating (soft material) hosted into a square concrete (hosting material) matrix is solved. Fig. 8.5 shows good agreement of the present method with

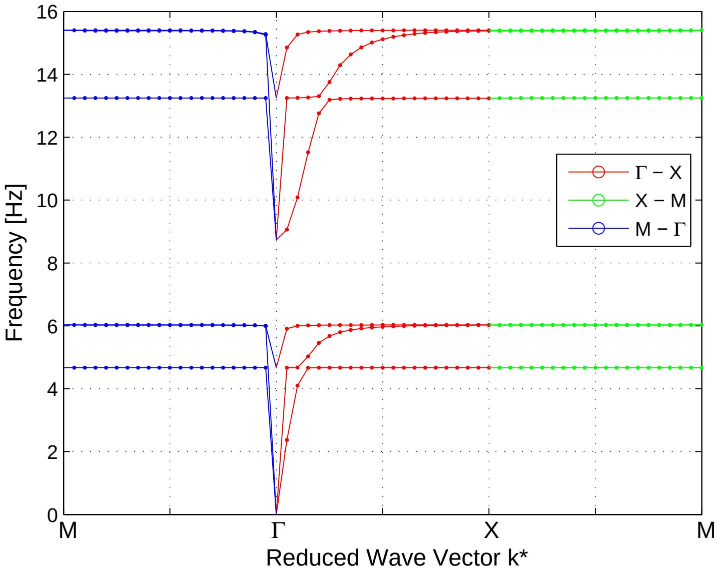

Figure 8.5: Dispersion curves for infinite periodic panels made of steel cylinders embedded into a rubber coating hosted into a square concrete matrix. Results are in perfect agreement with available literature.

literature available results [146].

After, a unit cell considering the soil as the matrix material is considered. The hard material core, made of concrete and with radius of $R_{hcm} = 0.25a$, is embedded into a rubber coating $R_{sm} = 0.45a$. Taking the lattice parameter $a = 1.0$ m, the dispersion curves of the infinite periodic structure are shown in Fig. 8.6. Segments $\Gamma - X$, $X - M$, $M - \Gamma$ on the abscissa represent waves travelling along the direction of $0°$, $0° - 45°$, $45°$ respectively and the vertical coordinate represents the frequency of the wave. Waves with frequencies that have no corresponding reduced wave vector k^* on the abscissa cannot propagate in the periodic structure, since there are no corresponding modes. In this case, the frequency gap is named "complete frequency band gap" and waves coming from all directions cannot travel in the periodic structure. In this case no wave vector can be found in the region $[11.13 - 13.09]$ Hz, between the third and the fourth dispersion curves.

Comparing Figs. 8.5 and 8.6 it clearly emerges that dispersion relations (and therefore attenuation zones) strongly depend on the mechanical and geometrical

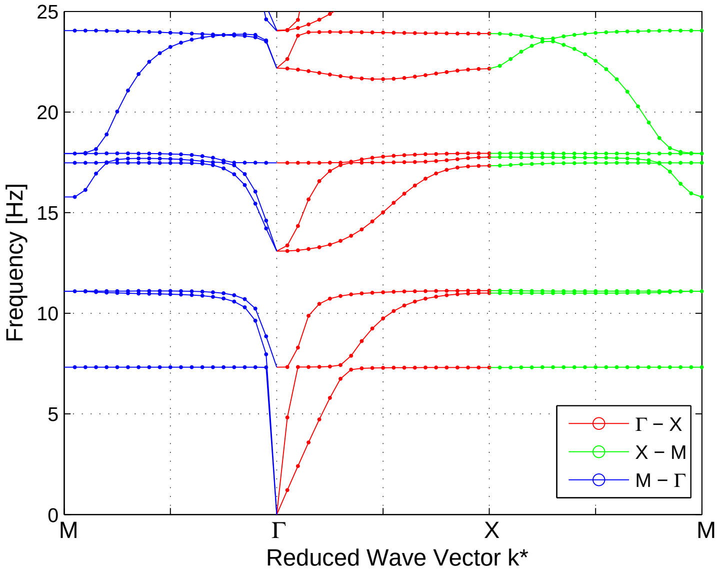

Figure 8.6: Dispersion curves for soil/rubber/steel arrangement with the following geometrical properties: $a = 1$ m, $R_{hcm} = 0.25a = 0.25$ m and $R_{sm} = 0.45a = 0.45$ m.

parameters of the PM. In the following, a comprehensive parametric study is performed in order to identify the most influential properties on the band gap frequency range and to understand how they modify the dispersion relations.

8.4 Parametric study

As mentioned before, waves with frequencies in the range of the AZs cannot propagate in the PM. As wave propagation in strongly influenced by mechanical and geometrical properties of the lattice, this makes PM innovative filters for mechanical waves. In fact different AZs can be achieved when different materials and geometries are proposed for the lattice. A comprehensive knowledge of how this parameters influence the AZs is of paramount importance to the PM design in order to produce proper AZs able to block the propagation of waves in a desired frequency range. The study is focused on vibrational properties connected with the mechanical/geometrical parameters of the structure, which can be engineered to provide special effects, such as:

i. frequency band gap shifting, i.e. the lower bound frequency (LBF) and upper bound frequency (UBF) of band gaps shift in frequency depending on the lattice parameters. This can produce significant variations in the width of the attenuation zones (WAZ);

ii. frequency band gap annihilation, i.e. LBF and UBF shift in opposite direction (LBF increases and UBF decreases) so that WAZ assumes the null value (the band gap no longer exists);

iii. frequency band gap nucleation, i.e. dispersion curves do not cover any more specific frequency ranges (a new band gap is formed).

With reference to the attenuation zone shown in Fig. 8.6, a comprehensive investigation of factors influencing the AZ is provided. Results are summarized for the different cases showing the lower bound frequency (LBF), upper bound frequency (UBF) and the width of attenuation zone (WAZ) changes as function of the parameter. Both geometrical (radius of the core R_{hcm} and of the soft material R_{sm}) and mechanical properties (Young modulus E, Poisson ratio ν, density ρ) are studied. The periodic constant is set $a = 1$ m. In the following parametric discussion one of the parameters changes, whereas all the other remain unchanged. The base settings are presented in Tab. 8.3.

Table 8.3: Base parameters settings and variations.

Material parameter	Base value	Variation range
a	1 [m]	-
R_{sm}	0.45 [m]	0.30 - 0.45 [m]
R_{hmc}	0.27 [m]	0 - 0.36 [m]
E_{hm}	$340{\cdot}10^6$ [Pa]	$1{\cdot}10^3$ - $500{\cdot}10^6$ [Pa]
ν_{hm}	0.25 [-]	0.1 - 0.4 [-]
ρ_{hm}	1750 [kg/m^3]	0.30 - 0.45 [kg/m^3]
E_{sm}	$1.37{\cdot}10^5$ [Pa]	$1{\cdot}10^3$ - $7{\cdot}10^5$ [Pa]
ν_{sm}	0.463 [-]	0.1 - 0.4 [-]
ρ_{sm}	1300 [kg/m^3]	1000 - 1800 [kg/m^3]
E_{hmc}	$30{\cdot}10^9$ [Pa]	$1{\cdot}10^9$ - $400{\cdot}10^9$ [Pa]
ν_{hmc}	0.25 [-]	0.1 - 0.4 [-]
ρ_{hmc}	2500 [kg/m^3]	1000 - 7000 [kg/m^3]

8.4.1 Filling fraction

Considering a typical square arrangements of the unit cell, the influence of the filling fraction, i.e. the ratio between the inclusion and matrix areas, on the attenuation zones is first investigated. Keeping $a = 1$ m, two cases are considered: (i) pile radius of the hard material core varying in the range $R_{hmc} \in [0, 0.36a]$ and rubber coating external radius $R_{sm} = 0.45a$; (ii) rubber coating external radius varying in the range $R_{sm} \in [0.30a - 0.45a]$ and pile radius of the hard material core $R_{hmc} = 0.27a$.

Dispersion curves are shown in Figs. 8.7 and 8.8, respectively. Results are interpreted by means of Fig. 8.9, where UBF, LBF and WAZ for the complete frequency band gap are presented. In both cases, dispersion curves shift producing changes in the attenuation zone (between the third and the fourth curve). The observed effects are of: (i) increasing the WAZ as the R_{hmc} increases or (ii) decreasing the WAZ as the R_{sm} increases. Besides the band gap itself undergoes a shifting process: (i) BG shifts towards higher frequencies as the R_{hmc} approaches $a/2$ and (ii) towards lower frequencies as the R_{sm} increases. Trends are not linear.

For sake of clarity, when the pile radius of the hard material core is $0.09a$, the complete band gap just started nucleating and it is barely visible. Contrary, when $R_{hcm} = 0.36a$ a large WAZ ranging from 17.71 Hz to 25.05 Hz is obtained. From a practical point of view, this range corresponds to the middle dominant frequencies of vibrations for rail traffic. Thus, commonly available pile diameters have potential applications in ground vibration reduction.

8.4.2 Hosting material parameters investigation

Mechanical properties of the hosting material (soil in the examined case) are important parameters in design of pile barriers. In fact, in practical applications, while soft coating and core material properties (elastic modulus, Poisson ratio, density) can generally be chosen, soil properties are given by the site condition and very few man-made adjustment can be done. They vary significantly due to different location conditions and different soil types, especially the soil modulus which ranges from 1 MPa to 200 MPa [147] (see Tab. 8.4), from types of soft soils, such as loose uniform sand, stiff clay, and soft clay to hard soils such as gravels.

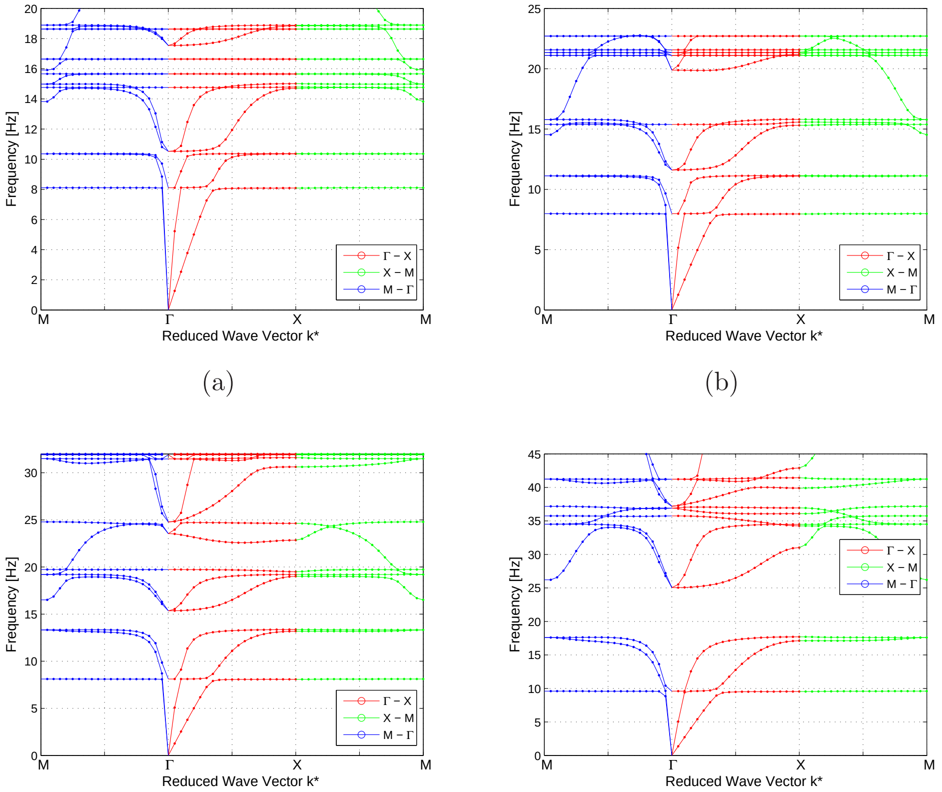

(a) (b)

(c) (d)

Figure 8.7: Influence of the filling fraction on dispersion modes in a soil/rubber/concrete PM: (a) $R_{hmc} = 0.09a$ (b) $R_{hmc} = 0.018a$, (c) $R_{hmc} = 0.27a$, (d) $R_{hmc} = 0.36a$.

Similarly, common soil Poisson ratio and density are in the range of $1800 - 2000$ kg/m^3 and $0.1 - 0.45$, respectively.

In this work $E_{hm} \in [1 - 500]$ MPa, $\nu_{hm} \in [0.1 - 0.4]$ and $\rho_{hm} \in [1600 - 2200]$ kg/m^3 will be used. Fig. 8.10 shows LBF, UBF and WAZ for different values of soil elastic modulus, Poisson ratio and density. These plots suggest that:

i. the most influencing parameter is the elastic modulus. For the considered PM, when a very soft and loose material is considered no band gaps are open. A band gap starts nucleating at $E > 85$ MPa, as shown in Fig. 8.11. Besides, WAZ increases as the hosting material rigidity increases up to 250 MPa. After that it stabilizes.

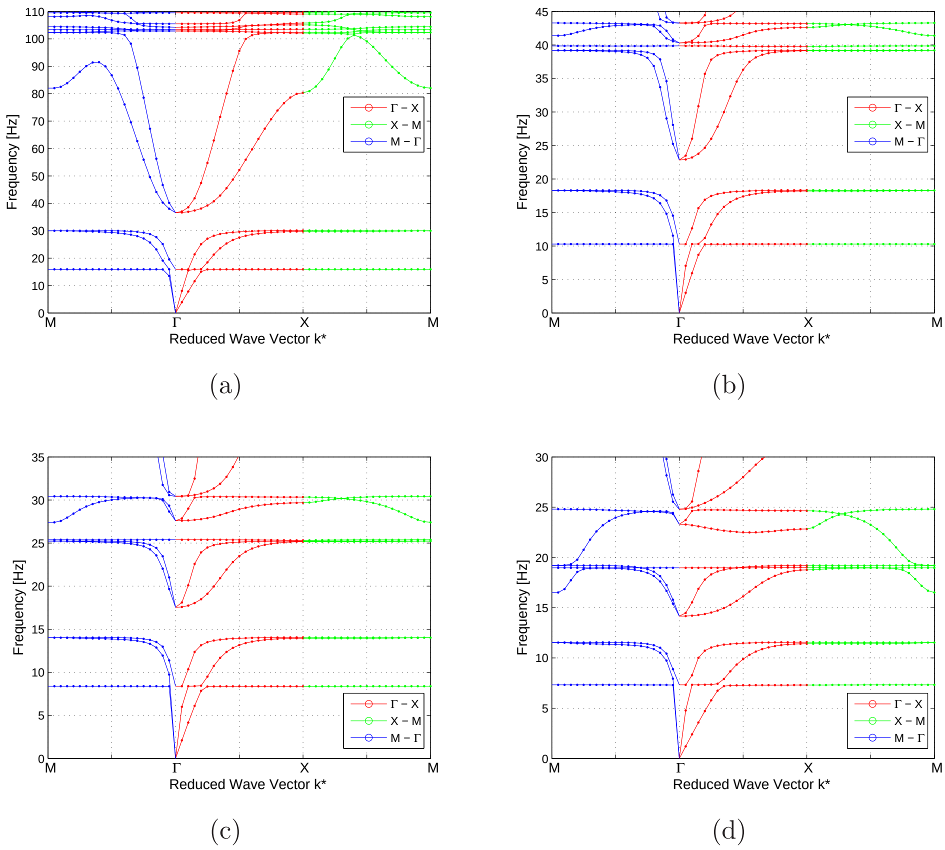

(a) (b)

(c) (d)

Figure 8.8: Influence of the filling fraction on dispersion modes in a soil/rubber/concrete PM: (a) $R_{sm} = 0.30a$ (b) $R_{sm} = 0.35a$, (c) $R_{sm} = 0.40a$, (d) $R_{sm} = 0.45a$.

ii. Poisson ratio has almost no influence on the dispersion relations.

iii. Hosting material density has little influence on the dispersion relations; in particular, the LBF is almost not influenced while the UBF linearly decreases as the density of the hosting material increases.

8.4.3 Hard material core parameters investigation

This study revealed that the elastic modulus and Poisson's ratio of the core have little influence on the BG if compared to the density, which is the most

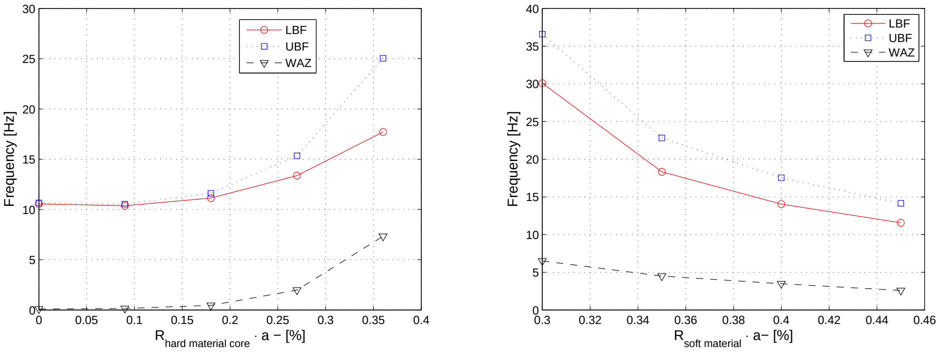

(a) (b)

Figure 8.9: Lower bound frequency (LBF), upper bound frequency (UBF) and width of attenuation zone (WAZ) for different filling fraction of the soil/rubber/concrete PM.

Table 8.4: Mechanical properties of the most common soils. Density ρ, Young modulus E and Poisson ratio ν are given.

Material	ρ [kg m^{-3}]	E [MPa]	ν [/]
Clay	1900	10 - 200	0.25 - 0.45
Sandy	1800	10 - 50	0.25 - 0.4
Gravel	2000	70 - 170	0.15 - 0.35
Dense sand	2000	35 - 70	0.15 - 0.35
Shale	2500	1'000 - 70'000	0.2 - 0.4
Granite	2700	10'000 - 70'000	0.1 - 0.3

sensitive and effective in altering the band of frequency gap. Therefore, the band of frequency gaps produced by different core materials are compared.

From Fig. 8.12, emerges that as the core density increases, LEF and UBF monotonically decreases rapidly. With $\rho = 7000$ kg/m^3 a LEF as low as 7.29 Hz can be achieved, which is appropriate for seismic isolation. It is also important to note that when the core density becomes very large, a low LEF as well as wider WAZ are achieved. This property is critical and helpful in constructing foundations with a low frequency gap.

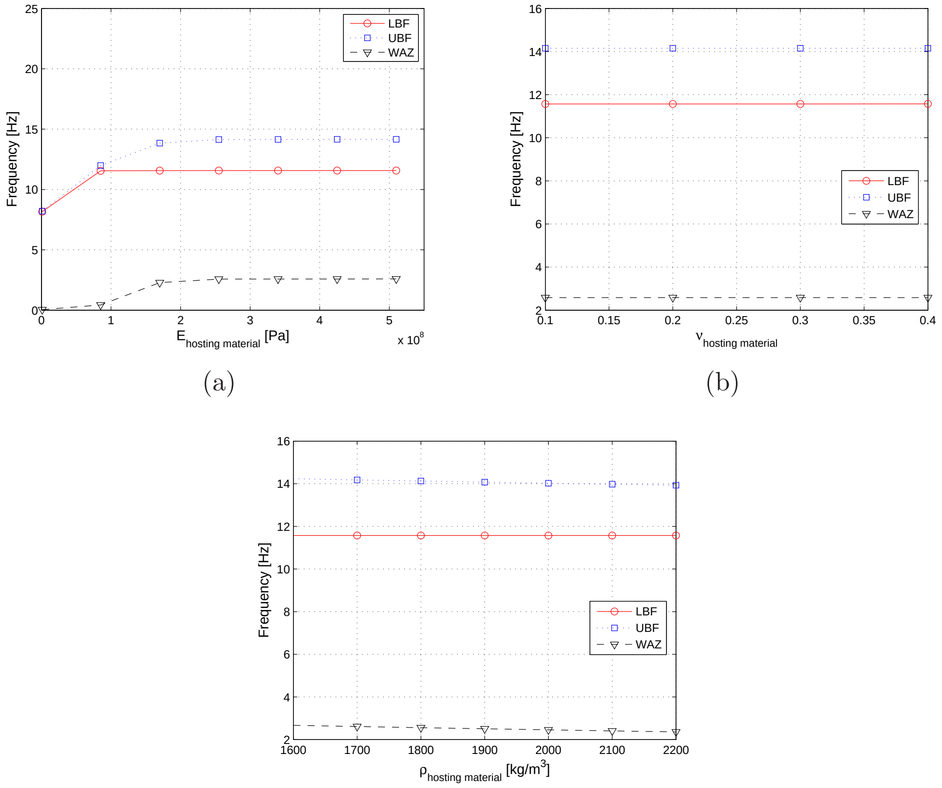

(a) (b)

(c)

Figure 8.10: Lower bound frequency (LBF), upper bound frequency (UBF) and width of attenuation zone (WAZ) for different values of elastic modulus, Poisson ratio and density for the hosting material.

8.4.4 Soft material parameters investigation

Fig. 8.13 shows LBF, UBF and WAZ behaviour as functions of E_{sm}, ν_{hm} and ρ_{hm}, respectively. It can be seen that using different values of rigidity for the coating layer, a maximum of WAZ can be achieved in proximity of $1 \cot 10^5$ Pa, while increasing it up to $1 \cot 10^5$ Pa, a band gap annihilation occurs, i.e. the complete band gap no more exists. Besides, increasing the rigidity of the coating layer, the BG shifts towards higher frequencies values, getting far from the frequencies of interest for seismic isolation. On the other hand, a higher value of Poisson ratio, allows larger BG to form. In the end, lower density of the coating layer leads to larger WAZ as well. This explains the necessity to maintain low elastic modulus

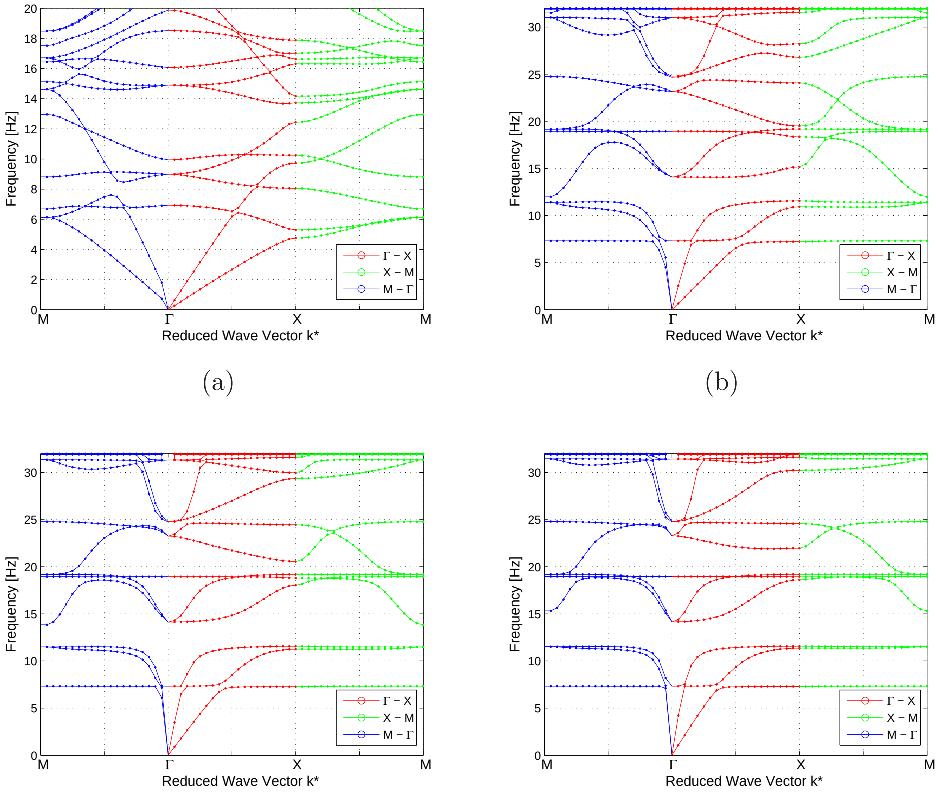

(a)

(b)

(c)

(d)

Figure 8.11: Influence of the hosting material elastic modulus E on the first 15 dispersion modes in a soil/rubber/concrete PM: (a) $E_{hm} = 1$ MPa (b) $E_{hm} = 85$ MPa, (c) $E_{hm} = 170$ MPa, (d) $E_{hm} = 255$ MPa.

and density for the coating layer.

8.5 Numerical validation

Effectiveness of the strong attenuation occurring in finite periodic system has been verified both numerically and experimentally. Very strong attenuation has been observed when the phononic region is made of 4 periods. Based on the above studies, an earthquake-proof barrier is here designed and tested numerically. It consists of a giant metamaterial structure arranged directly in the ground, so to prevent the wave to reach the building itself (see Fig. 8.2).

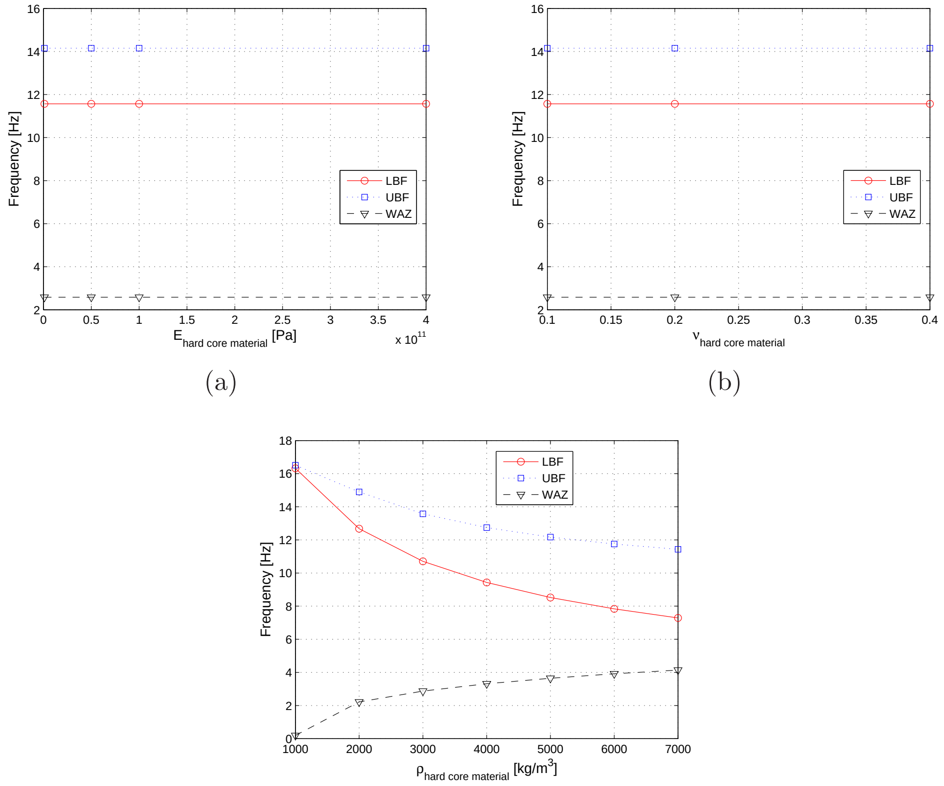

(a)

(b)

(c)

Figure 8.12: Lower bound frequency (LBF), upper bound frequency (UBF) and width of attenuation zone (WAZ) for different values of elastic modulus, Poisson ratio and density for the hard material core.

Based on the above results, a simple geometry constituting the giant phononic metamaterial is proposed and schematically presented in Fig. 8.14a. The hosting material is considered to be a loose sandy soil ($\rho = 1800$ kg/m^3, $E = 20$ MPa and $\nu = 0.4$) and inclusions are made of steel ($\rho = 7800$ kg/m^3, $E = 210$ GPa and $\nu = 0.3$). Lattice parameter is $a = 8$ m and external and internal radii of the inclusion are $R_e = 3$ m and $R_i = 2.7$ m, respectively. Its corresponding dispersion map clearly shows a band gap ranging from 6.3 to 8.1 Hz, as shown in Fig. 8.14b.

To verify vibration attenuation of the designed earthquake proof barrier, soil and four-storey frame structure dynamic response to different inputs for a (i) a soil hosting a phononic region and (ii) for an ordinary soil, as shown in Fig. 8.15 are numerically extracted. Both the structure and specific points of the ground

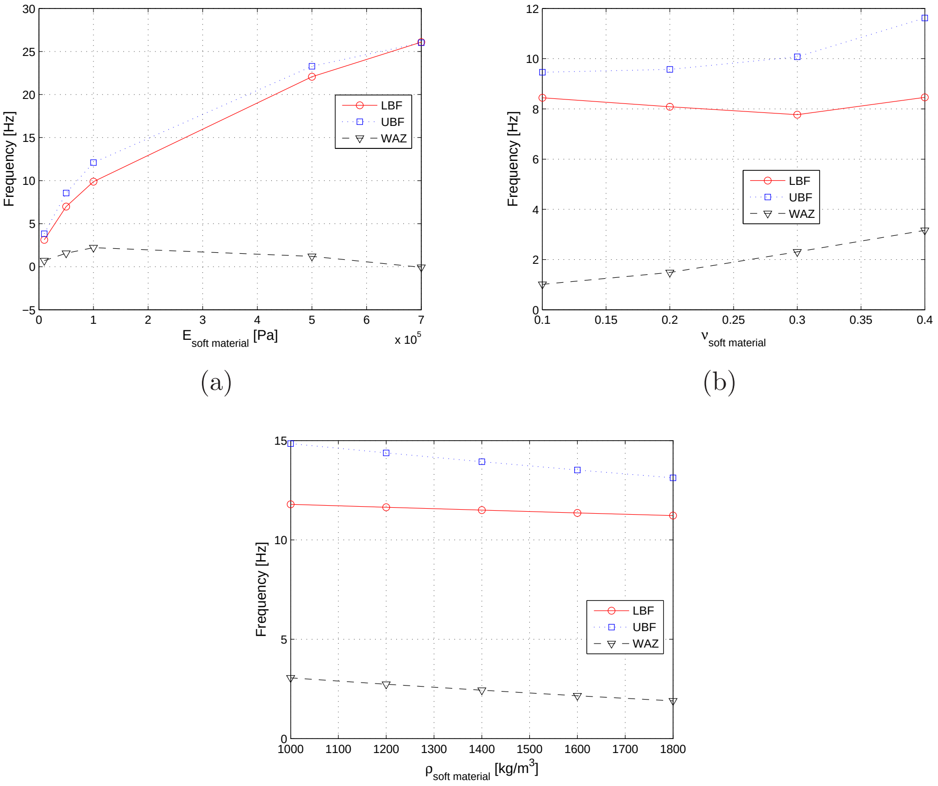

(a) (b)

(c)

Figure 8.13: Lower bound frequency (LBF), upper bound frequency (UBF) and width of attenuation zone (WAZ) for different values of elastic modulus, Poisson ratio and density for the soft material coating.

are monitored.

Fig. 8.15 illustrates the four-storey frame structure built above a loose sandy soil with an earthquake-proof barrier isolation system, as well as the same structure, built above the same soil without isolation capabilities. Mechanical properties (Young's modulus, Poisson's ratio and density) used in the analyses are given in Tab. 8.5.

8.5.1 Responses to incident waves

To numerically quantify the screening power of the giant acoustic metamaterial, both soil and structure responses to incident elastic waves are computed using

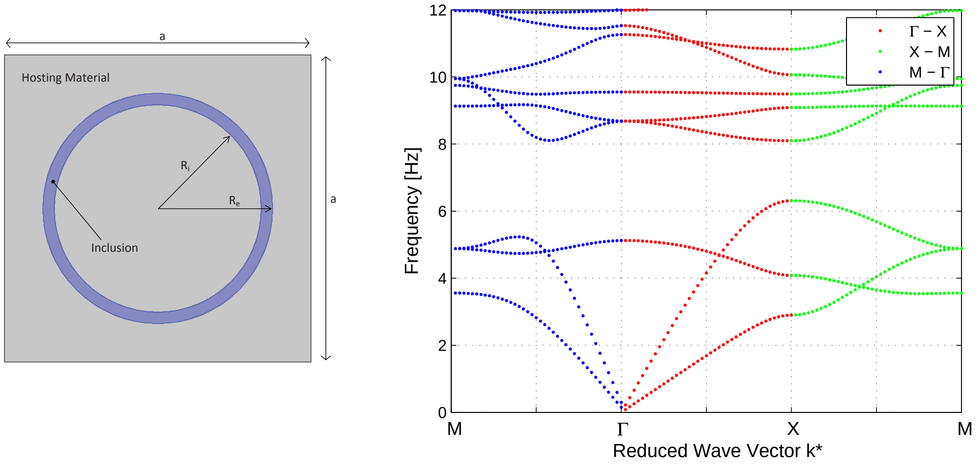

(a) (b)

Figure 8.14: (a) Schematic representation of the giant acoustic metamaterial constituting the earthquake-proof barrier. Hosting material is the ground itself, considered as a loose sandy soil. Inclusions are made of steel. (b) Dispersion map for the giant acoustic metamaterial.

Table 8.5: Mechanical properties of the materials used in the numerical simulations. Density ρ, Young modulus E and Poisson ratio ν are given.

Material	ρ [kg m^{-3}]	E [GPa]	ν [/]
Sandy soil	1800	0.010	0.4
Steel	2500	210	0.3
Concrete	2400	30	0.25

finite element method. First, a simple time-harmonic horizontal incident wave is considered. A displacement with unitary amplitude, as shown in Fig. 8.16, is applied.

The most significant wave propagation patterns are presented in Figs. 8.17 - 8.20, which show snapshots of the stress field at 1.25 s, 2.5 s, 5 s and 7.5 s, for both the case of soil with earthquake-proof barrier and ordinary soil, respectively. Numerical simulations clearly show that when the wave propagating reaches the phononic material, as the frequency content of the wave entirely belongs to the phononic system BG the wave is almost totally reflected back, preventing the building to be reached by the wave (see also Fig. 8.21). Fig. 8.22 provides a

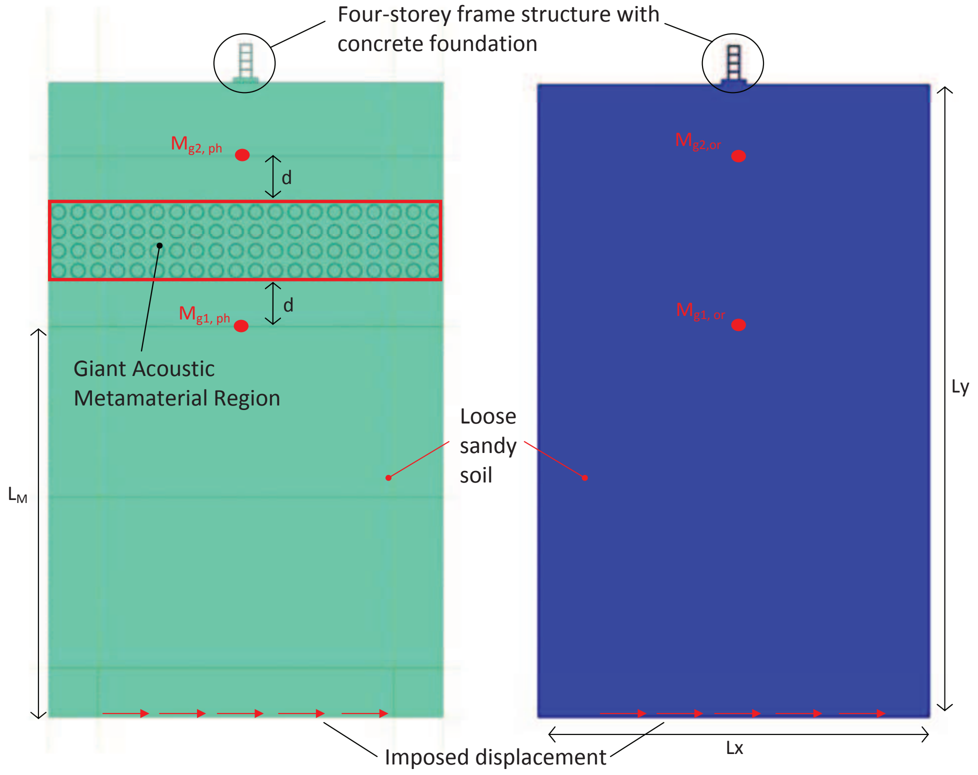

Figure 8.15: Four-storey frame structure built above an earthquake-proof barrier (left side) and on an ordinary loose sandy soil without isolation capabilities (right side).

zoom of the deformations occurring in the two cases.

At this point a seismic response to the El Centro earthquake[1] has been considered as the exciting horizontal displacement of the nodes at the bottom of the considered volume of soil. As the soil damping can reduce the seismic waves as well, in order to show only the reduction of the waves due to giant phononic barrier, no damping was introduced into the soil modelling. The normalized displacement time history and frequency content of the El Centro earthquake is shown in Fig. 8.23. The corresponding energy content of the monitored points

---

[1] El Centro earthquake occurred at 05:35 UTC on May 19 in the Imperial Valley in Southern California near the international border of the United States and Mexico. It had a magnitude of 6.9 and a maximum perceived intensity of X on the Mercalli intensity scale. The earthquake was characterized as a typical moderate-sized destructive event with a complex energy release signature. It was the strongest recorded earthquake to hit the Imperial Valley.

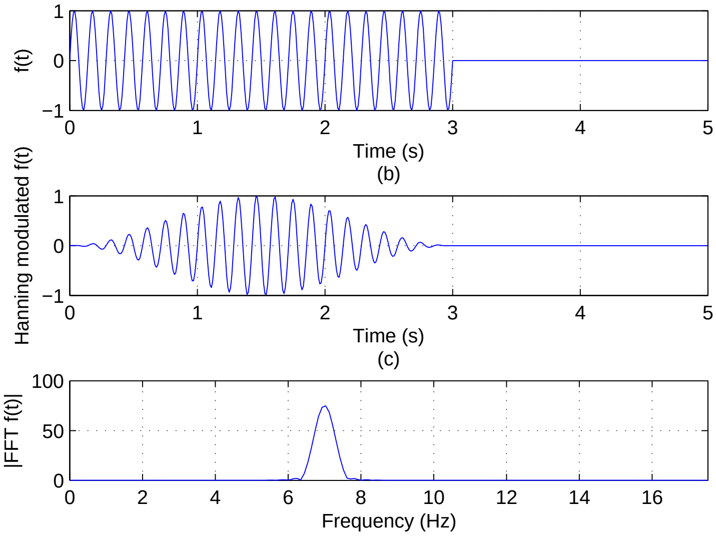

Figure 8.16: Imposed displacement time history for an artificially created horizontal elastic wave. It consists of a 21 cycles modulated Hanning signal with a 7 Hz central frequency.

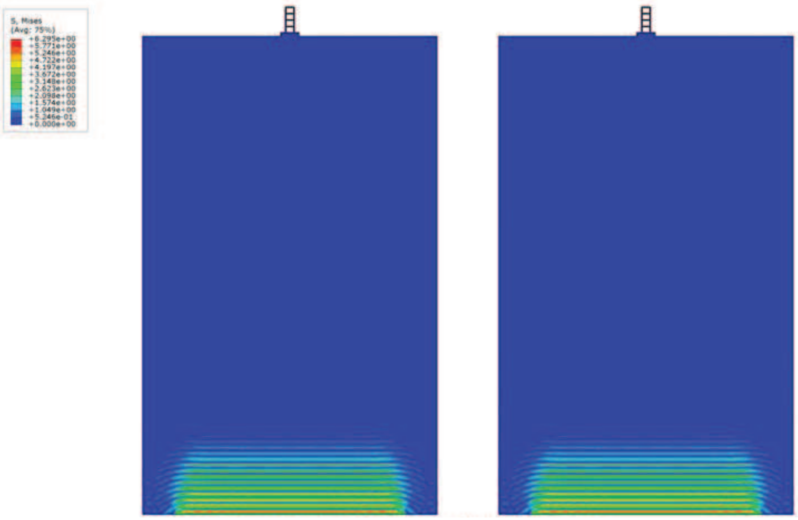

Figure 8.17: Snapshot of the wave propagation phenomenon at 1.25 s. Excitation wave time history is reported in Fig. 8.16.

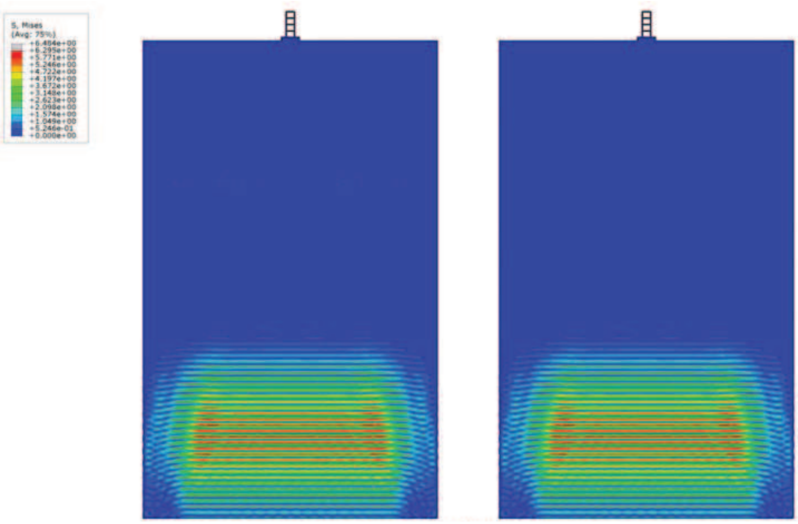

Figure 8.18: Snapshot of the wave propagation phenomenon at 2.5 s. Excitation wave time history is reported in Fig. 8.16.

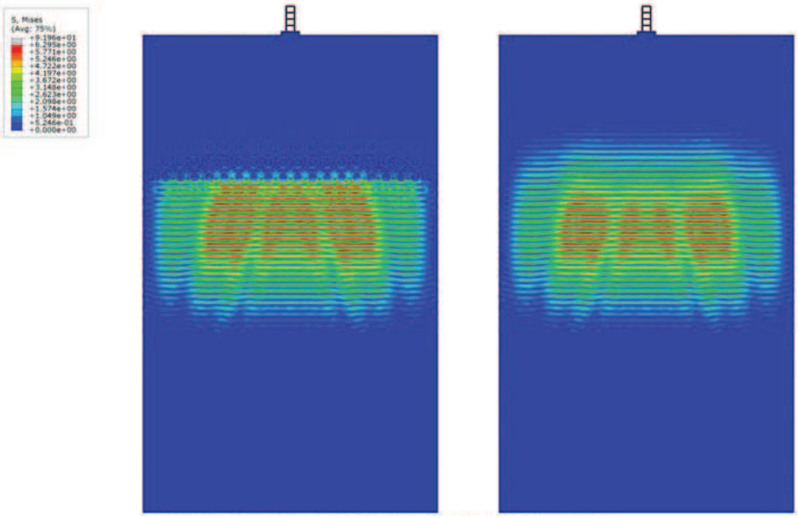

Figure 8.19: Snapshot of the wave propagation phenomenon at 5 s. Excitation wave time history is reported in Fig. 8.16.

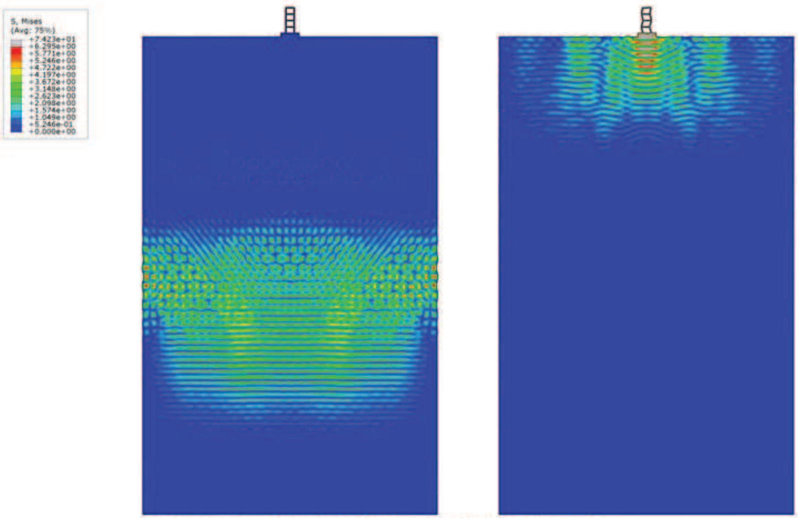

Figure 8.20: Snapshot of the wave propagation phenomenon at 7.25 s. Excitation wave time history is reported in Fig. 8.16.

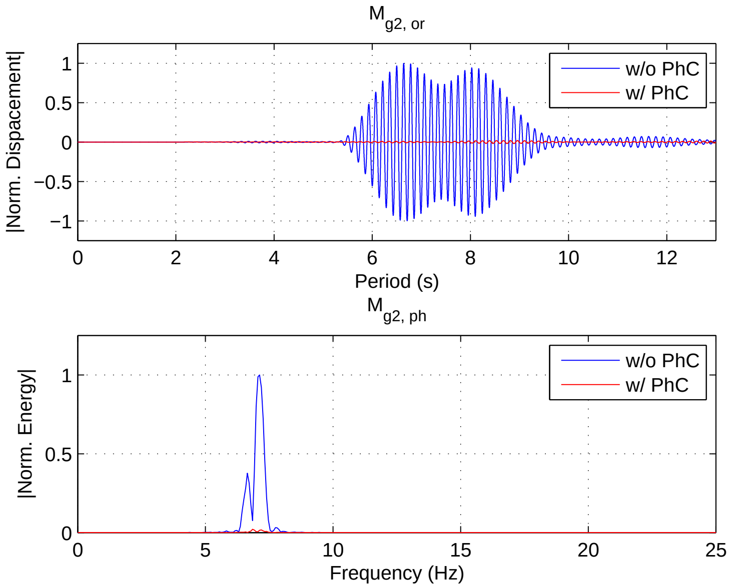

Figure 8.21: Time history and energy content of for the monitoring points.

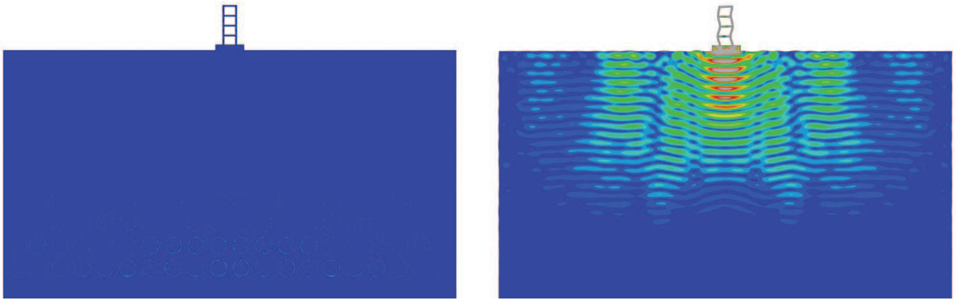
(a) (b)

Figure 8.22: Zoom of the displacement field of the four-storey frame built above a loose sandy soil with phononic isolation capabilities (a) and above the same soil without any PM barrier (b).

$M_{2g,ph}$ and $M_{2g,or}$ in the x-direction are shown in Fig. 8.24. As expected, the part of the input frequency contents falling inside the BGs are much lower if compared to the case of structure without phononic barrier.

8.6 Conclusions: some design considerations

In this study, attenuation of seismic waves via giant phononic metamaterials is numerically demonstrated. In particular, it has been shown that the seismic response of the structure can be greatly reduced when the incident waves are filtered by a phononic barrier with more than three unit cells.

In addition, parametric studies showed that the phononic barrier needs to be accurately designed depending of the soil properties within the which it will be embedded. In fact BGs location and width proved to strongly depend both on geometrical and physical properties of the unit cell constituent materials. Anyway, in general it is possible to infer that the most influential parameters are the filling fraction of the PM and the density of the hard material core, although matrix and coating properties also influence the BG frequency. However, a proper PM design should match the following requests at once: (i) having sufficiently high elastic modulus in order to support upper loads and (ii) having a large contrast in physical properties (mass densities more than elastic constants) between the inclusions and the host material.

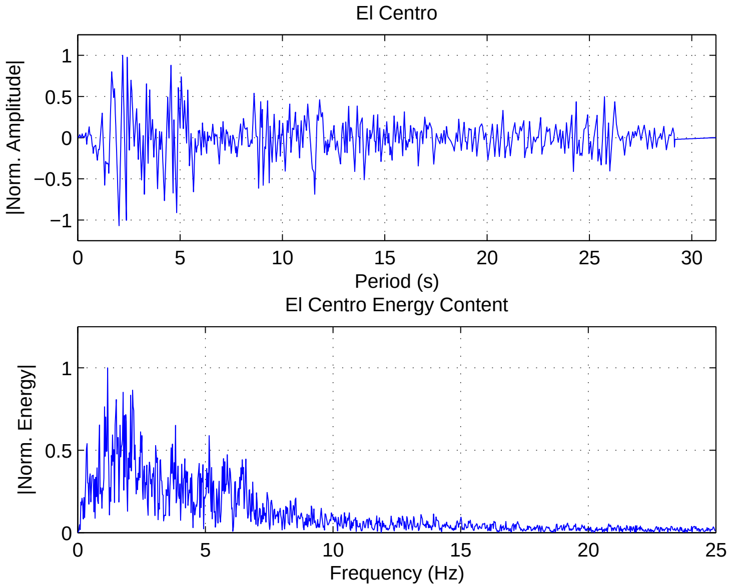

Figure 8.23: Time history and energy content for the El Centro earthquake.

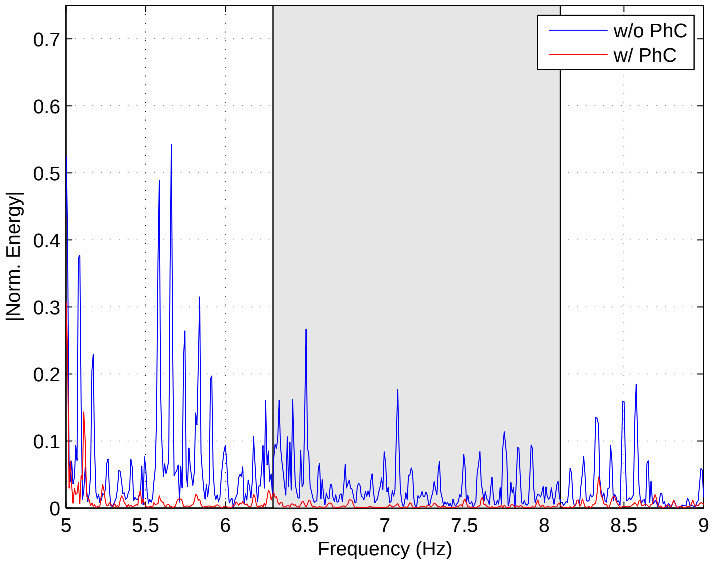

Figure 8.24: Energy content of the monitored point $M_{g,2}$ for an ordinary loose sandy soil without isolation capabilities and the same soil with an embedded PM barrier for the El Centro earthquake.

In conclusion, in this study the feasibility of an innovative passive isolation strategy is proved to be practical for civil structures. This almost total isolation will be of special significance to some emergency/critical structures such as hospitals, bridges, power plants, laboratories, medical facilities and so on, allowing impressive economic savings and structural safety.

References

[1] W. Ostachowicz, P. Kudela, M. Krawczuk, A. Zak, Guided Waves in Structures for SHM: The Time - domain Spectral Element Method, A John Wiley & Sons, Ltd., publication, Wiley, 2012. 1, 2, 70, 154, 159

[2] J. Achenbach, Wave propagation in elastic solids, North-Holland series in applied mathematics and mechanics, North-Holland Pub. Co., 1973. 2

[3] J. Davis, Wave propagation in solids and fluids, Wave propagation in electromagnetic media, Springer-Verlag, 1988. 2

[4] F. Simonetti, Sound propagation in lossless waveguides coated with attenuative materials, PhD thesis - Imperial College, London, 2003. 2

[5] J. L. Rose, Ultrasonic Waves in Solid Media, Cambridge University Press., 1999. 3, 11, 31

[6] M. Mazzotti, Numerical methods for the dispersion analysis of Guided Waves, PhD thesis - Alma Mater Studiorum, University of Bologna, Bologna, 2013. 3

[7] V. Romero-García, C. Lagarrigue, J.-P. Groby, O. Richoux, V. Tournat, Tunable acoustic waveguides in periodic arrays made of rigid square-rod scatterers: theory and experimental realization, Journal of Physics D: Applied Physics 46 (30) (2013) 305108. 3, 162

[8] R. Craster, S. Guenneau, Acoustic Metamaterials: Negative Refraction, Imaging, Lensing and Cloaking, Springer Series in Materials Science, Springer London, Limited, 2012. 3, 107, 149

[9] J. B. Pendry, A. J. Holden, W. J. Stewart, I. Youngs, Extremely low frequency plasmons in metallic mesostructures, Phys. Rev. Lett. 76 (1996) 4773–4776. 3

[10] Z. Liu, X. Zhang, Y. Mao, Y. Y. Zhu, Z. Yang, C. T. Chan, P. Sheng, Locally resonant sonic materials, Science 289 (5485) (2000) 1734–1736. 4

[11] R. M. Walser, Electromagnetic metamaterials (2001). 4

[12] F. Bilotti, L. Sevgi, Metamaterials: Definitions, properties, applications, and fdtd-based modeling and simulation, International Journal of RF and Microwave Computer-Aided Engineering 22 (4) (2012) 422–438. 4

[13] V. M. Shalaev, Optical negative-index metamaterials, Nature Photonics 1 (2007) 41–48. 4

[14] M. Sigalas, E. Economou, Band structure of elastic waves in two dimensional systems, Solid State Communications 86 (3) (1993) 141 – 143. 6, 80, 87, 88, 172

[15] P. A. Deymier, Acoustic Metamaterials and Phononic Crystals, Springer Series in Solid-State Sciences, Springer Berlin Heidelberg, 2013. 6, 80

[16] A. Marzani, Time-transient response for ultrasonic guided waves propagating in damped cylinders, International Journal of Solids and Structures 45 (25-26) (2008) 6347 – 6368. 11

[17] F. Treyssède, L. Laguerre, Investigation of elastic modes propagating in multi-wire helical waveguides, Journal of Sound and Vibration 329 (10) (2010) 1702 – 1716. 11

[18] T. Hayashi, W.-J. Song, J. L. Rose, Guided wave dispersion curves for a bar with an arbitrary cross-section, a rod and rail example, Ultrasonics 41 (3) (2003) 175 – 183. 12

[19] I. Bartoli, A. Marzani, F. Lanza di Scalea, E. Viola, Modeling wave propagation in damped waveguides of arbitrary cross-section, Journal of Sound and Vibration 295 (2006) 685–707. 12, 19, 26, 29, 38

[20] P. W., Loveday, Semi-analytical finite element analysis of elastic waveguides subjected to axial loads, Ultrasonics 49 (3) (2009) 298 – 300. 12

[21] L., Gavric, Finite element computation of dispersion properties of thin-walled waveguides, Journal of Sound and Vibration 173 (1) (1994) 113 – 124. 12

[22] A. H. Shah, W. Zhuang, N. Popplewell, J. B. C. Rogers, Guided waves in thin-walled structural members, Journal of Vibration and Acoustics 123 (3) (2001) 376–382. 12, 13

[23] S., Finnveden, Evaluation of modal density and group velocity by a finite element method, Journal of Sound and Vibration 273 (1-2) (2004) 51 – 75. 12

[24] A. Marzani, E. Viola, I. Bartoli, F. L. di Scalea, P. Rizzo, A semi-analytical finite element formulation for modeling stress wave propagation in axisymmetric damped waveguides, Journal of Sound and Vibration 318 (3) (2008) 488 – 505. 12, 38

[25] S. Coccia, I. Bartoli, A. Marzani, F. L. di Scalea, S. Salamone, M. Fateh, Numerical and experimental study of guided waves for detection of defects in the rail head, NDT & E International 44 (1) (2011) 93 – 100. 26, 31

[26] Matlab - release 2012a, www.matlab.com. 26

[27] M. Lowe, D. Alleyne, P. Cawley, Defect detection in pipes using guided waves, Ultrasonics 36 (15) (1998) 147 – 154. 31

[28] A. Demma, P. Cawley, M. Lowe, A. Roosenbrand, B. Pavlakovic, The reflection of guided waves from notches in pipes: a guide for interpreting corrosion measurements, NDT & E International 37 (3) (2004) 167 – 180. 31

[29] P. Rizzo, E. Sorrivi, F. L. di Scalea, E. Viola, Wavelet-based outlier analysis for guided wave structural monitoring: Application to multi-wire strands, Journal of Sound and Vibration 307 (12) (2007) 52 – 68. 31

[30] C. M. Lee, J. L. Rose, Y. Cho, A guided wave approach to defect detection under shelling in rail, NDT & E International 42 (3) (2009) 174 – 180. 31

[31] Z. Su, L. Ye, Y. Lu, Guided Lamb waves for identification of damage in composite structures: A review, Journal of Sound and Vibration 295 (3) (2006) 753 – 780. 31

[32] J. Ihn, F. Chang, Pitch-catch active sensing methods in structural health monitoring for aircraft structures, Structural Health Monitoring 7 (1) (2008) 5–19. 31

[33] A. Purekar, D. Pines, Damage detection in thin composite laminates using piezoelectric phased sensor arrays and guided Lamb wave interrogation, Journal of Intelligent Material Systems and Structures 21 (10) (2010) 995–1010. 31

[34] E. Dehghan Niri, A. Farhidzadeh, S. Salamone, A probabilistic framework for acoustic emission (ae) source localization in plate-like structures, Smart Materials and Structures 21 (3) (2012) 035009–16 pp. 31

[35] M. Niethammer, L. Jacobs, J. Qu, J. Jarrzynski, Time-frequency representations of Lamb waves, The Journal of the Acoustical Society of America 109(5) (2001) 1841–1847. 32

[36] J. Hong, K. Sun, Y. Kim, Dispersion-based short-time Fourier transform applied to dispersive wave analysis, The Journal of the Acoustical Society of America 117 (2005) 2949. 32

[37] A. Leger, M. C. Deschamps, Ultrasonic wave propagation in non homogeneous media, Springer, 2009. 32

[38] L. Ambrozinski, T. Stepinski, P. Packo, T. Uhl, Self-focusing Lamb waves based on the decomposition of the time-reversal operator using time–frequency representation, Mechanical Systems and Signal Processing 27 (2012) 337–349. 32

[39] R. Sicard, J. Goyette, D. Zellouf, A numerical dispersion compensation technique for time recompression of Lamb wave signals, Ultrasonics 40 (1-8) (2002) 727–732. 32, 40

[40] P. Wilcox, A rapid signal processing technique to remove the effect of dispersion from guided wave signals, Ultrasonics, Ferroelectrics and Frequency Control, IEEE Transactions on 50 (4) (2003) 419 –427. 32, 40

[41] L. De Marchi, A. Marzani, N. Speciale, E. Viola, A passive monitoring technique based on dispersion compensation to locate impacts in plate-like structures, Smart Materials and Structures 20 (2011) 1 – 9. 32, 37, 40, 54

[42] L. De Marchi, A. Marzani, N. Speciale, E. Viola, Prediction of pulse dispersion in tapered waveguides, NDT & E International 43 (3) (2010) 265–271. 33, 35

[43] M. El-Kettani, F. Luppé, A. Guillet, Guided waves in a plate with linearly varying thickness: experimental and numerical results, Ultrasonics 42 (1-9) (2004) 807–812. 34

[44] Y. Cho, Estimation of ultrasonic guided wave mode conversion in a plate with thickness variation, IEEE Transactions on Ultrasonics, Ferroelectrics and Frequency Control 47 (3) (2000) 591–603. 34

[45] P. Marical, M. E.-C. El-Kettani, M. Predoi, Guided waves in elastic plates with Gaussian section variation: Experimental and numerical results, Ultrasonics 47 (1-4) (2007) 1 – 9. 34

[46] M. V. M. Predoi, M. E. C. El-Kettani, Z. Hamitouche, C. C. Petre, Guided waves in plates with linear variation of thickness, The Journal of the Acoustical Society of America 123 (5) (2008) 3834–3834. 34

[47] C. He, Y. Zheng, J. Zhou, B. Wu, Waveform prediction of ultrasonic guided waves based on spectrum synthesis and phase velocity, Information - An International Interdisciplinary Journal 13 (6) (2010) 2135–2144. 35

[48] R. Edwards, B. Dutton, A. Clough, M. Rosli, Enhancement of ultrasonic surface waves at wedge tips and angled defects, Applied Physics Letters 99 (9) (2011) 094104–094104. 35

[49] Q. Deng, Z. Yang, Propagation of guided waves in bonded composite structures with tapered adhesive layer, Applied mathematical modelling 35 (11) (2011) 5369–5381. 35

[50] P. Bocchini, A. Marzani, E. Viola, Graphical user interface for guided acoustic waves, Journal of Computing in Civil Engineering 25 (3) (2011) 202–210. 38, 45

[51] L. De Marchi, A. Perelli, A. Marzani, A signal processing approach to exploit chirp excitation in Lamb wave defect detection and localization procedures, Mechanical Systems and Signal Processing 39 (1-2) (2012) 20–31. 40

[52] Abaqus - release 6.12, www.simulia.com. 42, 59, 66, 102

[53] F. Moser, L. J. Jacobs, J. Qu, Modeling elastic wave propagation in waveguides with the finite element method, NDT & E International 32 (4) (1999) 225 – 234. 43

[54] D. Gridin, R. Craster, J. Fong, M. Lowe, M. Beard, The high-frequency asymptotic analysis of guided waves in a circular elastic annulus, Wave Motion 38 (1) (2003) 67 – 90. 49

[55] T. Kundu, H. Nakatani, N. Takeda, Acoustic source localization in anisotropic plates, Ultrasonics 52 (6) (2012) 740 – 746. 54

[56] T. Hajzargerbashi, T. Kundu, S. Bland, An improved algorithm for detecting point of impact in anisotropic inhomogeneous plates, Ultrasonics 51 (3) (2011) 317 – 324. 54

[57] B. Park, H. Sohn, S. E. Olson, M. P. DeSimio, K. S. Brown, M. M. Derriso, Impact localization in complex structures using laser-based time reversal, Structural Health Monitoring 11 (5) (2012) 577–588. 54, 55, 61, 64

[58] H. W. Park, S. B. Kim, H. Sohn, Understanding a time reversal process in lamb wave propagation, Wave Motion 46 (7) (2009) 451 – 467. 55

[59] R.-K. Ing, M. Fink, Time-reversed Lamb waves, Ultrasonics, Ferroelectrics and Frequency Control, IEEE Transactions on 45 (4) (1998) 1032–1043. 55, 57

[60] R.-K. Ing, M. Fink, Time recompression of dispersive Lamb waves using a time reversal mirror-application to flaw detection in thin plates, in: Ultrasonics Symposium, 1996. Proceedings., 1996 IEEE, Vol. 1, 1996, pp. 659–663 vol.1. 55

[61] H. W. Park, H. Sohn, K. H. Law, C. R. Farrar, Time reversal active sensing for health monitoring of a composite plate, Journal of Sound and Vibration 302 (12) (2007) 50 – 66. 55, 57

[62] H. Sohn, M. P. DeSimio, S. E. Olson, K. Brown, M. Derriso, Impact localization in an aircraft fuselage using laser based time reversal (2011). 55

[63] M. Fink, Time-reversal acoustics, Scientific American (1999) 91 – 97. 57

[64] M. Fink, Time reversal of ultrasonic fields - part i: Basic principles, IEEE Transactions on Ultrasonics, Ferroelectrics and frequency control 39 (5) (1992) 555 – 566. 57

[65] F. Wu, J. Thiomas, M. Fink, Time reversal of ultrasonic fields - part ii: Experimental results, IEEE Transactions on Ultrasonics, Ferroelectrics and frequency control 39 (5) (1992) 567 – 578. 57

[66] D. Cassereau, M. Fink, Time reversal of ultrasonic fields - part iii: Theory of the closed time-reversal cavity, IEEE Transactions on Ultrasonics, Ferroelectrics and frequency control 39 (5) (1992) 579 – 592. 57

[67] B. E. Anderson, M. Griffa, C. Larmat, T. J. Ulrich, P. A. Johnson, Time reversal, Acoustics Today 4 (1) (2008) 5–16. 57

[68] B. Xu, V. Giurgiutiu, Single mode tuning effects on Lamb wave time reversal with piezoelectric wafer active sensors for structural health monitoring, Journal of Nondestructive Evaluation 26 (2-4) (2007) 123–134. 59

[69] L. De Marchi, A. Marzani, M. Miniaci, A dispersion compensation procedure to extend pulse-echo defects location to irregular waveguides, {NDT} & E International 54 (0) (2013) 115 – 122. 66

[70] N. Ashcroft, N. Mermin, Solid state physics, Science: Physics, Saunders College, 1976. 84

[71] M.-H. Lu, L. Feng, Y.-F. Chen, Phononic crystals and acoustic metamaterials, Materials Today 12 (12) (2009) 34 – 42. 87

[72] J. O. Vasseur, B. Djafari-Rouhani, L. Dobrzynski, M. S. Kushwaha, P. Halevi, Complete acoustic band gaps in periodic fibre reinforced composite materials: the carbon/epoxy composite and some metallic systems, Journal of Physics: Condensed Matter 6 (1994) 8759–8770. 87, 113

[73] K. Yu, T. Chen, X. Wang, A. Zhou, Large band gaps in phononic crystal slabs with rectangular cylinder inclusions parallel to the slab surfaces, Journal of Physics and Chemistry of Solids 74 (8) (2013) 1146 – 1151. 87, 98, 100, 107, 134

[74] K. L. Manktelow, M. J. Leamy, M. Ruzzene, Topology design and optimization of nonlinear periodic materials, Journal of the Mechanics and Physics of Solids 61 (12) (2013) 2433 – 2453. 87

[75] E. Baravelli, M. Ruzzene, Internally resonating lattices for bandgap generation and low-frequency vibration control, Journal of Sound and Vibration 332 (25) (2013) 6562 – 6579. 87

[76] X. Zhang, Z. Liu, Superlenses to overcome the diffraction limit, Nature Materials 7 (6) (2008) 435 – 441. 87, 149

[77] M. S. Kushwaha, P. Halevi, L. Dobrzynski, B. Djafari-Rouhani, Acoustic band structure of periodic elastic composites, Phys. Rev. Lett. 71 (1993) 2022–2025. 87, 88

[78] R. Mártinez-Sala, J. Sancho, J. V. Sánchez, V. Gomez, J. Llinares, F. Meseguer, Sound attenuation by sculpture, Nature 378 (6554) (1995) 241 – 241. 87, 161

[79] G. Wang, D. Yu, J. Wen, Y. Liu, X. Wen, One-dimensional phononic crystals with locally resonant structures, Physics Letters A 327 (56) (2004) 512 – 521. 87

[80] Y. Zhao, P. Wei, The band gap of 1D viscoelastic phononic crystal, Computational Materials Science 46 (3) (2009) 603 – 606. 87, 100

[81] A.-L. Chen, Y.-S. Wang, Study on band gaps of elastic waves propagating in one-dimensional disordered phononic crystals, Physica B: Condensed Matter 392 (12) (2007) 369 – 378. 87, 96

[82] M. Bavencoffe, B. Morvan, A.-C. Hladky-Hennion, J.-L. Izbicki, Experimental and numerical study of evanescent waves in the mini stopband of a 1D phononic crystal, Ultrasonics 53 (2) (2013) 313 – 319. 87

[83] S. A. El-Naggar, S. I. Mostafa, N. H. Rafat, Complete band gaps of phononic crystal plates with square rods, Ultrasonics 52 (4) (2012) 536 – 542. 87

[84] J.-H. Sun, T.-T. Wu, Propagation of acoustic waves in phononic-crystal plates and waveguides using a finite-difference time-domain method, Phys. Rev. B 76 (2007) 104304. 87, 149

[85] M. S. Kushwaha, P. Halevi, Band gap engineering in periodic elastic composites, Applied Physics Letters 64 (9) (1994) 1085–1087. 87

[86] J. O. Vasseur, P. A. Deymier, A. Khelif, P. Lambin, B. Djafari-Rouhani, A. Akjouj, L. Dobrzynski, N. Fettouhi, J. Zemmouri, Phononic crystal with low filling fraction and absolute acoustic band gap in the audible frequency range: A theoretical and experimental study, Phys. Rev. E 65 (2002) 056608. 87, 162

[87] Y. Pennec, J. O. Vasseur, B. Djafari-Rouhani, L. Dobrzyski, P. A. Deymier, Two-dimensional phononic crystals: Examples and applications, Surface Science Reports 65 (8) (2010) 229 – 291. 87, 89, 107, 150, 172

[88] J. O. Vasseur, P. A. Deymier, B. Chenni, B. Djafari-Rouhani, L. Dobrzynski, D. Prevost, Experimental and theoretical evidence for the existence of absolute acoustic band gaps in two-dimensional solid phononic crystals, Phys. Rev. Lett. 86 (2001) 3012–3015. 88, 162

[89] C. Goffaux, J. Sánchez-Dehesa, Two-dimensional phononic crystals studied using a variational method: Application to lattices of locally resonant materials, Phys. Rev. B 67 (2003) 144301. 88

[90] J. Chen, Y. Xia, X. Han, H. Zhang, Lamb waves in phononic crystal slabs: Truncated plane parallels to the axis of periodicity, Ultrasonics 52 (7) (2012) 920 – 924. 88, 95, 101, 108

[91] Y. Xu, X. Tian, C. Chen, Band structures of two dimensional solid/air hierarchical phononic crystals, Physica B: Condensed Matter 407 (12) (2012) 1995 – 2001. 88, 120, 122, 123

[92] A. Khelif, B. Aoubiza, S. Mohammadi, A. Adibi, V. Laude, Complete band gaps in two-dimensional phononic crystal slabs, Phys. Rev. E 74 (2006) 046610. 88, 113, 172

[93] J.-H. Sun, T.-T. Wu, Propagation of acoustic waves in phononic-crystal plates and waveguides using a finite-difference time-domain method, Phys. Rev. B 76 (2007) 104304. 88, 114

[94] L. Brillouin, Wave propagation in periodic structures: electric filters and crystal lattices, Dover Publications, Dover Publications, 1953. 93, 96, 100, 172

[95] O. Zienkiewicz, The finite element method in engineering science, McGraw-Hill, 1971. 93

[96] O. Zienkiewicz, The finite element method, McGraw-Hill, 1977. 93

[97] S. Sorohan, N. Constantin, M. Gavan, V. Anghel, Extraction of dispersion curves for waves propagating in free complex waveguides by standard finite element codes, Ultrasonics 51 (4) (2011) 503 – 515. 93, 109

[98] Z. He, H. Jia, C. Qiu, S. Peng, X. Mei, F. Cai, P. Peng, M. Ke, Z. Liu, Acoustic transmission enhancement through a periodically structured stiff plate without any opening, Phys. Rev. Lett. 105 (2010) 074301. 95

[99] Comsol multiphysics - release 4.3a, www.comsol.com. 98, 108, 109

[100] M. Bavencoffe, A.-C. Hladky-Hennion, B. Morvan, J.-L. Izbicki, Attenuation of lamb waves in the vicinity of a forbidden band in a phononic crystal, IEEE Transactions on ultrasonics ferroelectrics and frequency control 56 (9) (2009) 1960 – 1967. 100

[101] L. De Marchi, A. Marzani, M. Miniaci, A. Perelli, N. Testoni, Localization of defects in irregular waveguides by dispersion compensation and pulse compression, in: SPIE Smart Structures and Materials, Nondestructive Evaluation and Health Monitoring, International Society for Optics and Photonics, 2013, pp. 869517–869517. 101

[102] A. Khelif, A. Choujaa, S. Benchabane, B. Djafari-Rouhani, V. Laude, Experimental study of guiding and filtering of acoustic waves in a two dimensional ultrasonic crystal, Zeitschrift für Kristallographie 220 (2005) 836. 104

[103] M. Gei, A. B. Movchan, D. Bigoni, Band-gap shift and defect-induced annihilation in prestressed elastic structures, Journal of Applied Physics 105 (6) (2009) –. 107

[104] C. Goffaux, J. P. Vigneron, Theoretical study of a tunable phononic band gap system, Phys. Rev. B 64 (2001) 075118. 107

[105] X.-X. Su, Y.-F. Wang, Y.-S. Wang, Effects of poissons ratio on the band gaps and defect states in two-dimensional vacuum/solid porous phononic crystals, Ultrasonics 52 (2) (2012) 255 – 265. 107

[106] N. Boechler, J. Yang, G. Theocharis, P. G. Kevrekidis, C. Daraio, Tunable vibrational band gaps in one-dimensional diatomic granular crystals with three-particle unit cells, Journal of Applied Physics 109 (7) (2011) –. 107

[107] J.-Y. Yeh, Control analysis of the tunable phononic crystal with electrorheological material, Physica B: Condensed Matter 400 (12) (2007) 137 – 144. 107

[108] Z.-G. Huang, T.-T. Wu, Temperature effect on the bandgaps of surface and bulk acoustic waves in two-dimensional phononic crystals, Ultrasonics, Ferroelectrics and Frequency Control, IEEE Transactions on 52 (3) (2005) 365–370. 107

[109] J. Baumgartl, M. Zvyagolskaya, C. Bechinger, Tailoring of phononic band structures in colloidal crystals, Phys. Rev. Lett. 99 (2007) 205503. 107

[110] F. Chen, P. D. Wilcox, The effect of load on guided wave propagation, Ultrasonics 47 (14) (2007) 111 – 122. 109

[111] M. M. Sigalas, E. N. Economou, Attenuation of multiple-scattered sound, EPL (Europhysics Letters) 36 (4) (1996) 241. 111

[112] M. Sigalas, E. Economou, Elastic and acoustic wave band structure, Journal of Sound and Vibration 158 (2) (1992) 377 – 382. 116, 162

[113] M. S. Kushwaha, P. Halevi, L. Dobrzynski, B. Djafari-Rouhani, Acoustic band structure of periodic elastic composites, Phys. Rev. Lett. 71 (1993) 2022–2025. 116

[114] J. V. Sánchez-Pérez, D. Caballero, R. Mártinez-Sala, C. Rubio, J. Sánchez-Dehesa, F. Meseguer, J. Llinares, F. Gálvez, Sound attenuation by a two-dimensional array of rigid cylinders, Phys. Rev. Lett. 80 (1998) 5325–5328. 120

[115] J. V. Sánchez-Pérez, C. Rubio, R. Mártinez-Sala, R. Sánchez-Grandia, V. Gomez, Acoustic barriers based on periodic arrays of scatterers, Applied Physics Letters 81 (27) (2002) 5240–5242. 120

[116] D. P. Elford, L. Chalmers, F. V. Kusmartsev, G. M. Swallowe, Matryoshka locally resonant sonic crystal, The Journal of the Acoustical Society of America 130 (5) (2011) 2746–2755. 120, 127

[117] M. Garai, P. Guidorzi, European methodology for testing the airborne sound insulation characteristics of noise barriers in situ: Experimental verification and comparison with laboratory data, The Journal of the Acoustical Society of America 108 (3). 129, 132

[118] M. J. Leamy, Exact wave-based bloch analysis procedure for investigating wave propagation in two-dimensional periodic lattices, Journal of Sound and Vibration 331 (7) (2012) 1580 – 1596. 134

[119] S. Mohammadi, A. A. Eftekhar, W. D. Hunt, A. Adibi, High-q micromechanical resonators in a two-dimensional phononic crystal slab, Applied Physics Letters 94 (5). 134

[120] T.-T. Wu, Y.-T. Chen, J.-H. Sun, S.-C. S. Lin, T. J. Huang, Focusing of the lowest antisymmetric Lamb wave in a gradient-index phononic crystal plate, Applied Physics Letters 98 (17). 134

[121] Y.-F. Wang, Y.-S. Wang, Multiple wide complete bandgaps of two-dimensional phononic crystal slabs with cross-like holes, Journal of Sound and Vibration 332 (8) (2013) 2019 – 2037. 134, 135

[122] H. Pichard, O. Richoux, J.-P. Groby, Experimental demonstrations in audible frequency range of band gap tunability and negative refraction in two-dimensional sonic crystal, The Journal of the Acoustical Society of America 132 (4). 161

[123] T. Lu, G. Gao, S. Ma, F. Jin, T. Kim, Acoustic band gaps in two-dimensional square arrays of semi-hollow circular cylinders, Science in China Series E: Technological Sciences 52 (2) (2009) 303–312. 162

[124] M. Hirsekorn, P. Delsanto, N. Batra, P. Matic, Modelling and simulation of acoustic wave propagation in locally resonant sonic materials, Ultrasonics 42 (19) (2004) 231 – 235, proceedings of Ultrasonics International 2003. 162

[125] J. Huang, Z. Shi, Attenuation zones of periodic pile barriers and its application in vibration reduction for plane waves, Journal of Sound and Vibration 332 (19) (2013) 4423 – 4439. 169, 176

[126] R. Villaverde, Fundamental Concepts of Earthquake Engineering, Taylor & Francis Group, 2009. 170

[127] S.-H. Kim, M. P. Das, Seismic Waveguide of Metamaterials, Modern Physics Letters B 26 (2012) 50105. 170

[128] H. J. Xiang, Z. F. Shi, S. J. Wang, Y. L. Mo, Periodic materials-based vibration attenuation in layered foundations: experimental validation, Smart Materials and Structures 21 (11) (2012) 112003. 170

[129] B. Spencer, S. Nagarajaiah, State of the art of structural control, Journal of Structural Engineering 129 (7) (2003) 845–856. 171

[130] T. Soong, Active structural control: theory and practice, Longman Structural Engineering and Struc Series, Longman Scientific & Technical, 1990. 171

[131] T. K. Datta, A state of the art review on active control of structures, Journal of Earthquake Technology 40 (1) (2003) 1 – 17. 171

[132] G. Housner, L. Bergman, T. Caughey, A. Chassiakos, R. Claus, S. Masri, R. Skelton, T. Soong, B. Spencer, J. Yao, Structural control: Past, present, and future, Journal of Engineering Mechanics 123 (9) (1997) 897–971. 172

[133] M. D. Symans, M. C. Constantinou, Semi-active control systems for seismic protection of structures: a state-of-the-art review, Engineering Structures 21 (6) (1999) 469 – 487. 172

[134] C. Kittel, Introduction to Solid State Physics, Wiley, 2004. 172

[135] M. Torres, F. M. de Espinosa, Ultrasonic band gaps and negative refraction, Ultrasonics 42 (19) (2004) 787 – 790. 173

[136] E. L. Thomas, T. Gorishnyy, M. Maldovan, Phononics: Colloidal crystals go hypersonic, Nature Materials 5 (10) (2006) 773 – 774. 173

[137] A. H. Nayfeh, Sound waves in twodimensional ducts with sinusoidal walls, The Journal of the Acoustical Society of America 56 (3) (1974) 768–770. 173

[138] F. Meseguer, M. Holgado, D. Caballero, N. Benaches, J. Sánchez-Dehesa, C. López, J. Llinares, Rayleigh-wave attenuation by a semi-infinite two-dimensional elastic-band-gap crystal, Phys. Rev. B 59 (1999) 12169–12172. 173

[139] J. Bao, Z. Shi, H. Xiang, Dynamic responses of a structure with periodic foundations, Journal of Engineering Mechanics 138 (7) (2012) 761–769. 173

[140] H. J. Xiang, Z. F. Shi, S. J. Wang, Y. L. Mo, Periodic materials-based vibration attenuation in layered foundations: experimental validation, Smart Materials and Structures 21 (11) (2012) 112003. 174

[141] B. Alagoz, S. Alagoz, Towards earthquake shields: A numerical investigation of earthquake shielding with seismic crystals, Open Journal of Acoustics 1 (3) (2011) 63 – 69. 174, 175

[142] S. Brûlé, E. Javelaud, S. Enoch, S. Guenneau, Seismic metamaterial: how to shake friends and influence waves ?, 2013arXiv1301.7642B (2013) 1 – 9. 174, 175

[143] G. Gao, Z. Li, C. Qiu, Z. Yue, Three-dimensional analysis of rows of piles as passive barriers for ground vibration isolation, Soil Dynamics and Earthquake Engineering 26 (11) (2006) 1015 – 1027. 175

[144] T. dai Xia, M. miao Sun, C. Chen, W. yun Chen, X. Ping, Analysis on multiple scattering by an arbitrary configuration of piles as barriers for vibration isolation, Soil Dynamics and Earthquake Engineering 31 (3) (2011) 535 – 545. 175

[145] J. Huang, Z. Shi, Application of periodic theory to rows of piles for horizontal vibration attenuation, International Journal of Geomechanics 13 (2) (2013) 132–142. 176

[146] G. Jia, Z. Shi, A new seismic isolation system and its feasibility study, Earthquake Engineering and Engineering Vibration 9 (1) (2010) 75–82. 179

[147] J. Briaud, Y. Li, K. Rhee, Bcd: A soil modulus device for compaction control, Journal of Geotechnical and Geoenvironmental Engineering 132 (1) (2006) 108–115. 182